Struvite-derived layered double hydroxides: synthesis and applications in sustainable technology.

Samuel Roberts

Christ Church College

University of Oxford

A thesis submitted for the degree of

Doctor of Philosophy

Michaelmas 2024

This thesis is dedicated to the memory
of my grandfather
Roger Harrison

Acknowledgements

Personal

Firstly, I must thank Professor Dermot O'Hare for allowing me to join his group and for introducing me to the wonderful world of LDHs. Thank you for your support and guidance in my research. Then I must thank Dr Chunping Chen for all of her supervision, ideas and advice over the years; this project would not have been possible without you. I must also thank Dr Zoë Turner for her advice and for listening to all my thoughts on LDHs, far from her own world of organometallics. It seems somewhat fitting, from my perspective, that you are both leaving too and I wish you both the best of luck in your future ventures.

To my lab mates over the years, of which there have been many, thank you for making the O'Hare group such an amazing place to work and for providing so many incredible memories, both inside the lab and out. Katie and Claire, thank you for all the chats in our booth and for checking I wasn't going insane when I got unusual results. Keen bean, I hope the dog memes continue to bring you joy and hope that you go far as the face of women in STEM. Also, thank you for introducing me to your housemate Ríona, who became an adopted part of our lab group and a close friend. Ríona, I know we all thought you were terrifying when we first met you, but you have the kindest soul and I can't wait until we can go to the pub again. Sláinte. Claire 'Devlin', you are one of the most positive people I know, thank you for always suggesting a night out or getting us into some sort of mischief. *Emma* (in an Australian accent), the queen of core-shells, thank you for the many laughs over the divider and knowing what to say to make me smile. Matt, my son, I never would have known when I first met you as a Part II, that we would grow so close. I hope our cinema dates continue even after I've left. Look after S4 for me. Justin, it's been a long road we've walked together and I look forward to the road ahead; hopefully we can actualise some of our adventuring plans. Finally, Hugo and Josh, 'no way'! It feels wrong not to thank you both for the energy you brought to our booth and S4 last year. Good luck as you take up the baton, Josh.

To my CDT cohort, thank you for all the laughs throughout the taught course and during the COVID-19 pandemic. We really made the most of those bleak times. Who could ask for more than socially distanced wine and GeoGuessr?

Juxon, what a time to be alive. Thank you to all you contributed: Dom, Ellana, Nick, Winston, Katarina, and the various recurring characters who completed our sitcom of student life. I am so glad I agreed to Dom's proposal to join somewhat of a mystery house; the time we shared there I will remember for the rest of our lives. Thank you for all the dinners, holidays, and laughter; I hope there are many more to come. Dom, thank you for being an amazing housemate (in two different houses!), all the pints, delicious meals, and for listening to my mundane rundowns of lab life. Ellana (Sladé), you bring so much joy into every room, thank you for all the experiences that I never would have thought of trying on my own. Nicholas, I will forever cherish our 'late mornings at Juxon', thank you for trying to educate me literarily, I couldn't have asked for a better man to share ground floor life with. Wini, thank you for keeping me humble in badminton and helping to destroy Nick at boys' night. Uncle Zhu's chicken will forever be a staple of my culinary repertoire and I hope we can get away for many more adventures and curry. Kat, no one predicted it, but we got along like a house on fire. I regret that we only got to spend a year together, but thank you for introducing me to your amazing Persian cuisine.

To the boys (at various times) of York Place: Dom, John, and Alex. Thank you for all the support during this final year. John, thank you for all the carbonaras, you made an excellent addition to boys' night. Alex, thank you for all the gym advice, funny videos and BBQs. I am so glad that we convinced you to move in.

To my home friends: Kir, Will, Jake, Gaia, Tom, Arthur, Viv, Angel (and the many others too numerous to name here). Thank you for not forgetting me whilst I have been away in Oxford and for always making me feel welcome when I came back. I look forward to returning to the fold.

To my partner, Dr Maisie Vollans. Thank you for being the kindest, most thoughtful person on this planet and for all the encouragement and support over the years. Our many adventures together are some of my most cherished memories over the last few years and I look forward to the many more to come.

And finally I must thank my parents, Ann Harrison and Derek Roberts, for supporting me throughout this Doctorate, especially during the COVID-19 pandemic and during the writing of this thesis. I must give additional thanks to Ann for agreeing to proofread the many pages of this thesis.

Institutional

This project is part of the Oxford Inorganic Chemistry for Future Manufacturing Centre for Doctoral Training (OxICFM CDT) and is funded by both the EPSRC

and a range of industrial partners. Thank you for giving me the funding and also for the variety of opportunities for further learning you have provided over the years.

I would also like to thank Christ Church College and in particular the GCR for all the brilliant events I attended. The dinners, BOPs and Ball were like no other.

Abstract

This thesis discusses the development of sustainable and scalable synthesis methods for LDHs using green precursors, namely waste materials. Chapter 1 provides an introduction to LDHs, their applications, and a report of previously reported synthesis from waste. The climate crisis is discussed, as well as the technologies currently in development to meet international climate targets. The plastic crisis is also introduced and the need for alternative recycling technologies is explained.

Chapter 2 details the analytical techniques and synthesis protocols used throughout the subsequent chapters. In Chapter 3, reactions for the conversion of the waste mineral struvite ($MgNH_4PO_4 \cdot 6\,H_2O$), produced during wastewater treatment, into industrially relevant magnesium-based LDHs are developed. The materials produced are characterised in detail using a number of techniques, including X-Ray diffraction, surface area analysis, and scanning electron microscopy.

Amino silylether-modified LDHs are discussed in Chapter 4. The effect of the modification conditions is investigated as well as the effect of changing the organic, amine-containing, group. The performance of the materials for the direct air capture of CO_2 is evaluated and the isotherms are fitted to theoretical models to characterise the processes involved. Estimates of the process energy and productivity are also made.

In Chapter 5, the development of transition metal-doped struvite-derived LDHs is explored. These materials were used for the catalytic pyrolysis of polypropylene and their performance was evaluated.

Lastly, Chapter 6 provides a summary of the findings of the works in this thesis and suggests directions for future work. Additional data mentioned in the main text may be found in the Appendices.

Contents

Nomenclature

Below is a list of common terms and abbreviations in this thesis.

°C . . . . . Degrees Celsius

Å . . . . . Angstrom ($10^{-10}m$)

A-MgHPO$_4$. Amorphous dimagnesium phosphate

AMOST . . . . Aqueous miscible organic solvent treatment

CDL . . . . . Crystallite domain length

BET . . . . . Brunauer–Emmett–Teller

CHN . . . . . Carbon, hydrogen and nitrogen (elemental analysis)

CO$_2$ . . . . . Carbon dioxide

CP-MAS . . . Cross polarisation magic angle spinning

D.I. . . . . . Deionised water

DAC . . . . . Direct air capture

DI . . . . . N-2-aminoethyl-3-aminopropyl trimethoxysilane

DP-MAS . . . Direct polarisation magic angle spinning

DSC . . . . . Differential scanning calorimetry

EDX . . . . . Energy dispersive X-ray spectroscopy

FTIR . . . . . Fourier Transform infra-red

FWHM . . . . Full width at half maximum

g . . . . . Gram

GC . . . . . Gas chromatography

GC-MS . . . . Gas chromatography-mass spectrometry

GPC . . . . . Gel permeation chromatography

h . . . . . Hour(s)

HR-SEM . . . High resolution scanning electron microscopy

LDH . . . . . Layered double hydroxide

LDO . . . . . Layered double oxide

min . . . . . Minute(s)

mmol . . . . . Millimole ($10^{-3}mol$)

MOF . . . . . Metal organic framework

MONO . . . . 3-aminopropyl triethoxysilane

MONO-Me . . Trimethoxy[3-(methylamino)propyl]-silane

MONO-Ph . . N-[3-(trimethoxysilyl)propyl]aniline

NET . . . . . Negative emission technology

NMR . . . . . Nuclear magnetic resonance

NQS . . . . . Non-quaternary suppression

PEI . . . . . Polyethylenimine

PP . . . . . Polypropylene

RH . . . . . Relative humidity

RMSE . . . . . Root mean square error

RPM . . . . . Rotations per minute

RT . . . . . Room temperature

SEM . . . . . Scanning electron microscopy

SLDH . . . . . Struvite-derived layered double hydroxide

SS-NMR . . . Solid state nuclear magnetic resonance

SSA . . . . . Specific surface area

t . . . . . Tonne (1000 kg)

TGA . . . . . Thermogravimetric analysis

TPD . . . . . Temperature-programmed desorption

TPR . . . . . Temperature-programmed reduction

TRI . . . . . 3-[2-(2-aminoethylamino)ethylamino]propyl-trimethoxysilane

XRD . . . . . X-ray diffraction

y . . . . . Year

1

Introduction

Contents

1.1 Layered double hydroxides (LDHs)

1.1.1 LDH Structure

Layered double hydroxides are a class of lamellar inorganic materials with the general formula $[M_{1-x}M'_x(\mathrm{OH})_2]^{y+}[A^{n-}]_{y/n} \cdot z\,\mathrm{H_2O}$. M and M' are typically divalent and trivalent metal cations with $0.2 < x < 0.33$ for pure LDH phases, although larger ranges have been reported,[1] and A^{n-} is typically an inorganic anion.[2] These materials are also called hydrotalcite-like materials after the naturally occurring mineral hydrotalcite ($[\mathrm{Mg_6Al_2(OH)_{16}}][\mathrm{CO_3}] \cdot 4\,\mathrm{H_2O}$), although other natural minerals with the same structure exist, such as the mixed $\mathrm{Fe^{II/III}}$ phase fougèrite ($[\mathrm{Fe_6(OH)_{12}}][\mathrm{CO_3}] \cdot 3\,\mathrm{H_2O}$).[3] Synthetic hydrotalcite-like materials are often based on magnesium and aluminium; however, many metals including some transition metals and lanthanides may be used. There are also reports of using monovalent lithium or tetravalent titanium, zirconium, or tin.[4–7] The composition is not limited to binary combinations of metals, with tertiary and quaternary compositions frequently employed and up to novenary high entropy materials reported.[8,9]

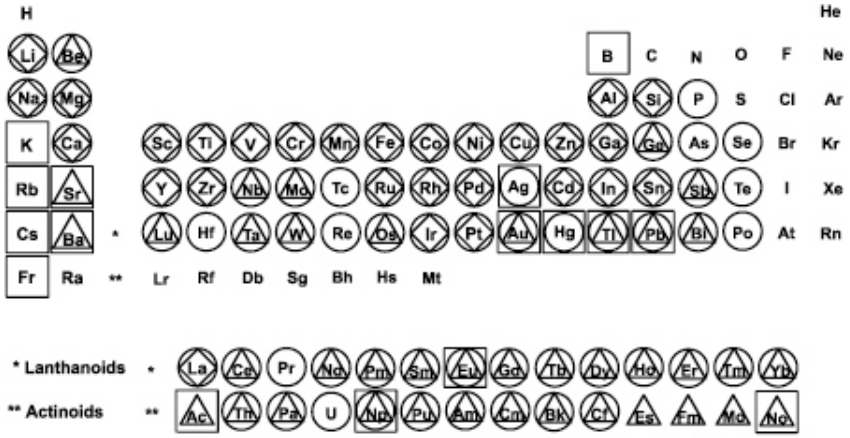

Figure 1.1: Periodic table detailing the metals reported for LDH synthesis. Adapted from Bravo-Suárez *et al.*[10] ◊ Reported in journals, △ Claimed in patents. □ Deviation from Shannon ionic radius of $\mathrm{Mg^{2+}} > 50\%$, ◯ Deviation from Shannon ionic radius of $\mathrm{Mg^{2+}} < 50\%$. Some elements have ionic radius deviations from $\mathrm{Mg^{2+}} > 50\%$ and $< 50\%$, due to variable oxidation states.

The structure of LDHs is closely related to that of the mineral brucite ($\mathrm{Mg(OH)_2}$). This adopts the $\mathrm{CdI_2}$ layered structure, with sheets of edge-sharing octahedra held

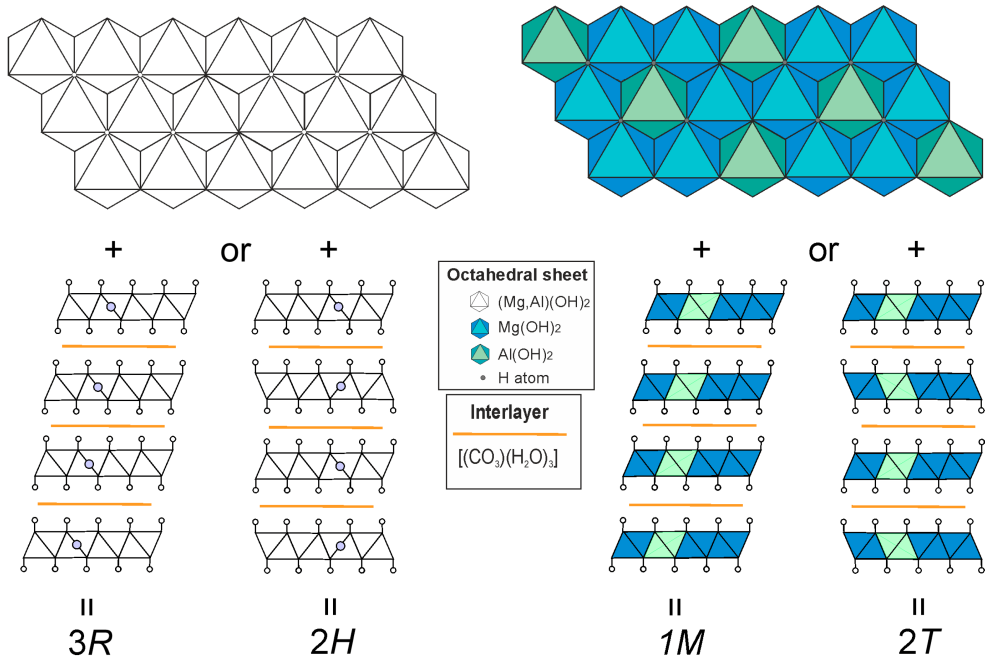

Figure 1.2: Common polytypes observed for the natural hydrotalcite-like mineral quinite ($[Mg_4Al_2(OH)_{12}][CO_3] \cdot 3\,H_2O$) without (left) or with (right) cation ordering. Reproduced from Zhitova *et al.*[13]

together by hydrogen bonding. In the hydrotalcite structure, there is partial substitution of the Mg^{2+} by Al^{3+} with charge balancing anions intercalated between the sheets.[11] The arrangement of these cations can be statistical or ordered, depending on the synthesis conditions.[12]

This substitution leads to to a change in the stacking of the metal hydroxide layers, with both rhombohedral and hexagonal polytypes found in natural minerals, with either two or three metal hydroxide layers per unit cell (Figure 1.2). Theoretically, there are three distinct two-layer, and nine three-layer, LDH stacking sequences, each representing a different polymorph[14] and infinite low-symmetry structures where the three-fold axis of adjacent layers are no longer coincident.[15] The three commonly reported polytypes are typically referred to as $3R_1$, $3R_2$ and $2H_1$, a nomenclature coined by Bookin and Drits, where the number refers to the number of layers in the unit cell and the letter to the crystal symmetry.[16] The three-layer rhombohedral polytypes $3R_1$ and $3R_2$ have stacking sequences of AC = CB = BA = AC and AC - BA - CB - AC, while the two-layer hexagonal $2H_1$ polytype has

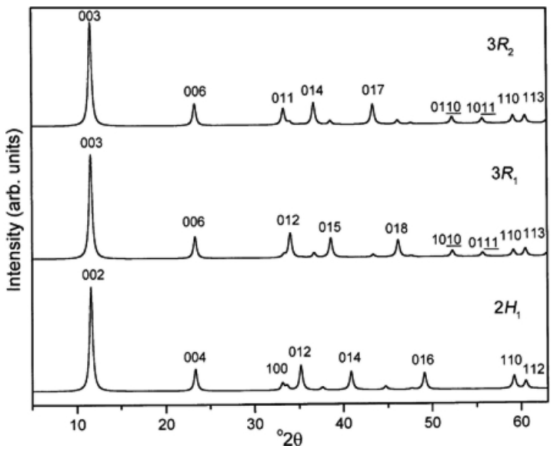

Figure 1.3: Simulated XRD patterns of $2H_1$, $3R_1$ and $3R_2$ LDH polytypes. Reproduced from Radha *et al.*[14]

a AC = CA = AC stacking sequence, where A, B and C represent the positions of the hydroxyl ions.[14] The $3R_1$ and $2H_1$ feature trigonal prismatic (=) interlayer sites, whilst $3R_2$ features octahedral sites (-).

Information on the crystal structure can be extracted from the X-ray diffraction patterns such as the a and c lattice parameters. LDHs have characteristic Bragg reflections: strong basal $(00l)$ reflections at low angle, $(10l)$ and $(01l)$ at medium angle and (110) at high angle. The basal reflections are directly related to the basal spacing of the material (the size of one metal hydroxide layer plus the interlayer), with the lowest angle reflection ($(00n)$ for an n-layer LDH) corresponding to $1/n$ of the c unit cell parameter. Similarly, the d-spacing of the 110 reflection gives half of the a unit cell parameter.

To distinguish between the different polytypes, variations can be observed in their X-ray diffraction patterns, with systematic absences for rhombohedral crystal structures at $-h + k + l = 3n$, but not for hexagonal crystal structures.[15] It is possible to further distinguish between the different rhombohedral or hexagonal phases from the relative intensity of the Bragg reflections. For example, the ratio of the $(h0l) : (h0(l+1))$ Bragg reflections is > 1 for $3R_1$ and < 1 for $3R_2$ (Figure 1.3).[16]

The preference for the symmetry adopted by the LDH is largely dictated by the anion used, as optimal bonding is achieved when the interlayer symmetry matches

the molecular symmetry.[17] For example, both CO_3^{2-} (D_{3h}) and SO_4^{2-} (T_d) have a three-fold symmetry axis (C_3) and, as such, LDHs containing them typically adopt the $3R_1$ polytype, which features trigonal prismatic sites (D_{3h}) in the interlayer space, which have a matching C_3 axis parallel to the c axis.

CO_3^{2-} anions oriented with their principal axis parallel to the c axis are able to hydrogen bond with hydroxyl groups from both the layers above and below.[17] This provides an enthalpic preference compared to the octahedral sites of other polytypes. The preference for the $3R_1$ polytype over the $2H_1$ polytype, which also features trigonal prismatic interlayer sites, is attributed to the eclipsed configuration of the cations in adjacent layers, leading to increased electrostatic repulsion.[17] Consequently, the $2H_1$ configuration has not been observed experimentally. The extensive bonding interactions associated with the CO_3^{2-} anion impart a preferential binding relative to other anions, thereby making the synthesis of "carbonate-free" LDHs challenging.[2]

The tetrahedral SO_4^{2-} anion has two potential orientations: along the C_3 axis, with one bond parallel to the stacking axis directed at one metal hydroxide layer, and the other three aligned with either the hydroxyl groups of the second layer, or along the S_4 axis with two bonds directed at each of the layers. The former is favoured, as it matches with the symmetry of the hydroxyl groups.[17] As there is a strong interaction with only one of the layers, there is no strong preference for the trigonal prismatic sites and natural $1H$ polytypes with octahedral interlayer sites are reported (such as zincwoodwardite, $[Zn_{1-x}Al_x(OH)_2][SO_4]_{x/2} \cdot nH_2O$).[18] The polytype preference is also dictated by inter-anion interactions and the hydration sphere. Studies on ZrCr-SO_4 LDHs by Mostarih and Roy show that they undergo reversible changes to their hydration levels with an associated variation in their basal spacing and, at certain values, undergo a structural transformation between two distinct $1H$ structures and a $3R$ polytype at the lowest levels of hydration.[19]

As the interactions between the layers are weak, LDHs are prone to stacking faults, which are defects where the displacement vector between two adjacent sheets differs

from that in the rest of the structure. This can result in, for example, a $3R_1$ polytype with a local symmetry of $2H_1$ or $3R_2$. The formation of these defects is entropically driven. This leads to a broadening of the $(10l)$ and $(01l)$ Bragg reflections.[14] Where stacking faults occur frequently enough to remove correlations between the cations in the stacking axis (known as turbostratic disorder), the profile of these reflections take on a "shark-fin" profile.

1.1.2 Layered double oxides (LDOs)

After thermal treatment, LDHs are converted to mixed metal oxides commonly referred to as layered double oxides (LDOs). The exact structure of these materials depends on the thermal conditions employed, with several distinct decomposition events occurring at different temperatures. The initial structural change is dehydration (<190 °C): physisorbed water is lost first, followed by interlayer water.[20] This is followed by dehydroxylation of the metal hydroxide layers (200 to 500 °C), causing collapse of the layered structure to an amorphous mixed oxide.[20] During this phase, the interstitial anion can interact directly with the metal cations and often undergoes its own thermal decomposition, such as the release of CO_2 from carbonate-based LDHs.[20–22] Further heating causes the metal oxide to become ordered with crystalline metal oxide phases formed (often spinel-like).[23] These LDO materials possess numerous basic sites and have been used to adsorb acidic environmentally damaging gases such as CO_2, SO_2, HCl and NO.[24,25]

LDOs formed under moderate temperatures (< 500 °C) exhibit a phenomenon, called reconstruction or the "memory effect", where they readily reform an LDH phase after exposure to liquid water or humidity. The exact mechanism of this process is a topic of debate in the literature and may vary between a topotactical mechanism at low calcination temperatures and direct synthesis at high temperatures (through a two-stage process: partial oxide dissolution and LDH precipitation).[26,27] This process can be used either to intercalate functional anions into the interlayer gallery to create functional materials, including bulky anions which cannot be directly intercalated such as DNA, vitamins, antibiotics and other biomolecules,[28]

or as an adsorption mechanism to remove unwanted anions, such as phosphate, from solution.[29,30]

1.1.3 LDH synthesis

There are two common LDH synthesis methods (coprecipitation and hydrothermal), although numerous others have been reported.[31] The chosen method should reflect the desired properties of the product. For all synthesis methods, there are a multitude of factors that will influence the properties of the resultant LDH, including, but not limited to, the temperature, pH, ageing time, stirring speed and ion concentration. An alkaline pH is required for LDH precipitation, with the exact value contingent on the metals used.[32] The ageing process facilitates Ostwald ripening which increases particle size via the selective dissolution of small particles.

Coprecipitation is the most common synthesis method for LDHs.[33] During this synthesis, two or more metal cations are precipitated at the same time from a supersaturated alkaline solution. The pH is typically kept constant throughout the reaction and the product is aged to increase crystallinity. This method often yields broad particle size distributions, as nucleation and crystallisation growth occur simultaneously. Modifications have been developed which allow for the separation of these steps to narrow the particle size distribution.[34] Hydrothermal synthesis involves placing the reaction mixture under hydrothermal conditions, providing an improved ageing process that is particularly valuable where the metal salts have low solubility.[35,36]

Other notable synthesis methods include: the urea hydrolysis method, where the pH is controlled via slow thermal decomposition of urea allowing for large, highly crystalline, uniform products;[35] the reconstruction method (mentioned previously) whereby LDHs are reversibly transformed into layered double oxides by thermal treatment at intermediate temperature followed by rehydration in water (taking up any anions present in the solution);[37] and the reverse micelle method where LDHs are grown from micro-emulsions in organic solvents which limit the LDH platelet size.[38]

Besides calcination and reconstruction, the other commonly employed post synthesis technique is called the aqueous miscible organic solvent treatment (AMOST) first reported by Wang and O'Hare.[39,40] This involves suspension of the LDH in an organic solvent, which partially replaces the water in the interlayer region, thus disrupting the hydrogen-bonding network between the layers.[41,42] This reduces the ease of a, b-face aggregation of the LDH during drying,[43] leading to significant increases in the surface area of the material (on the order of 10-fold to $> 300\,\mathrm{m^2\,g^{-1}}$).[39,44] A high surface area is particularly attractive for sorption and catalysis applications and, as such, numerous publications using the AMOST method for these applications exist in the literature.[42,45–53]

1.1.4 LDH applications

The many different metals and anions that may be included in the LDH structure cause LDHs to exhibit a great degree of compositional flexibility. As such, the physical properties of LDHs can be altered and tailored for use in many different applications such as electronics, adsorption and catalysis.[54–57]

Adsorption

LDHs have been extensively studied for adsorption processes. With both the ability to exchange anions included during their synthesis with those in solution and to bind species on their surfaces, they have been shown to be able to remove a wide range of contaminants. Water treatment is of growing concern, with increased amounts of aqueous toxic waste, contaminated with heavy metals from manufacturing, dyes from the textile industry and organic compounds from consumer products, agriculture and pharmaceuticals, requiring purification.[56]

LDHs have high adsorption capacities for numerous anionic dyes such as Congo red and methyl orange, with both physical and chemical adsorption mechanisms occurring.[58,59] Likewise, large organic molecules used as herbicides and pesticides such as N-phosphonomethyl glycine and 2,4-dinitrophenol, which are introduced

into water supplies by agricultural run-off, can also be removed.[60,61] Similarly, oxyanions such as arsenite, arsenate and phosphate can be removed from wastewater via anion exchange with nitrate-based LDHs.[62,63] Heavy metals such as U^{6+}, Pb^{2+}, Cu^{2+}, Co^{2+}, Ni^{2+}, Zn^{2+}, Cr^{6+} and Cd^{2+} can also be removed by LDHs, with various mechanisms of adsorption reported in the literature.[64–67]

Catalysis

LDHs have been extensively studied as catalysts, catalyst precursors and catalyst supports. These include applications in organic synthesis, electrochemistry, photochemistry and thermal chemistry. LDHs are attractive for catalytic purposes, as there is a uniform distribution of the metals throughout the sample.

NiFe LDHs have the highest oxygen evolution (OER) reaction (half reaction of water splitting) activity of any metal (hydr)oxides and have garnered attention due to their low cost.[68] $Ni(OH)_2$ hydroxide (a brucite-like material) demonstrates the highest OER performance of the 3d transition metal (oxy)hydroxides; however, its activity is significantly improved by the inclusion of Fe^{3+} within the layers. The precise mechanism underlying this enhancement in performance remains a topic of debate; nevertheless, the interaction between nickel and iron is crucial.

NiTi LDHs have been utilised as NO_x ($x = 1, 2$) photo-oxidation catalysts. These materials outperform commercial TiO_2 benchmark catalysts under simulated sunlight conditions and could be used for passive removal of these urban atmospheric pollutants from the air. The increases in performance were attributed to higher surface areas for adsorption and the 2D nature of the LDH sheets which hinders the charge carrier recombination.[46]

CuZnAl catalysts derived from layered double hydroxides have been shown to display improved activity for CO_2 hydrogenation to methanol when compared to conventionally prepared catalysts of the same composition. The Cu^0 nanoparticles are better dispersed on the catalyst surface with smaller diameters providing a higher Cu surface area.[69] The LDH-derived materials can also be modified with

promoters such as Y^{3+}, which increase the Cu surface area and thus the CO_2 conversion, and Zr^{4+} or interstitial F^-, which increase the basicity and methanol selectivity of the catalyst.[70,71]

Recently, numerous publications have reported single atom noble metal catalysts anchored to LDHs. There is a strong electronic coupling between the noble metal atoms and the anchoring site of the LDH, through which the catalytic activity may be tuned. Elements such as Ru, Ir, Au and Pt have been dispersed on LDHs in dilute solutions or via electrodeposition and used for a variety of reactions, including electrochemical water-splitting, electro-oxidation fuel cells and catalytic reforming.[72]

1.1.5 Principles of green chemistry

Green chemistry focuses on making chemical processes as sustainable and safe as possible. This involves reducing the waste and the hazards associated with any given reaction, as well as following the material through all stages of its lifecycle, from its feedstocks to its degradation pathway. The 12 principles of green chemistry, as proposed by Anastas and Warner in 1998, are listed in Table 1.1.[73]

Improving the safety of a process is relatively straightforward in theory, as this simply requires the minimisation or elimination of reagents and processes which are toxic or hazardous, hence decreasing the associated risk. In practice, this is difficult, as chemists typically opt for established procedures, and thus safety improvements require the development of new systems which achieve the same outcome using benign procedures. The rest of the framework focuses on minimising waste associated with both materials and energy use. Feedstocks should be renewable, leading to the idea of a circular economy where products are reclaimed at the end of their lives for breakdown and reuse rather than ending up as waste.[74] Those products which cannot be utilised should preferably have benign decomposition pathways designed into their structure to prevent their accumulation in the environment. As well as reducing the waste associated with the product itself, much of the framework

Table 1.1: The 12 principles of green chemistry.[73]

Principle	Description
1 Prevention	It is better to prevent waste than to treat or clean up waste after it has been created.
2 Atom economy	Synthetic methods should be designed to maximise incorporation of all materials used in the process into the final product.
3 Less hazardous chemical syntheses	Wherever practicable, synthetic methods should be designed to use and generate substances that possess little or no toxicity to human health and the environment.
4 Designing safer chemicals	Chemical products should be designed to preserve efficacy of function while reducing toxicity.
5 Safer solvents and auxiliaries	The use of auxiliary substances (e.g. solvents and separation agents) should be made unnecessary wherever possible and innocuous when used.
6 Design for energy efficiency	Energy requirements should be recognised for their environmental and economic impacts and should be minimised. Synthetic methods should be conducted at ambient temperature and pressure.
7 Use of renewable feedstocks	A raw material or feedstock should be renewable rather than depleting whenever technically and economically practicable.
8 Reduce derivatives	Unnecessary derivatization (use of blocking groups, protection/deprotection, temporary modification of physical/chemical processes) should be minimised or avoided if possible, because such steps require additional reagents and can generate waste.
9 Catalysis	Catalytic reagents (as selective as possible) are superior to stoichiometric reagents.
10 Design for degradation	Chemical products should be designed so that at the end of their function they break down into innocuous degradation products and do not persist in the environment.
11 Real-time analysis for pollution prevention	Analytical methodologies need to be further developed to allow for real-time, in-process monitoring and control prior to the formation of hazardous substances.
12 Inherently safer chemistry for accident prevention	Substances and the form of a substance used in a chemical process should be chosen to minimise the potential for chemical accidents, including releases, explosions, and fires.

focuses on minimising the waste produced during its production. Processes should be optimised to use the minimal amounts of reagents and energy; ideally, processes should function under ambient conditions, produce the minimum side products and use catalysts over stoichiometric reagents where they are needed. The mass efficiency of these processes are commonly evaluated using metrics such as the atom economy, $AE\% = \frac{\sum M_r(\text{product(s)})}{\sum M_r(\text{reactant(s)})}$, for the reaction occurring and E factor, $E = \frac{\text{kg waste}}{\text{kg product}}$, for the entire process.

1.1.6 Green LDH synthesis methods

When LDHs are compared to these criteria, it can be seen why they are typically considered green materials, with numerous publications reporting their use as catalysts for green processes.[75,76] Many LDHs are biocompatible and naturally occurring, thus posing little threat to the environment.[3,77,78] The common coprecipitation preparation route uses ambient conditions with water as the solvent. Their compatibility with other materials to produce hybrid or hierarchal products with other inherited properties attractive to green synthesis; for example, anchoring LDHs to magnetic Fe nanoparticles allows for easy and efficient separation of heterogeneous catalysts after the reaction is complete.[79] However, there are aspects of their synthesis which could be more sustainable, which are discussed herein.

Hydrothermal preparation routes are less green, requiring heating; the elevated pressures involved pose additional risks compared to reactions at ambient temperatures and pressures. An alternative method for synthesis at elevated temperatures is microwave synthesis. Microwave irradiation provides efficient internal heating via interaction with the dipoles and ions present in the solution compared to conventional heating methods, which involve thermal conduction from an external source through the reaction vessel.[80] LDHs produced using microwave synthesis are reported to be more dispersed than those produced using hydrothermal processes and exhibit enhanced adsorption capacities compared to traditionally synthesised LDHs.[81]

The atom efficiency of LDH synthesis is often far from 100%. Commonly, the metal salts used for the synthesis are metal nitrates or chlorides; however, these are not the desired interlayer anions and exist as spectator ions. Although these ions are not inherently toxic, they can cause environmental harm if released on an industrial scale into water sources. Large volumes of wastewater are also generated during the washing step to remove these unwanted ions, and water treatment adds an economic burden.

One method of improving the atom economy is the use of electrochemical synthesis. This removes the need to use a base, as hydroxide ions are generated at the cathode during the reduction reaction. As the change in pH occurs principally above the electrode surface, LDH formation is localised to the electrode surface.[82] This in situ method allows for control of the thickness of the deposited layer and allows for strong electronic coupling between the LDH and the electrode, which is desirable for electrochemical applications.[82,83] An alternative electrochemical synthesis method involves using sacrificial Zn and Al electrodes, which are electrolysed to provide the metal cations needed to form ZnAl LDH.[84]

A more traditional method to improve the atom economy uses metal hydroxides or oxides as reagents. For example, Newman *et al.* showed that MgAl LDH could be prepared from the hydrothermal reaction of MgO and Al_2O_3.[85] The use of solely metal oxide or hydroxides leads to a theoretical 100% atom economy:

$$4\,MgO + Al_2O_3 + 6\,H_2O + CO_2 \longrightarrow Mg_4Al_2(OH)_{12}CO_3,$$

compared to a typical coprecipitation using nitrate salts, which has an theoretical atom efficiency of 25.9% (ignoring the base used to modulate the pH):

$$4\,Mg(NO_3)_2 + 2\,Al(NO_3)_3 + 12\,NaOH + Na_2CO_3 \longrightarrow Mg_4Al_2(OH)_{12}CO_3 + 14\,NaNO_3.$$

This hydrothermal process occurs via a dissolution-precipitation reaction on the surface of the precursor materials, arising from the very low metal oxide precursor solubilities.[86] This necessitates elevated temperatures or pHs to increase the metal solubilities.[87] These reactions often do not go to completion, with brucite impurities

formed.[85,86,88] To overcome this, the reactivity of the precursors can be improved by decreasing the size of the particles using blending, ultrasonic treatment or wet grinding.[88]

Extending this methodology, Labuschagné *et al.* developed a cyclical method for the reaction of MgO and $Al(OH)_3$ with $NaHCO_3$ to produce high purity MgAl-CO_3 LDHs.[89] After the hydrothermal synthesis, the mother solution is separated from the product and the $NaHCO_3$ is regenerated via the addition of CO_2 gas. A similar cyclical route has also been reported by Zhang *et al.* using $Mg(OH)_2$, $Ca(OH)_2$, $AlCl_3$ and NH_4 to produce Ca-doped MgAl LDH.[90] After the hydrothermal reaction, the mother liquid is separated and concentrated, with the distilled water produced used to wash the product. The water is then reused for the next batch. Valente *et al.* showed that other metals (Ni, Cu, Zn, and Fe) can be incorporated into MgAl-NO_3 LDHs via addition of their nitrate salts to the reaction mixture.[91]

These cyclical methods reduce the amount of water the synthesis processes use, making them more sustainable. An alternative method to reduce the amount of water used is to employ mechanochemical synthesis. This involves the direct reaction of the solid precursors, without the need for water as a solvent, facilitated by mechanical energy provided by the milling process. A review by Intasa-ard *et al.* explores recent efforts in the mechanochemical synthesis of LDHs, concluding that this method is limited both by a lack of control over the particle morphology and by the presence of unreacted starting materials or by-products which are difficult to remove.[92]

1.1.7 LDH from waste

An alternative approach to improving the sustainability of LDH precursors is the utilisation of waste products (a renewable feedstock). This reduces the carbon footprint of the precursor materials by avoiding the environmental impact caused by the processing of the raw extracted mineral and by contributing to a circular economy. Typically, metals are leached from the waste material to produce the

metal-rich LDH precursor solutions and are then coprecipitated by addition of a base (commonly NaOH). However, a challenge to this approach is that waste materials can contain significant impurities and contain species not desirable for the target product. A list of publications found in the literature describing LDHs produced from waste products are detailed in Table 1.2. As noted by Jiang *et al.* in their review the majority of these are derived from red mud, slag, fly ash or wastewater.[93]

Of particular relevance to this thesis, recent work from our group has shown that struvite ($MgNH_4PO_4 \cdot 6\,H_2O$), a mineral produced during wastewater treatment, can be used as a precursor for MgAl LDH. This transformation occurs upon the addition of Na_2CO_3 and $Al(NO_3)_3 \cdot 9\,H_2O$ under alkaline conditions at elevated temperatures. It was also found that a pretreatment step, where the struvite is heated in NaOH to release NH_3 and form a reactive unknown intermediate phase, improved the efficiency of the process. The LDH materials produced using this synthesis method retain the typical "coffin" morphology of the struvite, suggesting a dissolution-precipitation mechanism.[94] They also have a high BET SSA ($184\,m^2\,g^{-1}$) and a high tap density ($0.68\,g\,cm^{-3}$), properties not commonly observed together, making them ideal for industrial applications such as sorption.[95]

These waste derived materials may be utilised for a variety of applications; many of these applications have been developed previously for conventional LDH materials. However, it appears pertinent that these more sustainably derived materials should be employed to provide technologies for environmental issues currently facing society. The development of materials to address two of these pressing issues is discussed later in this thesis and as such the following sections provide a background to these Chapters. Chapter 1.2.1 introduces the climate crisis and carbon capture technologies, while Chapter 1.3.1 introduces the plastic crisis and the current field of polyolefin chemical recycling to help frame the later discussions.

Table 1.2: Literature reports of waste derived LDHs.

LDH	Waste stream utilisation	Description	Reference
MgAl	$MgCl_2$ from sea bitterns, the liquid remaining after NaCl production from sea water.	Four plants using a colloid mill process with $AlCl_3$, NaOH and Na_2CO_3. NaOH is regenerated from the NaCl side product in an adjacent chloralkali plant.	Evans *et al.*[96]
MgAl	Struvite ($MgNH_4PO_4 \cdot 6\,H_2O$) from wastewater treatment.	The struvite was added to a NaOH solution before LDH was formed upon addition of $Al(NO_3)_3 \cdot 9\,H_2O$ and Na_2CO_3.	Kwok *et al.*[97]
MgAlFe	Sea bitterns and red mud from the Bayer process.	The metals were leached from the red mud and sea bitterns using HCl. The solutions were mixed and LDH coprecipitated using NaOH and Na_2CO_3.	Li *et al.*[98]
MgAlFe	Wastewater from acid activation of vermiculite ($((Mg, Fe)^{2+}, Fe^{3+})_3[(Al, Si)_4O_{10}](OH)_2 \cdot 4\,H_2O$).	LDH was coprecipitated from the wastewater using $(NH_4)_2CO_3$ and Na_2CO_3.	Stawiński *et al.*[99] Zhang *et al.*[100]
MgAl	Acidic process water from a Uranium mine.	A solution containing $NaAlO_2$ and NaOH from the Bayer process was added to the acidic process water (rich in Mg and Mn) to form LDH.	Douglas *et al.*[101]
MgAl	Waste serpentine tailings (WST, $Mg_3Si_2O_5(OH)_4$) and aluminium scraps.	WST were crushed, mixed with Na_2CO_3 and calcined to extract MgO via alkaline fusion. The MgO and aluminium scraps were dissolved in HNO_3 to produce the cation-rich LDH precursor solution for typical coprecipitation with NaOH and Na_2CO_3.	Zhu *et al.*[102]

LDH	Waste stream utilisation	Description	Reference
MgAl	Boron mud from boric acid and borax production and red mud from the Bayer process.	Boron mud (rich in Mg, Fe and Si) and red mud (rich in Al, Fe, Si) were mixed and calcined at 600 °C before conversion to LDH in a NaOH solution.	Hu *et al.*[103]
MgAl	Bischofite from salt lake water processing.	Bischofite ($MgCl_2 \cdot 6\,H_2O$) was dissolved in water and $AlCl_3 \cdot 6\,H_2O$ was added. LDH was formed by addition of NaOH and Na_2CO_3 with hydrothermal treatment.	Dong *et al.*[104] Zhang *et al.*[105]
MgTiAl	Blast furnace slag (BFS).	$(NH_4)_2SO_4$ was added to the BFS (rich in Ca, Si, Ti, Mg and Al) and the mixture calcined at 450 °C. The solid was immersed in solution and insoluble residues removed by centrifuge. LDH was coprecipitated from the solution by addition of NaOH.	Song *et al.*[106]
MgCaAl	Blast furnace slag (BFS).	The metals were extracted from the BFS (rich in Ca, Si, Ti, Mg and Al) in HCl solution and insoluble residues removed by centrifuge. $CeCl_3 \cdot 7\,H_2O$ was added and a LDH/$(Ce/Ti)O_2$ composite material was formed from the resulting solution upon addition of NaOH.	Song *et al.*[107]
MgCaAl	Blast furnace slag (BFS).	The metals were extracted from the BFS (rich in Ca, Si, Mg and Al) in HCl solution and insoluble residues removed by centrifuge or filtration. LDH was coprecipitated from the resulting solution upon addition of NaOH (and Na_2CO_3).	Gao *et al.*[108] Jiang *et al.*[109] Zhang *et al.*[110] Zhou *et al.*[111] Guo *et al.*[112]

LDH	Waste stream utilisation	Description	Reference
MgCaAl	Blast furnace slag (BFS).	The metals were extracted from the BFS (rich in Ca, Si, Mg and Al) mixed with MgO in HCl solution and insoluble residues removed by filtration. LDH was formed from the resulting solution upon addition of NaOH.	Li *et al.*[113]
CaMgAl	Dolomite ($MgCO_3CaCO_3$).[114]	Dolomite dissolved in a solution of $AlCl_3$ under hydrothermal conditions and undissolved residues removed. LDH was formed from the resulting solution upon addition of NaOH.	Mao *et al.*[115]
CaMgAl	Brine water from coal power plant.	$AlCl_3$ was added to brine water (rich in Ca and Mg) and Na_2CO_3 added to produce LDH.	Heraldy *et al.*[116]
CaMgAl	Asbestos from construction waste.	The asbestos waste (rich in Ca and Mg) was added to HCl to extract the metals. $Al(NO_3)_3 \cdot 9\,H_2O$ was added to produce the desired ratio of metals. LDH was formed from the resulting solution upon addition of NaOH.	Li.[117]
CaMnMgAl	Electric arc furnace slag from FeMn alloy manufacturing.	The metals were extracted from the slag (rich in Si, Mn, Ca, Mg and Al) in HCl, the insoluble residues removed by filtration and LDH coprecipitated by addition of NaOH.	Kim *et al.*[118]
CaMgFeAl	Biomass combustion ash and coal fly ash.	The biomass combustion ash (rich in Ca and Mg) and coal fly ash (rich in Fe, Al and Si) were added to HCl to dissolve the metal cations. The solution was centrifuged to remove undissolved residues and LDH was coprecipitated from the solution by addition of NaOH.	Wajima *et al.*[119]

LDH	Waste stream utilisation	Description	Reference
CaMgFe	Biomass combustion ash.	The biomass combustion ash (rich in Ca and Mg) was added to HCl to dissolve the metal cations. The solution was filtered and $FeCl_3 \cdot 6\,H_2O$ was added to produce the to produce the cation-rich LDH precursor solution for typical coprecipitation with NaOH and NaCl.	Suhara *et al.*[120]
CaMgAl	Steel slag from iron and steel industry.	The slag (rich in Ca, Mg and Al) was added to a HNO_3 solution and insoluble SiO_2 removed by filtration. LDH was coprecipitated from the solution by addition of NaOH and Na_2CO_3.	Liu *et al.*[121,122]
CaMgAlFe	Steelmaking slag.	The slag (rich is Ca, Mg, Al and Fe) was stirred in acetic acid to extract the metals and filtered to remove insoluble residues. The pH was adjusted with $Ca(OH)_2$ and LDH formed.	Wang *et al.*[123]
(Ca/Mg)Al	Carbide slag from an acetylene plant and red mud from the Bayer process.	The Carbide slag (rich in Ca) and red mud (rich in Al and Fe) were calcined (600 °C), mixed and heated in solution to form LDH.	Xiao *et al.*[124]
CaMgAl	Phosphorous tailings.	The tailings (rich in Ca and Mg) were calcined and the metals extracted in HCl. The desired metal ratio was achieved via addition of $MgCl_2 \cdot 6\,H_2O$ and $AlCl_3 \cdot 6\,H_2O$ and LDH coprecipitated by addition of NaOH.	Zhang *et al.*[125]
CaAl	Concrete sludge (waste concrete).	Ca was leached from the sludge by addition of acetic acid. $Al(NO_3)_3 \cdot 9\,H_2O$ was added and LDH coprecipitated using NaOH.	Hongo *et al.*[126]

LDH	Waste stream utilisation	Description	Reference
CaAl	Concrete sludge (waste concrete).	Ca was leached from the sludge by addition of HCl. $AlCl_3 \cdot 6\,H_2O$ was added and LDH coprecipitated using NaOH.	Liu *et al.*[127]
MAl	Dolomite from concrete waste and aluminium dross.	$Mg(OH)_2$, $Ca(OH)_2$ and $Al(OH)_3$ were prepared from the dolomite waste (rich in Ca and Mg) and aluminium dross via extraction with HCl and neutralisation with NH_3. The hydroxides were calcined before being combined to form LDHs via microwave-hydrothermal treatment with Na_2CO_3. M = Ca, Mg.	Abd-El-Raoof *et al.*[128]
CaAl	Blast furnace slag (BFS) from iron production.	BFS (rich in Ca, Si and Al) was dissolved in HCl solution. Silica gel was removed by filtration and LDH coprecipitated using NaOH.	Kuwahara *et al.*[129–134]
CaAl	Coal fly ash (CFS) from coal power plants.	CFS (rich in Si, Al and Ca) was dissolved in HCl. Silica gel was removed by filtration and LDH coprecipitated using NaOH.	Muriithi *et al.*[135]
CaAl	Waste paper fly ash or biomass fly ash from an industrial incinerator.	The fly ash (rich in Si, Ca and Al) was leached in HCl and filtered to remove the silica gel. LDH was coprecipitated directly from the solution via addition of NaOH.	Bouzar *et al.*[136]
CaNiFe	Eggshell biowaste.	Eggshells were calcined at 900 °C to produce CaO. This was dissolved in HNO_3 solution and $Fe(NO_3)_3 \cdot 9\,H_2O$ and $Ni(NO_3)_2 \cdot 6\,H_2O$ were added and LDH formed by coprecipitation using NaOH.	Jafari Foruzin *et al.*[137]

LDH	Waste stream utilisation	Description	Reference
CaM	Eggshell biowaste.	Eggshells were calcined at 900 °C to produce CaO. This was dispersed in water and LDH formed upon addition of $FeCl_3$ and $AlCl_3$. M = Fe, Al.	Li *et al.*[138]
CaFe	Eggshell biowaste.	Ca was extracted from the eggshells using HCl and the insoluble particles removed by filtration. $Fe(NO_2)_3 \cdot 9\,H_2O$ was added and LDH coprecipitated upon addition of NaOH. M = Fe, Al.	Abed *et al.*[139]
CaCr	Snail shell (Gastropod *A. achatina*).	Ca was extracted from the shells using HCl. $CrCl_3$ was added and LDH coprecipitated using NaOH and Na_2CO_3.	Adelagun *et al.*[140]
CaAl	Clam shell (*Mytella falcata*).	The shells were calcined at 900 °C to produce CaO. $AlCl_3 \cdot 6\,H_2O$ and the CaO were added to water and LDH formed after addition of NaCl and NaOH.	Henrique *et al.*[141]
MgCaAl	Aluminium beverage cans.	Sepiolite ($Mg_4Si_6O_{15}(OH)_2 \cdot 6\,H_2O$, sample also contained Ca) and aluminium cans were dissolved in HCl and filtered to remove undissolved residues. LDH was formed from the solution upon addition of NaOH.	Cheng *et al.*[142]
MAl	Aluminium saline slag from secondary or tertiary aluminium processing.	Aluminium was extracted from the slag by refluxing in NaOH solution. Metal salts (Cu, Ca, Co, Mg, Ni, Zn or (Zn and Ti) or (Zn and Fe)) were added to the solution and LDHs produced by coprecipitation using NaOH (and Na_2CO_3). M = Cu, Ca, Co, Mg, Ni, Zn, ZnTi or ZnFe.	Santamaría *et al.*[143–145] Murayama *et al.*[146] Boulahbal *et al.*[147,148] Gil *et al.*[149]

LDH	Waste stream utilisation	Description	Reference
MgAl	Secondary aluminium dross (SAD) waste.	The SAD was leached using HCl followed by reaction with NH_3 to form a gel and a secondary leaching with NaOH and filtration to remove insoluble impurities. Na_2CO_3 was added to the solution and LDH coprecipitated upon addition of $MgCl_2$.	Mahinroosta *et al.*[150]
MAl	Aluminium dross from aluminium recycling.	Aluminium was extracted from the dross using HCl. Metal salts (Mg, Ca or Zn) were added and LDH coprecipitated by addition of NaOH (and NH_4Cl or Na_2CO_3). M = Mg, Ca or Zn.	Murayama *et al.*[146,151,152] Galindo *et al.*[153–155]
MgNiAl	Aluminium dross.	$Al(OH)_3$ was produced from the dross by extraction in NaOH solution. LDH was formed after hydrothermal treatment of a solution of $Mg(NO_3)_2 \cdot 6\,H_2O$, $Ni(NO_3)_2 \cdot 6\,H_2O$, NaOH, Na_2CO_3 and the $Al(OH)_3$.	Zawrah *et al.*[156]
MgAl	Liquid concentrated waste (LCW) from wastewater treatment.	FeO(OH) and $Al(OH)_3$ were extracted from the LCW at pH 12 (NaOH) and 7.5 ($NaHCO_3$), respectively. $Mg(NO_3)_2 \cdot 6\,H_2O$ was added and LDH formed by addition of NaOH and Na_2CO_3 with hydrothermal treatment.	Zawrah *et al.*[157]
MgAl	Water-processing sludge.	The water-processing sludge was mixed with NaOH and calcined at 500 °C. $Mg(NO_3)_2 \cdot 6\,H_2O$ and hexamethylenetetramine were added and LDH produced after hydrothermal treatment.	Chen *et al.*[158]
MgAl	Weathered tropical soil.	The used soil (rich in Al) was mixed with MgO and NaOH in seawater to produce LDH.	Willems *et al.*[159]

LDH	Waste stream utilisation	Description	Reference
FeAl	Red mud from the Bayer process.	Red mud (rich in Al and Fe) was fused with NaOH at 600 °C and LDH formed after ultrasonic treatment in seawater.	Belviso *et al.*[160]
MgFeAl	Tungsten tailings.	Tungsten tailings (rich in Si, Al, Ca and Fe) were calcined at 650 °C before etching in HCl. $MgCl_2 \cdot 6\,H_2O$ was added to the solution and LDH formed upon addition of NaOH.	Wang *et al.*[161]
MgFeAl	Fly-ash from a coal power plant.	A solution of Al and Fe was prepared from the fly-ash and $MgCl_2 \cdot 6\,H_2O$. LDH was coprecipitated by addition of NaOH and Na_2CO_3.	Li *et al.*[98]
ZnAl	Red mud from the Bayer process.	Red mud (rich in Al and Fe) was wet milled with $Zn(NO_3)_2 \cdot 6\,H_2O$ and added to a Na_2CO_3 solution to obtain LDH/Fe_2O_3 composites.	Li *et al.*[162,163]
ZnAl	Aluminium sludge from water treatment plant.	$Al(OH)_3$ was produced from the aluminium sludge by extraction in H_2SO_4, filtration and precipitation using NH_3. The $Al(OH)_3$ was dissolved in HNO_3 and $Zn(NO_3)_2$ added to produce the metal cation solution. Zeolite was added and LDH grown upon its surface by addition of NaOH.	Han *et al.*[164]
CuAl	Red mud from the Bayer process.	Red mud (rich in Al and Fe) was wet milled with $Cu(NO_3)_2 \cdot 6\,H_2O$ and Na_2CO_3 to obtain LDH/Fe_2O_3 composites.	Gu *et al.*[165]

LDH	Waste stream utilisation	Description	Reference
MgFe	Acid mine drainage precipitate ochre (FeO(OH), $Fe(OH)_3$) from an ironstone mine.	Fe was extracted from the waste ochre using HCl. $Mg(NO_3)_3 \cdot 6\,H_2O$ was added and the LDH coprecipitated using NaOH and Na_2CO_3.	Perera-Solis *et al.*[166]
MgFe	"Rcopper" waste from the mining of copper.	Fe was extracted from the "Rcopper" waste in HCl. $MgCl_2 \cdot 6\,H_2O$ was added and LDH coprecipitated using NaOH.	Silva *et al.*[167]
MgFeAl	Red mud from the Bayer process and ferronickle slag produced during nickel refining.	The metals were leached from red mud (rich in Fe and Al) and ferronickel slag (rich in Mg) with HCl and LDH coprecipitated using NaOH.	Zhang *et al.*[168,169]
MgFeAl	Red mud from the Bayer process	Red mud (rich in Al, Ca and Fe) was mixed with MgO and calcined (550 °C, 600 °C or 650 °C). LDH was produced from the reaction of this powder with NaOH and Na_2CO_3.	Hu *et al.*[170] Jia *et al.*[171,172] Li *et al.*[173–175] Qian *et al.*[176]
MgFeAl	Red mud from the Bayer process	Red mud (rich in Al and Fe) was etched in HCl. $MgCl_2 \cdot 6\,H_2O$ or $Mg(NO_3)_2 \cdot 6\,H_2O$ was added and LDH coprecipitated using NaOH (and Na_2CO_3).	Qian *et al.*[177] Nascimento *et al.*[178]
MgFe	Acidic residual solution from a hot-dip galvanising plant.	$Mg(NO_3)_2 \cdot 6\,H_2O$ was added to the acidic residual solution (rich in Fe) and LDH coprecipitated using NaOH and Na_2CO_3.	Golban *et al.*[179–181]

LDH	Waste stream utilisation	Description	Reference
ZnAl	Zinc ash waste from the hot dip galvanising process.	Zn was extracted from the ash (rich in Fe and Zn) using HCl. Fe was precipitated and removed via addition of a small amount of H_2O_2 and ZnO. $Al(NO_3)_3 \cdot 9\,H_2O$ was added and LDH coprecipitated using NaOH and Na_2CO_3.	Cocheci *et al.*[182,183] Tămaş *et al.*[184]
ZnAl	Zinc cyanide-containing wastewater.	$Ni(NO_3)_2 \cdot 6\,H_2O$ was added to the wastewater to form $Ni(CN)_4{}^{2-}$. NaOH and $Al(NO_3)_3 \cdot 9\,H_2O$ are added forming LDH intercalated with $Ni(CN)_4{}^{2-}$.	Zhou *et al.*[185]
ZnCr	Wastewater from Zn and Cr plating.	The wastewaters were concentrated and the metals extracted by poly-acrylic acid-assisted ultrafiltration. Cr^{6+} was reduced to Cr^{3+} using $NaHSO_4$ and LDH coprecipitated from a mixture of the solutions using Na_2SO_4 and NaOH.	Fu *et al.*[186]
ZnCr	Wastewater from Cr plating.	Cr^{6+} was reduced to Cr^{3+} using $Na_2S_2O_5$, $ZnCl_2$ was added and LDH coprecipitated upon addition of NaOH.	Ma *et al.*[187]
ZnCr	Wastewater from electroplating.	The electroplating wastewater (rich in Zn and Cr) was added to Fe_3O_4 nanoparticles produced from pickling waste liquor. LDH was coprecipitated upon addition of NH_3 to form Fe_3O_4/LDH composites.	Chen *et al.*[188]
ZnFe	Wastewater from Zn plating.	LDH was coprecipitated from a solution of the wastewater and $FeCl_3$.	Ruan *et al.*[189]

LDH	Waste stream utilisation	Description	Reference
ZnCaAl	Wastewater from Zn plating and cement.	Ca and Al salts were added to simulated wastewater (containing CrO_4^{2-}, Zn^{2+} and NaOH) and LDH was produced with CrO_4^{2-} as the interlayer anion.	Zhang *et al.*[190]
Zn(Al/Fe)	Waste tyre ash.	The ash (rich in Zn, Al, Fe and Ca) was added to H_2SO_4 to extract the metals and filtered to remove the insoluble residue. The solution was neutralised with NaOH and LDH phases formed.	Wajima.[191]
NiAl	Waste from copper refining plant.	Ni was separated from the waste stream (rich in Cu, Fe, Zn and As) via precipitation of the Fe and sequential extraction with organic complexing agents. $Al(NO_3)_3 \cdot 9\,H_2O$ was added to the strip solution and LDH coprecipitated using NaOH.	Barik *et al.*[192]
NiAl	Spent electroless nickel (EN) plating bath.	Graphene oxide (GO), $Al(NO_3)_3 \cdot 9\,H_2O$ and NaOH were added to the spent EN plating bath (containing $NiSO_4$) and sonicated to produce LDH/GO composites.	Zhu *et al.*[193]
NiFe	Nickel plating wastewater.	LDH was produced from simulated wastewater using an electrocoagulation technique using iron electrodes and NaOH.	Ou *et al.*[194]
NiZnCr	Electroplating wastewater.	LDH are directly coprecipitated from the wastewater (containing Ni, Zn, and Cr) by mixing with NaOH.	Zhou *et al.*[195] Xu *et al.*[196]
ZnCuAl	Cu and Zn wastewater.	LDH are directly coprecipitated from the simulated wastewater (containing Zn, Cu and Al) by mixing with NaOH.	Wu *et al.*[197]

LDH	Waste stream utilisation	Description	Reference
MAl	Cu and Zn wastewater.	MgAl LDH seed crystals are added to (neutralised) simulated wastewater (containing (Zn^{2+} or Cu^{2+}) and Al^{3+}) and further LDH growth is observed. M = Zn, Cu	Laipan *et al.*[198]
ZnMgAl	Contaminated red mud drainage water.	$Al_2(SO_4)_3 \cdot 18\,H_2O$ was added to the drainage water (rich in Ca, Mg, Zn) and LDH coprecipitated by addition of NaOH.	Frau *et al.*[199]
ZnAsFe	As^{3+} wastewater.	LDH was formed upon the simultaneous addition of $ZnSO_4 \cdot 7\,H_2O$, $FeSO_4 \cdot 7\,H_2O$ and NaOH to the simulated wastewater.	Wang *et al.*[200]
ZnAsAl	As^{5+} wastewater.	LDH was formed upon the addition of $Zn(NO_3)_2 \cdot 6\,H_2O$, $Al(NO_3)_3 \cdot 9\,H_2O$ to the simulated wastewater (pH = 12).	Meng *et al.*[201]
MgAsAl	As^{5+} wastewater.	LDH was formed upon the addition of NaOH to a solution of $MgCl_2 \cdot 6\,H_2O$, $AlCl_3 \cdot 6\,H_2O$ and Na_2HAsO_4.	Sommella *et al.*[202]
ZnCuMgAl	Pyrite ore mining wastewater.	$MgSO_4 \cdot 7\,H_2O$ was added to simulated wastewater (containing Cu^{2+}, Zn^{2+}, Pb^{2+} and Al^{3+}) and LDH coprecipitated by addition of NaOH.	Peligro *et al.*[203]

1.2 Carbon dioxide capture

1.2.1 Climate crisis

Over the last two centuries, rapid technological advancements have been made that have led to widespread economic growth. These advances have been fuelled by the combustion of fossil fuels to provide the substantial amounts of energy required by a technologically advanced society. Several unforeseen consequences have been linked to fossil fuel use, including global warming, acid rain and smog formation from the gases and particulates formed during combustion. The most concerning of these issues is global warming; the average global temperature has risen by over 1 °C since 1850 and is predicted to increase further to 1.8 to 5.7 °C by 2100, according to some models,[204] and has been linked to rapid changes in climate leading to an increase in the number of humanitarian crises and economic and non-economic damage.[205–207] These temperature increases have been attributed to enhanced radiative forcing, largely due to increased levels of infrared active compounds in the atmosphere, commonly called greenhouse gases.[208] Carbon dioxide is one of these gases and although it not as efficient a greenhouse gas as methane, it exists at a much higher concentration in the atmosphere, causing 64% of the relative radiative forcing of increased global temperature (Figure 1.4(a)).[209,210] Of note, water vapour is the most abundant greenhouse gas providing approximately half of the total greenhouse effect. However, it has a relatively short atmospheric lifetime (9 days) and increases in atmospheric concentrations are the result of increased evaporation due to global temperature rises caused by long lived greenhouse gases.[211]

Over the last 70 years, the atmospheric CO_2 concentration has increased significantly from 310 ppm to 425 ppm.[214,215] Prior to the industrial revolution, CO_2 levels were at or below 280 ppm and had not exceeded 300 ppm over the last one million years.[216] In 2024, an estimated 41.6 Gt_{CO_2} were released globally.[217] Emissions come from a variety of sectors (Figure 1.4(b)), such as from combustion for transport (15.1%) or energy generation (27.5%), but there are also significant

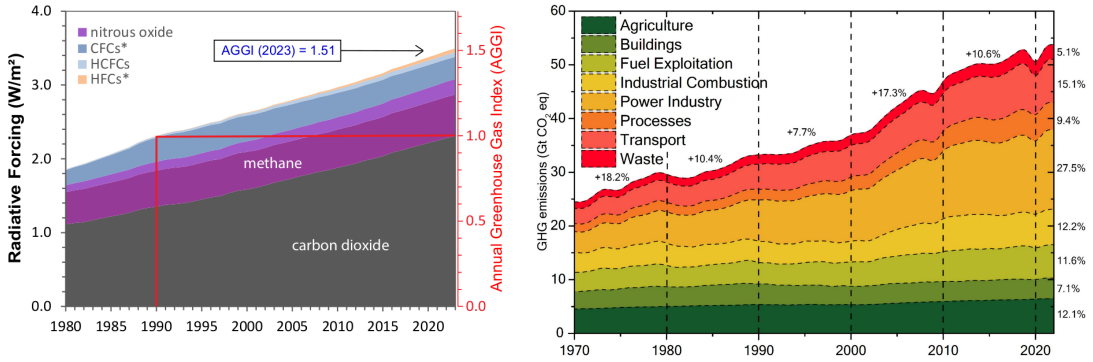

(a) (b)

Figure 1.4: (a) Radiative forcing, relative to 1750, of virtually all long-lived greenhouse gases. Reproduced from the NOAA annual greenhouse gas index.[212] (b) Trends in greenhouse gas emissions across sectors. Reproduced from Filonchyk *et al.*[213]

contributions from industrial processes (12.2%) such as cement production (5% of total emissions).[213,218]

In 2015, 196 countries signed the Paris Agreement, an international treaty aiming to limit global temperature increases to 2 °C above pre-industrial levels and pursue efforts to limit increases to 1.5 °C.[219] Analysis shows that to reach these targets, not only must carbon dioxide emissions be reduced significantly but previously released CO_2 must be removed actively (10 Gt_{CO_2} y^{-1} until 2050 and then 20 Gt_{CO_2} y^{-1} until 2100, Figure 1.5).[220]

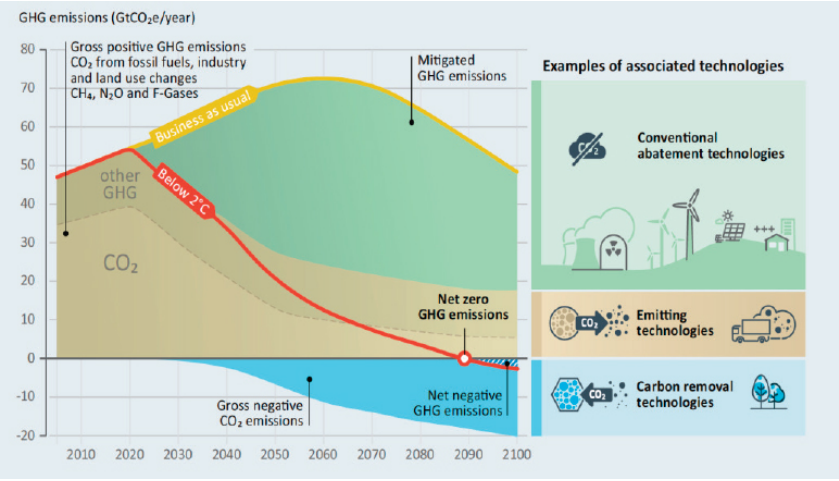

Figure 1.5: A scenario with the role of negative emissions technologies in reaching net zero emissions. For other types of greenhouse gas (e.g. methane, perfluorocarbons, and nitrous oxide), CO_2e signifies the equivalent amount of CO_2 which would have the same amount of radiative forcing.[221] Reproduced from The Emissions Gap Report 2017.[222]

1.2.2 Negative emission technology

Processes that actively remove carbon dioxide from the atmosphere are commonly called negative emission technologies (NETs). Historically, NETs have seen significantly less funding than renewable energy technologies. For example, in the United States, spending over the last 26 years on renewable energy was $ 27.65 billion compared to $ 3.7 billion for carbon sequestration, of which only $ 11 million was for NETs.[214,223] Recently, there has been more interest in NETs; for example, the European Commission is investing € 820 million in NETs between 2022 and 2026.[223]

NETs range from the enhancement of natural processes to the employment of artificial processes on an industrial scale, often called direct air capture (DAC) technologies (Figure 1.6). Natural processes which can be enhanced include reforestation and the use of fast-growing crops, which sequester CO_2 during photosynthesis; the carbon is then captured during bioenergy production and stored underground. These technologies are mature and can be rapidly deployed; however, they require significant amounts of arable land which leads to conflicts with agricultural interests.[221] Other processes include ocean macroalgae afforestation, enhanced dissolution in the ocean (ocean alkalinity enhancement) and enhanced rock weathering (the natural process of metal carbonate formation).[224–226] All of these processes are inexpensive to employ, yet there is a limit to their maximum

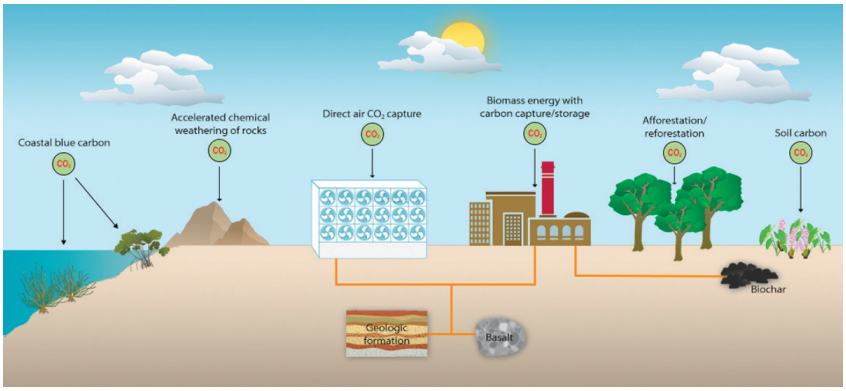

Figure 1.6: Types of negative emissions technologies (NETs). Reproduced from Negative Emissions Technologies and Reliable Sequestration: A Research Agenda.[221]

adsorption capacity and there are concerns about the environmental impact caused by large scale deployment of these processes.[227,228]

Several DAC processes have been developed, including the use of liquid or solid sorbents, membrane separation, cryogenic processes (formation of solid CO_2 via anti-sublimation), anionic exchange resins (moisture-swing adsorption) and electro-swing processes. Liquid and solid sorption processes are the most advanced technologies and several pilot plants have been deployed.

1.2.3 Direct air capture technologies

The first deployed DAC system used causticisation with $Ca(OH)_2$ to form $CaCO_3$ followed by calcination at high temperature to release the CO_2 and form CaO from which $Ca(OH)_2$ is reformed via the slake-lime process (reaction with water).[214] Kraft enhanced this process with the addition of NaOH, which enhances the carbonate solubility.[229]

Subsequently, aqueous amine sorbents were developed, which have lower energy requirements due to their lower regeneration temperatures and are commonly used industrially.[214] A plethora of different amines have been explored[230] with notable examples including monoethanolamine (MEA), diethanolamine (DEA), 2-amino-2-methyl-1-propanol (AMP), piperazine (PZ) and N-methyldiethanolamine (MDEA). Recent studies have explored the more environmentally friendly amines such as the amino acid guanidine.[231] Decomposition of the amino carbamates formed is slow and the thermal regeneration of the sorbent also requires heating of the solvent, leading to high energy costs ($\approx 10\,\mathrm{GJ\,t_{CO_2}^{-1}}$).[232] For comparison, energy derived from coal (the least carbon efficient fossil fuel source) produces $\approx 10.9\,\mathrm{GJ\,t_{CO_2}^{-1}}$.[233] Solid sorbents have also been extensively studied with porous materials such as

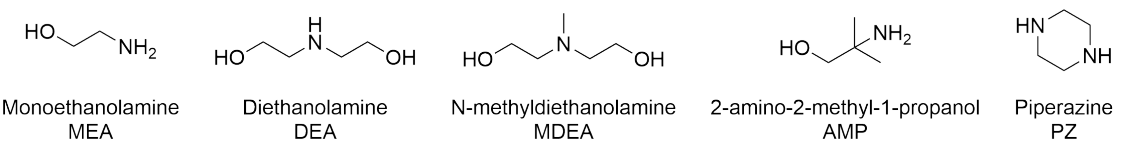

Figure 1.7: Common amines used in aqueous solutions for CO_2 capture.

zeolites, metal organic frameworks (MOFs) and activated carbon often employed. Physisorbents typically show low capacity at low pressures and low selectivity. As such, chemisorbents with basic functionalities are often employed, which exhibit higher uptake and selectivity. Solid alkali carbonates such as CaO, $Ca(OH)_2$ and K_2CO_3 are active for carbon capture under dilute conditions; however, their high operating and regeneration temperatures (650 °C and 900 °C respectively) make them better suited to post-combustion flue gas scrubbing.[234]

Basic functionalities may be added to porous materials via the addition of amine components. Of note is the Mg_2(dobpdc) (dobpdc^{4-} = 4,4 -dioxidobiphenyl-3,3 -dicarboxylate) family of metal-organic frameworks (MOFs); these materials display a cooperative insertion mechanism where the CO_2 is inserted into a metal-amine bond, forming chains of ammonium carbonate (Figure 1.8). The adsorption properties can thus be modulated by changing the metal framework or amine group used.[235] These materials often require dry operating conditions, as they exhibit poor CO_2/H_2O selectivity. Similarly to amine solutions, they also require thermal regeneration, although at lower temperatures than liquid sorbents (typically 90 to 120 °C), thus reducing the energy requirements ($\approx 5\,\mathrm{GJ\,t_{CO_2}}$).[232] Amine-modified solid sorbents are discussed further in Chapter 1.2.4.

Membrane separation relies on relative rates of diffusion through a membrane, driven by a partial pressure differential governed by Fick's law.[237] Air is typically compressed before separation to increase the pressure differential. High selectivity is needed to achieve significant separation; however, current sorbents with high selectivity have such low permeability that the rate of separation is impractical.[214]

Cryogenic separation is attractive, as it produces high purity CO_2 and doesn't require any extra chemicals or sorbents. This process cools air to −78 °C where deposition of CO_2 occurs, selectively removing it from the gas stream. This cooling process leads to substantially higher energy demands than other sorption processes ($50\,\mathrm{GJ_e\,t_{CO_2}^{-1}}$) and, as such, will only see applications in low temperature systems

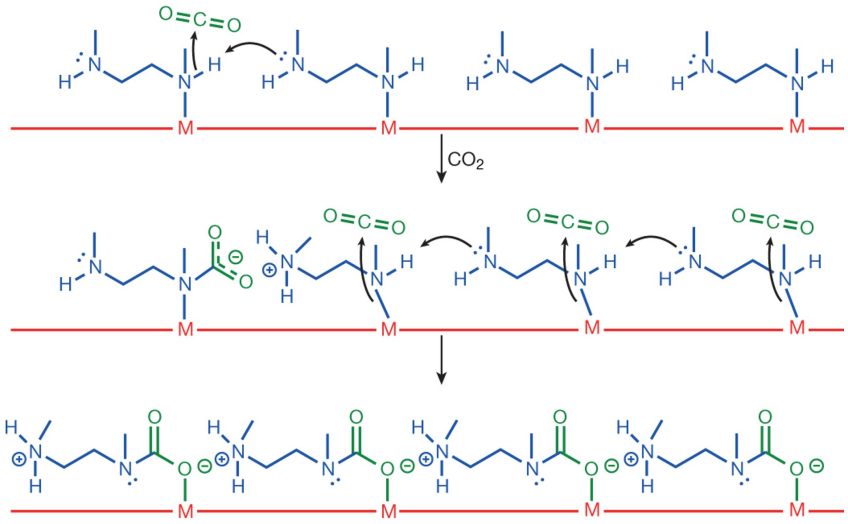

Figure 1.8: The mechanism of CO_2 adsorption at neighbouring M–mmen sites of a mmen–M_2(dobpdc) MOF. Formation of an ammonium carbamate species destabilises the amine coordinated at the next metal site, initiating the cooperative adsorption of CO_2. Reproduced from McDonald *et al.*[236]

where low temperature CO_2 is needed or where it can be used as a coolant in another low temperature process.[214,238]

Electrical sorption processes have the potential to be highly energy efficient as they do not require a gas compression or thermal regeneration of the sorbent. Two main types of electrochemical processes have been developed: redox active sorbents and pH swing processes. Redox active species are often oxygen sensitive, thereby limiting the scope of potential sorbents. A high selectivity is also needed to ensure a high faradic efficiency. Seo and Hatton demonstrated a potential system using the oxygen insensitive commercial dye neutral red, which was shown to have a minimal electrical energy demand of $1.477\,\mathrm{GJ_e\,t_{CO_2}^{-1}}$.[239] The reduction of the dye produces hydroxide ions, increasing the pH of the solution and binding CO_2. Oxidation of the dye has the opposite effect, releasing the CO_2. In pH swing processes, water electrolysis releases hydroxide ions and protons at the anion and cation respectively, changing the local pH of the solution. This pH change has been shown to facilitate binding and release of CO_2 in a $Ca(OH)_2/CaCO_3$ system. Under alkaline conditions $CaCO_3$ is formed via the reaction with air; a decrease in

pH promotes the release of CO_2 by dissolving the $CaCO_3$, eliminating the need for high temperature calcination.[240]

Current pilot plants with their scale and technology employed are detailed in Table 1.3.

1.2.4 Amine-modified solid sorbents

As previously mentioned, most commercial carbon capture processes use an alkaline liquid solvent (amine or metal hydroxide). However, the high heat capacities of the liquid lead to high regeneration energies, making them unsuitable for DAC applications. Solid supported amines have been developed to overcome these limitations, using a porous solid (with a lower heat capacity) to disperse amine functionalities. The use of this type of material for CO_2 capture was first reported by Tsuda *et al.* in 1992, using liquid suspensions of amine-modified silica gels, but subsequent work has focused on the use of dry powders.[244,245] These materials are typically grouped into three categories (Figure 1.9): Class 1 - Physical impregnation of an amine (typically a polymer such as polyethylenimine (PEI)), Class 2 - Covalently bound amines and Class 3 - In situ polymerisation via covalent grafting of an amine-containing monomer.[246] These materials typically contain a mixture of primary and secondary amines, but not tertiary amines. Although tertiary amines have been used in liquid based sorption systems, studies have shown tertiary amines perform poorly when used on a solid support, as they cannot form a alkylammonium carbamate ion pair, instead requiring humid conditions to form alkylammonium bicarbonate species.[247]

Class 1 sorbents were pioneered by Xu *et al.* in 2002 who showed that the polymer PEI dispersed on a MCM-41 solid support, demonstrating a two-times higher sorption capacity than that of the pure polymer; they dubbed the material as a "molecular basket for CO_2".[248] These are the easiest types of material to prepare, meaning they may be the most practical to employ on a large scale.[249]

Table 1.3: Summary of currently operational DAC plants.[241]

Company	Location	Year built	Capacity ($t_{CO_2}\,y^{-1}$)	Technology
Climeworks	Iceland	2017	50	Solid - amine-modified nanofibrillated cellulose[242] (Low temperature regeneration)
Climeworks	Italy	2018	150	Solid - amine-modified nanofibrillated cellulose[242] (Low temperature regeneration)
Climeworks	Iceland	2021	4000	Solid - amine-modified nanofibrillated cellulose[242] (Low temperature regeneration)
Climeworks	Iceland	2024	36 000	Solid - amine-modified nanofibrillated cellulose[242] (Low temperature regeneration)
GreenCap Solutions	Norway	2016	50	Solid - Zeolite at sub zero temperature (240 °C temperature swing)
NEG8 Carbon	Ireland	2023	1	Solid (Low temperature regeneration)
Mission Zero Technologies	UK	2023	50	Electrochemical
Nellie Technologies	UK	2024	115	Microalgal photobioreactor
ReCarbon	Netherlands	2022	4	Algae
Carboyn	Netherlands	2023	5	Solid - Modified fiber membrane (Low temperature regeneration)
Greenlyte Carbon Technologies	Germany	2023	100	Electrochemical
DACMA GmbH	Brazil	2023	15	Solid (Low temperature regeneration)[243]
DACMA GmbH	Germany	2024	60	Solid (Low temperature regeneration)[243]

Company	Location	Year built	Capacity ($t_{CO_2}\,y^{-1}$)	Technology
Neocarbon	Germany	2024	5	Low temperature regeneration
Neocarbon	Germany	2024	62	Low temperature regeneration
Carbominer	Austria	2022	1	Ion exchange/Electrochemical
RepAir Carbon	Israel	2023	1	Electrochemical
Planet Savers	Japan	2024	3.5	Solid - Zeolite (Low temperature regeneration)
Ecolair	Colombia	2023	60	
AirCapture	US	2023	100	Solid - Amine-based (Low temperature regeneration)
Carbon Collect	US	2022	30	Solid (Low temperature regeneration)
Holocene	US	2024	10	Liquid - Amine/Guanidine (Low temperature regeneration)
Avnos	US	2023	33	Ion exchange
Heirloom	US	2023	1000	Solid - $CaOH_2$ (High temperature regeneration)
280 Earth	US	2024	500	Solid (Low temperature regeneration)
Carbon engineering	Canada	2015	339	Liquid - KOH/CaO (High temperature regeneration)
Global Thermostat	US	2021	10	Solid - Amine-modified ceramic monolith (Low temperature regeneration)
Global Thermostat	US	2022	1000	Solid - Amine-modified ceramic monolith (Low temperature regeneration)
Global Thermostat	US (Hawaii)	2023	10	Algae

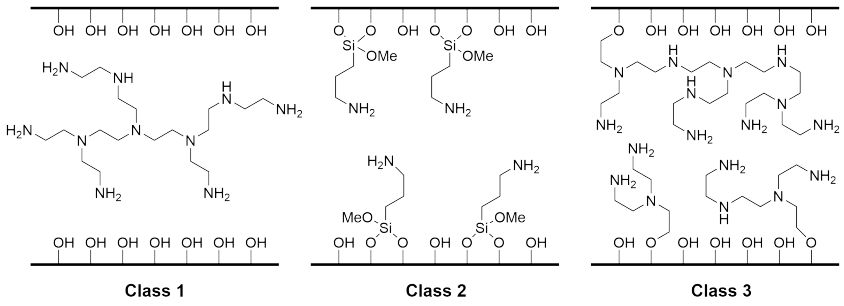

Figure 1.9: The three classes of amine-modified sorbents. Class 1: sorbent impregnated with amines (PEI shown here). Class 2: sorbent with covalently bound amine (amino silane shown here). Class 3: sorbent covalently bound to polymeric amine (in situ polymerised aziridine shown here).[260]

Class 2 sorbents were first reported by Tsuda *et al.*, as mentioned previously, using the hydrolysis-condensation polymerisation of amino silanes to form amino silica gels, but much subsequent work concerns the post-synthesis modification of supports, often using silane chemistry. Of note, Sayari's research group has published numerous works on the use of amino silane-modified MCM-41 for CO_2 removal from different gas streams.[250–256] These typically possess lower amine loadings, and thus smaller CO_2 capacities than those found in Class 1 sorbents, but display higher stability to degradation, due to the stronger interaction with the support.[257]

Class 3 sorbents were developed by Liang *et al.* via stepwise growth of melamine dendrimers from the surface amine groups in amino silane-modified mesocellular silicious foam. They are designed to bridge the gap between the previous two classes as they feature both abundant amino groups, similar to Class 1, and have strong interactions with the support, as in Class 2.[257,258] Subsequent work has explored the direct surface polymerisation of amine-containing monomers, using aziridine on the silica SBA-15.[259]

Of the materials commonly explored as solid amine capture materials, mesoporous silicas and metal-organic frameworks (MOFs) have attracted the most attention because they possess high surface areas and are easily amenable to amine modification. A recent review by Sodiq *et al.* shows that PEI/silica and $Mg_2(dobdc)(N_2H_4)_{1.8}$

(H_4dobdc = 2,5-dihydroxyl-1,4-benzenedicarboxylic acid) possess the highest DAC CO_2 absorption capacities for these classes of materials (2.36 and 4.58 mmol g^{-1}, respectively), but both have high material costs (£ 30 800 kg^{-1} (MCM-41 supplied by Sigma-Aldrich) and between $ 25 to 100 kg^{-1} for $Mg_2(dobdc)(N_2H_4)_{1.8}$).[261–264]

The commonly accepted mechanisms of reactions between these solid amines and CO_2 are shown in Figure 1.10. The primary amine acts as a Lewis base, reversibly binding CO_2 (a Lewis acid) to form a zwitterion. This then interacts with neighbouring groups to form an ammonium carbamate or carbamic acid complex. In the presence of moisture, H_2O can act as the Lewis base, forming an ammonium bicarbonate with stabilisation from an amine.

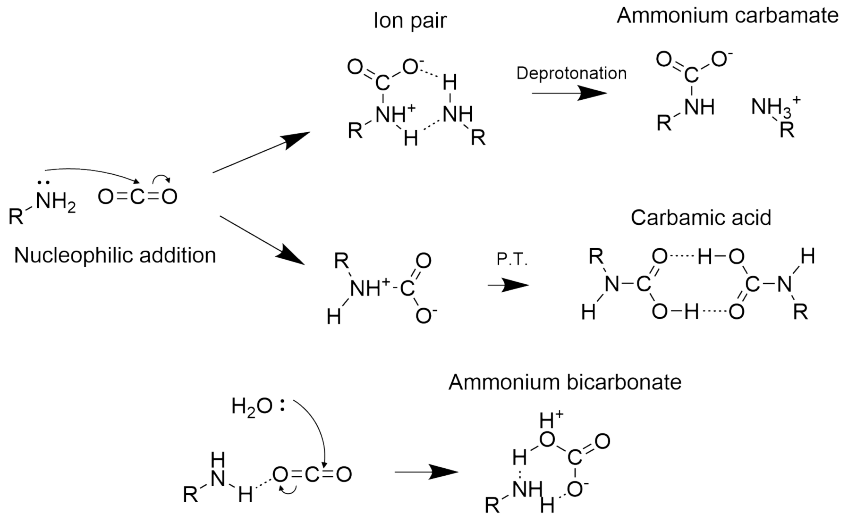

Figure 1.10: Proposed reaction mechanisms of CO_2 with a primary amine. Adapted from Huhe *et al.*[265]

The main challenge associated with DAC technologies is the cost per tonne of CO_2 captured which relates to the financial cost of building and running the plant (due to the high energy requirements) as well as the associated carbon emissions from the energy production, the offsetting of which reduces the relative efficiency of the capture process. Overcoming this challenge requires the sourcing of low-cost, low-carbon energy; employment of energy-efficient processes (such as the use of amine-modified sorbents with low regeneration temperatures) and the application

of sustainable sorbents with long lifetimes (to reduce the environmental impact of DAC infrastructure).

1.3 Plastic pyrolysis

1.3.1 Plastic crisis

The first man-made polymer was nitrocellulose (brand name Celluloid), created by Alexander Parkes in the 1850s, from the reaction of nitric acid and cellulose, and later developed into a commercial product by John Wesley Hyatt.[266] This was followed by Bakelite, the first fully synthetic polymer, created by Leo Baekeland in 1907 using the reaction of phenol and formaldehyde.[266] These were followed by modern plastics such as: polyvinyl chloride (PVC, commercialised in 1912)[266], poly(methyl methacrylate) (PMMA, 1924), polyethylene (PE, 1933), polyurethane (PU, 1937), nylon (1938), polyethylene terephthalate (PET, 1941) polystyrene (PS, 1944) and polypropylene (PP, 1954) which are still manufactured in significant quantities (Figure 1.11).[267,268] Today, plastics are found across society, including uses in agriculture, transportation, packaging, medicine, manufacturing and consumer goods.[269] Plastics possess several advantages over traditional materials: they require a lower energy of production over metal and glass, they are lightweight (ideal for transportation parts), have a lower cost than traditional materials and can be easily shaped into previously inaccessible forms, for uses such as packaging for fresh food.[269]

To keep up with demand, plastics production has steadily increased with 430 Mt of virgin plastic produced in 2019[270] which is expected to double by 2040.[271] 50% of

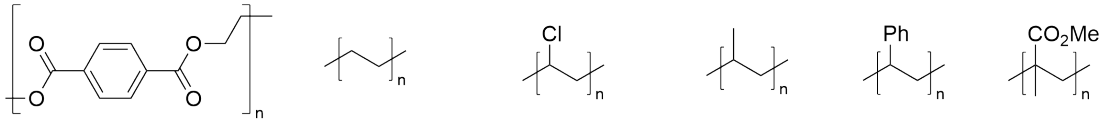

Figure 1.11: Different types of plastic.

this is used for single-use plastic[271] with 220 Mt tonnes of plastic waste produced in 2024.[272] Of all the plastic waste ever produced, only 9% has been recycled, 12% has been incinerated and the remaining 79% now sits in landfill.[273] This plastic waste is poorly managed and significant amounts enter the aquatic environment; for example there are an estimated 82 to 358 trillion plastic particles in the world's oceans (1.1 to 4.9 t).[274] This issue is of significant public concern, as plastics are reported to last indefinitely, leading to chronic exposure.[275] This timescale is not supported by evidence, with recent studies showing that plastic polymer degradation is significantly enhanced by sunlight and microbes.[275–277] Nonetheless, the lifetimes of plastics are still on the centennial timescale, making them persistent contaminants. Of significant worry are small pieces of plastic, called microplastics, which can be taken up by living organisms. The average person is estimated to consume 50000 microplastic particles annually through food and water, amid increasing concerns about about their deleterious effects on human health.[278,279]

There is therefore an urgent need to reduce the amount of plastic entering the environment, which necessitates both a reduction in the amount of plastic waste generated and additional recycling opportunities (Figure 1.12). The different types of plastic recycling are typically categorised as: primary, where polymers are remade into a similar product; secondary, reused for a different application, typically of lower value; tertiary or chemical recycling where it is converted into new chemical feedstocks and quaternary or energy recovery where it is incinerated for energy production (Figure 1.13).[281] Primary recycling requires pure materials and so is typically only utilised with waste from manufacturing and post-consumer materials of known origin. Where possible, primary and secondary recycling should be employed, as this reduces the need for virgin petrochemical feedstocks. These processes typically require grinding and reforming of the plastic, which causes polymer degradation, limiting the number of reprocessing cycles for a given polymer.[282] Quaternary recycling should be avoided where possible, as the energy produced is less than that saved in plastic production by recycling ($36\,\mathrm{kJ\,kg^{-1}}$ vs 60 to $88\,\mathrm{kJ\,kg^{-1}}$)[283] and releases significant amounts of CO_2 as well as toxic gases such as

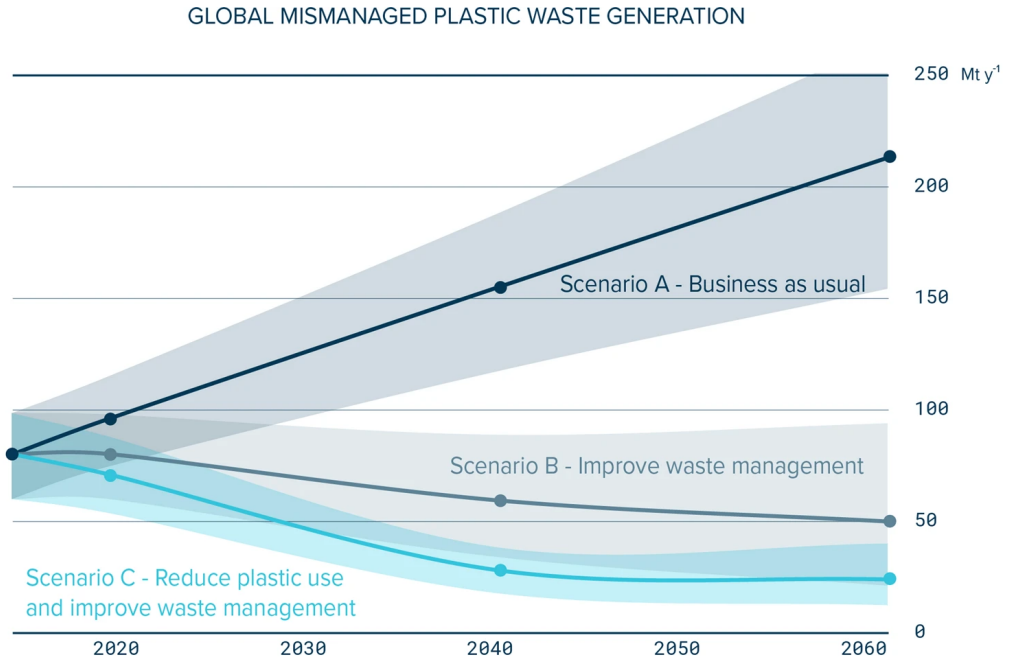

Figure 1.12: Future projections of global mismanaged plastic waste. Scenario A corresponds to an increase in plastic demand with GDP. Scenario B reflects an improvement in waste management infrastructure with GDP. Scenario C corresponds to the management of scenario B with a reduction in consumer demand (where plastics constitute 10% and 5% of municipal waste by 2020 and 2040 respectively). Reproduced from Lebreton *et al.*[280]

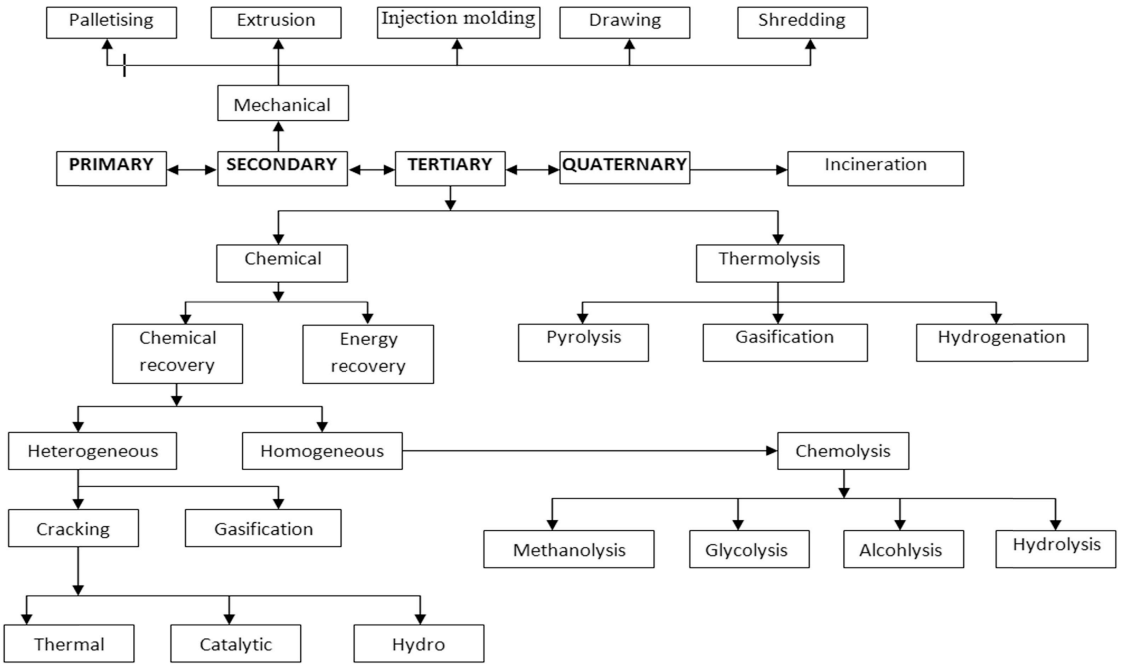

Figure 1.13: The different plastic waste recycling pathways. Reproduced from Singh *et al.*[281]

dioxins, furans, mercury and halogens.[284] This demonstrates the need for improved tertiary recycling technologies to process potentially contaminated or end-of-life waste such as post-consumer waste.

1.3.2 Tertiary recycling

Depending on the structure of the polymer (see Figure 1.11), several different methods for tertiary recycling exist. PET, commonly found in plastic water bottles, loses its ductility after mechanical recycling. It cannot therefore be reused for plastic bottles and is often converted into textile fibres.[285] However, the ether linkage present in the backbone is susceptible to chemolysis, typically solvolysis with ethylene glycol, methanol or water, to yield terephthalate-based monomers which can be re-polymerised to regenerate PET with the desired properties or other related materials.[286]

Polyolefins do not have such a reactive functionality, making their decomposition more difficult. These make up the majority of plastics produced, for instance the majority of plastics ever produced are: PE (36%), PP (21%), PVC (12%).[287] Strategies to introduce such functionalities include the use of a dehydrogenation catalyst to produce unsaturated (alkene) sites, which can then undergo olefin

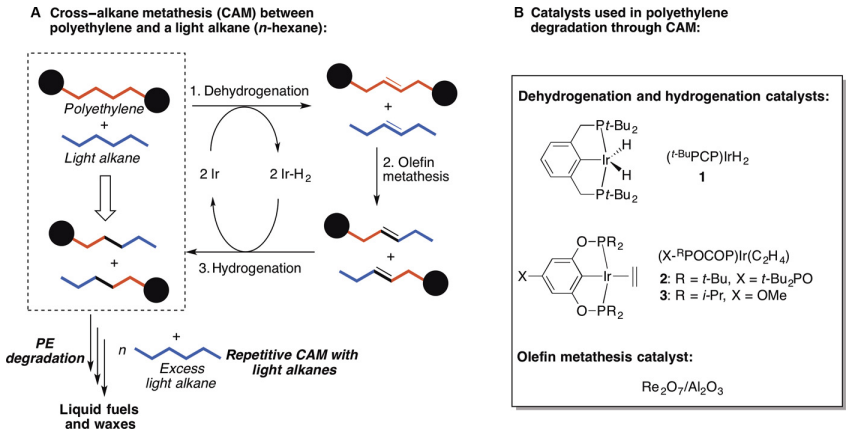

Figure 1.14: (**A**) PE degradation pathway through catalytic cross-alkane metathesis. Dehydrogenation of both PE and a light alkane (*n*-hexane used as an example) creates unsaturated olefins. Subsequently, cross-olefin metathesis followed by hydrogenation causes breakdown of PE chain into shorter chains. (**B**) Structures of the dehydrogenation and olefin metathesis catalysts used. Reproduced from Jia *et al.*[288]

metathesis to yield low molecular weight products for liquid fuels (Figure 1.14).[288] These are important proof of concept studies, but the use of expensive noble metal catalysts such as Ir for dehydrogenation and $Ru_2O_3$for the cross-metathesis reaction hinders their deployment at scale.[282]

The less expensive alternative is thermal pyrolysis. This involves the thermal degradation of the polymer under an inert atmosphere to yield lower molecular weight products. Thermal pyrolysis is typically classified as: slow pyrolysis, characterised by low heating rates ($< 10\,^{\circ}\mathrm{C\,min^{-1}}$ to 350 to 700 °C); fast pyrolysis ($< 300\,^{\circ}\mathrm{C\,min^{-1}}$ to 400 to 600 °C); flash pyrolysis, characterised by fast heating rates ($\approx 1000\,^{\circ}\mathrm{C\,s^{-1}}$ to $< 650\,^{\circ}\mathrm{C}$) and gasification pyrolysis at high temperatures ($\approx 1000\,^{\circ}\mathrm{C\,s^{-1}}$ to 700 to 1500 °C). Slow pyrolysis produces the most char (solids), with the liquid fraction increasing in fast and flash pyrolysis; gasification yields high gas yields.[289] Variations on thermal pyrolysis include heating via microwave (500 to 700 °C) and plasma (3000 to 8000 K, $10 \times 10^6\,\mathrm{K\,s^{-1}}$) pyrolysis.[290,291]

The products produced by thermal pyrolysis correspond to a statistical distribution caused by the competing reactions that occur.[292,293] Depending on the structure of the polymer, the types of reaction vary; experimentally observed modes are a combination of: elimination of small molecules (such as HCl from PVC); unzipping of monomers (seen in PMMA); cyclisation (seen in polyacrylonitrile); random scission of polymer chains (seen in PE); and formation of specific compounds.[294] Catalysts can be employed both to decrease the temperature needed for pyrolysis to occur and to improve the selectivity of the reaction. For example, addition of a binuclear macrocyclic Zr complex supported on Al_2O_3 to the thermal pyrolysis of PE reduces the temperature required by 50 °C (from 400 °C) and increases the molecular weight of the products from C_{7-16} to C_{48} via interactions of the thermally produced polymer radicals and the catalyst.[294] In comparison, Ni-impregnated zeolites produce almost exclusively C_{4-8},[295] whereas Zn-P-impregnated zeolites are selective for the formation of monocyclic aromatic hydrocarbons.[296] Additionally, a H_2 atmosphere may be used, which allows a hydrogenolysis reaction to occur,

changing the product distribution. In a system using a Ru catalyst, this suppressed methane formation and increased the molecular weight of the fuels produced.[297]

Pyrolysis of polypropylene is typically conducted at higher temperatures (500 to 900 °C) and catalysts are desired to yield non-wax low-molecular weight products at lower temperatures.[282] Target products include fuel range hydrocarbons (C_{5-16}) or H_2 production with simultaneous formation of valuable carbon products such as carbon nanotubes.[298,299] Catalysts should be low cost to make the process economical and, as such, much of the literature explores both natural (such as natural silica-aluminas: dolomite, diatomite, perlite and kaolin) and waste materials (such as red mud which is rich in Fe_2O_3) as catalysts.[300,301]

1.4 Thesis overview

The aims of this thesis are to develop sustainable and scalable synthesis methods for LDHs and investigate their potential applications in industrially relevant sustainable technology applications. A description of the analytical techniques employed for analysis and the synthetic protocols used are given in Chapter 2. Chapter 3 explores the use of the mineral struvite ($MgNH_4PO_4 \cdot 6\,H_2O$) as a source of magnesium for MgAl LDH synthesis. The initial studies focus on the methodology previously reported by our group,[95,97] after which an alternative, two-step synthesis is explored to yield materials with high surface areas. Different aluminium sources are also explored. Chapter 4 focuses on the surface modification of LDHs using organo-functionalised silyl ethers and their performance for the capture of carbon dioxide from the atmosphere. The effect of the reaction conditions on the performance was investigated, as well as the effect of the nature of the organic, amine-containing, functionality. Finally, Chapter 5 details the doping of other elements within the LDH materials and studies their catalytic performance for the catalytic pyrolysis of PP. Their performance is compared to traditionally synthesised LDHs to investigate the effect of surface area and phosphate on the catalytic performance.

References

(1) J.-Y. Lee, G.-H. Gwak, H.-M. Kim, T.-i. Kim, G. J. Lee and J.-M. Oh, *Appl. Clay Sci.*, 2016, **134**, 44–49.

(2) F. Cavani, F. Trifirò and A. Vaccari, *Catal. Today*, 1991, **11**, 173–301.

(3) S. J. Mills, A. G. Christy, J.-M. R. Génin, T. Kameda and F. Colombo, *Mineral. Mag.*, 2012, **76**, 1289–1336.

(4) S.-L. Wang, C.-H. Lin, Y.-Y. Yan and M. K. Wang, *Appl. Clay Sci.*, 2013, **72**, 191–195.

(5) S. Velu, V. Ramaswamy and S. Sivasanker, *Chem. Commun.*, 1997, 2107–2108.

(6) S. Velu, K. Suzuki, M. Okazaki, T. Osaki, S. Tomura and F. Ohashi, *Chem. Mater.*, 1999, **11**, 2163–2172.

(7) X. Shu, W. Zhang, J. He, F. Gao and Y. Zhu, *Solid State Sci.*, 2006, **8**, 634–639.

(8) D. S. Argüello, L. C. Cabana Saavedra, S. M. Mendoza, M. I. Oliva, E. Rodríguez-Castellón, N. F. Bálsamo, G. A. Eimer and M. E. Crivello, *Catal. Today*, 2024, **427**, 114415.

(9) X. Yu, B. Wang, C. Wang, C. Zhuang, Y. Yao, Z. Li, C. Wu, J. Feng and Z. Zou, *Small*, 2021, **17**, 2103412.

(10) J. J. Bravo-Suárez, E. A. Páez-Mozo and S. T. Oyama, *Quím. Nova*, 2004, **27**, 601–614.

(11) S. Miyata, *Clays Clay Miner.*, 1975, **23**, 369–375.

(12) K. Jayanthi and P. V. Kamath, *Dalton Trans.*, 2013, **42**, 13220–13230.

(13) E. S. Zhitova, R. M. Sheveleva, A. A. Zolotarev and S. V. Krivovichev, *Crystals*, 2023, **13**, 839.

(14) A. V. Radha, C. Shivakumara and P. V. Kamath, *Clays Clay Miner.*, 2005, **53**, 520–527.

(15) L. Pachayappan, S. Nagendran and P. V. Kamath, *Cryst. Growth & Des.*, 2017, **17**, 2536–2543.

(16) A. S. Bookin and V. A. Drits, *Clays Clay Miner.*, 1993, **41**, 551–557.

(17) W. Hofmeister and H. V. Platen, *Crystallogr. Rev.*, 1992, **3**, 3–26.

(18) *Neues Jahrbuch fü r Mineral. Monatshefte*, 2000, **2000**, 455–465.

(19) R. Mostarih and A. de Roy, *J. Phys. Chem. Solids*, 2006, **67**, 1058–1062.

(20) W. Yang, Y. Kim, P. K. T. Liu, M. Sahimi and T. T. Tsotsis, *Chem. Eng. Sci.*, 2002, **57**, 2945–2953.

(21) A. Shimamura, E. Kanezaki, M. I. Jones and J. B. Metson, *J. Solid State Chem.*, 2012, **186**, 116–123.

(22) K. Matsuda, N. Iio, M. Kawashimo, A. Okuda, R. Fukuzaki, N. Tarutani, K. Katagiri and K. Inumaru, *Inorg. Chem.*, 2023, **62**, 17276–17287.

(23) T. Moroz, L. Razvorotneva, T. Grigorieva, M. Mazurov, D. Arkhipenko and V. Prugov, *Appl. Clay Sci.*, 2001, **18**, 29–36.

(24) L. Santamaría, S. A. Korili and A. Gil, *Chem. Eng. J.*, 2023, **455**, 140551.

(25) T. Kameda, Y. Takahashi, S. Kumagai, Y. Saito, S. Fujita, I. Itou, T. Han and T. Yoshioka, *Inorg. Chem. Commun.*, 2022, **135**, 109108.

(26) R. M. M. Santos, J. Tronto, V. Briois and C. V. Santilli, *J. Mater. Chem. A*, 2017, **5**, 9998–10009.

(27) G. Mascolo and M. C. Mascolo, *Microporous Mesoporous Mater.*, 2015, **214**, 246–248.

(28) V. K. Ameena Shirin, R. Sankar, A. P. Johnson, H. V. Gangadharappa and K. Pramod, *J. Control. Release*, 2021, **330**, 398–426.

(29) H. Tagaya, A. Ogata, T. Kuwahara, S. Ogata, M. Karasu, J.-i. Kadokawa and K. Chiba, *Microporous Mater.*, 1996, **7**, 151–158.

(30) M. K. Motandi, Z. Zhang, S. Inkoua and L. Yan, *Environ. Prog. & Sustain. Energy*, 2022, **41**, e13744.

(31) M. R. Othman, Z. Helwani, Martunus and W. J. N. Fernando, *Appl. Organomet. Chem.*, 2009, **23**, 335–346.

(32) M. V. Bukhtiyarova, *J. Solid State Chem.*, 2019, **269**, 494–506.

(33) X. Duan and D. Evans, *Layered Double Hydroxides*, Springer, 2006.

(34) Y. Zhao, F. Li, R. Zhang, D. G. Evans and X. Duan, *Chem. Mater.*, 2002, **14**, 4286–4291.

(35) J.-M. Oh, S.-H. Hwang and J.-H. Choy, *Solid State Ionics*, 2002, **151**, 285–291.

(36) L. Liao, N. Zhao and Z. Xia, *Mater. Res. Bull.*, 2012, **47**, 3897–3901.

(37) L. M. Parker, N. B. Milestone and R. H. Newman, *Ind. & Eng. Chem. Res.*, 1995, **34**, 1196–1202.

(38) G. Hu and D. O'Hare, *J. Am. Chem. Soc.*, 2005, **127**, 17808–17813.

(39) Q. Wang and D. O'Hare, *Chem. Commun.*, 2013, **49**, 6301–6303.

(40) C. Chen, M. Yang, Q. Wang, J.-C. Buffet and D. O'Hare, *J. Mater. Chem. A*, 2014, **2**, 15102–15110.

(41) V. Erastova, M. T. Degiacomi, D. O'Hare and H. C. Greenwell, *RSC Adv.*, 2017, **7**, 5076–5083.

(42) J. Kuljiraseth, A. Wangriya, W. Klysubun and S. Jitkarnka, *Radiat. Phys. Chem.*, 2020, **172**, 108782.

(43) C. Chen, A. Wangriya, J.-C. Buffet and D. O'Hare, *Dalton Trans.*, 2015, **44**, 16392–16398.

(44) M. Yang, O. McDermott, J.-C. Buffet and D. O'Hare, *RSC Adv.*, 2014, **4**, 51676–51682.

(45) J. Fragoso, J. Balbuena, M. Cruz-Yusta, I. Pavlovic, M. Sánchez and L. Sánchez, *Constr. Build. Mater.*, 2023, **394**, 132241.

(46) A. Pastor, C. Chen, G. de Miguel, F. Martin, M. Cruz-Yusta, J.-C. Buffet, D. O'Hare, I. Pavlovic and L. Sánchez, *Chem. Eng. J.*, 2022, **429**, 132361.

(47) J. Kuljiraseth, A. Wangriya, J. M. C. Malones, W. Klysubun and S. Jitkarnka, *Appl. Catal. B: Environ.*, 2019, **243**, 415–427.

(48) M. Li, C. Chen, T. Ayvalı, H. Suo, J. Zheng, I. F. Teixeira, L. Ye, H. Zou, D. O'Hare and S. C. E. Tsang, *ACS Catal.*, 2018, **8**, 4390–4401.

(49) X. Zhu, C. Chen, H. Suo, Q. Wang, Y. Shi, D. O'Hare and N. Cai, *Energy*, 2019, **167**, 960–969.

(50) C. Chen, M. Greenwood, J.-C. Buffet and D. O'Hare, *Green Chem.*, 2020, **22**, 3117–3121.

(51) Z. Wang, L. Huang, T. Reina, A. Efstathiou and Q. Wang, *Catalysts*, 2020, **10**, 1168.

(52) T. Zhang, F. He, J. Zhang and F. Gu, *Int. J. Hydrog. Energy*, 2023, **48**, 5940–5952.

(53) X. Zhu, C. Chen, Y. Shi, D. O'Hare and N. Cai, *Adsorption*, 2020, **26**, 1127–1135.

(54) C.-W. Jeon, S.-S. Lee and I.-K. Park, *ACS Appl. Mater. & Interfaces*, 2019, **11**, 35138–35145.

(55) H. Cho, C.-W. Jeon, B. D. On, I.-K. Park, S. Choi, J. Jang and G. Wang, *Adv. Mater. Interfaces*, 2021, **8**, 2001990.

(56) B. M. V. d. Gama, R. Selvasembian, D. A. Giannakoudakis, K. S. Triantafyllidis, G. McKay and L. Meili, *Molecules*, 2022, **27**, 4900.

(57) A. A. Altalhi, E. A. Mohamed and N. A. Negm, *Energy Adv.*, 2024, **3**, 2136–2151.

(58) D. N. Ahmed, L. A. Naji, A. A. H. Faisal, N. Al-Ansari and M. Naushad, *Sci. Rep.*, 2020, **10**, 2042.

(59) M. El-Abboubi, N. Taoufik, F. Mahjoubi, A. Oussama, F. Kzaiber and N. Barka, *Mater. Today: Proc.*, 2021, **37**, 3894–3897.

(60) A. Khenifi, Z. Derriche, C. Mousty, V. Prévot and C. Forano, *Appl. Clay Sci.*, 2010, **47**, 362–371.

(61) D. Chaara, I. Pavlovic, F. Bruna, M. A. Ulibarri, K. Draoui and C. Barriga, *Appl. Clay Sci.*, 2010, **50**, 292–298.

(62) K.-W. Jung, S. Y. Lee, J.-W. Choi, M.-J. Hwang and W. G. Shim, *Chem. Eng. J.*, 2021, **420**, 129775.

(63) B. Wadi, A. Golmakani, V. Manovic and S. A. Nabavi, *Ind. & Eng. Chem. Res.*, 2021, **60**, 13309–13317.

(64) X. Liang, Y. Zang, Y. Xu, X. Tan, W. Hou, L. Wang and Y. Sun, *Colloids Surf. A: Physicochem. Eng. Asp.*, 2013, **433**, 122–131.

(65) L. Guo, Y. Zhang, J. Zheng, L. Shang, Y. Shi, Q. Wu, X. Liu, Y. Wang, L. Shi and Q. Shao, *Adv. Compos. Hybrid Mater.*, 2021, **4**, 819–829.

(66) X. Zhang, R. Shan, X. Li, L. Yan, Z. Ma, R. Jia and S. Sun, *Water Sci. Technol.*, 2021, **83**, 975–984.

(67) G. N. Pshinko, *J. Chem.*, 2013, **2013**, 347178.

(68) A. Vazhayil, L. Vazhayal, J. Thomas, S. Ashok C and N. Thomas, *Appl. Surf. Sci. Adv.*, 2021, **6**, 100184.

(69) N. Dewangan, W. M. Hui, S. Jayaprakash, A.-R. Bawah, A. J. Poerjoto, T. Jie, A. Jangam, K. Hidajat and S. Kawi, *Catal. Today*, 2020, **356**, 490–513.

(70) P. Gao, F. Li, N. Zhao, F. Xiao, W. Wei, L. Zhong and Y. Sun, *Appl. Catal. A: Gen.*, 2013, **468**, 442–452.

(71) P. Gao, F. Li, L. Zhang, N. Zhao, F. Xiao, W. Wei, L. Zhong and Y. Sun, *J. CO2 Util.*, 2013, **2**, 16–23.

(72) X. Duan, T. Li, X. Jiang, X. Liu, L. Xin, H. Yang, Y. Kuang and X. Sun, *Mater. Reports: Energy*, 2022, **2**, 100146.

(73) P. T. Anastas and J. C. Warner, *Green chemistry: Theory practice*, 1998, **29**, 14821–42.

(74) O. E. Ogunmakinde, W. Sher and T. Egbelakin, *Clean Technol. Environ. Policy*, 2021, **23**, 899–914.

(75) M. S. Alhumaimess, I. Hotan Alsohaimi, H. M. Hassan, M. Y. El-Sayed, M. S. Alshammari, O. F. Aldosari, H. M. Alshammari and M. M. Kamel, *J. Saudi Chem. Soc.*, 2020, **24**, 321–333.

(76) D. Dumbre, V. R. Choudhary and P. Selvakannan, *Polyhedron*, 2016, **120**, 180–184.

(77) F. Duda, M. Kieke, F. Waltz, M. E. Schweinefuß, M. Badar, P. P. Müller, K.-H. Esser, T. Lenarz, P. Behrens and N. K. Prenzler, *J. Mater. Sci. Mater. Med.*, 2015, **26**, 9.

(78) G. Rathee, A. Awasthi, D. Sood, R. Tomar, V. Tomar and R. Chandra, *Sci. Rep.*, 2019, **9**, 16225.

(79) D. Azarifar, M. Tadayoni and M. Ghaemi, *Appl. Organomet. Chem.*, 2018, **32**, DOI: 10.1002/aoc.4293.

(80) P. Priecel and J. A. Lopez-Sanchez, *ACS Sustain. Chem. & Eng.*, 2019, **7**, 3–21.

(81) S. Chilukoti and T. Thangavel, *Inorg. Chem. Commun.*, 2019, **100**, 107–117.

(82) E. Musella, I. Gualandi, M. Giorgetti, E. Scavetta, F. Basile, A. Rivalta, E. Venuti, F. Corticelli, M. Christian, V. Morandi and D. Tonelli, *Appl. Clay Sci.*, 2021, **202**, 105949.

(83) Y. Vlamidis, E. Scavetta, M. Giorgetti, N. Sangiorgi and D. Tonelli, *Appl. Clay Sci.*, 2017, **143**, 151–158.

(84) G. Huang, L. Jiang, L. Shao, X. Yang and J. Huang, *Colloids Surf. A: Physicochem. Eng. Asp.*, 2020, **597**, 124785.

(85) S. P. Newman, W. Jones, P. O'Connor and D. N. Stamires, *J. Mater. Chem.*, 2002, **12**, 153–155.

(86) Z. P. Xu and G. Q. Lu, *Chem. Mater.*, 2005, **17**, 1055–1062.

(87) J. A. Dyer, N. C. Scrivner and S. K. Dentel, *Environ. Prog.*, 1998, **17**, 1–8.

(88) W. N. Budhysutanto, H. J. M. Kramer, D. van Agterveld, A. G. Talma and P. J. Jansens, *Chem. Eng. Res. Des.*, 2010, **88**, 1445–1449.

(89) F. J. W. J. Labuschagné, A. Wiid, H. P. Venter, B. R. Gevers and A. Leuteritz, *Green Chem. Lett. Rev.*, 2018, **11**, 18–28.

(90) Y. Zhang, J. Wang, X. Liu, P. Gao, C. Gong and L. Lei, *Environ. Prog. & Sustain. Energy*, 2015, **34**, 234–239.

(91) J. S. Valente, M. S. Cantu and F. Figueras, *Chem. Mater.*, 2008, **20**, 1230–1232.

(92) S. Intasa-ard, K. Imwiset, S. Bureekaew and M. Ogawa, *Dalton Trans.*, 2018, **47**, 2896–2916.

(93) Y. Jiang, Z. Shen, C.-S. Tang and B. Shi, *Sci. Total. Environ.*, 2023, **903**, 166245.

(94) S. Shaddel, S. Ucar, J.-P. Andreassen and S. W. Østerhus, *J. Environ. Chem. Eng.*, 2019, **7**, 102918.

(95) W. L. J. Kwok, Ph.D. Thesis, University of Oxford, 2020.

(96) D. G. Evans and X. Duan, *Chem. Commun.*, 2006, 485–496.

(97) W. L. J. Kwok, H. Suo, C. Chen, D. W. J. Leung, J.-C. Buffet and D. O'Hare, *Green Chem.*, 2021, **23**, 1616–1620.

(98) L. Li, Y. Qian, H. Zhang, H. Han and P. Qiao, *Polym. Polym. Compos.*, 2019, **28**, 14–25.

(99) W. Stawiński, A. Węgrzyn, G. Mordarski, M. Skiba, O. Freitas and S. Figueiredo, *Appl. Clay Sci.*, 2018, **161**, 6–14.

(100) Y. Zhang, T. Zhou, B. Louis, F. Yu, J. Dan and Q. Wang, *Catalysts*, 2017, **7**, 105.

(101) G. B. Douglas, L. A. Wendling, R. Pleysier and M. G. Trefry, *Mine Water Environ.*, 2010, **29**, 108–115.

(102) P. Zhu, B. Xia, H. Li, H. Liu and G. Qian, *Environ. Eng. Sci.*, 2020, **38**, 99–106.

(103) P. Hu, Y. Zhang, F. Lv, W. Tong, H. Xin, Z. Meng, X. Wang and P. K. Chu, *Water Environ. J.*, 2017, **31**, 145–157.

(104) H. Dong, C. Zhang, Y. Weng, T. Wang, S. Xu, S. Ma, S. Yang and Y. Chen, *J. Clean. Prod.*, 2024, **483**, 144321.

(105) C. Zhang, H. Dong, T. Wang, Y. Li, S. Xu, Y. Que and Y. Chen, *Fuel*, 2024, **359**, 130395.

(106) N. Song, Y. Cai, L. Sun, P. Hu, Q. Zhou, J. Wu and J. Wang, *Materials*, 2022, **15**, 1514.

(107) Z. Song, H. Gao, G. Liao, W. Zhang and D. Wang, *J. Alloy. Compd.*, 2022, **901**, 163525.

(108) H. Gao, Z. Song, W. Zhang, X. Yang, X. Wang and D. Wang, *J. Environ. Sci.*, 2017, **53**, 68–77.

(109) H. Jiang, H. Guo, P. Li, Y. Li and B. Yan, *RSC Adv.*, 2019, **9**, 6054–6063.

(110) W. Zhang, H. Cheng, S. Peng, D. Li, H. Gao and D. Wang, *Water Res.*, 2020, **169**, 115265.

(111) H. Zhou, J. Ai, H. Gao, W. Zhang and D. Wang, *Colloids Surf. A: Physicochem. Eng. Asp.*, 2020, **604**, 125300.

(112) H. Guo, H. Jiang, Y. Li, B. Yan and P. Li, *J. Environ. Eng.*, 2019, **145**, 04019051.

(113) X. Li, L. Wang, B. Chen, Y. Xu, H. Wang, F. Jin, Z. Shen and D. Hou, *Appl. Clay Sci.*, 2024, **249**, 107262.

(114) Y. Agrawal, T. Gupta, S. Siddique and R. K. Sharma, *Innov. Infrastruct. Solut.*, 2021, **6**, 205.

(115) N. Mao, C. H. Zhou, J. Keeling, S. Fiore, H. Zhang, L. Chen, G. C. Jin, T. T. Zhu, D. S. Tong and W. H. Yu, *Appl. Clay Sci.*, 2018, **159**, 25–36.

(116) E. Heraldy, K. D. Nugrahaningtyas, F. B. Sanjaya, A. A. Darojat, D. S. Handayani and Y. Hidayat, *IOP Conf. Series: Mater. Sci. Eng.*, 2016, **107**, 012025.

(117) S. Li, *J. Mater. Cycles Waste Manag.*, 2019, **21**, 1242–1249.

(118) T.-H. Kim, I. T. Hong and J.-M. Oh, *Environ. Sci. Nano*, 2018, **5**, 183–190.

(119) T. Wajima and A. Suhara, *IOP Conf. Series: Earth Environ. Sci.*, 2021, **626**, 012018.

(120) A. Suhara and T. Wajma, *Int. J. Environ. Sci. Dev.*, 2020, **11**, 317–321.

(121) G. Liu, J. Yang and X. Xu, *Sci. Rep.*, 2020, **10**, 10273.

(122) G. Liu, J. Yang and X. Xu, *Molecules*, 2020, **25**, 4355.

(123) C. Wang, Y. Chen, X. Shang, X. Hou, H. Li and Z. Guo, *Mater. Lett.*, 2016, **173**, 115–118.

(124) L. Xiao, Y. Li, Q. Kong and Y. Lan, *Environ. Sci. Pollut. Res.*, 2022, **29**, 11893–11906.

(125) H. Zhang, L. Jin, H. Wu, Z. Zhang, J. Yu, W. Zhang, Y. Pan and Z. Pan, *Polymers*, 2022, **14**, 725.

(126) T. Hongo, Y. Tsunashima and A. Yamasaki, *Sustain. Mater. Technol.*, 2017, **12**, 23–26.

(127) X. Liu, Y. Zhi, Y. Yuan, H. Zhong, Y. Chen, G. Shi and M. Yang, *Appl. Clay Sci.*, 2025, **265**, 107682.

(128) F. Abd-El-Raoof, A. Tawfik, S. Komarneni and S. E. Ahmed, *Constr. Build. Mater.*, 2019, **207**, 10–16.

(129) Y. Kuwahara, S. Tamagawa, T. Fujitani and H. Yamashita, *Bull. Chem. Soc. Jpn.*, 2016, **89**, 472–480.

(130) Y. Kuwahara and H. Yamashita, *ISIJ Int.*, 2015, **55**, 1531–1537.

(131) Y. Kuwahara, T. Ohmichi, T. Kamegawa, K. Mori and H. Yamashita, *J. Mater. Chem.*, 2010, **20**, 5052–5062.

(132) Y. Kuwahara and H. Yamashita, *J. CO2 Util.*, 2013, **1**, 50–59.

(133) Y. Kuwahara, K. Tsuji, T. Ohmichi, T. Kamegawa, K. Mori and H. Yamashita, *ChemSusChem*, 2012, **5**, 1523–1532.

(134) Y. Kuwahara, K. Tsuji, T. Ohmichi, T. Kamegawa, K. Mori and H. Yamashita, *Catal. Sci. & Technol.*, 2012, **2**, 1842–1851.

(135) G. N. Muriithi, L. F. Petrik, W. M. Gitari and F. J. Doucet, *Powder Technol.*, 2017, **312**, 299–309.

(136) B. Bouzar, Y. Mamindy-Pajany and C. Hurel, *Waste Biomass Valori.*, 2023, **14**, 3923–3945.

(137) L. Jafari Foruzin, Z. Rezvani and B. Habibi, *Appl. Clay Sci.*, 2020, **188**, 105511.

(138) S. Li, F. Wang, X. Jing, J. Wang, J. Saba, Q. Liu, L. Ge, D. Song and M. Zhang, *Mater. Chem. Phys.*, 2012, **132**, 39–43.

(139) M. F. Abed and A. A. H. Faisal, *Adsorpt. Sci. & Technol.*, 2023, **2023**, DOI: 10.1155/2023/1475278.

(140) R. O. A. Adelagun, N. A. Oladoja, I. A. Ololade and A. S. Adeyemo, *Am. J. BioScience*, 2017, **5**, 13–24.

(141) D. C. Henrique, D. C. Henrique, J. R. S. Solano, V. T. Barbosa, A. O. S. Silva, C. B. Dornelas, J. L. S. Duarte and L. Meili, *Colloids Surf. A: Physicochem. Eng. Asp.*, 2022, **644**, 128752.

(142) F. Cheng, J. Pan, C. Zhao, W. Li, Y. Peng, Z. Zhang, Y. Lin and G. Chen, *Appl. Clay Sci.*, 2024, **261**, 107599.

(143) L. Santamaría, F. Devred, E. M. Gaigneaux, M. A. Vicente, S. A. Korili and A. Gil, *Microporous Mesoporous Mater.*, 2020, **309**, 110560.

(144) L. Santamaría, M. López-Aizpún, M. García-Padial, M. A. Vicente, S. A. Korili and A. Gil, *Appl. Clay Sci.*, 2020, **187**, 105486.

(145) L. Santamaría, M. A. Vicente, S. A. Korili and A. Gil, *J. Alloy. Compd.*, 2020, **843**, 156007.

(146) N. Murayama, I. Maekawa, H. Ushiro, T. Miyoshi, J. Shibata and M. Valix, *Int. J. Miner. Process.*, 2012, **110-111**, 46–52.

(147) A. I. Boulahbal, L. Santamaría, R. Bourzami, A. S. Bendrihem, M. Boutahala, S. A. Korili and A. Gil, *Miner. Eng.*, 2024, **219**, 109067.

(148) A. I. Boulahbal, L. Santamaría, A. Azizi, M. Boutahala, S. A. Korili and A. Gil, *Miner. Eng.*, 2023, **204**, 108413.

(149) A. Gil, E. Arrieta, M. A. Vicente and S. A. Korili, *Chem. Eng. J.*, 2018, **334**, 1341–1350.

(150) M. Mahinroosta and A. Allahverdi, *Process. Saf. Environ. Prot.*, 2024, **188**, 617–628.

(151) N. MURAYAMA, T. MIYOSHI, T. HAYASHI and J. SHIBATA, *Resour. Process.*, 2014, **61**, 32–38.

(152) N. MURAYAMA, J. SHIBATA, K. SAKAI, S. NAKAJIMA and H. YAMAMOTO, *Resour. Process.*, 2006, **53**, 6–11.

(153) R. Galindo, I. Padilla, R. Sánchez-Hernández, J. I. Robla, G. Monrós and A. López-Delgado, *J. Environ. Chem. Eng.*, 2015, **3**, 2552–2559.

(154) R. Galindo, A. López-Delgado, I. Padilla and M. Yates, *Appl. Clay Sci.*, 2014, **95**, 41–49.

(155) R. Galindo, A. López-Delgado, I. Padilla and M. Yates, *Appl. Clay Sci.*, 2015, **115**, 115–123.

(156) M. F. Zawrah, E. E. Ghanaym, H. E. H. Sadek, S. A. El Defrawy and O. A. M. Ali, *Ceram. Int.*, 2019, **45**, 17598–17610.

(157) M. F. Zawrah, S. A. El Defrawy, O. A. M. Ali, H. E. H. Sadek and E. E. Ghanaym, *Ceram. Int.*, 2018, **44**, 9950–9957.

(158) H. Chen, H. Wu, Y. Dai, H. Shi, X. Sun, F. Qiu and T. Zhang, *J. Clean. Prod.*, 2024, **478**, 143944.

(159) E. Willems, N. Van Velthoven, E. Smolders and M. Everaert, *Appl. Clay Sci.*, 2024, **261**, 107580.

(160) C. Belviso, A. Piancastelli, M. Sturini and S. Belviso, *Microporous Mesoporous Mater.*, 2020, **299**, 110108.

(161) F. Wang, H. Liu and L. Yan, *J. Build. Eng.*, 2023, **77**, 107409.

(162) Q. Li, G. Wei, Y. Yang, Z. Li, L. Zhang and Q. Huang, *J. Hazard. Mater.*, 2020, **394**, 122566.

(163) Q. Li, G. Wei, Y. Yang, Z. Li, L. Zhang, L. Shao and S. Lai, *Catal. Sci. & Technol.*, 2020, **10**, 7365–7377.

(164) Y. Han, Y.-J. Hu, J. Lian, S.-Z. Yang and Z.-N. Qi, *Huanjing Kexue/Environmental Sci.*, 2019, **40**, 3660–3667.

(165) J. Gu, G. Wei, Y. He, Y. Zhang, D. Xiong, L. Zhang, Y. Zhou and S. He, *J. Water Process. Eng.*, 2024, **68**, 106517.

(166) D. D. Perera-Solis, M. Pimlott, E. Fidment, A. Whiting and H. C. Greenwell, *Minerals*, 2019, **9**, 681.

(167) L. N. da Silva, D. d. S. Moraes, S. C. A. Santos and J. A. M. Corrêa, *Appl. Clay Sci.*, 2018, **161**, 163–168.

(168) S. Zhang, Q. Wang, P. Puthiaraj and W.-S. Ahn, *J. CO2 Util.*, 2019, **34**, 395–403.

(169) S. Zhang, J. Lee, B. Li, T. Zhang, S.-H. Baeck and S. E. Shim, *Korean J. Chem. Eng.*, 2024, **41**, 829–838.

(170) P. Hu, Y. Zhang, F. Lv, X. Wang, W. Tong, Z. Meng, P. K. Chu and A. Zhang, *Environ. Eng. Sci.*, 2017, **34**, 721–730.

(171) C. X. Jia, X. L. Chen and Y. Qian, *Plast. Rubber Compos.*, 2014, **43**, 46–53.

(172) C. Jia, Y. Qian, X. Chen and Y. Liu, *Polym. Eng. & Sci.*, 2014, **54**, 2918–2924.

(173) L. Li, Y. Qian and C. Jiao, *Polym. Eng. & Sci.*, 2014, **54**, 766–776.

(174) L. Li, Y. Qian and C. M. Jiao, *J. Therm. Anal. Calorim.*, 2013, **114**, 45–55.

(175) L. Li, Y. Qian, H. Han, P. Qiao and H. Zhang, *Polym. Polym. Compos.*, 2020, **29**, 842–853.

(176) Y. Qian, S. Zhou and X. Chen, *Polym. Adv. Technol.*, 2017, **28**, 353–361.

(177) Y. Qian, K. Jiang and L. Li, *e-Polymers*, 2019, **19**, 129–140.

(178) R. S. Nascimento, J. A. M. Corrêa, B. A. M. Figueira, P. A. Pinheiro, J. H. Silva, P. T. C. Freire and S. Quaranta, *Appl. Clay Sci.*, 2022, **222**, 106482.

(179) A. Golban, L. Lupa, L. Cocheci and R. Pode, *Crystals*, 2019, **9**, 514.

(180) A. Golban, L. Lupa, L. Cocheci and R. Pode, *Environ. Eng. Manag. J.*, 2020, **19**, 235–245.

(181) A. Golban, L. Cocheci, R. Lazau, L. Lupa and R. Pode, *Desalin. Water Treat.*, 2018, **131**, 317–327.

(182) L. Cocheci, L. Lupa, R. Lazău, R. Vodă and R. Pode, *J. Alloy. Compd.*, 2019, **787**, 332–343.

(183) L. Cocheci, L. Lupa, M. Gheju, A. Golban, R. Lazău and R. Pode, *Clean Technol. Environ. Policy*, 2018, **20**, 1105–1112.

(184) A. Tămaş, I. Cozma, L. Cocheci, L. Lupa and G. Rusu, *Front. Chem.*, 2020, **8**, 573535.

(185) J. Z. Zhou, Y. Liang, J. Zhang, L. Li, Y. Xu, X. Ruan, G. Qian and Z. P. Xu, *J. Hazard. Mater.*, 2014, **279**, 141–147.

(186) D. Fu, T. A. Kurniawan, R. Avtar, P. Xu and M. H. D. Othman, *Chemosphere*, 2021, **271**, 129861.

(187) D. Ma, T. Liu, M. Shao, W. Shi, X. Kong and X. Duan, *ChemistrySelect*, 2024, **9**, e202404149.

(188) D. Chen, Y. Li, J. Zhang, W. Li, J. Zhou, L. Shao and G. Qian, *J. Hazard. Mater.*, 2012, **243**, 152–160.

(189) X. X. Ruan, S. Huang and H. Chen, *Adv. Mater. Res.*, 2012, **610-613**, 538–541.

(190) J. Zhang, Y. Li, J. Zhou, D. Chen and G. Qian, *J. Hazard. Mater.*, 2012, **205-206**, 111–117.

(191) T. Wajima, *J. Physics: Conf. Ser.*, 2024, **2738**, 012037.

(192) G. Barik, E. Padhan, B. Dash, K. Sarangi and T. Subbaiah, *Miner. Eng.*, 2014, **69**, 107–112.

(193) X.-H. Zhu, F. Xie, J. Li and G.-P. Jin, *J. Environ. Chem. Eng.*, 2015, **3**, 1055–1060.

(194) J. Ou, J. Yan, T. Xu, Z. Jiang, H. Tan, S. He, B. Hu and G. Yu, *J. Mol. Liq.*, 2021, **335**, 116246.

(195) J. Z. Zhou, Y. Y. Wu, C. Liu, A. Orpe, Q. Liu, Z. P. Xu, G. R. Qian and S. Z. Qiao, *Environ. Sci. & Technol.*, 2010, **44**, 8884–8890.

(196) Y. Xu, J. Zhang, J. Zhou, C. Chen, Q. Liu, G. Qian and Z. P. Xu, *Chem. Eng. J.*, 2013, **215-216**, 411–417.

(197) L. Wu, B. Peng, Q. Li, Q. Wang, X. Yan, Q. Lin and C. Ji, *Environ. Sci. Pollut. Res.*, 2019, **26**, 19665–19675.

(198) M. Laipan, M. Zhang, Z. Wang, R. Zhu and L. Sun, *Sci. Total. Environ.*, 2024, **914**, 169954.

(199) F. Frau, R. Atzori, C. Ardau, D. Medas, F. Podda, E. Dore, A. Idini, G. Tempesta and G. Agrosì, *J. Environ. Manag.*, 2020, **271**, 111043.

(200) Q. Wang, Q. Lin, Q. Li, K. Li, L. Wu, S. Li and H. Liu, *J. Hazard. Mater.*, 2021, **403**, 123920.

(201) Z. Meng, F. Lv, X. Li, Q. Zhang, P. K. Chu, S. Komarneni and Y. Zhang, *Microporous Mesoporous Mater.*, 2016, **227**, 137–143.

(202) A. Sommella, A. G. Caporale, M. A. Denecke, S. Mangold, M. Pigna, A. Santoro, R. Terzano and A. Violante, *J. Hazard. Mater.*, 2015, **300**, 504–512.

(203) F. R. Peligro, I. Pavlovic, R. Rojas and C. Barriga, *Chem. Eng. J.*, 2016, **306**, 1035–1040.

(204) N. Scafetta, *Geosci. Front.*, 2024, **15**, 101774.

(205) S. Marzi, J. Mysiak, A. H. Essenfelder, J. S. Pal, L. Vernaccini, M. N. Mistry, L. Alfieri, K. Poljansek, M. Marin-Ferrer and M. Vousdoukas, *Glob. Environ. Chang.*, 2021, **71**, 102393.

(206) M. Auffhammer, *J. Econ. Perspect.*, 2018, **32**, 33–52.

(207) O. Serdeczny, E. Waters and S. Chan, *Non-economic loss and damage in the context of climate change: understanding the challenges*, eng, Discussion Paper 3/2016, Bonn, 2016.

(208) K. P. Shine, R. Derwent, D. J. Wuebbles, J.-J. Morcrette and A. Apling, in *Climate change: The IPCC scientific assessment*, Cambridge University Press, 1990, pp. 41–68.

(209) A. E. Galashev and O. R. Rakhmanova, *Russ. J. Phys. Chem. B*, 2013, **7**, 346–353.

(210) D. A. Vallero and T. M. Letcher, in *Unraveling Environmental Disasters*, ed. D. A. Vallero and T. M. Letcher, Elsevier, Boston, 2013, pp. 183–220.

(211) NASA Science Editorial Team, *Steamy Relationships: How Atmospheric Water Vapor Amplifies Earth's Greenhouse Effect*, 2022, `https://science.nasa.gov/earth/climate-change/steamy-relationships-how-atmospheric-water-vapor-amplifies-earths-greenhouse-effect/` (visited on 21/04/2025).

(212) E. Dlugokencky, P. Tans, X. Lan, A. Crotwell, T. Conway, L. Waterman, T. Mefford, P. Lang, M. Madronich, J. Mund, D. Neff, S. Wolter, D. Kitzis, E. Moglia, B. Hall, G. Dutton, I. Vimont, B. Miller, M. Crotwell, R. Myers, C. Siso, D. Mondeel, S. Clingan, J. Elkins, T. Thompson and S. Montzka, *The NOAA Annual Greenhouse Gas Index (AGGI)*, 2024, `https://gml.noaa.gov/aggi/aggi.html` (visited on 02/01/2025).

(213) M. Filonchyk, M. P. Peterson, H. Yan, A. Gusev, L. Zhang, Y. He and S. Yang, *Sci. Total. Environ.*, 2024, **944**, 173895.

(214) S. Chowdhury, Y. Kumar, S. Shrivastava, S. K. Patel and J. S. Sangwai, *Energy & Fuels*, 2023, **37**, 10733–10757.

(215) US National Oceanic and Atmospheric Administration Global Monitoring Laboratory, *Trends in CO2, CH4, N2O, SF6*, `https://gml.noaa.gov/ccgg/trends/` (visited on 11/01/2025).

(216) D. Lüthi, M. Le Floch, B. Bereiter, T. Blunier, J.-M. Barnola, U. Siegenthaler, D. Raynaud, J. Jouzel, H. Fischer, K. Kawamura and T. F. Stocker, *Nature*, 2008, **453**, 379–382.

(217) P. Friedlingstein, M. O'Sullivan, M. W. Jones, R. M. Andrew, J. Hauck, P. Landschützer, C. Le Quéré, H. Li, I. T. Luijkx, A. Olsen, G. P. Peters, W. Peters, J. Pongratz, C. Schwingshackl, S. Sitch, J. G. Canadell, P. Ciais, R. B. Jackson, S. R. Alin, A. Arneth, V. Arora, N. R. Bates, M. Becker, N. Bellouin, C. F. Berghoff, H. C. Bittig, L. Bopp, P. Cadule, K. Campbell, M. A. Chamberlain, N. Chandra, F. Chevallier, L. P. Chini, T. Colligan, J. Decayeux, L. Djeutchouang, X. Dou, C. Duran Rojas, K. Enyo, W. Evans, A. Fay, R. A. Feely, D. J. Ford, A. Foster, T. Gasser, M. Gehlen, T. Gkritzalis, G. Grassi, L. Gregor, N. Gruber, Ö. Gürses, I. Harris, M. Hefner, J. Heinke, G. C. Hurtt, Y. Iida, T. Ilyina, A. R. Jacobson, A. Jain, T. Jarníková, A. Jersild, F. Jiang, Z. Jin, E. Kato, R. F. Keeling, K. Klein Goldewijk, J. Knauer, J. I. Korsbakken, S. K. Lauvset, N. Lefèvre, Z. Liu, J. Liu, L. Ma, S. Maksyutov, G. Marland, N. Mayot, P. McGuire, N. Metzl, N. M. Monacci, E. J. Morgan, S.-I. Nakaoka, C. Neill, Y. Niwa, T. Nützel, L. Olivier, T. Ono, P. I. Palmer, D. Pierrot, Z. Qin, L. Resplandy, A. Roobaert, T. M. Rosan, C. Rödenbeck, J. Schwinger, T. L. Smallman, S. Smith, R. Sospedra-Alfonso, T. Steinhoff, Q. Sun, A. J. Sutton, R. Séférian, S. Takao, H. Tatebe, H. Tian, B. Tilbrook, O. Torres, E. Tourigny, H. Tsujino, F. Tubiello, G. van der Werf, R. Wanninkhof, X. Wang, D. Yang, X. Yang, Z. Yu, W. Yuan, X. Yue, S. Zaehle, N. Zeng and J. Zeng, *Earth Syst. Sci. Data*, 2024, preprint, DOI: `10.5194/essd-2024-519`.

(218) D. J. M. Flower and J. G. Sanjayan, *Int. J. Life Cycle Assess.*, 2007, **12**, 282–288.

(219) *Paris Agreement*, UNTC XXVII 7.d, `https://unfccc.int/sites/default/files/english_paris_agreement.pdf`.

(220) S. Chowdhury, M. Rakesh, S. Medhi, S. Shrivastava, R. Dehury and J. S. Sangwai, *Energy & Fuels*, 2023, **37**, 5270–5290.

(221) National Academies of Sciences, Engineering and Medicine, *Negative Emissions Technologies and Reliable Sequestration: A Research Agenda*, The National Academies Press, Washington, DC, 2019.

(222) A. Olhoff and J. Christensen, in *The Emissions Gap Report 2017: A UN Environment Synthesis Report*, United Nations Environment Programme (UNEP), 2017, pp. 1–2.

(223) D. Casaban, S. Ritchie and E. Tsalaporta, *Sustain. Chem. Clim. Action*, 2022, **1**, 100009.

(224) D. Moreira and J. C. M. Pires, *Bioresour. Technol.*, 2016, **215**, 371–379.

(225) S. Caserini, D. Pagano, F. Campo, A. Abbà, S. De Marco, D. Righi, P. Renforth and M. Grosso, *Front. Clim.*, 2021, **3**, 575900.

(226) R. D. Schuiling and P. Krijgsman, *Clim. Chang.*, 2006, **74**, 349–354.

(227) D. McLaren, *Process. Saf. Environ. Prot.*, 2012, **90**, 489–500.

(228) J. S. Campbell, S. Foteinis, V. Furey, O. Hawrot, D. Pike, S. Aeschlimann, C. N. Maesano, P. L. Reginato, D. R. Goodwin, L. L. Looger, E. S. Boyden and P. Renforth, *Front. Clim.*, 2022, **4**, 4:879133.

(229) R. Baciocchi, G. Storti and M. Mazzotti, *Chem. Eng. Process. Process. Intensif.*, 2006, **45**, 1047–1058.

(230) F. Meng, Y. Meng, T. Ju, S. Han, L. Lin and J. Jiang, *Renew. Sustain. Energy Rev.*, 2022, **168**, 112902.

(231) N. J. Williams, C. A. Seipp, F. M. Brethomé, Y.-Z. Ma, A. S. Ivanov, V. S. Bryantsev, M. K. Kidder, H. J. Martin, E. Holguin, K. A. Garrabrant and R. Custelcean, *Chem*, 2019, **5**, 719–730.

(232) R. Custelcean, K. A. Garrabrant, P. Agullo and N. J. Williams, *Cell Rep. Phys. Sci.*, 2021, **2**, 100385.

(233) M. P. E. G. Steen, *Greenhouse Gas Emissions from Fossil Fuel Fired Power Generation Systems.* Tech. rep., European Commission Joint Research Centre Institute for Advanced Materials, 2001.

(234) E. S. Sanz-Pérez, C. R. Murdock, S. A. Didas and C. W. Jones, *Chem. Rev.*, 2016, **116**, 11840–11876.

(235) R. L. Siegelman, T. M. McDonald, M. I. Gonzalez, J. D. Martell, P. J. Milner, J. A. Mason, A. H. Berger, A. S. Bhown and J. R. Long, *J. Am. Chem. Soc.*, 2017, **139**, 10526–10538.

(236) T. M. McDonald, J. A. Mason, X. Kong, E. D. Bloch, D. Gygi, A. Dani, V. Crocellà, F. Giordanino, S. O. Odoh, W. S. Drisdell, B. Vlaisavljevich, A. L. Dzubak, R. Poloni, S. K. Schnell, N. Planas, K. Lee, T. Pascal, L. F. Wan, D. Prendergast, J. B. Neaton, B. Smit, J. B. Kortright, L. Gagliardi, S. Bordiga, J. A. Reimer and J. R. Long, *Nature*, 2015, **519**, 303–308.

(237) A. Hussain, *Sep. Sci. Technol.*, 2012, **47**, 1857–1865.

(238) S. K. S. Boetcher, M. J. Traum and T. von Hippel, *Clim. Chang.*, 2020, **158**, 517–530.

(239) H. Seo and T. A. Hatton, *Nat. Commun.*, 2023, **14**, 313.

(240) C. Zhou, J. Ni, H. Chen and X. Guan, *Sustain. Energy & Fuels*, 2021, **5**, 4355–4367.

(241) Direct Air Capture Coalition, *Global DAC deployments*, `https://daccoalition.org/global-dac-deployments/` (visited on 04/01/2025).

(242) G. Leonzio, O. Mwabonje, P. S. Fennell and N. Shah, *Sustain. Prod. Consum.*, 2022, **32**, 101–111.

(243) B. Scharrer and J. Spitzner, WO/2024/115391, 2024.

(244) T. Tsuda, T. Fujiwara, Y. Taketani and T. Saegusa, *Chem. Lett.*, 1992, **21**, 2161–2164.

(245) T. Tsuda and T. Fujiwara, *J. Chem. Soc. Chem. Commun.*, 1992, 1659–1661.

(246) W. Li, S. Choi, J. H. Drese, M. Hornbostel, G. Krishnan, P. M. Eisenberger and C. W. Jones, *ChemSusChem*, 2010, **3**, 899–903.

(247) J. J. Lee, C.-H. Chen, D. Shimon, S. E. Hayes, C. Sievers and C. W. Jones, *J. Phys. Chem. C*, 2017, **121**, 23480–23487.

(248) X. Xu, C. Song, J. M. Andresen, B. G. Miller and A. W. Scaroni, *Energy & Fuels*, 2002, **16**, 1463–1469.

(249) P. Bollini, S. A. Didas and C. W. Jones, *J. Mater. Chem.*, 2011, **21**, 15100–15120.

(250) P. J. E. Harlick and A. Sayari, in *Studies in Surface Science and Catalysis*, ed. J. Čejka, N. Žilková and P. Nachtigall, Elsevier, 2005, vol. 158, pp. 987–994.

(251) P. J. E. Harlick and A. Sayari, *Ind. & Eng. Chem. Res.*, 2006, **45**, 3248–3255.

(252) P. J. E. Harlick and A. Sayari, *Ind. & Eng. Chem. Res.*, 2007, **46**, 446–458.

(253) R. Serna-Guerrero, E. Da'na and A. Sayari, *Ind. & Eng. Chem. Res.*, 2008, **47**, 9406–9412.

(254) Y. Belmabkhout, G. De Weireld and A. Sayari, *Langmuir*, 2009, **25**, 13275–13278.

(255) Y. Belmabkhout and A. Sayari, *Adsorption*, 2009, **15**, 318–328.

(256) Y. Belmabkhout, R. Serna-Guerrero and A. Sayari, *Ind. & Eng. Chem. Res.*, 2010, **49**, 359–365.

(257) N. Sun, Z. Tang, W. Wei, C. E. Snape and Y. Sun, *Front. Energy Res.*, 2015, **3**.

(258) Z. Liang, B. Fadhel, C. J. Schneider and A. L. Chaffee, *Adsorption*, 2009, **15**, 429–437.

(259) J. C. Hicks, J. H. Drese, D. J. Fauth, M. L. Gray, G. Qi and C. W. Jones, *J. Am. Chem. Soc.*, 2008, **130**, 2902–2903.

(260) X. Shi, H. Xiao, H. Azarabadi, J. Song, X. Wu, X. Chen and K. S. Lackner, *Angewandte Chem. Int. Ed.*, 2020, **59**, 6984–7006.

(261) A. Sodiq, Y. Abdullatif, B. Aissa, A. Ostovar, N. Nassar, M. El-Naas and A. Amhamed, *Environ. Technol. & Innov.*, 2023, **29**, 102991.

(262) S. Choi, M. L. Gray and C. W. Jones, *ChemSusChem*, 2011, **4**, 628–635.

(263) P.-Q. Liao, X.-W. Chen, S.-Y. Liu, X.-Y. Li, Y.-T. Xu, M. Tang, Z. Rui, H. Ji, J.-P. Zhang and X.-M. Chen, *Chem. Sci.*, 2016, **7**, 6528–6533.

(264) A. Sinha, L. A. Darunte, C. W. Jones, M. J. Realff and Y. Kawajiri, *Ind. & Eng. Chem. Res.*, 2017, **56**, 750–764.

(265) F. N. U. Huhe, J. King and S. S. C. Chuang, *Res. on Chem. Intermed.*, 2023, **49**, 791–817.

(266) R. Geyer, in *Mare Plasticum - The Plastic Sea: Combatting Plastic Pollution Through Science and Art*, ed. M. Streit-Bianchi, M. Cimadevila and W. Trettnak, Springer International Publishing, Cham, 2020, pp. 31–47.

(267) Philippe Chalmin, *Field Actions Sci. Rep.*, 2019, 6–11.

(268) M. Gilbert, in *Brydson's Plastics Materials (Eighth Edition)*, ed. M. Gilbert, Butterworth-Heinemann, 2017, pp. 1–18.

(269) P. G. C. Nayanathara Thathsarani Pilapitiya and A. S. Ratnayake, *Clean. Mater.*, 2024, **11**, 100220.

(270) Y. Shiran, J. de la Fuente, C. Ragot, L. von Boetticher, L. Fuchs, D. Mauth, S. Lingeswaran, J. Hahn and U. Stein, *Towards Ending Plastic Pollution by 2040*, tech. rep., Nordic Council of Ministers 2023, 2023.

(271) W. Tan, D. Cui and B. Xi, *Front. Environ. Sci. & Eng.*, 2021, **15**, 50.

(272) S. Perreard, J. Boucher, M. Gallato, M. I. Gomis, P. Mazzatorta, A. Gaboury and N. Voirin, *Plastic Overshoot Day*, tech. rep., EA-Earth Action, Lausanne, Switzerland, 2024.

(273) S. K. Ghosh and A. P, *Waste Manag. & Res.*, 2019, **37**, 1061–1062.

(274) M. Eriksen, W. Cowger, L. M. Erdle, S. Coffin, P. Villarrubia-Gómez, C. J. Moore, E. J. Carpenter, R. H. Day, M. Thiel and C. Wilcox, *PLOS ONE*, 2023, **18**, e0281596.

(275) C. P. Ward and C. M. Reddy, *Proc. Natl. Acad. Sci. United States Am.*, 2020, **117**, 14618–14621.

(276) C. P. Ward, C. J. Armstrong, A. N. Walsh, J. H. Jackson and C. M. Reddy, *Environ. Sci. & Technol. Lett.*, 2019, **6**, 669–674.

(277) R. Jain, A. Gaur, R. Suravajhala, U. Chauhan, M. Pant, V. Tripathi and G. Pant, *Sci. Total. Environ.*, 2023, **905**, 167098.

(278) K. D. Cox, G. A. Covernton, H. L. Davies, J. F. Dower, F. Juanes and S. E. Dudas, *Environ. Sci. & Technol.*, 2019, **53**, 7068–7074.

(279) M. Raffaele, P. Francesco, S. Celestino, F. Gianluca, G. Laura, S. Tatiana, D. Nunzia, S. Lucia, L. G. Rosalba, F. Chiara, P. Valeria, M. Maurizio, S. Mario, S. Fabio, V. Gennaro, V. Carmine, C. Albino, A. Giulio, S. Antonio, S. Giuseppe, M. Davida, E. Renata, A. Simona, F. Giovanni, F. Angelo, G. Simona, C. Silvana, S. F. C, M. Giulia, O. Fabiola, F. Franca, P. Iacopo, P. Pasquale, B. Emanuele, L. Carmine, B. M. L, M. Ciro, C. A. E, R. Sanjay, C. Antonio, D. Bruno, I. Pasquale and P. Giuseppe, *New Engl. J. Med.*, 2024, **390**, 900–910.

(280) L. Lebreton and A. Andrady, *Palgrave Commun.*, 2019, **5**, 6.

(281) N. Singh, D. Hui, R. Singh, I. P. S. Ahuja, L. Feo and F. Fraternali, *Compos. Part B: Eng.*, 2017, **115**, 409–422.

(282) A. Rahimi and J. M. García, *Nat. Rev. Chem.*, 2017, **1**, 0046.

(283) J. Morris, *J. Hazard. Mater.*, 1996, **47**, 277–293.

(284) R. Verma, K. S. Vinoda, M. Papireddy and A. N. S. Gowda, *Procedia Environ. Sci.*, 2016, **35**, 701–708.

(285) F. Gao, *Handbook of plastics recycling*, ed. Francesco Paolo La Mantia, Rapra Technology, 2002, p. 441.

(286) G. Güçlü, T. Yalçınyuva, S. Özgümüş and M. Orbay, *Thermochim. Acta*, 2003, **404**, 193–205.

(287) R. Geyer, J. R. Jambeck and K. L. Law, *Sci. advances*, 2017, **3**, e1700782.

(288) X. Jia, C. Qin, T. Friedberger, Z. Guan and Z. Huang, *Sci. Adv.*, 2016, **2**, e1501591.

(289) G. Singh, K. S. Lakhi, S. Sil, S. V. Bhosale, I. Kim, K. Albahily and A. Vinu, *Carbon*, 2019, **148**, 164–186.

(290) P. H. M. Putra, S. Rozali, M. F. A. Patah and A. Idris, *J. Environ. Manag.*, 2022, **303**, 114240.

(291) R. R. Guddeti, R. Knight and E. D. Grossmann, *Ind. & Eng. Chem. Res.*, 2000, **39**, 1171–1176.

(292) G. Elordi, G. Lopez, M. Olazar, R. Aguado and J. Bilbao, *J. Hazard. Mater.*, 2007, **144**, 708–714.

(293) T. M. Kruse, H.-W. Wong and L. J. Broadbelt, *Macromolecules*, 2003, **36**, 9594–9607.

(294) S. Lal, K. S. Anisia and A. Kumar, *Appl. Catal. A: Gen.*, 2006, **303**, 9–17.

(295) S. Wong, N. Ngadi, T. A. Tuan Abdullah and I. M. Inuwa, *Ind. & Eng. Chem. Res.*, 2016, **55**, 2543–2555.

(296) X. Zhang, H. Yang, Z. Chen, X. Wang, H. Feng, J. Zhang, J. Yu, S. Gao and D. Lai, *Fuel*, 2024, **357**, 129897.

(297) C. Wang, T. Xie, P. A. Kots, B. C. Vance, K. Yu, P. Kumar, J. Fu, S. Liu, G. Tsilomelekis, E. A. Stach, W. Zheng and D. G. Vlachos, *JACS Au*, 2021, **1**, 1422–1434.

(298) E. Butler, G. Devlin and K. McDonnell, *Waste Biomass Valori.*, 2011, **2**, 227–255.

(299) F. Ramzan, B. Shoukat, M. Y. Naz, S. Shukrullah, F. Ahmad, I. Naz, M. M. Makhlouf, M. U. Farooq and K. Kamran, *Thermochim. Acta*, 2022, **715**, 179294.

(300) B. Csutoras and N. Miskolczi, *Bioresour. Technol.*, 2024, **400**, 130676.

(301) A. López, I. de Marco, B. M. Caballero, M. F. Laresgoiti, A. Adrados and A. Aranzabal, *Appl. Catal. B: Environ.*, 2011, **104**, 211–219.

2

Experimental details

Contents

2.1 Characterisation techniques

2.1.1 Gas isotherms

N_2 isotherms were collected on either a Micromeritics TriStar II 3030 instrument or a Micromeritics 3Flex instrument. Samples were degassed at 110 °C overnight before analysis. Measurement settings for the Tristar II Plus were: adsorption measurements were collected at regular intervals (10 s equilibration time) up to 990 mbar and back down to 5 mbar in a liquid N_2 bath (−196 °C). Measurement settings for the 3Flex were in situ degass at 110 °C for 2 h, adsorption measurements were then collected (10 s equilibration time) every 0.8923 mbar to 10 mbar then at regular intervals up to 990 mbar and back down to 5 mbar in a liquid N_2 bath (−196 °C). Specific surface areas (SSA) were determined using the Brunauer-Emmett-Teller (BET) method in the associated instrument software. Pore distributions were modelled in the same software using using the DFT Pore Size option with either the "N2 - DFT Model" kernel function which is calculated for slit-like pore geometries on graphite for LDH materials or "N2 - Cylindrical Pores - Oxide Surface" kernel function which is derived from silica and zeolite materials. Pore sizes are characterised by the definition given by Rouquerol *et al.*: micropore (< 2 nm), mesopore (> 2 nm and < 50 nm) and macropore (> 50 nm).[1]

CO_2 isotherms were collected on a Micromeretics 3Flex instrument. Samples were degassed ex situ for 1 h at 120 °C before analysis. Samples were then degassed in situ for 4 h at 120 °C before analysis. During analysis, the degas mantle was used to maintain the sample temperature at the desired level (25, 35, 45 and 55 °C). Adsorption measurements were collected every 0.025 mmol g^{-1} up to 10 mbar, then every 10 mbar to 100 mbar and every 100 mbar to 1000 mbar.

2.1.2 Linear adsorption equations

Langmuir isotherm

The Langmuir isotherm:

$$\theta_A = \frac{q_e}{q_m} = \frac{K_L^A C_e}{1 + K_L^A C_e}$$

(where θ_A is the fractional occupancy of adsorption sites, C_e is the concentration of adsorbate at equilibrium (partial pressure), q_e and q_m are the equilibrium and maximum concentrations of the adsorbate on the surface and K_L^A is the Langmuir or equilibrium constant) is one of the simplest expressions for describing the adsorption process. It assumes the adsorbate behaves as an ideal gas at isothermal conditions which can form a monolayer by reversibly occupying a finite number of identical sites. It can then be derived using different methods including the kinetic consideration of the reaction between an adsorbate molecule (A_g) and an empty site (S) to produce an adsorbed species (A_{ad}): $A_g + S \rightleftharpoons A_{ad}$. The separation factor

$$R_L = \frac{1}{1 + K_L^A C_0}$$

where C_0 is the initial concentration of adsorbate indicates the type of adsorption: unfavourable ($R_L > 1$), linear ($R_L = 1$), favourable ($0 < R_L < 1$) and irreversible ($R_L = 0$).

Freundlich isotherm

The Freundlich isotherm

$$\theta_A = \alpha_F C_e^{C_F}$$

(where α_F and C_F are fitting parameters) is an empirical relationship which allows for surface heterogeneity and as such is disfavoured for isotherms with a theoretical basis. It is an empirical modification to Henry's equation ($q_e = K_{HE} C_e$) to account for adsorption site saturation. This equation does not have a limit on the rate of adsorption; however, this has been shown experimentally not to be the case and so the model fails above a saturation concentration. Isotherms that fit this model likely have heterogeneous sites, but this alone does not prove it.

Temkin isotherm

The Temkin isotherm modifies the Langmuir isotherm by allowing for adsorbate interactions on the surface. In experiments, the heat of adsorption (ΔH_{ad}) was

commonly seen to decrease with increasing coverage; it is therefore modelled as being proportional to the coverage as

$$\Delta H_{ad} = \Delta H^0_{ad}(1 - \alpha_T \theta)$$

(where ΔH^0_{ad} is the heat of adsorption at zero coverage and α). This leads to a varying equilibrium constant

$$K^A_L = K^{A,0}_L e^{\Delta H^0_{ad}(1-\alpha_T\theta)/k_b T}.$$

This arises from rate equations of the form $r_a = k_a C_e e^{-\alpha\theta}, r_d = k_d e^{\beta\theta}$ which at equilibrium ($r_a = r_b$) leads to $\theta = \frac{1}{\alpha+\beta}\ln(\frac{k_a}{k_d}C_e)$ which can be rewritten in the commonly used form $\theta = \frac{k_b T}{b_T}\ln(K_T C_e)$.

Elovich isotherm

The Elovich isotherm

$$\theta_A = K_e C_e e^{-\theta}$$

is also an adaptation of the Langmuir model, although not obviously apparent from the form of the equation. The adsorption rate is changed to be defined as decreasing exponentially with coverage ($r_a = k_a C_e e^{-\theta}$) implying strongly heterogeneous sites where those with the highest ΔH_{ad} react first and has thus often been used to model chemisorption processes.[2]

2.1.3 Scatchard analysis

Scatchard analysis was developed to evaluate the number of binding sites present in receptor ligand systems such as binding by enzymes. This analysis assumes a Langmuir model can describe the interaction with each site and then rearranges the Langmuir equation shown above:

$$\begin{aligned} q_e &= q_m \frac{K^A_L C_e}{1 + K^A_L C_e} \\ \frac{q_e}{C_e} &= K^A_L q_m - K^A_L q_e \end{aligned} \tag{2.1}$$

A plot of $\frac{q_e}{C_e}$ vs q_e for a homogeneous adsorbent will be linear and the values of K^A_L and q_m can be estimated from the gradient and intercept. For heterogeneous

adsorbents, the gradient of the plot changes as the strength of the adsorption site varies, giving insight into the degree of heterogeneity. Tangents to different regions of the data may be drawn each of which will give a different set of binding parameters for the region fitted. The decision of which regions to fit is subjective to the user and requires the assumption that the energy distribution of the sites can be grouped into discrete groups limiting its usefulness.[3]

2.1.4 Non-linear adsorption isotherms

Non-linear isotherms were modelled using the pyGAPS python framework using the built-in models.[4]

Multisite Langmuir models

The double site (DSLangmuir) and triple site Langmuir (TSLangmuir) models are extensions to the Langmuir model discussed above. Assuming a material contains several distinct types of homogeneous sites each with their own capacity and affinity, each can be modelled by its own Langmuir isotherm with the total uptake equal to the sum of the uptakes on each type of site:

$$n(p) = \sum_{i=1}^{k_{sites}} n_{m_i} \frac{K_i p}{1 + K_i p}$$

The Langmuir (single site), DSLangmuir (double site) and TSLangmuir (triple site) models are where $k_{sites} = 1, 2, 3$ respectively.

Freundlich model

The Freundlich model is as described previously:

$$n(p) = K p^{1/m}$$

Quadratic model

The quadratic model extends the Langmuir model by allowing each site to bind a second molecule with an interaction between the molecules in the same site. This gives the sites four possible states: empty, a degenerate pair of singly filled and a

double filled state. From the energy of each state, the amount adsorbed at a given pressure can be derived via statistical mechanics:[5]

$$n(p) = n_m \frac{2Kp + 2\phi K^2 p^2}{1 + 2Kp + \phi K^2 p^2}$$

where n_m is the total number of sites giving a maximum adsorption capacity of $2n_m$ and ϕ is a factor which describes the adsorbate-adsorbate interactions:

$$\phi \begin{cases} = 1 & \text{non-interacting} \\ > 1 & \text{attractive} \\ < 1 & \text{repulsive} \end{cases}$$

Attractive interactions lead to a convex loading at low pressures as they aid in further adsorption and this is commonly used to describe systems where the the adsorbate-adsorbate interactions are stronger than the energy of adsorption.

Temkin model

The Temkin model used by pyGAPS differs from the one described previously, still assuming the enthalpy of adsorption is a linear function of coverage, but using an asymptotic approximation described by Simon *et al.* to yield a different equation for the loading:

$$n(p) = n_m \frac{Kp}{1 + Kp} \left[1 + \theta \frac{Kp}{1 + Kp} \left(\frac{Kp}{1 + Kp} - 1 \right) \right]$$

where the correction term tends to zero as $p \to 0$ and $p \to \infty$.[6]

Toth model

The Toth model is an empirical modification to the Langmuir equation with an exponent parameter which allows for heterogeneity of the sites:

$$n(p) = n_m \frac{Kp}{\sqrt[t]{1 + (Kp)^t}}$$

Jensen-Seaton model

The Jensen-Seaton model is an empirical model developed to address the issue that the adsorption isotherm should not reach a plateau at high pressures as the adsorbed phase can be compressed. The model interpolates between Henry's law at low pressure and a compressibility asymptote at high pressure:

$$n(p) = Kp\left[1 + \left(\frac{Kp}{a(1+bp)}\right)^{c}\right]^{-1/c}$$

where K is the Henry constant, a is the maximum loading without compression, b is the compressibility of the adsorbed phase and c is an empirical constant.

2.1.5 Isosteric enthalpy of adsorption

The isosteric enthalpies of adsorption were calculated using the Clausius-Clapeyron equation:

$$\left(\frac{\partial \ln(P)}{\partial T}\right)_{n_a} = -\frac{\Delta H_{ads}}{RT^2} \tag{2.2}$$

which can be rearranged to:

$$\Delta H_{ads} = -R\frac{\partial \ln(P)}{\partial \frac{1}{T}}$$

Multiple isotherms of the same material were collected at different temperatures and a plot of $\ln(P)$ against $1/T$ at constant loading gives a straight line with a gradient of $-\Delta H_{ads}/R$. This approach assumes a constant enthalpy of adsorption, so it is suggested that the isotherms are collected within a narrow temperature range ($\Delta T < 20\,\mathrm{K}$) to avoid large variations in enthalpy which lead to unrealistic values.[7] It also requires the assumptions of the Clausius-Clapeyron equation to be satisfied: ideal behaviour of the gas in the bulk phase and a negligible adsorbed volume. These assumptions can break down at higher pressures and for heavy adsorbates.

2.1.6 X-ray diffraction

Powder X-ray diffraction (XRD) patterns were collected on either a PANAnalytical X'Pert Pro Diffractometer or a Bruker D8 advance instrument. Measurement details for the X'Pert Pro were: Cu K_α radiation (λ_{α_1} = 1.540 57 Å, λ_{α_2} = 1.544 33 Å); powder samples were loaded into stainless steel sample holders and measured from 3-70° with a step size of 0.0167°. Measurement details for the Bruker D8 were: Cu K_α radiation (λ_{α_1} = 1.540 57 Å, λ_{α_2} = 1.544 33 Å) with an energy discriminating detector (that rejects other wavelengths from sources such as Cu K_β, or fluorescence); powder samples were loaded into PMMA sample holders or mounted with grease onto glass slides and measured from 5-70° with a step size of 0.5954°. Air sensitive samples were loaded in a glove box and sealed within a similar sample holder for measurement. High resolution XRD patterns were measured at the Diamond Light Source on the I11 beamline (λ =0.825 276 Å). Samples were loaded into quartz capillaries for measurement and heated to 900 °C at 12 °C min^{-1} using a hot air blower.

Crystallite size analysis was conducted using the Scherrer equation (Equation 2.3) on the appropriate Bragg reflection:

$$\tau = \frac{K\lambda}{\beta \cos\theta} \tag{2.3}$$

where τ is the mean size of the crystalline domains ($\leq$ grain size $\leq$ particle size), K is a dimensionless shape factor (typical value of 0.94) which varies with the crystallite shape, λ is the X-ray wavelength, β is the line broadening at half the reflections intensity (full width at half maximum (FWHM) or $\Delta 2\theta$ (in radians)) and θ is the Bragg angle. The Scherrer equation is used for determining the size of crystallites smaller than 100 nm, which is the crystallite size relevant to materials discussed within this thesis.[8] The Scherrer constants for hexagonal crystals, as described by Lele and Anantharaman,[9] are given in Table 2.1 for ($\rho = \frac{p_H}{p_W}$) $\rho = 2$ disc, $\rho = 1$ approximately spherical and $\rho = 0.5$ needle. As LDHs are known to form approximate discs, the values for $\rho = 2.0$ were used. These values are

Table 2.1: Scherrer constants (K) for hexagonal crystallites of varying aspect ratios.[9]

Reflection	$\rho = 2.0$	$\rho = 1.0$	$\rho = 0.5$
001	0.63	1.00	1.59
110	1.31	1.04	0.82

simply proportionality constants and the values for K in both axis deviate further from unity the greater the aspect ratio of the disc.[10] These values are chosen for convenience and the crystallite sizes derived are thus not absolute, but allow comparison between samples.

Unknown crystalline phases were identified using the QUALX2.0 software[11] with the POW_COD database.

2.1.7 Fourier transform infrared spectroscopy

Fourier transform infrared (FTIR) spectrums were recorded on a ThermoScientific Nicolet iS5 spectrometer fitted with an iD3 attenuated total reflection stage. Transmittance was recorded in the range 400 to 4000 cm^{-1} at 4 cm^{-1} resolution.

2.1.8 Differential scanning calorimetry

Differential scanning calorimetry (DSC) measurements were collected using a Perkin Elmer DSC6000. Approximately 10 mg of sample were loaded in aluminium samples pans that were crimped and pierced to allow outgassing. The samples were degassed at 120 °C before heating and cooling cycles at 5 and 10 $\mathrm{K\,min}^{-1}$. The total excess heat flow during the heating step was integrated and the value for an empty pan subtracted. The heat was normalised by the sample mass and divided by the temperature change to give the average heat capacity. The heat capacity of the sample was taken as the average of the values calculated at the two ramp rates.

2.1.9 Nuclear magnetic resonance

^{29}Si, ^{13}C, and ^{27}Al magic-angle spinning (MAS) solid-state nuclear magnetic resonance (NMR) spectra were acquired by Dr Nick Rees at the University of Oxford

using a Bruker Avance IIIHD spectrometer at 79.4, 100.5 and 104.2 MHz respectively (9.4 T). Samples were packed in 4 mm O.D. rotors and spun at 10 kHz. For ^{27}Al MAS solid-state NMR, to acquire quantitative MAS spectra, a single pulse excitation was implemented with a brief pulse duration (0.23 µs). A total of 7000 scans were collected with a 0.01 s delay. The ^{27}Al chemical shift is referenced to an aqueous solution of $Al(NO_3)_3$ (0 ppm). ^{13}C CP-MAS NMR spectra were obtained employing a cross-polarisation sequence using a variable X-amplitude spin-lock pulse along with spinal64 proton decoupling. A total of 15,000 transients were acquired with a contact time of 0.5 to 1.5 ms and a recycle delay of 0.5 to 1.5 s. All ^{13}C spectra were referenced to adamantane as a secondary reference. ^{29}Si CP-MAS NMR spectra were similarly measured through cross-polarisation sequencing with a variable X-amplitude spin-lock pulse and spinal64 proton decoupling. A total of 35,000 transients were acquired with a contact time of 2 to 4 ms and a recycle delay of 1.5 s. All ^{29}Si spectra were referenced against kaolinite as a secondary reference.

Non-quaternary suppression (NQS) also known as "dipolar dephasing" or "interrupted decoupling" is a technique used to distinguish between quaternary carbon atoms and those with one or two hydrogen substituents. Prior to acquisition of the free induction decay, the proton decoupling is turned off for ≈40 µs which suppresses the signals of carbons with ^{13}C – ^{1}H dipolar interactions (methine –CH= and methylene $-CH_2-$). Groups such as methyl ($-CH_3$), which rapidly rotate, undergo motional averaging of the dipolar interactions leading to unexpected intensity.[12]

2.1.10 Elemental analysis

Carbon, hydrogen and nitrogen components were measured (CHN analysis) by Orfhlaith McCullough at the London Metropolitan University using a Thermo Scientific ThermoFlash 2000 analyser. Samples are placed in a tin capsule which melts within a combustion chamber, where the sample is oxidised within an oxygen-helium stream. The reaction gases are passed over a catalyst to ensure complete combustion and a Cu catalyst to reduce NO_x to N_2 and remove excess oxygen.

The gases are then separated and analysed by gas chromatography equipped with a thermal conductivity detector (TCD).[13]

Other elements were measured by inductively coupled plasma optical emission spectroscopy (ICP OES) by Dr Nigel Howard at the University of Cambridge. Samples were dissolved in HNO_3 and diluted to approximately 1 ppm. The solution is introduced into a high-temperature plasma which excites the ions, causing them to emit characteristic wavelengths of light which are separated by a spectrometer and measured by a detector.

2.1.11 Pyrolysis gas analysis

Thermogravimetric analysis-mass spectrometry

The gases evolved during the pyrolysis of polypropylene/SLDH blends during thermogravimetric analysis were analysed by an attached Hiden Analytical HPR-20 EGA MS. A heated capillary is introduced within the TGA setup next to the sample pan furnace which feeds the input of the mass spectrometer. H_2 ($m/z = 2$) N_2 ($m/z = 18$) and ions from $m/z = 29$ to 150 were measured using the Faraday cup detector.

Batch pyrolysis gas chromatography-mass spectrometry

Gas samples were taken using a 250 µL syringe through a septum port on the batch reactor after polypropylene pyrolysis. The samples were analysed using a Agilent 7820A GC system equipped with a GS-CarbonPLOT column and Agilent 5977E MSD. The heating program consisted of a temperature ramp from 50 to 300 °C at 10 °C min^{-1} and a 15 min hold. Peak spectra were extracted using Agilent MassHunter Qualitative analysis software and identified via comparison with the NIST database with further identification using the NIST MS Search 2.2 software.

Batch pyrolysis gas chromatography

The outlet port of the batch reactor after polypropylene pyrolysis was connected to the inlet of the automated gas sampling system of an Agilent 8860 GC System. The

gas sampling system was set up to take two 1 mL gas samples: one setup measured the quantity of light gases (H_2, O_2, N_2, CH_4, CO) and the other measured the hydrocarbon products (heavy gases). The light gas system (Ar flow) used in series a PPQ backflush column to exclude heavier molecules, a Mol Sieve analytical column for further compound separation, a TCD detector to measure non-combustible gases (H_2 (the flame ionisation detector (FID) uses a H_2 flame), O_2 and N_2), a methaniser (Ni catalyst converts CO to CH_4) and an FID to measure CH_4 and reduced CO. The hydrocarbon system passed the gas sample into an inlet under He flow where the sample was diluted to an appropriate level (from splitless to 1:100) and then used a GS-CarbonPLOT column for separation and FID for detection. Peak areas were converted to ppm for the light gases using calibrations derived from external standards. Hydrocarbon conversions were calculated by comparison to the CH_4 peak (known concentration) using the effective carbon number to estimate the response factor ($R.F. = \sum^{n_{aliphatic}} 1 + \sum^{n_{olefinic}} 0.95 + + \sum^{n_{ketone}} 0.2$)[14,15] This method although empirically derived is based on the principle that a FID is ultimately a CH_4 detector, detecting CHO^+ ions formed by the reaction of $CH + O \longrightarrow CHO^* \longrightarrow CHO^+ + e^-$. Alkanes are fully converted via reaction of H radicals in the flame to CH_4 giving them a response factor proportional to their carbon number while other types of carbon are subject to competing reaction paths which reduce the amount of CH_4 formed (C_2H_4 and C_2H_2 for unsaturated molecules and CO for O-containing molecules) and thus their relative responses.

2.1.12 Temperature programmed reduction

Temperature programmed reduction (TPR) experiments were conducted using an Micromeretics Autochem II system. Approximately 0.1 g of sample was loaded into the sample tube for analysis. A 50 mL min^{-1} 10% H_2 in N_2 gas flow was passed through the sample and after a stable signal was reached, the temperature was ramped up to 800 °C at 10 K min^{-1}.

2.1.13 Temperature programmed desorption

Temperature programmed desorption (TPD) experiments were conducted using an Micromeritics AutoChem II system. Approximately 0.1 g of sample was loaded into the sample tube for analysis. The sample was degassed under He flow at 120 °C for 1 h before cooling to ambient temperature. CO_2 was loaded onto the sample by passing a gas flow through the sample for 0.5 h followed by desorption of physisorbed species by flow of He for at least 1 h until a stable signal was reached. The temperature was then ramped up to 120 °C at 0.5 K min^{-1}.

2.1.14 Thermal gravimetric analysis

Thermal gravimetric analysis (TGA) of samples was conducted using a PerkinElmer TGA 8000 instrument. Approximately 10 mg of sample were loaded into an alumina crucible and heated under N_2 flow at the desired ramp rate (typically 10 K min^{-1}) to the desired temperature (typically 800 °C).

Where applicable other gases were introduced using a connected GMD 8000 gas mixing device.TGA-MS experiments used the attached Hiden Analytical HPR-20 EGA MS as described previously.

2.1.15 Gel-permeation chromatography

Gel-permeation chromatography (GPC) was performed by Ms Liv Thobru, Ms Sara Rund Herum, and Ms Rita Jenssen (Norner AS, Norway) on a high temperature gel-permeation chromatograph with an IR5 infrared detector. Samples were prepared by dissolution in 1,2,4-trichlorobenzene (TCB) containing 300 ppm of 3,5-di-tert-butyl-4-hydroxytoluene (BHT) at 160 °C for 90 min and then filtered with a 10 µm SS filter before being passed through the GPC column. The samples were run under a flow rate of 0.5 mL min^{-1} using TCB containing 300 ppm BHT as mobile phase, with 1 mg mL^{-1} BHT added as a flow rate marker. The GPC column and detector temperature were set at 145 and 160 °C respectively.

2.1.16 Tap density

Tap density was calculated by a standard testing method (ASTM D7481-09). The powder was filled into a volumetric cylinder and a precise weight of the sample (m) was measured. The cylinder was repeatedly tapped firmly, by hand, against a hard surface and the volume was measured after 1000 taps (V_t). The tap density is then defined as:

$$\text{Tap density} = \frac{m}{V_t}$$

2.1.17 High-resolution scanning electron microscopy

High-resolution scanning electron microscopy with energy dispersive X-ray spectroscopy (HR-SEM-EDX) was performed on a Carl Zeiss Merlin Instrument, fitted with an Oxford Instruments Xmax 150 mm^2 EDX by Meng Lyu, Emma Southall, Claire Coulthard, and Matthew Williams. Scanning electron microscopy images were taken at a working distance of 8.5 mm, with probe currents and voltages of 200 pA and 3 kV, respectively. Analytical elemental mapping was conducted at a working distance of 8.5 nm, with probe currents and voltages of 500 pA and 6 kV respectively. Samples were prepared by dispersing a small amount of powdered sample in distilled water or ethanol, and then dried on a silicon wafer attached to a metal stub. Prior to imaging, a $\approx$ 8 nm layer of chromium was deposited on all samples using a Lecia ACE600 coater.

References

(1) J. Rouquerol, D. Avnir, C. W. Fairbridge, D. H. Everett, J. M. Haynes, N. Pernicone, J. D. F. Ramsay, K. S. W. Sing and K. K. Unger, 1994, **66**, 1739–1758.

(2) J. Debord, M. Harel, J.-C. Bollinger and K. H. Chu, *Chem. Eng. Sci.*, 2022, **262**, 118012.

(3) K. V. Kumar, S. Gadipelli, C. A. Howard, W. Kwapinski and D. J. L. Brett, *J. Mater. Chem. A*, 2021, **9**, 944–962.

(4) P. Iacomi and P. L. Llewellyn, *Adsorption*, 2019, **25**, 1533–1542.

(5) H. Swenson and N. P. Stadie, *Langmuir*, 2019, **35**, 5409–5426.

(6) C. M. Simon, J. Kim, L.-C. Lin, R. L. Martin, M. Haranczyk and B. Smit, *Phys. Chem. Chem. Phys.*, 2014, **16**, 5499–5513.

(7) A. Nuhnen and C. Janiak, *Dalton Trans.*, 2020, **49**, 10295–10307.

(8) A. Monshi, M. R. Foroughi and M. R. Monshi, *World J. Nano Sci. Eng.*, 2012, **02**, 154–160.

(9) S. Lele and T. R. Anantharaman, *Proc. Indian Acad. Sci. - Sect. A*, 1966, **64**, 261–274.

(10) J. I. Langford and D. Louër, *J. Appl. Crystallogr.*, 1982, **15**, 20–26.

(11) A. Altomare, N. Corriero, C. Cuocci, A. Falcicchio, A. Moliterni and R. Rizzi, *J. Appl. Crystallogr.*, 2015, **48**, 598–603.

(12) D. Bryce, G. Bernard, M. Gee, M. Lumsden, K. Eichele and R. Wasylishen, *Can. J. Anal. Sci. Spectrosc.*, 2001, **46**, 46–82.

(13) London Metropolitan University, *Elemental analysis service*.

(14) T. Holm, *J. Chromatogr. A*, 1999, **842**, 221–227.

(15) E. C. Apel, J. G. Calvert, J. P. Greenberg, D. Riemer, R. Zika, T. E. Kleindienst, W. A. Lonneman, K. Fung and E. Fujita, *J. Geophys. Res. Atmospheres*, 1998, **103**, 22281–22294.

3

Synthesis of layered double hydroxides from struvite

Contents

3.1 Introduction

Conventionally, layered double hydroxides (LDHs) are prepared using metal salts, such as nitrates or chlorides, for laboratory-scale synthesis and metal oxides for cost-effective industrial-scale production.[1,2] These processes generally necessitate preparatory stages involving precursor materials, thereby increasing both the cost and the environmental ramifications of LDH production. For instance, the reaction between nitric acid and a metal salt leads to the production of $Mg(NO_3)_2$ or $Al(NO_3)_3$, the calcination of magnesite ($MgCO_3$) results in the formation of MgO,[3] and the Bayer process is utilised to produce Al_2O_3.[4] In the synthesis process, the employment of metal salts in place of metal oxides or hydroxides results in the mother liquor containing significant quantities of spectator ions, thereby diminishing the atom efficiency and producing substantial waste that requires management. Consequently, the production of LDHs by utilising these materials neither incorporates the principles of a circular economy (as it depletes non-renewable resources) nor aligns with the principles of green chemistry. This study investigates the feasibility of utilising the mineral struvite ($MgNH_4PO_4 \cdot 6\,H_2O$) as a magnesium source for the synthesis of MgAl-LDHs in a manner that enhances sustainability by employing a low-cost, readily accessible waste material, thereby eliminating the need for metal salts.

3.1.1 Struvite ($MgNH_4PO_4 \cdot 6\,H_2O$)

Struvite ($MgNH_4PO_4 \cdot 6\,H_2O$) belongs to the family of magnesium ammonium phosphates. It occurs naturally and frequently forms when ammonia and phosphate

derived from the decomposition of organic matter are introduced to magnesium (Mg) that is inherently present in soil or water environments. Conditions of high pH, low temperature, and elevated concentrations of the relevant ions enhance the probability of its formation. This compound was first identified by Georg Ludwig Ulex in 1845 within a medieval midden, an archeological feature composed primarily of organic waste.[5] Struvite is often observed as a constituent of kidney and urinary tract calculi (stones) in both humans and animals. These formations are often facilitated by urease-producing bacterial infections, which supply the ammonia necessary for the crystallisation of struvite.

In industrial contexts, struvite is frequently encountered within wastewater treatment systems. Magnesium, inherently present in the water stream from hard water sources and sewer management,[6] combines with ammonia—released from urea during anaerobic digestion—and with phosphate, which originates from organic materials and detergents. This precipitation may lead to the obstruction of pipes, pumps, and ancillary equipment, consequently requiring plant downtime for the remediation of blockages. Due to the substantial financial implications, various strategies have been devised to mitigate and prevent the formation of struvite. These strategies encompass physical methods, such as the replacement of pipes, mechanical grinding, and hydrojetting; chemical approaches, including the use of HCl and other acids to dissolve blockages, and the engineered precipitation within a dedicated vessel by the addition of a Mg source, typically $MgCl_2$ or $Mg(OH)_2$; and electrical techniques, where a sacrificial Mg anode induces struvite precipitation on the surface without necessitating pH adjustment.[7]

Ammonia and phosphate are two of the three primary macronutrients essential for plant growth, and their recovery is crucial to mitigate eutrophication—characterised by the excessive proliferation of algae and macrophytes in aquatic environments due to the enrichment of vital nutrients, leading to oxygen depletion—and to prevent environmental detriment in downstream aquatic systems. Phosphorus is a limited resource, with an estimated seven billion tons of remaining reserves that could be

exhausted within the next 100 to 250 years. The extraction of phosphate from wastewater presents a viable strategy to decrease dependence on mined phosphate rock and to prolong the sustainability of global reserves. Dedicated precipitation methods offer a solution to avert blockages while facilitating the recovery of phosphate and ammonia from waste streams, thereby preventing eutrophication and enabling phosphate reclamation.

Struvite, exhibiting limited solubility ($169.2\,\mathrm{mg\,L^{-1}}$ at $25\,^{\circ}\mathrm{C}$),[8] has been employed as a slow-release fertiliser due to its constituent ions (Mg^{2+}, NH_4^+, and PO_4^{3-}). Despite this, struvite derived from wastewater is frequently categorised as waste under legal frameworks in numerous countries, thereby inhibiting its utilisation as a fertiliser and relegating it to landfill disposal. Annually, 9784 to 12 057 t of struvite is generated within the European Union alone, and the portion that is marketed as fertiliser often suffers from undervaluation at € 0 to $100\,\mathrm{t^{-1}}$. As a result, exploring alternative applications for this material is imperative for its integration into a circular economy. Utilising struvite as a precursor for LDH synthesis presents itself as a promising application. This approach facilitates the recovery and reuse of magnesium, alongside the reclamation of phosphate and ammonia sequestered within struvite, thereby contributing to the material's valorisation by producing an LDH compound amenable to diverse applications.

3.1.2 Properties of struvite

Struvite is characterised as an orthorhombic crystal belonging to the space group $Pmn2_1$, exhibiting cell dimensions $a = 6.9410\,\text{Å}$, $b = 6.1370\,\text{Å}$, and $c = 11.1990\,\text{Å}$. It is non-centrosymmetric, comprising layers of hydrogen-bonded PO_4^{3-} tetrahedra, NH_4^+ tetrahedra, and $Mg(H_2O)_6^{2+}$ octahedra. The absence of inversion symmetry results in the non-equivalence of opposing crystal faces, which consequently grow at disparate rates. Furthermore, this lack of symmetry allows the material's ferroelectric, piezoelectric, and pyroelectric properties.[9] Shaddel *et al.* demonstrated that the morphology of struvite crystals can be regulated by the pH and ammonia concentration.[10] At low pH levels, struvite assumes a hemimorphic wedge or coffin

morphology characterised by asymmetrically developed [001] and [00$\bar{1}$] facets. As the pH increases, twinned crystals exhibit an X-shaped morphology, while at high pH (> 9), dendritic crystals emerge as a result of extensive surface nucleation, indicative of a diffusion-controlled process rather than a kinetically-controlled one. An examination of the properties of the struvite acquired from Alfa Aesar and utilised in this study is presented to facilitate comparison with the resultant products derived from it as discussed herein.

The elemental analysis results for struvite composition are presented in Table 3.1. The experimentally determined mass percentages are in agreement with the theoretical values and fall within the accepted analytical error margins ($\pm 0.3\,\%$), with the exception of magnesium. Previously reported instances of elevated values in commercially sourced struvite are attributed to the presence of unreacted precursors.[11]

Table 3.1: Elemental composition (wt%) of struvite purchased from Alfa Aesar determined by CHN and ICP analysis.

	C	H	N	Mg	P
Struvite	0.21	6.42	5.3	12.36	12.35
Theoretical	0.00	6.57	5.71	9.90	12.62

The powder XRD pattern of struvite is shown in Figure 3.1. The peaks can be indexed to that reported in the literature (R050540 RRUFF Project)[12] and are sharp, indicating the material is highly crystalline.

The FTIR spectrum of struvite is presented in Figure 3.2, with its corresponding assignments detailed in Table 3.2. The spectrum's principal characteristics include a broad absorption observed between 2200 to 3400 cm^{-1}, attributable to various N−H and O−H stretching vibrations within $NH_4{}^+$ and H_2O. Additionally, a sharp absorption band at 1436 cm^{-1} is associated with the v_4 antisymmetric stretching mode of $NH_4{}^+$, while another sharp absorption band at 977 cm^{-1} corresponds to the v_1 antisymmetric stretching vibration of $PO_4{}^{3-}$. Furthermore, a sharp absorption band at 744 cm^{-1}, which is not consistently documented in literature, has been

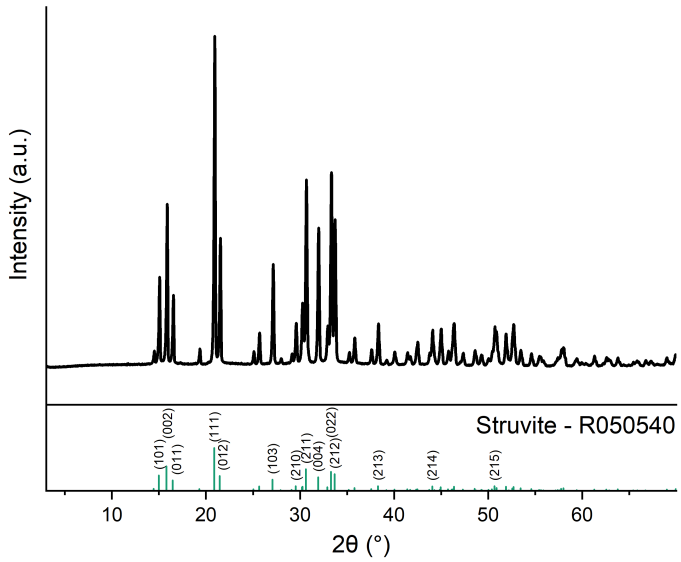

Figure 3.1: XRD pattern of struvite from Alfa Aesar. Bragg reflections can be indexed to the pattern below (RRUFF Project R050540 - Struvite).[12]

linked to the bending mode of a P−O−P linkage,[15] potentially due to a $Mg_3P_2O_7$ impurity.[16]

The thermogravimetric analysis (TGA) curve for struvite is presented in Figure 3.3. A distinct thermal event is observed with an onset at 66 °C, culminating in a maximum weight reduction at 136 °C. Throughout this event, 47% of the mass is lost, followed by an additional 7.25% loss upon further heating. This initial mass reduction is attributed to the simultaneous evolution of NH_3 and H_2O from the structure. It has previously been demonstrated that the number of thermal events is dependent upon the heating rate.[17] Assuming $1\,\mathrm{mol}_{NH_3}\,\mathrm{mol}^{-1}_{\mathrm{Struvite}}$ is liberated in this step, the remaining weight loss corresponds with a loss of $5.46\,\mathrm{mol}_{H_2O}\,\mathrm{mol}^{-1}_{\mathrm{Struvite}}$:

$$MgNH_4PO_4 \cdot 6\,H_2O \xrightarrow{\Delta} MgHPO_4 \cdot 0.54\,H_2O + NH_3\uparrow + 5.46\,H_2O\uparrow$$

showing almost complete evolution by 188 °C. The total weight loss of 54.25% corresponds to further loss of H_2O and the formation of magnesium pyrophosphate ($Mg_2P_2O_7$) ($\frac{0.5 * M_{r\mathrm{Mg_2P_2O_7}}}{M_{r\mathrm{MgNH_4PO_4 \cdot 6\,H_2O}}} = \frac{0.5 * 222.55}{245.41} = 0.453$) :

$$MgNH_4PO_4 \cdot 6\,H_2O \xrightarrow{\Delta} 0.5\,Mg_2HP_2O_7 + NH_3\uparrow + 6.5\,H_2O\uparrow$$

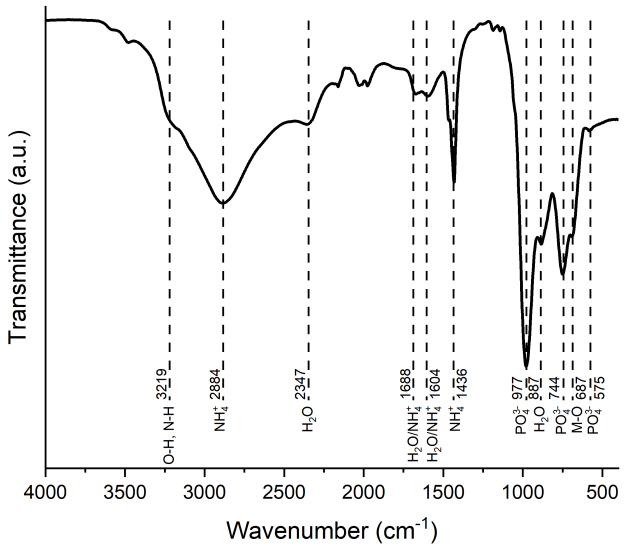

Figure 3.2: FTIR pattern of struvite from Alfa Aesar. Absorption bands are assigned in Table 3.2.

Table 3.2: Functional group assignments for absorption bands seen in struvite (Figure 3.2).

Functional group assignment		Wavenumber (cm^{-1})
PO_4^{3-}	v_1 symmetric stretching vibration[13,14]	977
	v_4 asymmetric bending vibration[13,14]	563
NH_4^+	v_1 symmetric stretching vibration[13]	2884
	v_2 symmetric bending vibration[13]	1604 and 1688
	v_3 asymmetric stretching vibration[13]	3219
	v_4 asymmetric bending vibration[13]	1436
H_2O	H–O–H stretching vibration[13,14]	3219
	H–O–H stretching vibration (cluster)[13,14]	2347
	H–O–H bending vibration[13,14]	1604 and 1688
	H–O–H wagging vibration[13,14]	887
M–O	M–O vibration[13,14]	687

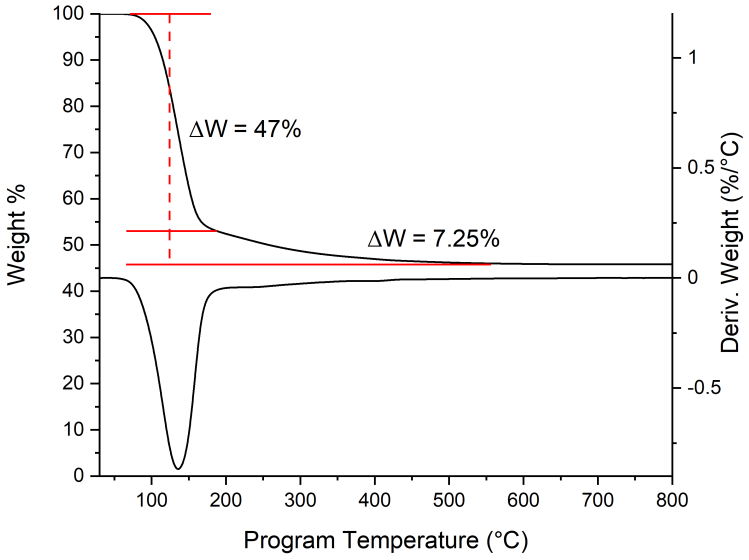

Figure 3.3: TGA thermal curve of struvite from Alfa Aesar.

as reported in the literature.[18]

N_2 adsorption isotherms of the material (degassed at 30 °C) show minimal uptake with negligible porosity and surface area.

Scanning Electron Microscopy (SEM) images of a struvite crystal are presented in Figure A.4. The crystal exhibits well-defined faceting and possesses a needle-like morphology with a length of 42 µm. Figure A.4(d) depicts a comparable particle, which seems to have detached from a larger crystal structure.

3.2 Synthesis of LDHs from struvite

Previously reported studies have demonstrated that struvite possesses the potential to yield magnesium-containing LDHs. This was achieved through a two-step process wherein: 1) the struvite was activated with NaOH to eliminate NH_4^+, resulting in an intermediate tentatively described as metastable $MgNaPO_4 \cdot 6\,H_2O$, differing from the $MgNaPO_4 \cdot 7\,H_2O$ phase reported by Mathew *et al.*;[19,20] and 2) a reaction with $Al(NO_3)_3 \cdot 9\,H_2O$ and Na_2CO_3 was conducted to form MgAl LDHs via an in-situ transformation.[21] This synthesis approach was used as an initial framework to optimise the reaction conditions. Struvite procured from Alfa Aesar (ammonium magnesium phosphate hexahydrate, 98%, Figure 3.1) is consistently utilised throughout the experiments described in this thesis. LDHs synthesised from struvite are referred to as SLDHs and their calcined products as SLDOs.

3.2.1 Effect of reaction temperature

Previous investigations have demonstrated that under analogous reaction conditions, the temperature exerts a substantial influence on the specific surface area of the resultant materials.[20] Consequently, this parameter was the initial focus of inquiry in the present study. A detailed account of the reaction conditions is provided in Chapter 3.4.2. Figure 3.4 shows the powder XRD pattern of SLDHs synthesised at 65, 75 and 85 °C. In all samples, the characteristic Bragg reflections indicative of an LDH phase were distinctly observed, and the absence of peaks attributable to the struvite precursor signified the successful conversion of struvite to LDH. Nonetheless, Bragg reflections corresponding to a brucite ($Mg(OH)_2$) phase are also discernible, particularly the (110) reflection at 58.5°. The (001) reflection at 18° is significantly weaker than anticipated, suggesting low crystallinity along the *c* axis, while the (011) reflection coincides with the (015) reflection of the LDH.

The crystallite domain length (CDL) and lattice parameters have been derived from the (003) and (110) reflections and are detailed in Table 3.3. The *a* lattice

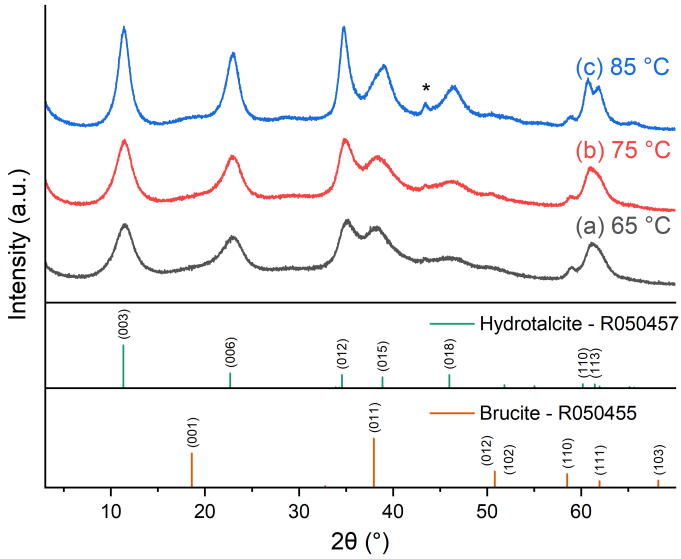

Figure 3.4: Powder XRD patterns of SLDHs produced via the previously reported method at different temperatures. Peaks can be indexed to the patterns below (RRUFF Project R050457 - Hydrotalcite and R050455 - Brucite).[12] * indicates a reflection due to the sample holder.

Table 3.3: Variation of lattice parameters (a, c) of the SLDHs and their respective crystallite domain lengths (CDL) with the reaction temperature extracted from Figure 3.4.

Temperature	d_{110} (nm)	a (nm)	CDL_a (nm)	d_{003} (nm)	c (nm)	CDL_c (nm)
65 °C	0.152	0.304	8.329	0.774	2.321	2.704
75 °C	0.152	0.304	9.640	0.776	2.328	2.995
85 °C	0.153	0.305	13.117	0.777	2.332	4.106

parameter, associated with the metal-metal distance, remains constant, suggesting a stable Mg:Al ratio akin to that observed in natural hydrotalcite (Mg:Al = 3:1).[22] However, the c parameter exhibits an increase, indicating an expansion in the basal spacing ($d_{003} = 0.774$ to $0.777\,\text{nm}$). This minor alteration may result from variations in the signal-to-noise ratio. Natural hydrotalcite exhibits a basal spacing of $d_{003}, = 0.760\,\text{nm}$,[22] while pure phosphate LDHs are recorded with an increased $d_{003} = 0.788$ to $1.191\,\text{nm}$, contingent upon the pH conditions during synthesis, as a consequence of the enlarged dimensions of the hydrated anion,

as documented in the literature.[23] The SLDHs d_{003} are positioned between these values, suggesting the presence of a combination of the two anions (carbonate and phosphate), corroborating previously reported characteristics of SLDHs.[20]

The FTIR spectra of the SLDHs are depicted in Figure 3.5. The most prominent absorption feature, occurring between 600 to 900 cm^{-1}, originates from the M-O stretching modes (M = Mg, Al). Absorption bands corresponding to both PO_4^{3-} (1039 cm^{-1}, a combination of antisymmetric and symmetric P – O stretches, as well as an antisymmetric P – OH stretch if HPO_4 is present) and CO_3^{2-} (1365 cm^{-1}, an antisymmetric C – O stretch) are observed, which indicates that the phase comprises a mixture of the two anions, corroborating the findings from the X-ray diffraction results. Furthermore, there are absorption bands associated with interlayer water (1644 cm^{-1}, bending) and hydroxyl groups (broad 3448 cm^{-1}), which consist of several overlapping bands with a shoulder attributed to –OH anion interactions.[24] Also present is a sharp absorption band (3698 cm^{-1}, –OH) arising from the brucite impurity.[25] The spectra are also missing the characteristic bands seen for struvite

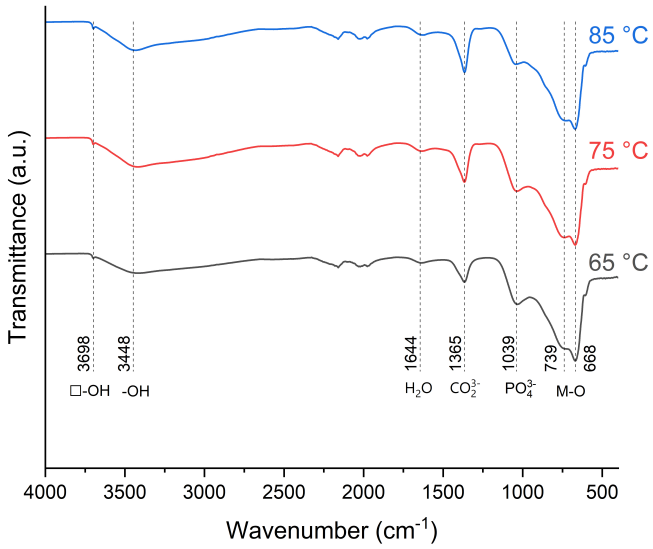

Figure 3.5: FTIR spectra of SLDHs produced via the previously reported method at different temperatures. □ indicates a peak arising from brucite.

(NH_4^+: 2884 and 1436 cm^{-1}, Figure 3.2), confirming the successful transformation of the precursor material.

SEM images of the SLDHs reveal that these materials are predominantly composed of microparticles up to 20 µm (as shown in Figures 3.6, A.2 and A.3). There are two morphologies present: prolate coffin-lid particles (Figure 3.6(b)) which bear a resemblance to the struvite precursor (Figure A.4) and equant agglomerations (Figures 3.6(c) and 3.6(d)). The persistence of the coffin-lid morphology suggests that the struvite does not completely dissolve during the activation phase. Instead, the SLDH likely forms directly from the precursor through a dissolution-precipitation mechanism. Additionally, small agglomerations are discernible on the surface of these coffin-lid particles, and it is plausible that the larger agglomerations are entirely encased prisms. The origin of these morphological growths remains

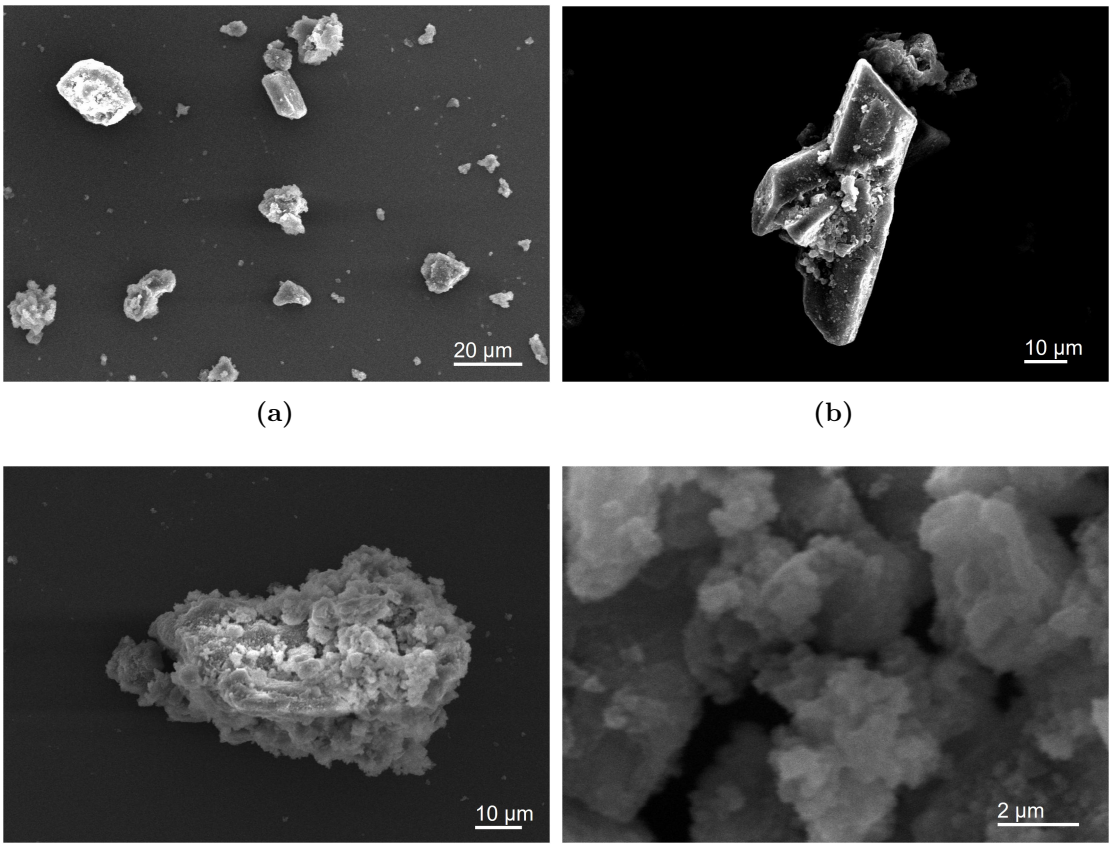

(a) **(b)**

(c) **(d)**

Figure 3.6: SEM images of SLDHs produced via the previously reported method at 65 °C.

ambiguous; it is uncertain whether they emerge on the surface, as seeded layered double hydroxide grows outwards, similar to observations made for *core@shell* LDH on SiO_2,[26] or if they initially form in solution from dissolved Mg components and subsequently adhere to the surface. Comprehensive investigations focusing on the morphological transformations through the synthesis process are required to elucidate the underlying mechanisms distinguishing these two potential pathways.

The N_2 isotherms of the synthesised SLDHs are depicted in Figure 3.7. These isotherms conform to IUPAC Type II, signifying gas adsorption on either non-porous or macro-porous solids, and exhibit H3 hysteresis loops that are characteristic of non-rigid aggregates of plate-like particles, typically observed in clays, where the desorption branch closes at the cavitation-induced limit p/p^0.[27] The specific surface area (SSA) is determined using Brunauer-Emmett-Teller (BET) analysis, yielding values of 17, 20 and 100 $m^2\,g^{-1}$ for SLDHs synthesised at 65, 75 and 85 °C respectively. This demonstrates that an increase in reaction temperature leads to an enhancement in surface area, attributable to the increase of both

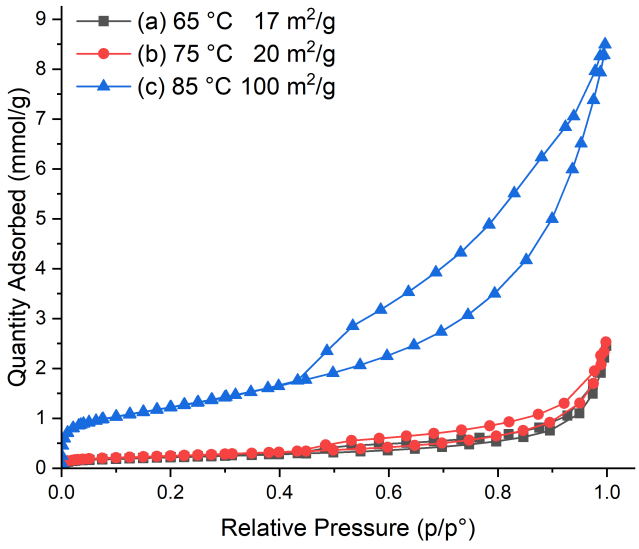

Figure 3.7: N_2 adsorption/desorption isotherms of SLDHs produced via the previously reported method at different temperatures. SSA of samples calculated via the BET method are given in the legend.

micropores (1.35 nm) and mesopores (2 to 40 nm) (Figure A.1). Still, the surface areas are substantially lower than those previously documented ($184\,m^2\,g^{-1}$),[21] indicating important variations in reaction conditions that must play a pivotal role in modulating the LDH surface area during synthesis.

3.2.2 Effect of base used during struvite decomposition

The presence of brucite impurities is undesirable, prompting efforts to optimise the synthesis process to inhibit its formation. To determine whether brucite formation occurs during the activation step or subsequently during the LDH synthesis intermediate samples were prepared. In these experiments, the struvite was subjected to the activation step (stirred in NaOH solution) followed by filtration and washing, thereby isolating it prior to the introduction of Na_2CO_3 and $Al(NO_3)_3 \cdot 9\,H_2O$ (fully described in Chapter 3.4.3).

Figure 3.8 presents the XRD patterns of the isolated intermediates. At reaction temperatures of both 65 and 85 °C, broad Bragg reflections attributed to brucite are discernible ((011) at 38° and (110) at 59°), indicating that the impurity previously observed in the SLDH products is formed during this initial stage. Additional phases detected include hydromagnesite ($Mg_5(CO_3)_4(OH)_2 \cdot 4\,H_2O$) ((011) at 15° and (022) at 31°), with the carbonate source attributed to carbonic acid formed by the dissolution of atmospheric CO_2, and an unidentified amorphous phase characterised by a broad reflection centred around 32°. Amorphous phases are frequently associated with the decomposition of struvite,[28] yet the position of the observed amorphous peak deviates from that documented by Bayuseno and Schmahl for struvite decomposed in aqueous environments.[29] Instead, it bears resemblance to the amorphous phase generated through the thermal treatment of newberyite ($MgHPO_4 \cdot 3\,H_2O$) as it undergoes the loss of waters of crystallisation. At 65 °C, sharp peaks characteristic of the struvite precursor reveal a reduced dissolution rate at lower activation temperatures, alongside the emergence of additional distinct crystalline reflections attributable to a newly formed phase. Phase identification

showed that the sharpest reflections of this material visually match to the struvite-type material hazenite ($KNaMg_2(PO_4)_2 \cdot 14\,H_2O$),[30] and further scrutiny of existing literature revealed a better match to the K substituted ammonium analogue ($NH_4NaMg_2(PO_4)_2 \cdot 14\,H_2O$) previously grown from a bacterial culture by Yang *et al.*[31] The structure is related to struvite; however, every other layer of $Mg(H_2O)_6$ octahedra and $(NH_4)O_6$ polyhedra in the struvite structure is substituted by a layer of $Mg(H_2O)_6$ octahedra and$(Na)O_6$ trigonal prisms. This publication appears to be the sole report of this material, while the majority of previous literature suggests a direct conversion to the fully Na substituted $MgNaPO_4 \cdot 7\,H_2O$.[32,33] Hence, this result constitutes the first report of its direct laboratory synthesis, indicating that its formation does not require a biological source to facilitate its formation and possibly suggesting this is an intermediary phase formed during the conversion to the fully substituted phase previously reported.

Investigations by Pettauer *et al.* on the hydration of MgO into $Mg(OH)_2$ showed brucite self-adjusts the pH of the solution to 10.5 to 11 based on its solubility ($pK_{sp} = 16.3$).[34] This results in a change in the limiting factor of formation of brucite from the rate of brucite precipitation to the rate of Mg source dissolution at lower pH. Thus, it was investigated if a comparable effect could be observed within the struvite-brucite system, potentially inhibiting brucite growth by reducing the pH of the system.

Figure 3.9 shows the XRD patterns of the SLDHs formed after reducing the amount of 1 M NaOH solution from 20 to 10 mL during the activation step. Decreasing the amount of NaOH yielded SLDH with reduced amounts of brucite impurities, evidenced by the decrease of the (110) Bragg reflection at 59° and a decrease in intensity at 38° due to the loss of the (011) reflection. This suggests that a decrease in pH is effective in inhibiting the formation of the brucite impurities.

However, the SLDH produced with reduced quantities of NaOH exhibited a reduction in crystallinity (Table 3.4), suggesting a decrease in the LDH crystal growth rate. This may arise due to a decrease in the amount of the intermediate product

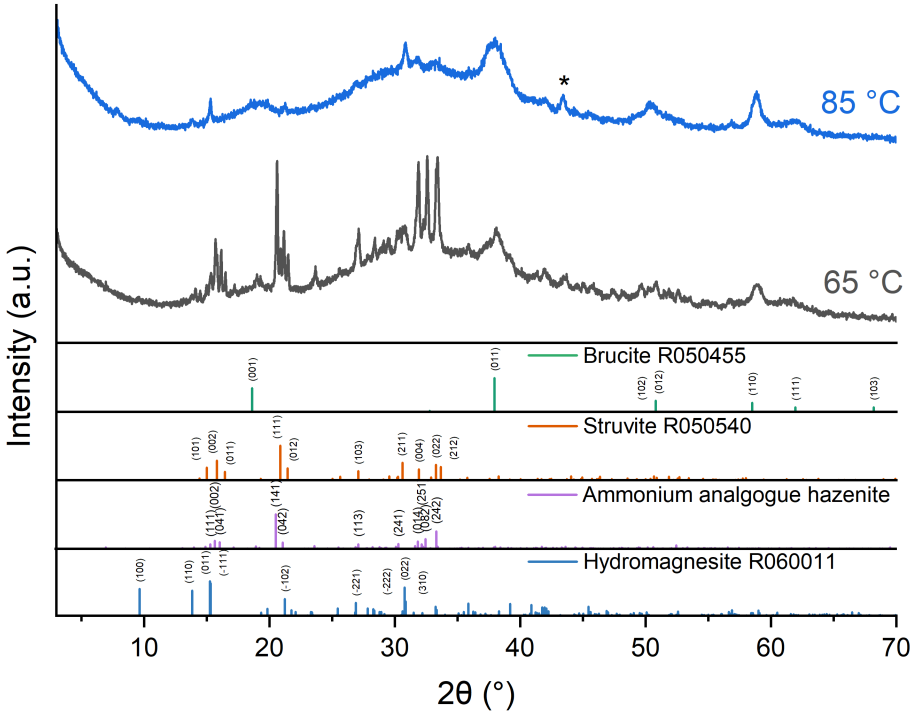

Figure 3.8: XRD patterns of intermediate products isolated after the activation step. Peaks can be indexed to the patterns below (RRUFF Project[12] R050455 - Brucite, R050540 - Struvite and R060011 - Hydromagnesite and the ammonium analogue of hazenite[31]). * indicates a reflection due to the sample holder.

formed, that acts as the active LDH precursor, with lower conversion from struvite due to a reduced solubility at decreased pH. Increasing the struvite activation time from 1 to 1.5 h lead to an increase in the crystallinity of SLDH to values comparable to the SLDH prepared with 20 mL NaOH showing that this was successful in increasing the amount of LDH precursor.

Analysis of the intermediate phases formed by this preparation method using the reduced amount of base and the extended pretreatment time (10 mL 1 M NaOH and 1.5 h, Chapter 3.4.5) was performed with the XRD patterns displayed in Figure 3.10 (full pattern depicted in Figure A.5). It shows a number of sharp Bragg reflections arising from both struvite and the previously observed ammonium analogue of hazenite ($NH_4NaMg(PO_4)_2 \cdot 14\,H_2O$). The intensity of the crystalline reflections

Table 3.4: Variation of lattice parameters (a, c) of the SLDHs and their respective crystallite domain lengths (CDL) with changes to the activation conditions (at 65 °C) extracted from 3.9. Samples are denoted by the amount of 1 M NaOH used and the length of the activation step

Activation conditions	d_{110} (nm)	a (nm)	CDL_a (nm)	d_{003} (nm)	c (nm)	CDL_c (nm)
20 mL, 1 h	0.152	0.304	8.329	0.774	2.321	2.704
10 mL, 1 h	0.151	0.303	6.322	0.782	2.346	2.156
10 mL, 1.5 h	0.152	0.304	8.160	0.784	2.352	2.793

relative to the amorphous hump is significantly higher than that seen previously (Figure 3.8) indicating the transformation to this amorphous phase is slower under reduced amounts of NaOH.

Although reducing the amount of NaOH in the activation step effectively removed the brucite impurity, it did not lead to a large increase in the BET SSA compared to previous work from our group (23.0 and 23.9 $m^2 g^{-1}$ vs 184 $m^2 g^{-1}$)[20] (Figure A.6), indicating a different key reaction condition is responsible.

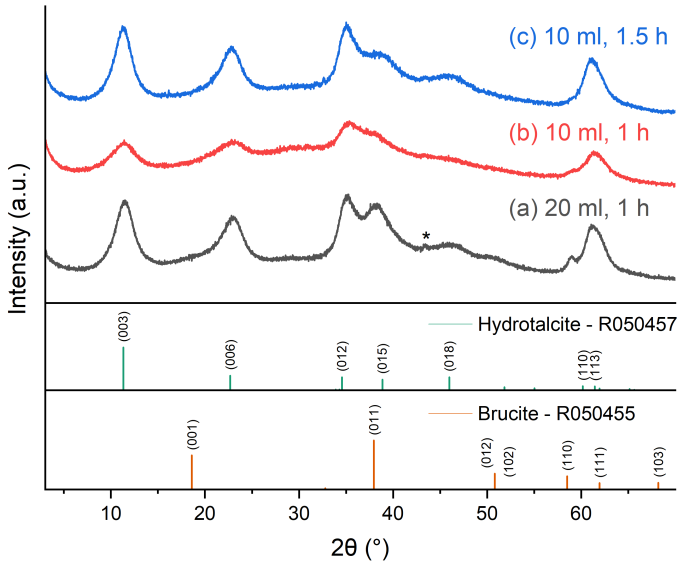

Figure 3.9: XRD patterns of SLDHs produced using varying activation steps, labelled by the amount of 1 M NaOH used and the activation time. Peaks can be indexed to the patterns below (RRUFF Project R050457 - Hydrotalcite and R050455 - Brucite).[12] * indicates a reflection due to the sample holder.

3.2.3 Effect of heating ramp rate

In the previous reactions, the struvite slurry was placed into an oil bath pre-heated to the desired temperature, leading to rapid heating of the solution. To investigate if a slower ramp rate would be more beneficial, the reaction was placed into an oil bath at room temperature and gradually heated to the target temperature over a period of approximately 20 min, prior to the activation step (Chapter 3.4.6).

The XRD patterns of the SLDHs produced are shown in Figure 3.11. While the characteristic Bragg reflections for LDH are clearly seen, there are still reflections from the ammonium analogue of hazenite when using 20 mL of 1 M NaOH or struvite when using 10 mL and a reflection at 59° assigned to the 110 Bragg reflection of brucite. As seen previously, a reduction in the amount of base used reduced the amount of brucite impurity observed, but also reduced the crystallinity of the SLDH. A greater amount of residual struvite also confirms the activation step is hindered by decreasing the amount of base and this prevents conversion of the struvite into LDH. A repeat of the synthesis (Figure 3.11 c) also shows

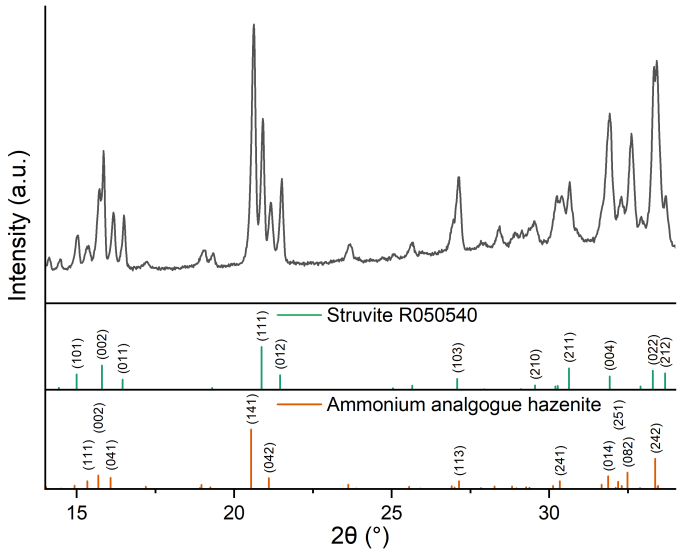

Figure 3.10: XRD patterns of intermediate produced using 10 mL 1 M NaOH used and a 1.5 h activation time. Peaks can be indexed to the patterns above (RRUFF Project<empty citation> R050540 - Struvite and the ammonium analogue of hazenite).[12,31]

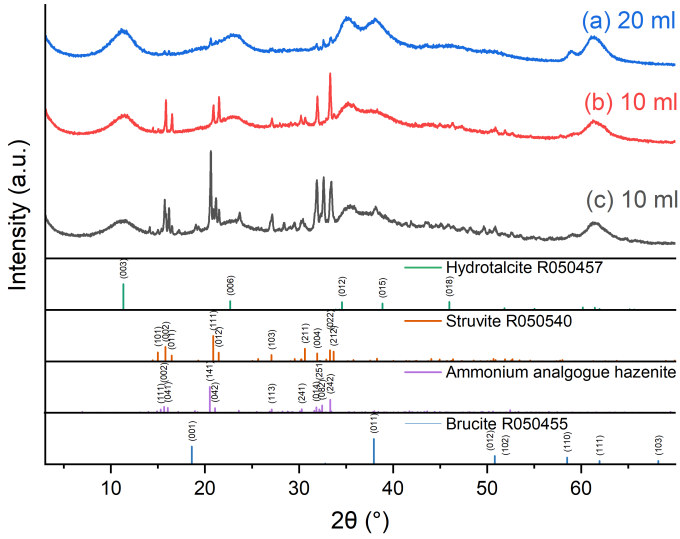

Figure 3.11: XRD patterns of SLDHs using varying activation steps, labelled by the amount of 1 M NaOH used. The reaction was done at 65 °C with an activation time of 1 h + the heating period (approximately 20 min). (a) uses the original 20 mL 1 M NaOH, (b) the reduced amount of 10 mL and (c) is a repeat of (b). Peaks can be indexed to the patterns above (RRUFF Project[12] R050457 - Hydrotalcite, R050540 - Struvite and R050455 - Brucite and the ammonium analogue of hazenite).[31]

peaks from the ammonium analogue of hazenite seen previously (Figure 3.10). Unexpectedly, the addition of the preheating step, increasing the length of time for the activation step, seems to have prevented the transformation of struvite into LDH despite an extended time being beneficial previously (Figure 3.10). Thus, rapid heating of the struvite slurry appears to be beneficial if it is to be used as an LDH precursor. Potentially, fast heating of the struvite leads to rapid NH_3 liberation which produces pores in the structure, increasing its surface area and allowing faster conversion via diffusion pathways within the particles.

This change of heating ramp rate in the activation step is reflected in the intermediates formed (Chapter 3.4.7, powder XRD pattern Figure 3.12, full pattern A.7). After the slow heating step, there is still the mixture of struvite and the crystalline ammonium analogue of hazenite phase, but from the relative peak intensities at 20.1 and 20.9° ((141) reflection of ammonium analogue of hazenite vs (111) of struvite) we can see much less struvite is converted. Unconverted struvite in the

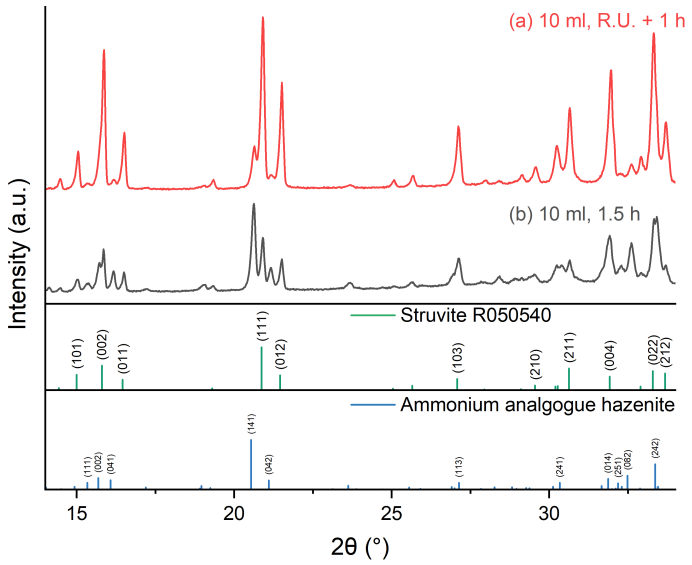

Figure 3.12: XRD patterns of intermediate produced using varying activation steps, labelled by the amount of 1 M NaOH used and the activation time. R.U. = Ramp Up (approximately 20 min). Peaks can be indexed to the patterns below (RRUFF Project[12] R050540 - Struvite and the ammonium analogue of hazenite).[31]

product was not observed for the previously discussed synthesis conditions, even where full conversion was not seen in the intermediate products (Figure 3.8) and so it can be concluded that slow heating of the struvite prevents it from reacting not only during the activation step, but also during the LDH synthesis.

3.2.4 Effect of precursor particle size

To test whether the decrease in reactivity was due to a decrease in the surface area of the intermediate product, the struvite precursor was ground to increase its intrinsic surface area by decreasing the particle sizes. The XRD pattern of the produced SLDH is shown in Figure 3.13. The SLDH is free of impurities; the sharp reflections from both the struvite and the ammonium analogue of hazenite are absent as well as the peak at 59° from brucite, indicating that an increase in surface area is key to the struvite conversion under short reaction times.

SEM images of the SLDH made from ground struvite are shown in Figure 3.14. There are fewer particles with defined sharp edges, and the average particle size

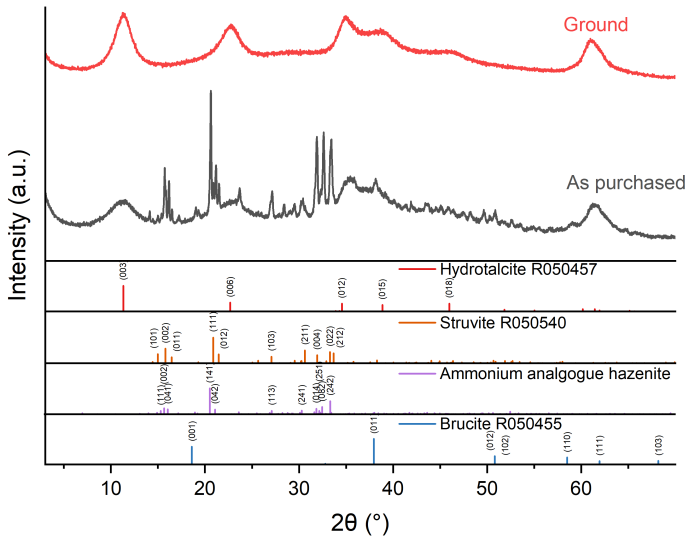

Figure 3.13: XRD patterns of SLDH produced with or without grinding the struvite precursor prior to use. Peaks can be indexed to the patterns above (RRUFF Project[12] R050457 - Hydrotalcite, R050540 - Struvite and R050455 - Brucite and the ammonium analogue of hazenite).[31]

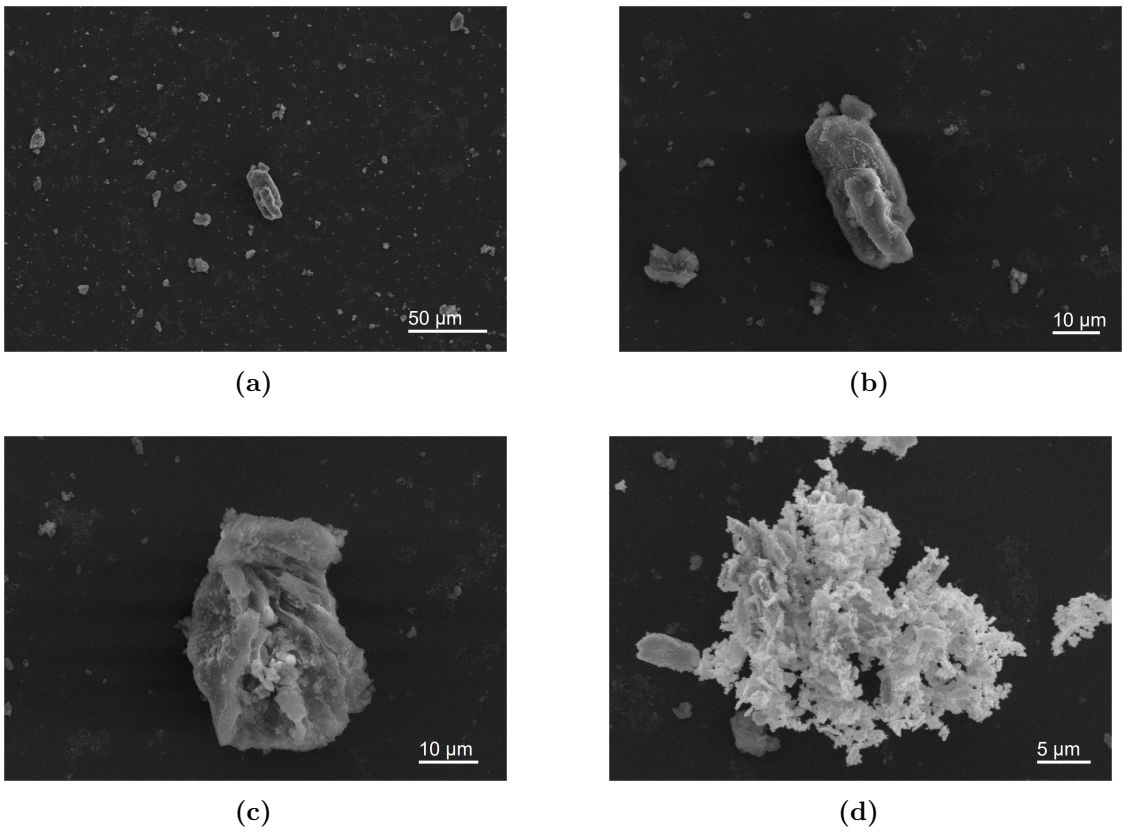

(a) **(b)**

(c) **(d)**

Figure 3.14: SEM images of SLDH made from ground struvite.

is decreased ($\leq$ 34.5 µm). However, the BET SSA of the sample is still low (18.8 $m^2 g^{-1}$) which is similar to all the previous SLDHs made at 65 °C (Figure A.8).

3.2.5 Conclusions

The reactions discussed so far show the conversion of struvite to LDH is complex, involving multiple phases. The activation step involves conversion of struvite to a mixture of brucite, hydromagnesite and an amorphous phase, or to an ammonium analogue of hazenite, depending on the amount of base used. These phases can all be converted to LDH except for brucite and, as such, the amount of base used in the activation step is crucial. The heating rate used in the activation step also has a significant role in the purity of the product. Slower heating rates lead to incomplete struvite transformation due to slower conversion to the intermediate, which can be overcome by a reduction in the struvite particle size. Although it is shown that impurity phases can be avoided by varying the reaction conditions, the BET SSA of the pure SLDHs is still low compared to those previously reported ($\approx$ 20 $m^2 g^{-1}$ vs 184 $m^2 g^{-1}$).[20]

3.3 Two-step synthesis of SLDHs

3.3.1 Development

Although pure LDH phases were produced according to the two step process previously reported, the surface areas that made the materials attractive were not realised and as such alternative synthesis protocols were investigated. Measuring the N_2 isotherms for struvite required a reduced degassing temperature of 30 °C, as the struvite was found to decompose when heated under vacuum at 110 °C. Interestingly, these decomposed samples possessed high surface areas (317 $m^2 g^{-1}$, A.12 a). A similar result was reported by Hövelmann *et al.* who found heating struvite in a drying oven to be a reproducible method for producing an amorphous Mg-phosphate with a high surface area and well defined pore structure.[18] The broad amorphous reflections observed in the XRD pattern of the degassed sample (Figure

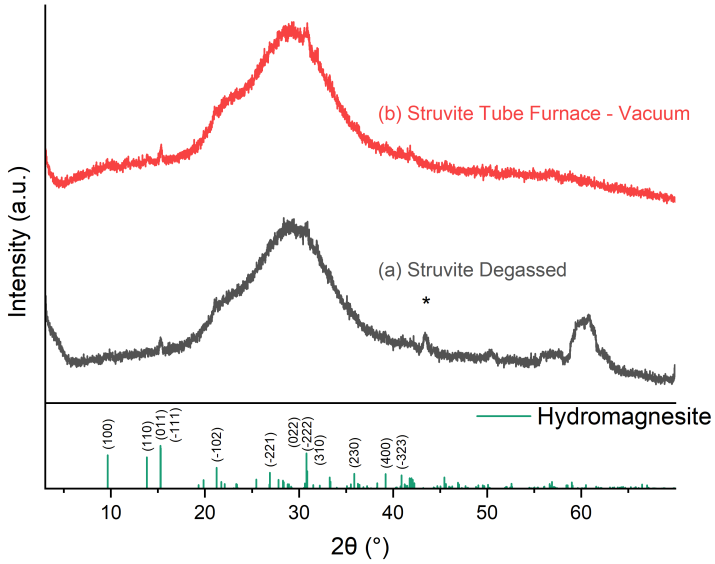

Figure 3.15: XRD of struvite calcined under vacuum. Sharp reflections can be indexed to the pattern below (RRUFF Project R060011 - Hydromagnesite).[12] * indicates a reflection due to the sample holder.

3.15) matched that reported by Hövelmann *et al.* but also appeared similar to the amorphous phase formed by struvite after activation as seen in the intermediate products discussed previously (Figure 3.8). As this previous amorphous intermediate phase was seemingly transformed to LDH, thereby acting as an active Mg source for LDH synthesis it was investigated whether the amorphous phase formed by thermal degradation of struvite would also serve as a Mg source and potentially serve as a template for the production of LDH that maintains the high surface area and porosity.

It was found that similar intermediate products could be produced in the laboratory by calcination under vacuum in a tube furnace at 110 °C (Chapter 3.4.8). As shown in Figure 3.15 b, the amorphous peaks appear at 22 and 29° and low-intensity Bragg reflections from the hydromagnesite are observable at 15.2, 21.2 and 30.8°. This agrees with work investigating the structural transformation of struvite by Sarkar[35] who found that struvite decomposes above 55 °C in air to form an amorphous product determined to be $MgHPO_4$ via TGA (Figure 3.3).[18] This amorphous material is referred to as A-$MgHPO_4$ henceforth. The elemental composition is

Table 3.5: Elemental composition (wt%) of A-$MgHPO_4$ formed by calcination of struvite. Also given are the theoretical composition of $MgHPO_4$ and the calculated formula $MgHPO_4 \cdot 1.28\,H_2O \cdot 0.31\,NH_3\,[Mg(OH)_2]_{0.3}$

	C	H	N	Mg	P
Measured	0.34	2	2.68	19.55	19.09
Theoretical	0.00	0.84	0.00	20.21	25.75
Calculated	0.00	3.09	2.61	19.02	18.65

given in Table 3.5 as well as the theoretical and calculated composition of the estimated formula: $MgHPO_4 \cdot 1.28\,H_2O \cdot 0.31\,NH_3\,[Mg(OH)_2]_{0.3}$. The Mg:P ratio is 1.3:1, the same as in the parent struvite material (Table 3.1) and the decomposition product of the unknown Mg impurity is assigned to $Mg(OH)_2$ for the calculation of the theoretical formula. A minor concentration of nitrogen is observed, which is ascribed to the entrapment of ammonia within the framework, given the absence of observable struvite reflections.

LDH was then prepared from this A-$MgHPO_4$ using a variable pH coprecipitation method. The addition of $Al(NO_3)_3 \cdot 9\,H_2O$ and an excess of Na_2CO_3 to A-$MgHPO_4$ (produced using a vacuum oven at 110 °C) under alkaline conditions yielded LDH products (Chapter 3.4.9, Figure 3.16).

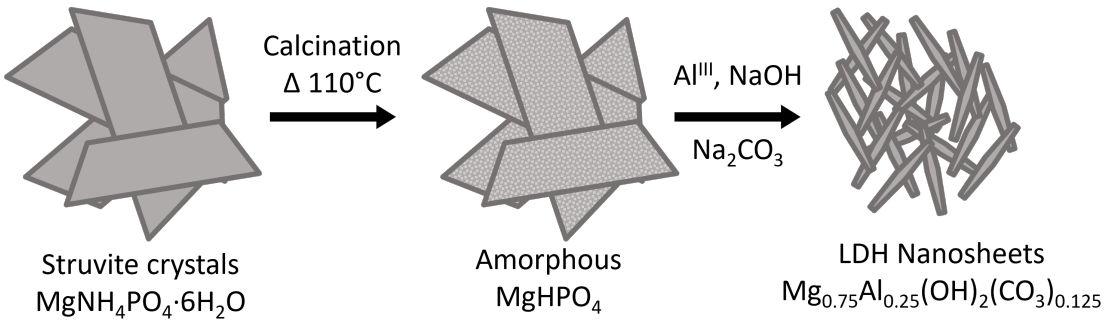

Figure 3.16: Synthesis scheme for SLDHs via A-$MgHPO_4$.

The XRD patterns of the products produced at room temperature (RT, ≈ 20 °C) and at 80 °C are presented in Figure 3.17. At both temperature, SLDHs are formed with all the characteristic LDH Bragg reflections observed ((003), (006), (012), (015), (018), (110), (113) at 11.3, 22.7, 34.6, 38.9, 46.0, 60.2 and 61.5°, respectively).

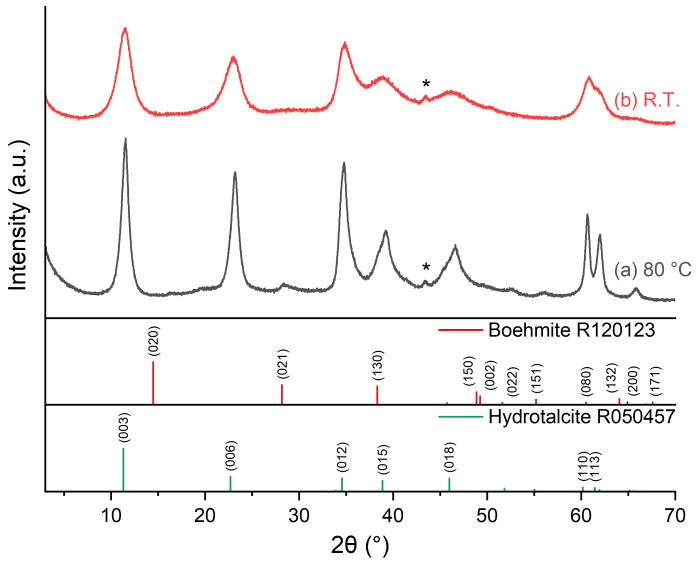

Figure 3.17: XRD of SLDH derived from A-$MgHPO_4$. Peaks can be indexed to the patterns below (RRUFF Project R050457 - Hydrotalcite and R120123 - Böhmite).[12] * indicates a reflection due to the sample holder.

Table 3.6: Variation of lattice parameters (a, c) of the SLDHs derived from A-$MgHPO_4$ and their respective crystallite domain lengths (CDL) with changes to the synthesis temperature extracted from Figure 3.17. RT means room temperature ($\approx 20\,^{\circ}C$).

Temperature	d_{110} (nm)	a (nm)	CDL_a (nm)	d_{003} (nm)	c (nm)	CDL_c (nm)
20 °C	0.152	0.305	8.105	0.773	2.319	3.536
80 °C	0.153	0.305	22.325	0.769	2.307	6.439

At elevated temperatures, the crystallinity of the products is increased, (Table 3.6) most notably by the resolution of the (110) and (113) Bragg reflections and the appearance of the (01 10), (01 11) and (116) Bragg reflections at 52.7, 56.2 and 65.8°, respectively. This is likely due to an increase in solubility and reaction rate at higher temperature increasing the speed of crystal growth. In the sample synthesised at elevated temperature, the $(01l)$ peaks ((012), (015), (018)) are broader than the $(00l)$ and $(hk0)$ peaks. This is indicative of disorder in the layer stacking where both the $3R_1$ and $3R_2$ LDH phases are present (differing only by the direction of rotation between layers).[36] There is also an unknown reflection at 28.3°, which is also seen in the experimental patterns reported for LDH with this type of disorder,[36]

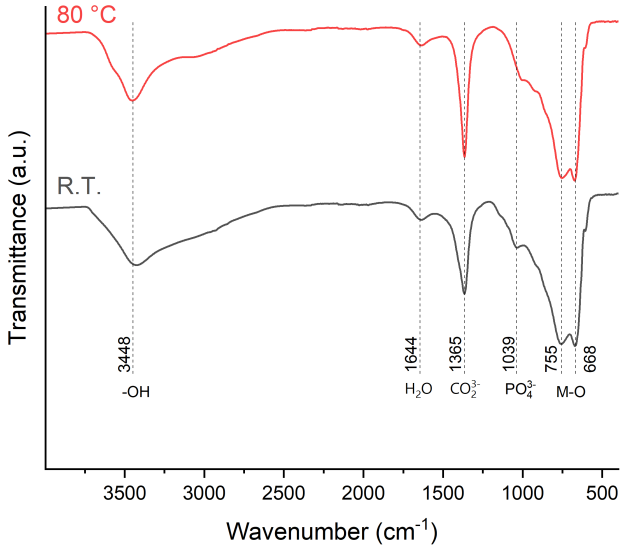

Figure 3.18: FTIR of SLDH derived from A-$MgHPO_4$.

potentially attributable to the (021) reflection of boehmite (γ–AlO(OH), a common LDH impurity),[37,38] although the (020) reflection is not observed.

FTIR spectra of the SLDHs produced via this method (Figure 3.18) show similar spectra to the previously discussed materials (Figure 3.5) with a mixture of both phosphate and carbonate ions present. However, the CO_3^{2-} absorption for SLDHs made using this new method is much stronger with an associated decrease in the PO_4^{3-} absorption showing a change in the ratio of the two anions in the product, likely driven by the larger excess of Na_2CO_3 used during the synthesis.

HR-SEM images of the SLDH produced at 80 °C are shown in Figure 3.19. Although the morphology of the precursor is not clearly seen, there are still large particles (20 µm) present (Figure 3.19(a)). Under higher magnification (Figure 3.19(d)), the surface of the particles is seen to consist of a dense network of intergrown hexagonal platelets approximately 20 nm thick and 65 to 250 nm wide. The platelet morphology is typical of LDHs and, as the observed size is greater than that derived by the Scherrer equation, 6.4 nm thick and 22.3 nm wide (Equation 2.3, Table 3.6), this suggests that the LDH platelets contain multiple crystallites.

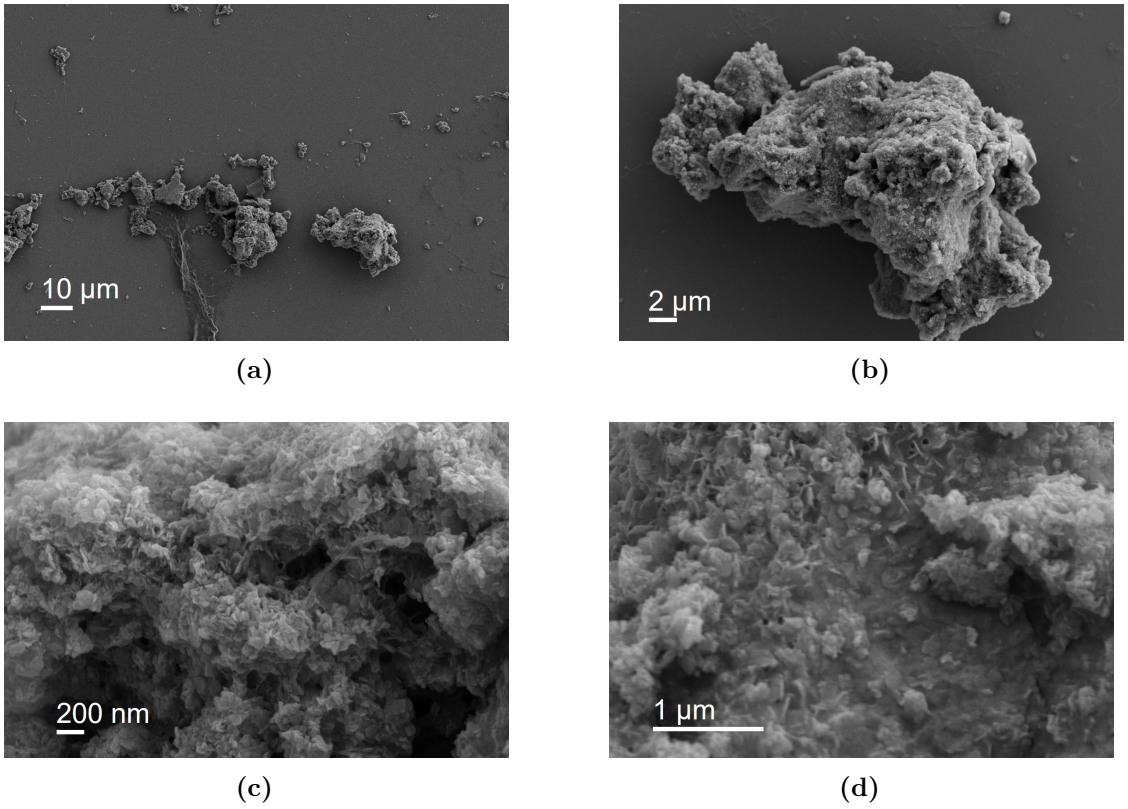

Figure 3.19: HR-SEM images of SLDH made from A-$MgHPO_4$.

Figure 3.20 shows the N_2 adsorption/desorption isotherms of the SLDHs. Both samples synthesised at RT and at 80 °C show increased surface areas to those made by the previous method (51.7 and 167.2 $m^2\,g^{-1}$ vs $\approx 20\,m^2\,g^{-1}$). The isotherms have very similar forms to those discussed previously: IUPAC Type II shape (corresponding to adsorption of gas on a non-porous or macro-porous solid) and display H3 hysteresis loops (indicative of non-rigid aggregates of plate-like particles commonly seen for clays). The pore size distribution is displayed in Figure 3.21. The SLDH show a range of pore sizes with micropores at $\approx$ 13 Å and a broad distribution of mesopores from 25 to 400 Å. The increase in surface area is associated with an increase in the amount of both micropores and mesopores with a noticeable increase in the amount of mesopores in the range 80 to 200 Å. The increased surface area indicated that porous A-$MgHPO_4$ precursor does impart an increase in surface area to the SLDH produced. The two step synthesis method is also less complex (the products of the in situ pretreatment step used previously varied with factors such

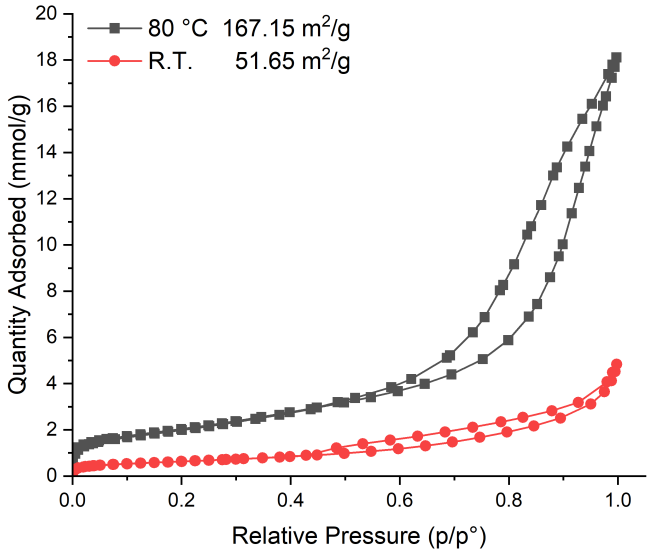

Figure 3.20: N_2 adsorption/desorption isotherms of SLDH derived from A-$MgHPO_4$. BET SSAs are given in the legend. RT means room temperature.

as the amount of base and ramp rate used) making it easier to scale up; coupled with the high SSA observed, this methodology was therefore chosen for further investigation over the previously reported method discussed previously.

3.3.2 Optimisation of struvite calcination

The diameter of the tubes used for the tube furnace limited the size of the sample boats that could be used and significant bumping occurred due to the liberation of NH_3 and H_2O during the calcination if the boat was filled with too much sample. Thus, in order to scale up production of A-$MgHPO_4$ through the struvite calcination method, alternative calcination setups were investigated. A larger diameter tube furnace and a muffle furnace were investigated as alternative setups (Chapter 3.4.8). Figure A.9 shows the XRD of the materials produced from these different calcination setups. A flow of N_2 was found to produce the same amorphous product as under vacuum and full conversion was found to be complete after two hours. Interestingly, under static air (muffle furnace) or low flow rates of N_2 (tube furnace) a different product was observed with sharp Bragg reflections indexed to dittmarite ($MgNH_4PO_4 \cdot H_2O$). This is also in agreement with Sarkar[35] and several

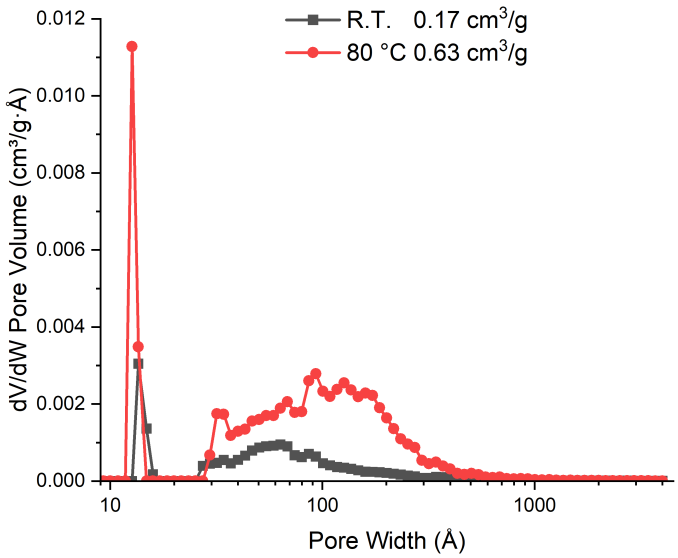

Figure 3.21: Pore size distribution calculated using a density functional theory model (slit) on N_2 adsorption isotherms of SLDH derived from A-$MgHPO_4$ (Figure 3.20). The pore volumes at $p/p^0 = 1$ of the samples are given in the legend.

other investigations in which dittmarite forms in the presence of excess water or moderate hydrostatic pressure.[29]

$$\underset{\text{Struvite}}{MgNH_4PO_4 \cdot 6\,H_2O} \xrightarrow{\Delta,\,\text{Humid}} \underset{\text{Dittmarite}}{MgNH_4PO_4 \cdot H_2O} + 4\,H_2O\uparrow$$

This observation appears to go against Le Chatelier's principle if both phases are in equilibrium with struvite. However, Farhana showed that a high relative humidity (RH) suppressed dittmarite formation in favour of newberyite ($MgHPO_4 \cdot 3\,H_2O$), indicating it is not in equilibrium below this level of humidity, although it has been shown to rehydrate to struvite in the presence of excess water.[28,35] As such, dittmarite is only formed when the humidity is below the struvite equilibrium vapour pressure (85% RH). A further equilibrium describing the transformation of dittmarite to the amorphous phase would explain the suppression in the presence of humidity; however, dittmarite is more stable than struvite and decomposes at 235 °C and so would not be converted at the calcination temperature of 110 °C. As such, it is speculated that the final water of crystallisation of the struvite has a lower vapour pressure and is only lost when the humidity of the calcination atmosphere

is below this value. Evidence for this process is seen in the gradual continual loss of water observed upon heating with peak NH_3 loss, occurring after the peak H_2O loss, shown by Hövelmann *et al.*[18]

HR-SEM of the A-$MgHPO_4$ produced under N_2 and vacuum are shown in Figures A.10 and A.11. The morphology of the struvite precursor is maintained in both samples; however, the surfaces of the materials are noticeably different. Samples prepared under vacuum display large cracks in the surface ($\approx 500\,nm$) compared to samples prepared under N_2 which show small pores ($\approx 50\,nm$).

These differences can be observed in the pore size distributions shown in Figure A.13. The samples prepared in both atmospheres show some micropores (12.4 Å for struvite calcined under N_2, and 14.2 and 17.0 Å for struvite calcined under vacuum), but the sample prepared under N_2 also displays a range of mesopores (70 to 400 Å) corresponding to the small pores observed on the surface. The differences in pore size also lend support to the previous hypothesis that faster liberation of NH_3 exposes more of the struvite for reaction (Chapter 3.2.3).

Noticeably, the BET surface area for both materials is lower than that observed for the struvite decomposed during degassing, likely due to differences in the rate of decomposition (Figure A.12). The higher surface area for the struvite decomposed during degassing arises due to an increase in both the amount of micropores (seen at 11.7 Å) and the formation of a large number of small mesopores ranging in size from 27 to 50 Å. The differences in pore distributions are also visible in the shape of the isotherms. They all can be classified as Type II isotherms displaying a sharp uptake at high p/p^0 caused by multilayer adsorption. The type of hysteresis that is observed changes with the preparation method, reflecting the changes in pore structure: the struvite calcined under vacuum displays a narrow hysteresis loop closing at high p/p^0 (0.875), classified as a H1 arising from delayed condensation in a narrow range of mesopores; the struvite decomposed during degassing shows a H3 loop with the lower limit at the cavitation induced p/p^0, which can indicate that not all of the macropores in the pore network are completely filled; while the

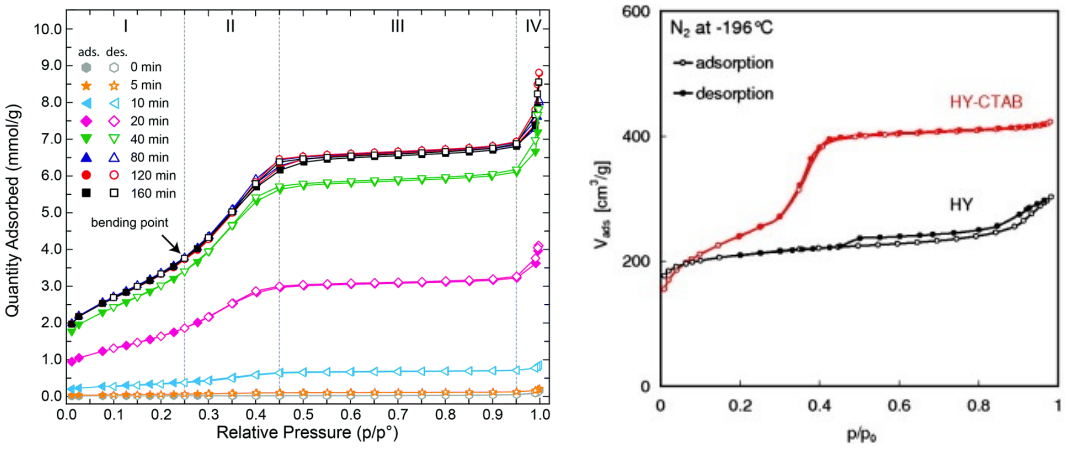

Figure 3.22: N_2 adsorption–desorption isotherms of: (a) struvite powders after thermal treatment at 90 °C for 5 to 160 min. Reproduced from Hövelmann *et al.*[18] (b) normal and templated HY type zeolites. Reproduced from Mańko *et al.*[39]

struvite calcined under N_2 has a large loop classified as H5 which arises from pore structures containing both open and partially blocked mesopores.[27] The struvite decomposed during degassing also displays an unusual double knee feature which does not appear within the IUPAC framework.[27] The adsorption before the initial knee is sharp, arising from the filling of the micropores before a increasing linear region, reminiscent of a Type IV(b) where a second sharp uptake occurs during pore condensation within small mesopores and a plateau indicating a lack of large mesopores. This is the same shape as the isotherms reported by Hövelmann *et al.*[18] (Figure 3.22(a)) and a similar shape of isotherm in the low pressure region was reported by Mańko *et al.* for templated Zeolite Y (Figure 3.22(b)) containing both micropores and mesopores.[39]

SLDHs were prepared from the three products formed from the different calcination methods (using a muffle furnace in air or in a tube furnace under N_2 or vacuum) at both RT and 80 °C and the XRD patterns are shown in Figure 3.23. The patterns of the products at each temperature appear similar, regardless of the precursor used, with only minor differences in their crystallinity (Table 3.7). As seen previously, synthesis at elevated temperature yields a more crystalline product (Figure 3.17). The most significant difference is seen in the SLDHs made using

the struvite calcined in the muffle furnace (containing dittmarite) which are more crystalline than those prepared using struvite calcined in the tube furnace (under vacuum or N_2) at both synthesis temperatures. This is attributed to the presence of dittmarite in the calcined product (Figure A.9), but may be due to differences in solubility between dittmarite and A-$MgHPO_4$ or a buffering effect by the NH_3 released upon its dissolution (an ammonium buffer is typically $pH \approx 10$, $pK_a = 9.25$).[40]

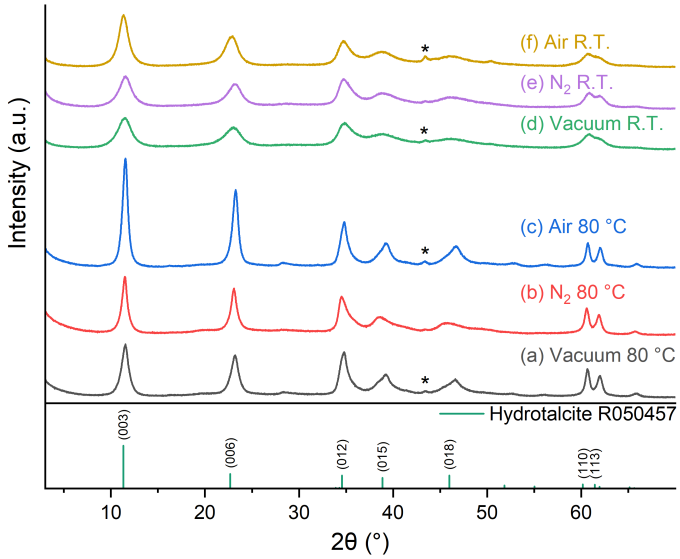

Figure 3.23: XRD of SLDH derived from A-$MgHPO_4$ under different conditions. Peaks can be indexed to the patterns below (RRUFF Project R050457 - Hydrotalcite).[12] * indicates a reflection due to the sample holder.

Table 3.7: Variation of lattice parameters (a, c) of the SLDHs derived from A-$MgHPO_4$ prepared under different calcination conditions and their respective crystallite domain lengths (CDL) at RT ($\approx 20\,^{\circ}C$) and $80\,^{\circ}C$ extracted from Figure 3.23.

Setup, Temp.	d_{110} (nm)	a (nm)	CDL_a (nm)	d_{003} (nm)	c (nm)	CDL_c (nm)
Vacuum $80\,^{\circ}C$	0.153	0.305	22.325	0.769	2.307	6.442
N_2 $80\,^{\circ}C$	0.153	0.306	20.056	0.772	2.315	8.300
Air $80\,^{\circ}C$	0.153	0.305	23.337	0.768	2.304	8.813
Vacuum RT	0.152	0.305	8.105	0.773	2.319	3.531
N_2 RT	0.152	0.305	10.565	0.767	2.301	3.778
Air RT	0.153	0.305	8.710	0.780	2.339	4.836

The BET SSA are summarised in Figure 3.24 with the isotherms and pore size distributions presented in Figures A.14 and A.15, respectively. There are clear trends between the samples: SLDHs synthesised at elevated temperatures show higher SSAs and the surface area is correlated with the precursor used (A-$MgHPO_4$ N_2 > A-$MgHPO_4$ Vacuum > A-$MgHPO_4$ Air (with dittmarite impurity)). Comparing the two samples produced from struvite calcined in the tube furnace (A-$MgHPO_4$ N_2 and A-$MgHPO_4$ Vacuum), the surface area correlates with that observed in the precursor indicating the templating effect of the A-$MgHPO_4$. Thus, since A-$MgHPO_4$ N_2 produced SLDH with the highest SSA, this precursor was used for subsequent experiments at 80 °C. Subsequent calcinations were conducted in a vertical tube furnace where the struvite was fluidised under N_2 flow to ensure homogeneous removal of H_2O throughout the sample on larger scales.

Samples stored in sample vials show slow conversion to hydromagnesite (Figure A.16), suggesting reaction with CO_2 in the atmosphere, so samples were kept in a desiccator prior to use. A summary of the mineral transformations observed is given in Figure 3.25.

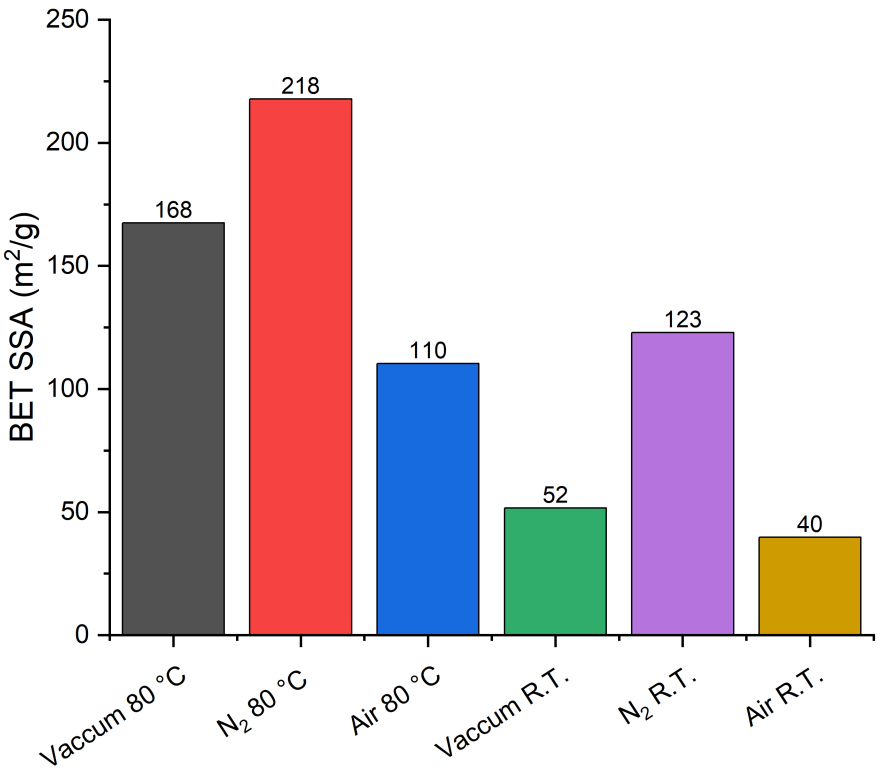

Figure 3.24: BET SSAs of SLDH made from struvite calcined under different conditions. RT means room temperature (≈ 20 °C).

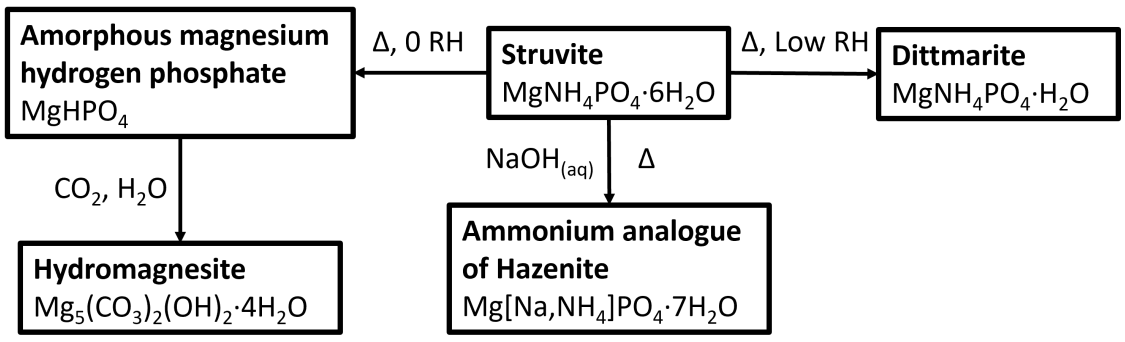

Figure 3.25:
Summary of the mineral transformations of struvite observed.

3.3.3 Scale up

These initial reactions yielded approximately 0.1 g of material and so the reaction was scaled up to yield more material for characterisation and to test its applicability for industrial adoption. The reaction was successfully scaled 5 and 50 times, increasing the yield from 0.1 to 5 g (Chapter 3.4.10). Figure 3.26 a to c show the XRD patterns of the SLDHs produced. The patterns show pure phases with the SLDHs becoming more crystalline with the scale of the reaction, showing an increase in CDL in both the parallel and perpendicular axis (Table 3.8).

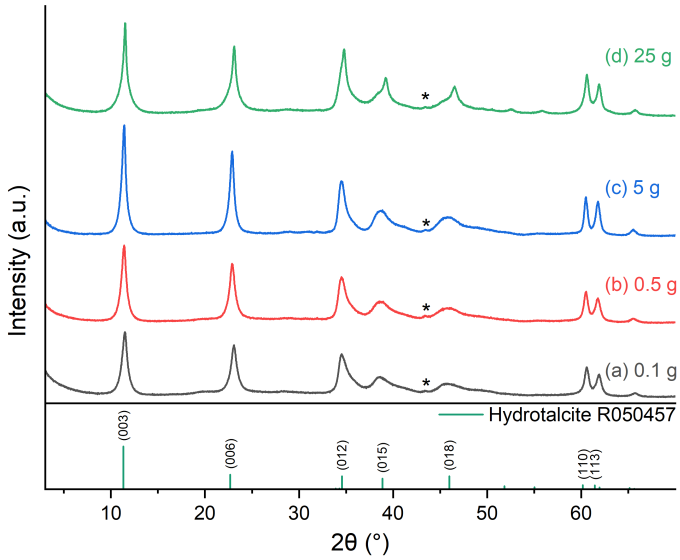

Figure 3.26: XRD patterns made from A-$MgHPO_4$ from different scale reactions, denoted by yield of SLDH. Peaks can be indexed to the patterns below (RRUFF Project R050457 - Hydrotalcite).[12] * indicates a reflection due to the sample holder.

Table 3.8: Variation of lattice parameters (a, c) of the SLDHs derived from A-$MgHPO_4$ on different reaction scales and their respective crystallite domain lengths (CDL) extracted from Figure 3.26.

Reaction scale (g)	d_{110} (nm)	a (nm)	CDL_a (nm)	d_{003} (nm)	c (nm)	CDL_c (nm)
0.1	0.153	0.306	20.056	0.772	2.315	8.288
0.5	0.153	0.306	22.950	0.777	2.332	8.821
5	0.153	0.306	28.544	0.778	2.333	10.320
25	0.153	0.306	19.697	0.771	2.312	8.502

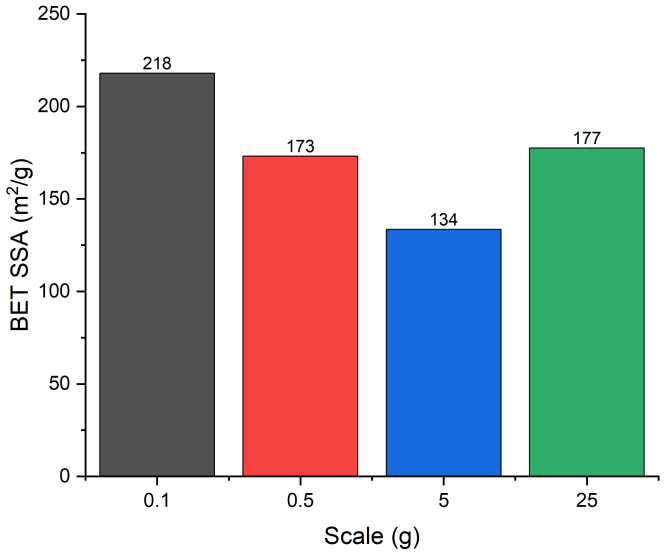

Figure 3.27: Summary of BET SSAs of SLDH produced from A-$MgHPO_4$ on different scales.

Figure A.17 a to c shows the N_2 adsorption/desorption isotherms of the SLDHs. The BET SSA remains high on all reaction scales; however, as the reaction scale increases, there is a decrease in SSA (to 173 and 134 $m^2\,g^{-1}$ from 218 $m^2\,g^{-1}$, Figure 3.27). As this correlates with the increase in crystallinity, it suggests that larger platelets are formed which have a lower surface area per volume. The calculated pore size distributions are shown in Figure A.18 with all samples showing a similar distribution micropores of 13 Å and a range of mesopores of 20 to 200 Å.

Further scale up to 25 g was achieved using a 5 L bench-top process reactor. This features an impeller and a heated jacket, ensuring thorough mixing and even heating of the reaction mixture. The XRD pattern of the SLDH produced is shown in Figure 3.26 d. There is a reduction in crystallinity (Table 3.8); however, the Bragg reflections have an unusual profile with sharp tips and broad tails. This is characteristic of nanomaterials with bimodal particle sizes where the peak shape is the sum of a broad and sharp peak at the same 2θ.[41] Evidence of crystallites with increased size is the appearance of the (10 10) and (01 11) Bragg reflections at 52.6° and 5.9°.

The BET SSA of the SLDH produced on this scale is $177\,m^2\,g^{-1}$ (Figure A.17 d). This is similar to the sample produced at the 0.5 g scale and, as they both display similar CDLs (Table 3.8), it also fits the trend between crystallinity and surface area.

HR-SEM and EDX mapping of the particles produced on the 25 g scale are presented in Figures 3.28 and 3.29. An overview of the particles is shown in Figure 3.28(a) with a range of particle sizes with the largest $\approx$ 50 µm. This particle retains the coffin morphology of the struvite precursor (Figure 3.28(b)) as seen for the previously reported method (Figure 3.6(b)). The presence of a range of particles sizes, along with retention of the parent morphology, suggests that the particles fragment under the reaction conditions, rather than a bottom up process where smaller particles agglomerate. Further magnification (Figure 3.28(c) and 3.28(d)) reveals the surface of the particles are formed from intergrown platelets, a typical morphology for LDH.

EDX mapping of these particles shows a homogeneous distribution of the expected elements (Mg, Al, C, O, P, Figures 3.29(c) to 3.29(g)) throughout, confirming complete conversion of the A-$MgHPO_4$ precursor to SLDH.

HR-SEM images of the SLDHs produced on the 0.1, 0.5 and 5 g scales are shown in Figures A.19, A.20 and A.21. The SLDHs produced on the small scale (0.1 and 0.5 g) do not show the struvite morphology, suggesting the large precursor particles are broken up during synthesis on this scale with the largest particles observed $\approx$ 20 µm in size. On the intermediate scale (5 g), the particle morphology is clearly retained; Figure A.21(b) shows how the A-$MgHPO_4$ particle is converted to the LDH phase. Where the A-$MgHPO_4$ has dissolved, large cracks are present on the surface of the crystal with LDH platelets within it ($\approx$ 30 nm thick and 600 nm wide). This is direct evidence of the solid-solid transformation previously proposed.

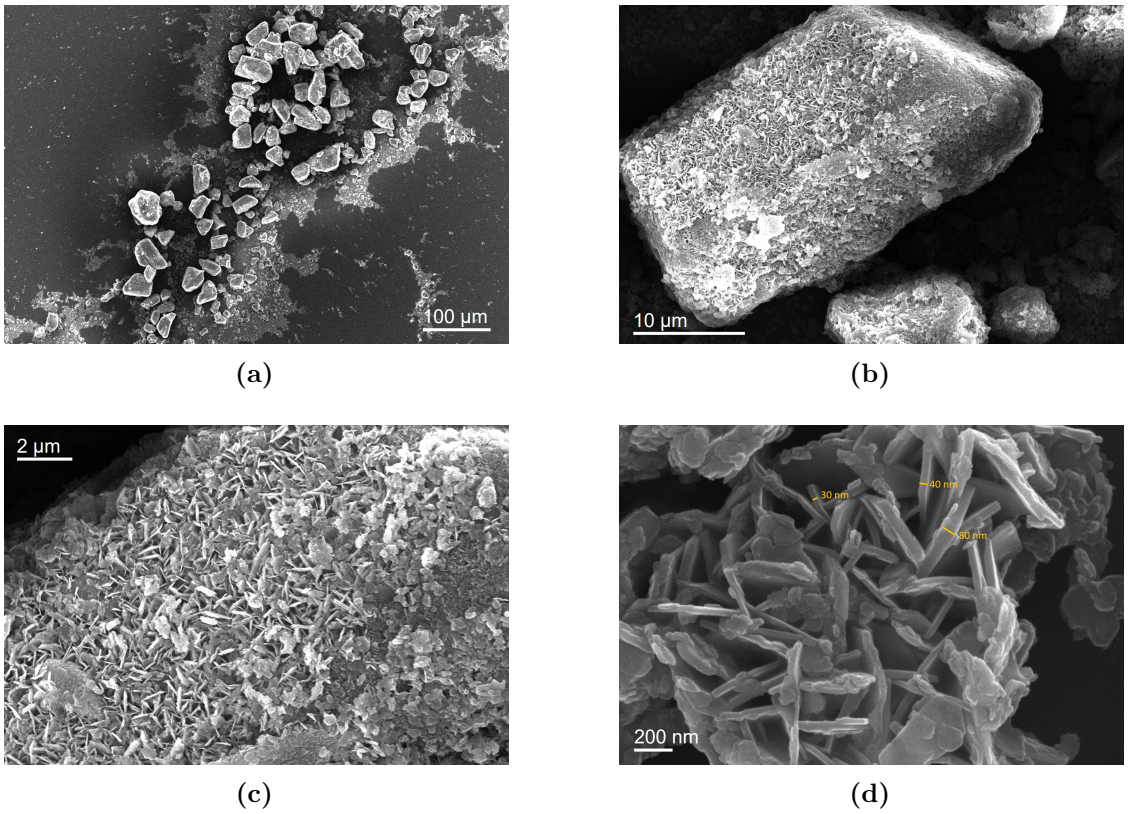

Figure 3.28: HR-SEM images of SLDH made from A-$MgHPO_4$ on 25 g scale.

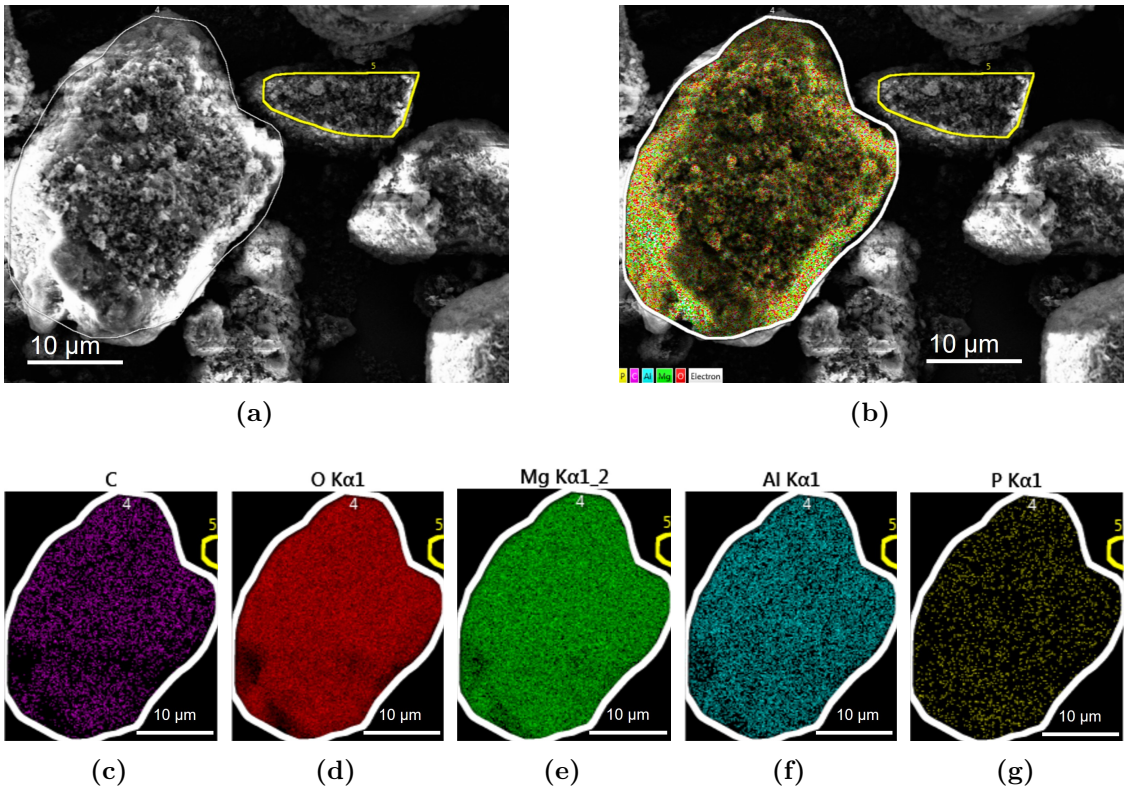

Figure 3.29: HR-SEM EDX images of SLDH made from A-$MgHPO_4$ on 25 g scale.

Table 3.9: Elemental composition (wt%) of SLDH and that calculated for the derived formula ($[Mg_{0.769}Al_{0.231}(OH)_2][(CO_3)_{0.121}] \cdot (H_3PO_4)_{0.025} \cdot 0.2\,H_2O$).

	C	H	N	Al	Mg	P	Na
Measured	2.01	3.37	0.00	8.59	25.8	1.07	0.03
Calculated	2.01	3.45	0.00	8.63	25.87	1.07	0.00

The elemental composition of the SLDH produced at 25 g is given in Table 3.9. Presuming an entirely LDH phase, this results in a composition of

$$[Mg_{0.769}Al_{0.231}(OH)_2][(CO_3)_{0.121}] \cdot (H_3PO_4)_{0.025} \cdot 0.2\,H_2O.$$

The Mg:Al ratio aligns closely with the anticipated value derived from the ratio of precursor materials used (3.34 compared to 3), while the Al:CO_3 ratio closely aligns with the theoretical value (1.91 in contrast to 2). Although phosphate is still detected, its concentration significantly lower in comparison to carbonate, being approximately 4.84 times less prevalent.

To investigate the composition of the SLDH, SS-NMR experiments on the SLDH produced at 25 g were conducted to determine the local environments present.

^{27}Al DP-MAS NMR (Figure 3.30) shows the major Al environment is 6-coordinated at 8.7 ppm which is expected for Al in the octahedral sites of the LDH structure.[42] Mg_3Al LDHs are reported to have broader resonances than Mg_2Al LDHs as there is no cation ordering within the materials leading to a disorder based distribution of chemical shifts. There is also a minor environment at 66.7 ppm which is in the range that typically corresponds to a 4-coordinated environment. Upon calcination, Al cations migrate to tetrahedral sites within the structure, but these are not seen in pristine LDHs.[43] Surface modified LDHs (with silanes) have been shown to develop resonances in this region and thus this environment may develop from the binding of another species such as phosphate on the surface.[44] LDHs formed from the reconstruction of LDOs under high phosphate concentrations have been shown to develop a similar broad resonance (66 ppm) which is likely the same species.[45] A peak at $\approx$ 65 ppm has also been observed as a minor environment in amorphous aluminium hydroxide which may be present as an impurity.[46]

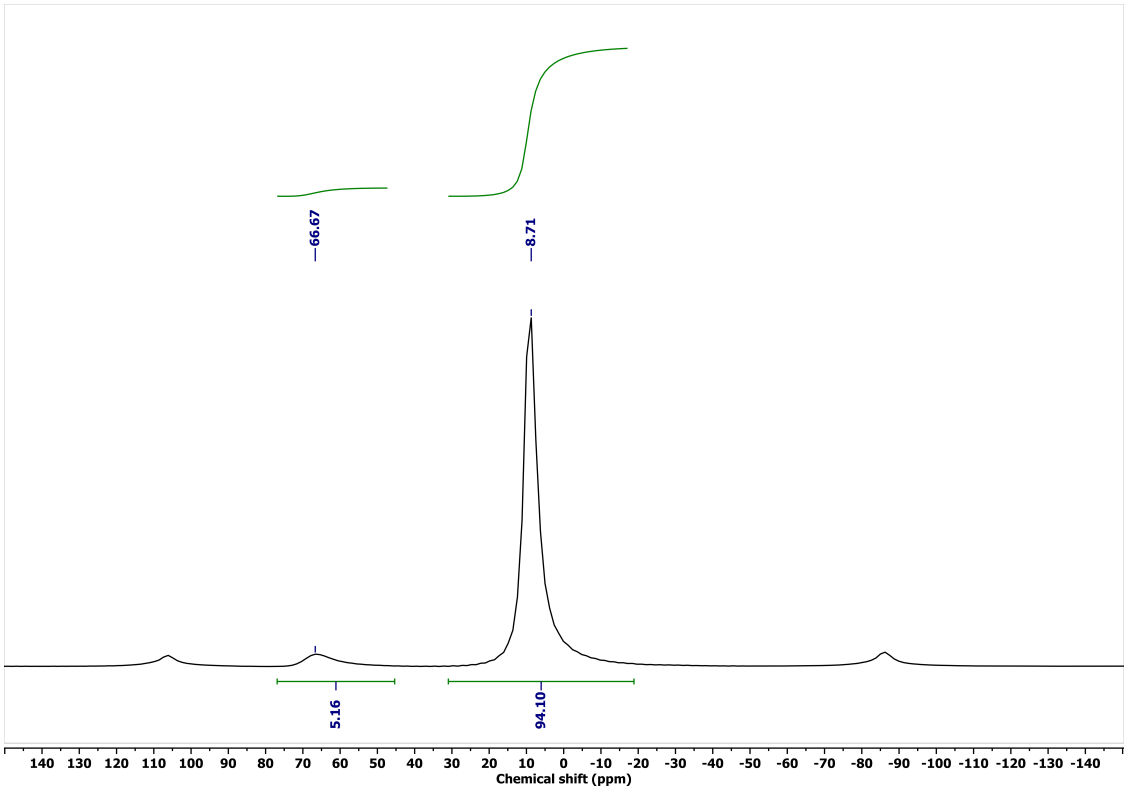

Figure 3.30: ^{27}Al DP-MAS NMR of SLDH at 10 kHz

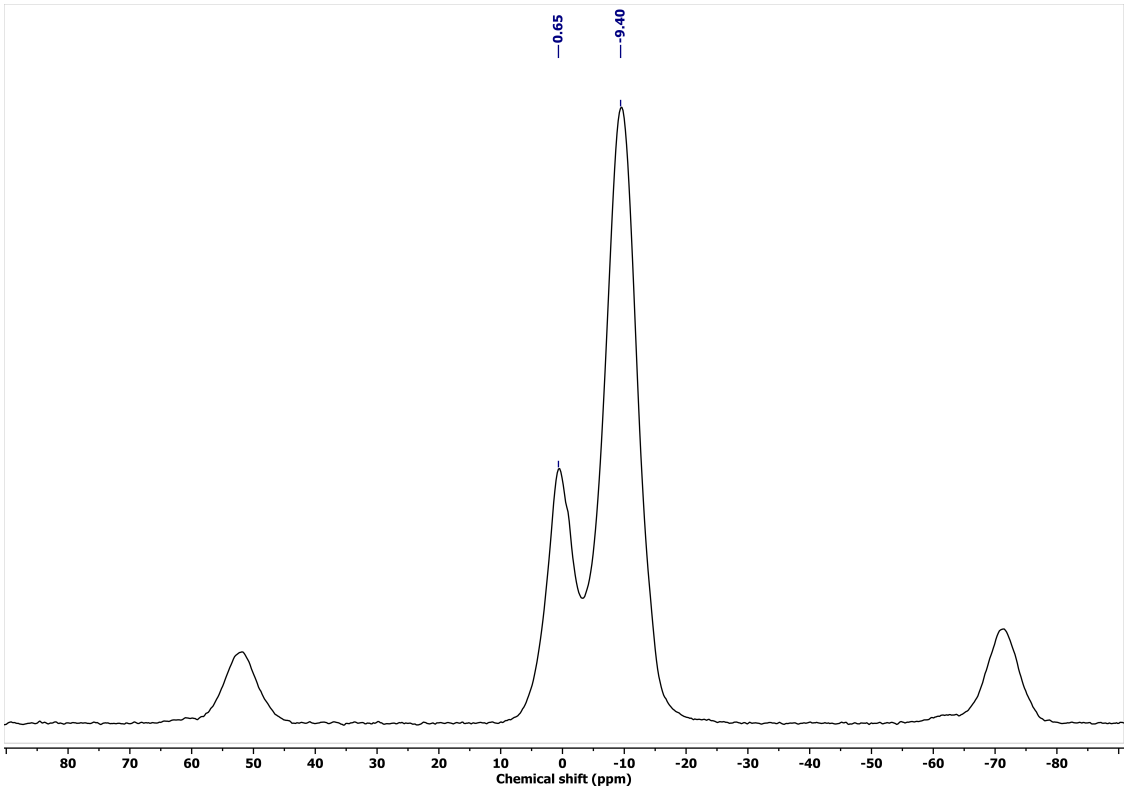

Figure 3.31: ^{31}P CP-MAS NMR of SLDH at 10 kHz

^{31}P CP-MAS NMR (Figure 3.31) shows two P environments: one at 0.65 ppm, attributed to overlapping signals of monodentate and bidentate surface bound phosphate (2.6 to 3.2 ppm and −1.4 to −0.9 ppm)[47] and one at −9.4 ppm, attributed to adsorption on amorphous aluminium hydroxide.[48] Amorphous aluminium hydroxide has been shown to form during LDH synthesis to different extents depending on the synthesis method and can be undetectable in powder XRD and TEM analysis.[49,50] The ^{27}Al environment for amorphous aluminium hydroxide appears as a broad resonance at 14.5 ppm overlapping with the LDH Al environment, and is likely the cause of the asymmetry seen (Figure 3.30). Intercalated phosphate produces a resonance at ≈ 8.5 ppm,[47] which is not observed. This suggests that the phosphate does not displace the carbonate ion by ion exchange as theorised by Zhao *et al.* due to its higher charge,[51] in agreement with the basal spacing observed (≈ 2.3 nm), which is similar to those observed for pure carbonate phases, far lower than that reported for phosphate phases (2.8 nm).[52] This is likely due to the major species in solution being HPO_4^{2-}, which has a lower ion affinity than CO_3^{2-}.[38,53]

^{13}C CP-MAS NMR (Figure 3.32) shows one major resonance, with a shoulder at 170 ppm, which can be de-convoluted into three resonances at 170, 168 and 165 ppm. Ishihara *et al.* assigned two resonances in MgAl hydrotalcite at 170 and 167 ppm to CO_3^{2-} and HCO_3^- or a differently coordinated CO_3^{2-} respectively.[54] HCO_3^- resonances typically occur at 161 ppm ($NaHCO_3$)[55], but chemisorbed CO_2 on MgAl LDO show resonances at 167 and 165 ppm for monodentate and bidentate bound carbonate which match well with the shifts observed here.[56] There are two unexpected peaks at 22.6 and 63.3 ppm which match with the CH_3 and CH carbons of isopropyl alcohol ($CH_3CH(OH)CH_3$) suggesting contamination of the sample or the rotors used.

The thermal decomposition of the material is shown in Figure 3.33. There are three stages of decomposition, with weight losses of 17.2, 17.5 and 6.3 % of the starting mass each. Up to 230 °C, there is a steady weight loss from physisorbed water before a sharp peak in the derivative thermal trace above 150 °C from loss

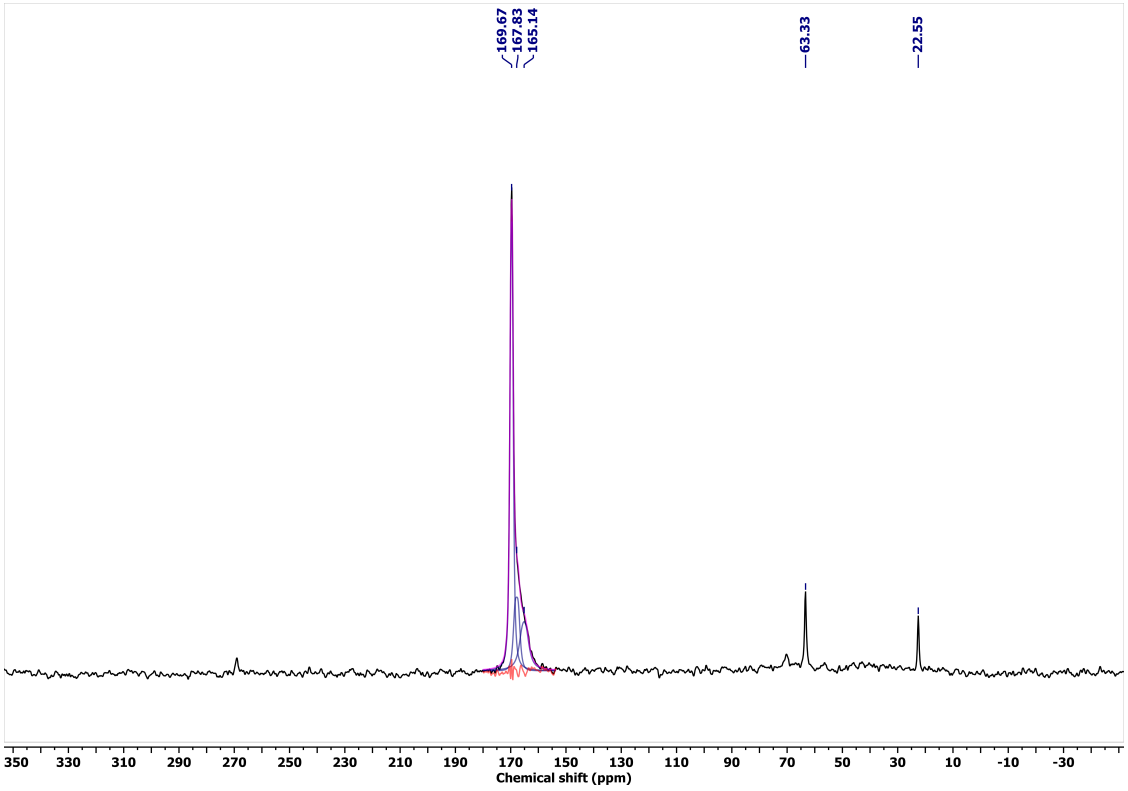

Figure 3.32: ^{13}C CP-MAS NMR of SLDH at 10 kHz

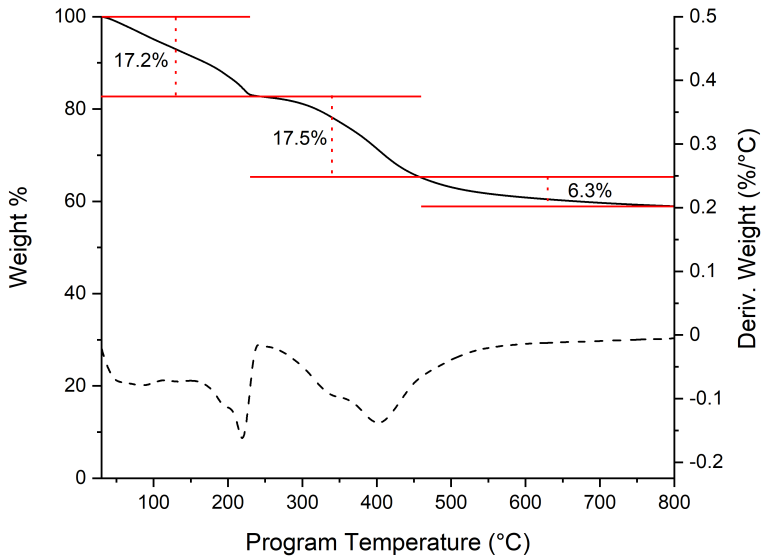

Figure 3.33: TGA analysis of SLDH produced on a 25 g scale. The derivative trace is shown below (dotted line) and calculated mass changes between 30 to 230 °C, 230 to 460 °C and 460 to 800 °C are included.

of the interlayer water.[57] The second thermal event is due to decomposition of the LDH structure with dehydroxylation and decarboxylation releasing further H_2O and CO_2. The two peaks observed in the derivative thermal analysis have been assigned in the literature to the decomposition of the different metal hydroxide sites: Mg_2Al-OH (350 °C) and Mg_3-OH (400 °C).[57–60] Mass loss above this region is attributed to further decarboxylation as the structure changes to a solid solution of MgO and Al_2O_3.[57,58]

To further investigate the thermal evolution of the material, variable temperature powder XRD experiments were conducted. Figure A.22 shows XRD patterns at 50 °C increments, with representative patterns from the different stages of thermal evolution shown in Figure 3.34. There is no observable change in the pattern below 150 °C, after which the reflections from the layered structure become weaker, with only the basal and (110) reflections remaining. Figure A.23 shows the variation of the d spacing of the (003) Bragg reflection with temperature. Below 100 °C, typical thermal expansion is observed before the basal spacing collapses from 0.777 to 0.657 nm between 150 to 275 °C. This change of 1.2 nm corresponds to the loss of interlayer water molecules with previous studies on synthetic hydrotalcite showing this change occurring between two distinct phases with non-overlapping reflections.[57,58] By 400 °C, the LDH reflections are no longer observable and reflections corresponding to a periclase-type (MgO) phase appear, growing stronger as the temperature increases further up to 900 °C. Various phases have been reported for the high temperature decomposition products of LDHs; typically, a mixture of oxides such as spinel ($MgAl_2O_4$), aluminium oxide (Al_2O_3), magnesium oxide (MgO) or an amorphous solid solution.[57,58,62] Although Al can be included in the periclase (MgO) structure,[63] it is considered more likely that the bulk of the aluminium is within an amorphous phase. Reaction of Al and phosphate species at high temperatures have been shown form amorphous species and this may prevent the formation of crystalline Al phases at elevated temperatures.[64] Shimamura *et al.* reported a study on the thermal decomposition of PO_4 intercalated LDHs with similar phase changes seen.[65] They also observed a gradual shift

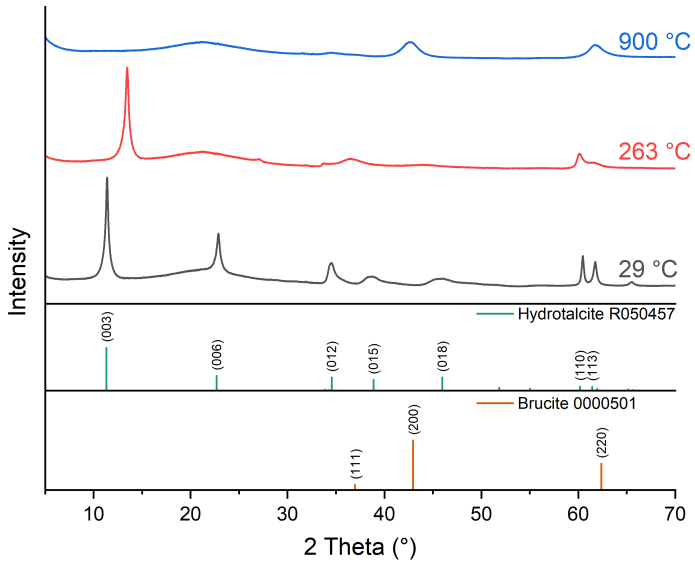

Figure 3.34: Variable temperature powder XRD patterns of $Mg_2Fe_{0.5}Al_{0.5}$ SLDH. Pattern measured at λ =0.825 276 Å and converted to the equivalent pattern at λ_{α_1} = 1.540 57 Å for ease of comparison. Peaks can be indexed to the patterns below (RRUFF Project R050457 - Hydrotalcite, and AMCSD 0000501 - Periclase).[12,61]

in basal spacing and describe the intermediate dehydrated LDH phase as slowly transitioning between polytypes ($3R1$ to $1H$), which would result in the Bragg reflections observed (263 °C) indexed to (001) (13.4°), (002) (27°), (100) (33.7°), (101) (36.5°) and (110) (60.1°). They also suggest there is evidence for phosphate ions bonding between the layers; however, the basal spacing observed (0.85 nm) is much larger than seen for the SLDHs discussed here, providing further evidence the phosphate is not intercalated.

3.3.4 Solid content

The initial reaction had a solid content (recovered product divided by reaction volume), yielding approximately 10 g L^{-1} or 100 L kg^{-1} SLDH. For this method to be utilised on a large scale, it is desirable to increase the solid content by reducing the reaction volume. The amount of reagents used were kept the same, but the volume of D.I. water used was reduced two and four times (to 5 and 2.5 mL from 10 mL). The XRD patterns of the SLDHs produced are shown in Figure 3.35. There

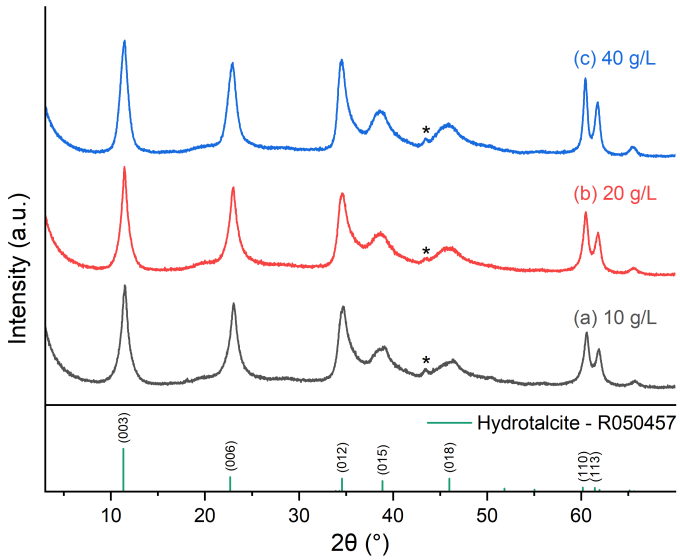

Figure 3.35: XRD patterns of SLDHs made from A-$MgHPO_4$ from reactions with different solid contents. Denoted by approximate yield of SLDH per reaction volume. * indicates a reflection due to the sample holder. Peaks can be indexed to the patterns below (RRUFF Project R050457 - Hydrotalcite and R050455 Brucite).[12]

Table 3.10: Variation of lattice parameters (a, c) of the SLDHs derived from A-$MgHPO_4$ from reactions with different solid contents extracted from Figure 3.35.

Solid content ($g\,L^{-1}$)	d_{110} (nm)	a (nm)	CDL_a (nm)	d_{003} (nm)	c (nm)	CDL_c (nm)
10	0.153	0.306	15.651	0.771	2.313	6.343
20	0.153	0.306	17.636	0.772	2.317	6.590
40	0.153	0.306	23.673	0.776	2.328	6.206

is little variation in the patterns as the solid content is increased and, importantly, no new impurity peaks present, showing the solid content can be increased without varying the composition of the products. The crystallinity of the products in the a direction increases with the solid content (Table 3.10), likely due to the increased pH.[66] Reducing the volume by two times again (eight times from the initial reaction) failed to produce an LDH product, as the slurry became too viscous for mixing to occur.

The N_2 adsorption/desorption isotherms are presented in Figure 3.36 and show there is little variation in the BET SSA with the concentration of the reaction.

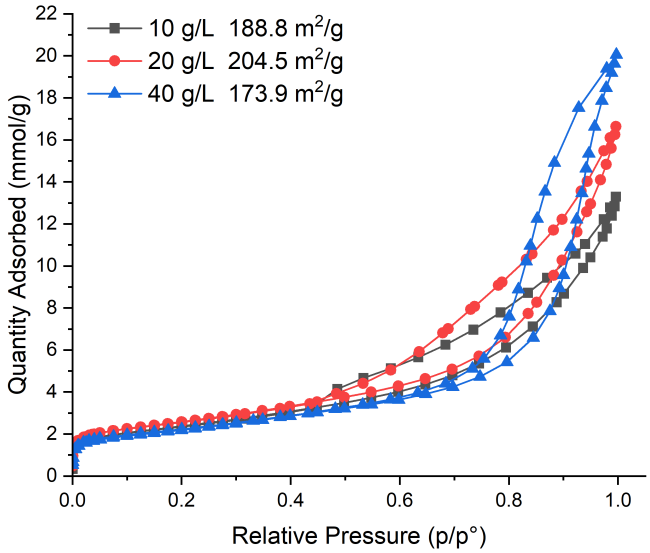

Figure 3.36: N_2 adsorption/desorption isotherms of SLDHs made from A-$MgHPO_4$ from reactions with different solid contents. SSA of samples calculated via the BET method are given in the legend.

Deviations are observed above $p/p^0 = 0.7$ suggesting changes to the pore size distribution. Figure A.24 shows the calculated pore size distribution with all samples possessing a large amount of micropores (12 Å) and a range of mesopores from 20 to 400 Å. A shift in the mesopore distribution to larger pore sizes causes the hysteresis loops to close at high pressures, with a corresponding increase in the total pore volume observed (0.46 to 0.7 $cm^3\,g^{-1}$).

3.3.5 Alternative Al sources

In order to make the process greener and improve the atom economy, other sources of Al (e.g. gibbsite ($Al(OH)_3$) and sodium aluminate ($NaAlO_2$)) were considered. $Al(NO_3)_3$ is made by the reaction of $Al(OH)_3$ with HNO_3:

$$Al(OH)_3 + 3\,HNO_3 \longrightarrow Al(NO_3)_3 + 3\,H_2O$$

As the nitrate anion is not included in the LDH product, it can be considered an unnecessary spectator which should be avoided where possible.

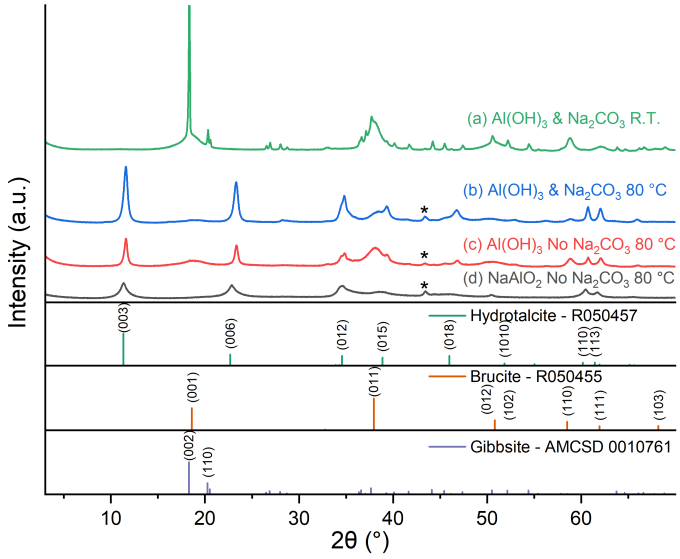

Figure 3.37: Powder XRD patterns of SLDH made from gibbsite with or without Na_2CO_3 at RT ($\approx 20\,°C$) or 80 °C. * indicates a reflection due to the sample holder. Peaks can be indexed to the patterns below (RRUFF Project R050457 - Hydrotalcite, R050455 Brucite and AMCSD 0000501 - Gibbsite).[12,61]

Table 3.11: Variation of lattice parameters (a, c) of the SLDHs made from $Al(OH)_3$ and $NaAlO_2$, extracted from Figure 3.37.

Reagents	d_{110} (nm)	a (nm)	CDL_a (nm)	d_{003} (nm)	c (nm)	CDL_c (nm)
$Al(OH)_3$ & Na_2CO_3 80 °C	0.153	0.305	31.435	0.765	2.294	12.009
$Al(OH)_3$ No Na_2CO_3 80 °C	0.153	0.305	20.985	0.763	2.290	14.982
$NaAlO_2$ No Na_2CO_3 80 °C	0.153	0.306	13.269	0.779	2.336	5.921

Use of an analogous procedure to that discussed previously (Chapter 3.3.1, Chapter 3.4.12), with gibbsite replacing aluminium nitrate, produced an LDH phase at 80 °C but not at RT (Figure 3.37 a and b), likely due to the low solubility of gibbsite at RT ($K_{sp} = 10^{-33.8}$ at 25 °C).[67] The presence of significant amounts of $Mg(OH)_2$ is attributed to the reaction of A-$MgHPO_4$ under alkaline conditions with a low Al concentration. This is caused by the slower dissolution kinetics of $Al(OH)_3$ compared to $Al(NO_3)_3 \cdot 9\,H_2O$. At RT, the presence of the LDH phase was not detected. The observed sharp reflections, corresponding to unreacted gibbsite, suggest that the dissolution kinetics are inadequate in the absence of heating.

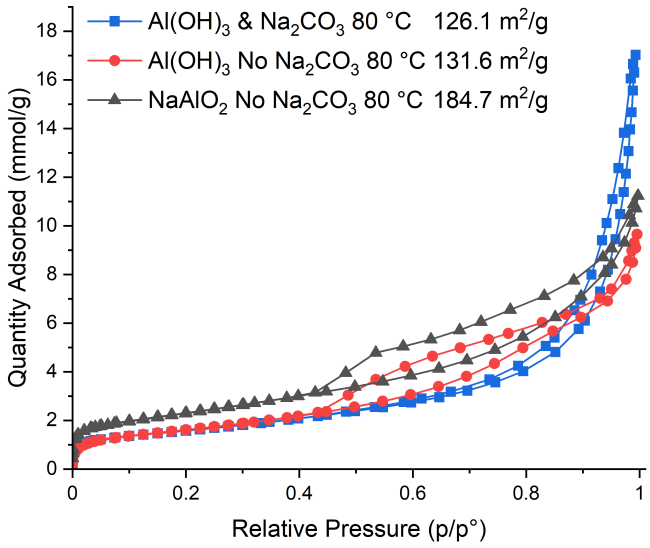

Figure 3.38: N_2 adsorption/desorption isotherms of SLDH made from gibbsite or sodium aluminate with or without Na_2CO_3 at 80 °C. SSA of samples calculated via the BET method are given in the legend.

In pursuit of further enhancing the atom efficiency, the reaction was conducted omitting the addition of Na_2CO_3, which still resulted in the formation of an LDH phase at 80 °C. The crystallinity in the *a* axis is reduced, indicating that the lower concentration of carbonate anions retards the growth rate of the LDH layers (Table 3.11), and there is also an increase in the amount of brucite impurity formed.

The N_2 adsorption/desorption isotherms of the two LDH containing products are shown in Figure 3.38. Both samples show lower SSAs than the SLDH made using aluminium nitrate (126.1 and 131.6 $m^2\,g^{-1}$ vs 167.2 $m^2\,g^{-1}$, Figure 3.20), likely due to the significant brucite impurities, but still comparable, indicating that changing the Al source does not significantly affect the SSA of the SLDH produced. The hysteresis loops for the two SLDHs also differ in shape, due to a change in the mesopore distribution (Figure A.25); the sample prepared without Na_2CO_3 possesses mesopores with a larger average size (maximum $\frac{dV}{dW}$ at 86.3 Å vs 63.4 Å), but a smaller total volume (0.59 $cm^3\,g^{-1}$ vs 0.33 $cm^3\,g^{-1}$).

To investigate if a more soluble Al source would prevent brucite formation, sodium

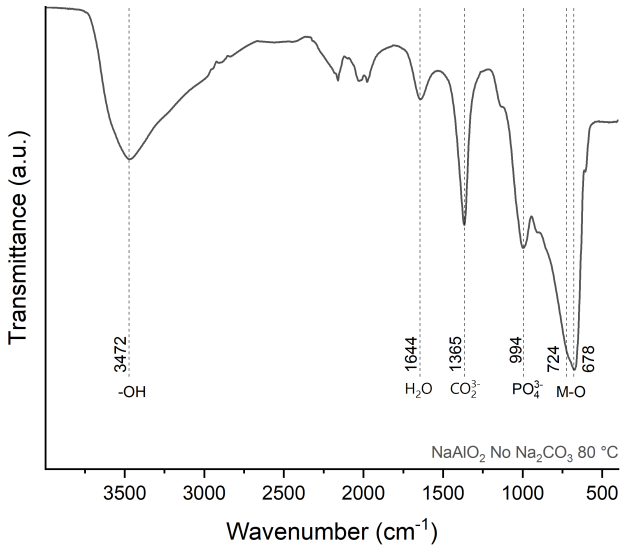

Figure 3.39: FTIR spectra of SLDH made from $NaAlO_2$.

aluminate (described as $NaAlO_2$ (anhydrous) or $NaAl(OH)_4$ (hydrated)) was used (Chapter 3.4.13, Figure A.26); this is used industrially as a soluble equivalent to $Al(OH)_3$. Sodium aluminate is formed by dissolving gibbsite in 25% aqueous NaOH solution near the boiling point and precipitates upon cooling. The use of sodium aluminate as the aluminium source effectively yielded LDH devoid of brucite impurities, as intended; however, it also displays reduced crystallinity (Figure 3.37 d, Table 3.11). The exclusive use of sodium aluminate, in the absence of additional base, was ineffective in generating LDH materials, which is attributed to insufficient alkalinity of the solution.

The FTIR spectra of the SLDH product formed using $NaAlO_2$ is shown in Figure 3.39 and shows similar absorption bands to the previously discussed materials (Figure 3.5), with a mixture of both phosphate and carbonate ions present. Notably, even without the addition of Na_2CO_3 there is still a strong absorption band from $CO_3{}^{2-}$, suggesting reaction with dissolved atmospheric CO_2 and a strong preference over the $PO_4{}^{3-}$ anion.

The N_2 isotherm (Figure 3.38) shows that the material has a similar hysteresis loop

to that made with $Al(OH)_3$ (due to their similar mesopore distributions A.25), but with a higher surface area ($184.7\,m^2\,g^{-1}$), due to an higher volume of micropores (11.8 Å) .

3.3.6 Effect of reaction time

To better understand the transformation of A-$MgHPO_4$ into SLDH and to investigate if the reaction time could be reduced, different reaction times (0.66, 1, 1.5, 2, 2.5, 3, 4, 5, 6.5, 16, 24, 48 and 72 h) were studied to see their effect on the SLDH produced. An analogous procedure to that previously developed was used (Chapter 3.3.1, Chapter 3.4.14), varying the reaction time and without the addition of Na_2CO_3. The formation of the LDH phase was found to be rapid and poorly crystalline SLDH was observed after the shortest reaction time tested (40 min, Figure A.27). The crystallinity was seen to vary over the course of the reaction time, reaching a maximum at 16 h (with the true maximum likely between 6.5 and 16 h) before decreasing again (the extracted CDLs are shown in Figure 3.40, Table A.1). A decrease in crystallite size indicates that the SLDHs are not stable to dissolution and further crystallites may be formed by secondary nucleation, decreasing the average size.[68] After 24 h, there is a noticeable shoulder on the (006) Bragg reflection attributed to the (001) reflection of brucite, which increases in intensity in the 48 and 72 h samples, indicating that some of the dissolved Mg from the SLDH re-precipitates as brucite.

The N_2 isotherms are shown in Figure A.28 with the changes in SSA with the reaction time also shown in Figure 3.40. All the isotherms are of IUPAC Type II shape with H3 hysteresis loops, as seen previously (Figure 3.20), which increase in size with the reaction time, indicating an increase in porosity. The surface area rises linearly from $26.6\,m^2\,g^{-1}$ (1.5 h) to $68.7\,m^2\,g^{-1}$ at 16 h where peak crystallite size was measured. Interestingly, the surface area then rapidly increases as the crystallite size decreases, up to 146.4 and $225.2\,m^2\,g^{-1}$ after 24 and 48 h, respectively. Smaller particles have a higher intrinsic surface area, but the increase in surface area is also accompanied by a large increase in pore volume (0.22 to

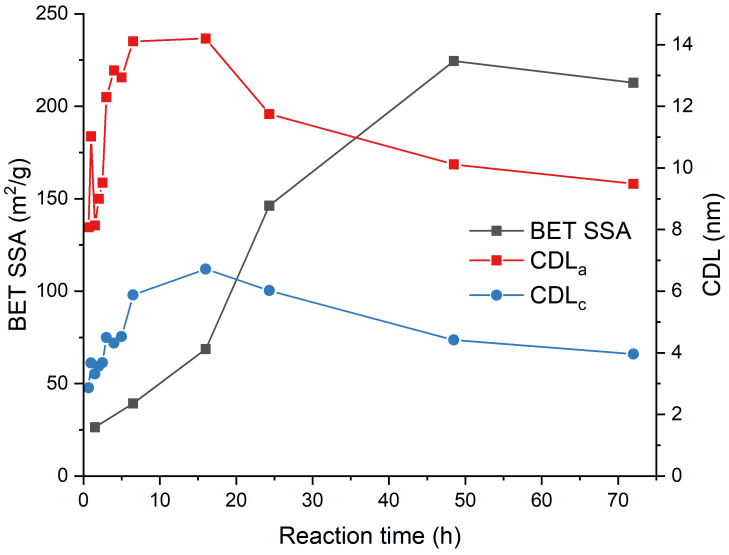

Figure 3.40: Variation of crystallite domain lengths and BET SSA for SLDHs vs the reaction time. See Table A.1 and Figure A.28

0.45 $cm^3\,g^{-1}$, Figure A.29) from the formation of both micropores and additional mesopores in the range of 20 to 150 Å, likely formed upon the LDH dissolution. At higher reaction time, there is a decrease in the surface area attributed to the increasing impurity fraction. This behaviour differs from that reported by Panda *et al.* who showed the crystallite size of conventionally synthesised MgAl CO_3 LDHs increased linearly with time, as expected for the diffusion limited Ostwald ripening process, and may be due to the presence of PO_4^{3-}.[69]

The FTIR spectra for the different SLDH are shown in Figure A.30. The initial spectra for SLDH made using 1 and 6.5 h reaction times display similar absorption bands to those discussed previously (Figure 3.18), with absorption bands seen for $-OH$ (3448 cm^{-1}), H_2O (1644 cm^{-1}), CO_3^{2-} (1365 cm^{-1}), PO_4^{3-} (1029 cm^{-1}) and M−O (600 to 900 cm^{-1}), but also a weak absorption at1134 cm^{-1}) which is attributed to a vibration of HPO_4^{2-} or $P_2O_7^{4-}$ in unreacted A-$MgHPO_4$.[70,71] This additional absorption decreases with time and is not significant in the samples made using a reaction time of $\geq$ 16 h, indicating complete conversion. After a longer reaction time ($\geq$ 16 h), the CO_3^{2-} absorption (1365 m^{-1}) starts to decrease

whilst the phosphate concentration increases ($992\,\mathrm{cm}^{-1}$, normalised to the M–O absorption). This indicates an anion exchange mechanism is occurring, which, given the preference of LDH for carbonate over phosphate as observed in the initial precipitation, is unlikely to be occurring within the LDH, especially since phosphate uptake is reported to saturate in LDHs after $< 5\,\mathrm{h}$.[72] As noted previously from the SS-NMR results (Figure 3.30), there is an unknown tetrahedral Al environment present within the products and the phosphate is likely bonded to an amorphous Al phase (Figure 3.31). Glemza, Parent and Welsh reported the synthesis of high surface area (250 to $350\,\mathrm{m}^2\,\mathrm{g}^{-1}$) amorphous aluminium phosphate gels ($AlPO_4$) under similar reaction conditions:

$$Al(NO_3)_3 \cdot 9\,H_2O + NH_4H_2PO_4 \longrightarrow AlPO_4 + NH_3 + 3\,HNO_3 + 9\,H_2O$$

which display a mixture of O_h (minor) and T_d (major) Al environments.[73] Sequestration of dissolved Al may explain why brucite is formed at extended reaction times. Given that brucite is only a minor phase observed by XRD at extended ageing times, suggesting only minor dissolution of the SLDH product, and that the T_d environment observed by SS-NMR is relatively small, the high surface area observed is still attributed to the LDH phase.

3.4 Experimental details

3.4.1 Reagents and chemicals

Struvite ($MgNH_4PO_4 \cdot 6\,H_2O$) was purchased from Alfa Aesar. Aluminium nitrate ($Al(NO_3)_3 \cdot 9\,H_2O$), sodium hydroxide (NaOH) and sodium carbonate (Na_2CO_3) were purchased from Sigma Aldrich. 1 M NaOH was made by dissolving 40 g of NaOH in 1 L of deionised (D.I.) water.

Struvite derived LDH products are denoted as SLDH.

3.4.2 Effect of temperature on SLDH

2.7609 g (11.25 mmol) of struvite was suspended in 20 mL of 1 M NaOH at the desired temperature (65, 75 and 85 °C) under N_2 flow connected to a HCl bubbler and stirred at 500 RPM for 1 h. 1.5899 g (15 mmol) Na_2CO_3 was added to the suspension and stirred for 5 min. A solution of 1.4067 g (3.75 mmol) $Al(NO_3)_3 \cdot 9\,H_2O$ in 20 mL of D.I. water was then added dropwise (2 mL/min) and the pH of the solution kept at 11.5 via addition of additional 1 M NaOH. The mixture was allowed to age for 2 h before being filtered and washed with D.I. water until the filtrate was at pH 7. The solid residue was then dried overnight at 30 °C under vacuum.

3.4.3 Effect of temperature on intermediate phase

2.7609 g (11.25 mmol) of struvite was suspended in 20 mL of 1 M NaOH at the desired temperature (65 and 85 °C) under N_2 flow connected to a HCl bubbler and stirred at 500 RPM for 1 h. The suspension was filtered and washed with D.I. water until the filtrate was at pH 7. The solid residue was then dried overnight at 30 °C under vacuum.

3.4.4 Effect of NaOH during activation on SLDH

2.7609 g (11.25 mmol) of struvite was suspended in 10 mL of 1 M NaOH at 65 °C under N_2 flow connected to a HCl bubbler and stirred at 500 RPM for 1 h or 1.5 h. 1.5899 g (15 mmol) Na_2CO_3 was added to the suspension and stirred for 5 min. A solution of 1.4067 g (3.75 mmol) $Al(NO_3)_3 \cdot 9\,H_2O$ in 20 mL of D.I. water was then added dropwise (2 mL/min) and the pH of the solution kept at 11.5 via addition of additional 1 M NaOH. The mixture was allowed to age for 2 h before being filtered and washed with D.I. water until the filtrate was at pH 7. The solid residue was then dried overnight at 30 °C under vacuum.

3.4.5 Effect of NaOH during activation (intermediate)

2.7609 g (11.25 mmol) of struvite was suspended in 10 mL of 1 M NaOH at 65 °C under N_2 flow connected to a HCl bubbler and stirred at 500 RPM for 1 h or 1.5 h.

The suspension was filtered and washed with D.I. water until the filtrate was at pH 7. The solid residue was then dried overnight at 30 °C under vacuum.

3.4.6 Effect of heating ramp rate on SLDH

2.7609 g (11.25 mmol) of struvite was suspended in 10 mL of 1 M NaOH at room temperature under N_2 flow connected to a HCl bubbler and stirred at 500 RPM before being heated to 65 °C after which it was left to continue stirring for 1 h or 1.5 h. 1.5899 g (15 mmol) Na_2CO_3 was added to the suspension and stirred for 5 min. A solution of 1.4067 g (3.75 mmol) $Al(NO_3)_3 \cdot 9\,H_2O$ in 20 mL of D.I. water was then added dropwise (2 mL/min) and the pH of the solution kept at 11.5 via addition of additional 1 M NaOH. The mixture was allowed to age for 2 h before being filtered and washed with D.I. water until the filtrate was at pH 7. The solid residue was then dried overnight at 30 °C under vacuum. For the SLDH made from ground struvite, the powder was ground in a pestle and mortar for 5 min before use.

3.4.7 Effect of heating ramp rate on intermediate phase

2.7609 g (11.25 mmol) of struvite was suspended in 10 mL of 1 M NaOH at room temperature under N_2 flow connected to a HCl bubbler and stirred at 500 RPM before being heated to 65 °C after which it was left under stirring for 1 h or 1.5 h. The suspension was filtered and washed with D.I. water until the filtrate was at pH 7. The solid residue was then dried overnight at 30 °C under vacuum. For the sample made with ground struvite, the struvite powder was ground in an alumina pestle and mortar for 10 min prior to use.

3.4.8 Struvite calcination

The initial amorphous $MgHPO_4$ (A-$MgHPO_4$) sample was prepared under the degassing conditions described above (Chapter 2.1.1). Similar samples were prepared in the laboratory by placing 10 g of struvite in either a crucible (muffle furnace) or alumina boat (tube furnace under N_2 or vacuum) and heating to 110 °C at

10 K/min. Samples were heated for 16 h before being cooled and collected. For further scale up, 10 to 60 g struvite were loaded into a tube with sintered inserts and placed within a vertical furnace. The powder was fluidised under a high flow of N_2 and heated to 200 °C at 10 K/min and held for 2 h before being cooled and collected.

3.4.9 Synthesis of SLDH from A-$MgHPO_4$

0.2 g (1.66 mmol) A-$MgHPO_4$, 0.2079 g (0.55 mmol) $Al(NO_3)_3 \cdot 9\,H_2O$ and 0.2646 g (2.5 mmol) Na_2CO_3 were added to 10 mL 1 M NaOH and stirred at room temperature (RT, ≈ 20 °C) or 80 °C for 20 h at 1000 RPM. The mixture was then filtered and washed with D.I. water until the filtrate was at pH 7. The solid residue was then dried overnight at 30 °C under vacuum.

3.4.10 Scale up of SLDH synthesis from A-$MgHPO_4$

The 0.1 g scale reaction is as described in Chapter 3.4.9. For the 5 and 50 times scale (0.5 and 5 g), the synthesis method was the same but the amounts of reagents used were: 0.758 g (5.74 mmol A-$MgHPO_4 \cdot 0.32\,H_2O$, 0.717 g (1.91 mmol) $Al(NO_3)_3 \cdot 9\,H_2O$ and 1.52 g (50 mmol) Na_2CO_3 in 50 mL 1 M NaOH or 6.904 g (57.4 mmol A-$MgHPO_4$, 7.173 g (19.1 mmol) $Al(NO_3)_3 \cdot 9\,H_2O$ and 15.2 g (500 mmol) Na_2CO_3 in 500 mL 1 M NaOH.

For the 250 times scale, 25.2588 g (210 mmol) A-$MgHPO_4$, 26.2591 g (70 mmol) $Al(NO_3)_3 \cdot 9\,H_2O$, 3.7097 g (35 mmol) Na_2CO_3 and 70 g (1750 mmol) NaOH were added to 1.75 L D.I. water in a 5 L Chemglass jacketed reactor, equipped with an impeller and baffles, heated to 80 °C. The suspension was stirred vigorously for 20 h at 440 RPM. The reactor was then emptied and the mixture filtered under vacuum and washed with D.I. water until the filtrate was at pH 7. The solid residue was then dried overnight at 30 °C under vacuum.

3.4.11 Effect of solid content on SLDH synthesis from A-$MgHPO_4$

0.1443 g (1.2 mmol) A-$MgHPO_4$, 0.1501 g (0.4 mmol) $Al(NO_3)_3 \cdot 9\,H_2O$ and 0.4 g (2.5 mmol) NaOH were added to x mL D.I. water ($x = 10, 5, 2.5, 1.25, 1$) and stirred at 80 °C for 20 h at 750 RPM. The mixture was then filtered and washed with D.I. water until the filtrate was at pH 7. The solid residue was then dried overnight at 30 °C under vacuum.

3.4.12 Alternative Al sources for SLDH - $Al(OH)_3$

0.1804 g (1.2 mmol) A-$MgHPO_4$, 0.0390 g (0.5 mmol) $Al(OH)_3$ and 0.2120 g (2 mmol) Na_2CO_3 were added to 10 mL 1 M NaOH and stirred at room temperature (RT, ≈ 20 °C) or 80 °C for 20 h at 1000 RPM. The mixture was then filtered and washed with D.I. water until the filtrate was at pH 7. The solid residue was then dried overnight at 30 °C under vacuum.

3.4.13 Alternative Al sources for SLDH - $NaAlO_2$

0.2886 g (2.4 mmol) A-$MgHPO_4$, 0.0624 g (0.8 mmol) $NaAlO_2$ and 0.2120 g (2 mmol) Na_2CO_3 were added to 10 mL 1 M NaOH and stirred at 80 °C for 20 h at 1000 RPM. The mixture was then filtered and washed with D.I. water until the filtrate was at pH 7. The solid residue was then dried overnight at 30 °C under vacuum.

3.4.14 Effect of reaction time on SLDH

0.2886 g (2.4 mmol) A-$MgHPO_4$ and 0.3002 g (0.8 mmol) $Al(NO_3)_3 \cdot 9\,H_2O$ were combined together under alkaline conditions (20 mL 1 Molar NaOH) and heated at 80 °C under stirring for the different reaction times chosen. The mixture was then filtered and washed with D.I. water until the filtrate was at pH 7. The solid residue was then dried overnight at 30 °C under vacuum.

3.5 Conclusions and future work

The previously reported synthesis method to produce LDH materials from the waste mineral struvite has been shown to be highly sensitive to the reaction conditions used. During the activation step, a multitude of phases can be observed depending on the amount of base used, including a scarcely mentioned ammonium analogue of hazenite. There are numerous struvite-type materials containing different metals (Fe, Co, Ni, Zn, Mn)[31]; further work could be conducted to investigate if this is a general pathway to produce other materials with a mixture of NH_4^+ and Na^+ cations. Optimisation of the SLDH synthesis prevented the formation of impurities, but the surface area of the products was low compared to that previously reported ($\approx 20\,m^2\,g^{-1}$ vs $184\,m^2\,g^{-1}$).

A new synthesis pathway was developed using the amorphous $MgHPO_4$ product formed on struvite thermal degradation. After reaction with $Al(NO_3)_3 \cdot 9\,H_2O$ and Na_2CO_3 under alkaline conditions, pure LDH phases were produced with surface areas $> 200\,m^2\,g^{-1}$. The particles were observed to maintain the morphology of the struvite precursor by SEM imaging, as in the previously reported method. The synthesis was shown to be scalable up to 25 g and the reaction volume could be decreased without the formation of impurities or changes to the material produced.

It was shown the atom economy could be improved by using $NaAlO_2$ as the aluminium source; without the addition of a CO_3^{2-} source, CO_2 is sequestered from the atmosphere and preferentially intercalated over the PO_4^{3-} present in the reaction mixture. Further work should assess PO_4^{3-} recovery from the supernatant. Replacement of NaOH with KOH may allow for the recovery of potassium phosphates (KH_2PO_4 and K_2HPO_4) for use as fertilisers.[74,75] The formation pathway is complex with a period of LDH crystal growth followed by dissolution, where the surface area increases significantly. Further optimisation of the reaction temperature may lead to shorter reaction times, as high surface areas were only observed when the reaction time was ≥ 1 d.

References

(1) M. V. Bukhtiyarova, *J. Solid State Chem.*, 2019, **269**, 494–506.

(2) Z. P. Xu and G. Q. Lu, *Chem. Mater.*, 2005, **17**, 1055–1062.

(3) J. Nobre, H. Ahmed, M. Bravo, L. Evangelista and J. de Brito, *Materials*, 2020, **13**, 4752.

(4) S. A. Hosseini, A. Niaei, D. Salari, S. A. Hosseini, A. Niaei and D. Salari, *Open J. Phys. Chem.*, 2011, **01**, 23–27.

(5) G. L. Ulex, *Memoirs Proc. Chem. Soc.*, 1845, **3**, 106.

(6) X. Cen, H. Duan, Z. Hu, X. Huang, J. Li, Z. Yuan and M. Zheng, *Water Res.*, 2023, **247**, 120788.

(7) J. H. Kim, B. m. An, D. H. Lim and J. Y. Park, *Water Res.*, 2018, **132**, 200–210.

(8) M. I. H. Bhuiyan, D. S. Mavinic and R. D. Beckie, *Environ. Technol.*, 2007, **28**, 1015–1026.

(9) R. Cabassi, D. Delmonte and J. Prywer, *CrystEngComm*, 2024, **26**, 5826–5829.

(10) S. Shaddel, S. Ucar, J.-P. Andreassen and S. W. Østerhus, *J. Environ. Chem. Eng.*, 2019, **7**, 102918.

(11) L. Bianchi, K. Kirwan, L. Alibardi, M. Pidou and S. Coles, *J. Therm. Anal. Calorim.*, 2019, **142**, 1–12.

(12) *Highlights in Mineralogical Crystallography*, ed. T. Armbruster and R. M. Danisi, DE GRUYTER, 2015.

(13) C. K. Chauhan and M. J. Joshi, *J. Cryst. Growth*, 2013, **362**, 330–337.

(14) C. K. Chauhan and M. J. Joshi, *J. Cryst. Growth*, 2014, **401**, 221–226.

(15) S. F. Valle, A. S. Giroto, V. Dombinov, A. A. Robles-Aguilar, N. D. Jablonowski and C. Ribeiro, *Sci. Rep.*, 2022, **12**, 14176.

(16) R. Mahajan and R. Prakash, *Mater. Chem. Phys.*, 2020, **246**, 122826.

(17) R. L. Frost, M. L. Weier and K. L. Erickson, *J. Therm. Anal. Calorim.*, 2004, **76**, 1025–1033.

(18) J. Hövelmann, T. M. Stawski, R. Besselink, H. M. Freeman, K. M. Dietmann, S. Mayanna, B. R. Pauw and L. G. Benning, *Nanoscale*, 2019, **11**, 6939–6951.

(19) M. Mathew, P. Kingsbury, S. Takagi and W. E. Brown, *Acta Crystallogr. Sect. B Struct. Crystallogr. Cryst. Chem.*, 1982, **38**, 40–44.

(20) W. L. J. Kwok, Ph.D. Thesis, University of Oxford, 2020.

(21) W. L. J. Kwok, H. Suo, C. Chen, D. W. J. Leung, J.-C. Buffet and D. O'Hare, *Green Chem.*, 2021, **23**, 1616–1620.

(22) F. Cavani, F. Trifirò and A. Vaccari, *Catal. Today*, 1991, **11**, 173–301.

(23) R. L. Frost, A. W. Musumeci, M. O. Adebajo and W. Martens, *J. Therm. Anal. Calorim.*, 2007, **89**, 95–99.

(24) M. Shabanian, M. Hajibeygi and A. Raeisi, in *Layered Double Hydroxide Polymer Nanocomposites*, Elsevier, 2020, pp. 77–101.

(25) M. Qu, M. Yuan, S. Liu, J. He, M. Xue, X. Liu, S. Li and J. He, *J. Mater. Sci.*, 2018, **53**, 396–408.

(26) C. Chen, R. Felton, J.-C. Buffet and D. O'Hare, *Chem. Commun.*, 2015, **51**, 3462–3465.

(27) M. Thommes, K. Kaneko, A. V. Neimark, J. P. Olivier, F. Rodriguez-Reinoso, J. Rouquerol and K. S. Sing, *Pure Appl. Chem.*, 2015, **87**, 1051–1069.

(28) S. Farhana, MA thesis, University of British Columbia, Vancouver, 2015.

(29) A. P. Bayuseno and W. W. Schmahl, *Environ. Technol.*, 2020, **41**, 3591–3597.

(30) H. Yang, H. J. Sun and R. T. Downs, *Am. Mineral.*, 2011, **96**, 675–681.

(31) H. Yang, L. Martinelli, F. Tasso, A. R. Sprocati, F. Pinzari, Z. Liu, R. T. Downs and H. J. Sun, 2014, **99**, 1761–1766.

(32) E. Company, M. Farrés, J. Colprim and A. Magrí, *Sci. Total. Environ.*, 2022, **847**, 157574.

(33) B. Tansel, G. Lunn and O. Monje, *Chemosphere*, 2018, **194**, 504–514.

(34) M. Pettauer, A. Baldermann, S. Eder and M. Dietzel, *Cryst. Growth & Des.*, 2024, **24**, 3085–3092.

(35) A. K. Sarkar, *J. Mater. Sci.*, 1991, **26**, 2514–2518.

(36) G. S. Thomas, M. Rajamathi and P. V. Kamath, *Clays Clay Miner.*, 2004, **52**, 693–699.

(37) A. N. Ay, B. Zümreoglu-Karan, A. Temel and L. Mafra, *Appl. Clay Sci.*, 2011, **51**, 308–316.

(38) M. Everaert, K. Slenders, K. Dox, S. Smolders, D. De Vos and E. Smolders, *J. Colloid Interface Sci.*, 2018, **520**, 25–32.

(39) M. Mańko, R. Chal, P. Trens, D. Minoux, C. Gérardin and W. Makowski, *Microporous Mesoporous Mater.*, 2013, **170**, 243–250.

(40) L. Konermann, *J. Am. Soc. Mass Spectrom.*, 2017, **28**, 1827–1835.

(41) C. F. Holder and R. E. Schaak, *ACS Nano*, 2019, **13**, 7359–7365.

(42) A. Di Bitetto, E. André, C. Carteret, P. Durand and G. Kervern, *J. Phys. Chem. C*, 2017, **121**, 7276–7281.

(43) L. Jin, X. Zhou, F. Wang, X. Ning, Y. Wen, B. Song, C. Yang, D. Wu, X. Ke and L. Peng, *Nat. Commun.*, 2022, **13**, 6093.

(44) C. Chen, J.-C. Buffet and D. O'Hare, *Dalton Trans.*, 2020, **49**, 8498–8503.

(45) M. P. Bernardo, F. K. V. Moreira, L. A. Colnago and C. Ribeiro, *Colloids Surf. A: Physicochem. Eng. Asp.*, 2016, **497**, 53–62.

(46) T. Isobe, T. Watanabe, J. B. d'Espinose de la Caillerie, A. P. Legrand and D. Massiot, *J. Colloid Interface Sci.*, 2003, **261**, 320–324.

(47) L. Lundehøj, J. Cellier, C. Forano and U. G. Nielsen, *J. Phys. Chem. C*, 2019, **123**, 24039–24050.

(48) C. Liu, M. Zhang, G. Pan, L. Lundehøj, U. G. Nielsen, Y. Shi and H. C. B. Hansen, *Appl. Clay Sci.*, 2019, **177**, 82–90.

(49) S. S. C. Pushparaj, C. Forano, V. Prevot, A. S. Lipton, G. J. Rees, J. V. Hanna and U. G. Nielsen, *J. Phys. Chem. C*, 2015, **119**, 27695–27707.

(50) L. B. Staal, S. S. Charan Pushparaj, C. Forano, V. Prevot, D. B. Ravnsbæk, M. Bjerring and U. G. Nielsen, *J. Mater. Chem. A*, 2017, **5**, 21795–21806.

(51) X.-J. Zhao, Y.-Q. Zhu, S.-M. Xu, H.-M. Liu, P. Yin, Y.-L. Feng and H. Yan, *Phys. Chem. Chem. Phys.*, 2020, **22**, 19758–19768.

(52) M. Badreddine, A. Legrouri, A. Barroug, A. De Roy and J. P. Besse, *Mater. Lett.*, 1999, **38**, 391–395.

(53) M. Everaert, K. Dox, J. A. Steele, D. De Vos and E. Smolders, *J. Colloid Interface Sci.*, 2019, **537**, 151–162.

(54) S. Ishihara, P. Sahoo, K. Deguchi, S. Ohki, M. Tansho, T. Shimizu, J. Labuta, J. P. Hill, K. Ariga, K. Watanabe, Y. Yamauchi, S. Suehara and N. Iyi, *J. Am. Chem. Soc.*, 2013, **135**, 18040–18043.

(55) H. E. Gottlieb, V. Kotlyar and A. Nudelman, *J. Org. Chem.*, 1997, **62**, 7512–7515.

(56) A. Lund, G. V. Manohara, A.-Y. Song, K. M. Jablonka, C. P. Ireland, L. A. Cheah, B. Smit, S. Garcia and J. A. Reimer, *Chem. Mater.*, 2022, **34**, 3893–3901.

(57) W. Yang, Y. Kim, P. K. T. Liu, M. Sahimi and T. T. Tsotsis, *Chem. Eng. Sci.*, 2002, **57**, 2945–2953.

(58) K. Matsuda, N. Iio, M. Kawashimo, A. Okuda, R. Fukuzaki, N. Tarutani, K. Katagiri and K. Inumaru, *Inorg. Chem.*, 2023, **62**, 17276–17287.

(59) G. Yu, Y. Zhou, R. Yang, M. Wang, L. Shen, Y. Li, N. Xue, X. Guo, W. Ding and L. Peng, *J. Phys. Chem. C*, 2015, **119**, 12325–12334.

(60) P. Kenyon, S. Roberts, Z. R. Turner, N. H. Rees and D. O'Hare, *J. Phys. Chem. C*, 2024, **128**, 12249–12258.

(61) R. Downs and M. Hall-Wallace, *Am. Mineral.*, 2003, **88**, 247–250.

(62) T. Moroz, L. Razvorotneva, T. Grigorieva, M. Mazurov, D. Arkhipenko and V. Prugov, *Appl. Clay Sci.*, 2001, **18**, 29–36.

(63) J. A. Van Orman, C. Li and K. L. Crispin, *Phys. Earth Planet. Interiors*, 2009, **172**, 34–42.

(64) D. Hahn, A. Masoudi Alavi, V. Hopp and P. Quirmbach, *J. Am. Ceram. Soc.*, 2021, **104**, 6625–6642.

(65) A. Shimamura, E. Kanezaki, M. I. Jones and J. B. Metson, *J. Solid State Chem.*, 2012, **186**, 116–123.

(66) A. Seron and F. Delorme, *J. Phys. Chem. Solids*, 2008, **69**, 1088–1090.

(67) C. R. Frink and M. Peech, *Soil Sci. Soc. Am. J.*, 1962, **26**, 346–347.

(68) E. Bernard, W. J. Zucha, B. Lothenbach and U. Mäder, *Cem. Concr. Res.*, 2022, **152**, 106674.

(69) H. S. Panda, R. Srivastava and D. Bahadur, *Bull. Mater. Sci.*, 2011, **34**, 1599–1604.

(70) M. V. Ramlogan and A. A. Rouff, *J. Therm. Anal. Calorim.*, 2016, **123**, 145–152.

(71) T. L. K. Dao, K. A. Tieu and B. H. Tran, *Phys. Chem. Chem. Phys.*, 2022, **24**, 20282–20293.

(72) J. Das, B. S. Patra, N. Baliarsingh and K. M. Parida, *Appl. Clay Sci.*, 2006, **32**, 252–260.

(73) R. Glemza, Y. O. Parent and W. A. Welsh, *Catal. Today*, 1992, **14**, 175–188.

(74) H.-W. Olfs, L. O. Torres-Dorante, R. Eckelt and H. Kosslick, *Appl. Clay Sci.*, 2009, **43**, 459–464.

(75) D. E. Hogg and M. R. J. Toxopeus, *New Zeal. J. Agric. Res.*, 1970, **13**, 887–895.

4

CO_2 capture using SLDHs

Contents

4.1 Introduction

As discussed in Chapter 1.2.1, the rapid rise in the CO_2 concentration in the atmosphere due to anthropogenic emissions has led to the ongoing climate crisis. Negative emission technologies are needed to meet international goals set out to

deal with this problem. The types of technology ready to be employed at scale are: enhancement of natural sequestration processes (reforestation and enhanced rock weathering); bioenergy carbon capture and storage; and direct air capture (DAC) and storage. DAC and storage is not limited by the land requirements of the other two types and can be built where it is most convenient, but does carry a higher energy and cost requirement. To overcome these limitations, cheap and long lasting sorbents with a low process energy are needed. The criteria for lowering the process energy are fast sorption/desorption kinetics, low energy of regeneration and a high capture capacity.

As discussed in Chapter 1.2.4, much of the work developing these adsorbents has been done with mesoporous silicas as the support material. Layered double hydroxides (LDHs) have the same abundance of surface hydroxyl groups as silica and, with a relatively low cost (\$1 to 25 kg^{-1}), offer a cheaper alternative support material which can be modified in the same way. As such, LDH-derived LDOs have been used to produce Class 1 sorbents by supporting polyethyleneimine (PEI) with high adsorption capacities of 2.27 $mmol\,g^{-1}$ and enhanced thermal stability up to 300 °C, due to a strong amine-support interaction.[1]

They have also been used to produce Class 2 materials via a silane grafting reaction. This was first shown by Park *et al.* by grafting (3-aminopropyl)triethoxysilane (MONO) onto dodecylsulfate intercalated ZnCr LDH.[2] Wang *et al.* then used a similar method, utilising dodecylsulfate intercalation of MgAl LDH to enable the exfoliation of the sheets which were grafted with 3-aminopropyl-triethoxysilane (MONO), *N*-2-aminoethyl-3-aminopropyl-trimethoxysilane (DI) and N1-(3-Trimethoxysilylpropyl)diethylenetriamine (TRI), and tested for the capture of pure CO_2 with a capacity of around 1 $mmol\,g^{-1}$.[3] Changing the number of amine groups per silane (MONO = 1, DI = 2, TRI = 3) leads to an increase in the amine loading ($mmol_N\,g^{-1}$) of the material, yielding higher CO_2 capacities. However, there is not a linear relationship between the increased amine loading and the CO_2 capacity as the longer chains can cause pore blocking, leading to issues with diffusion

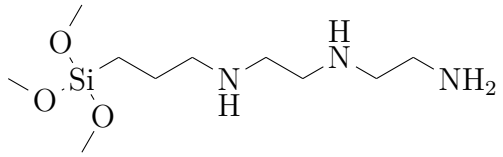

Figure 4.1: Structure of N^1-(3-Trimethoxysilylpropyl)diethylenetriamine (TRI).

and the accessibility of active sites.[4] The CO_2 capacity of the modified LDH at room temperature was not directly related to the amine loading with 2.39, 5.14 and 6.01 $mmol_N\,g^{-1}$, providing CO_2 capacities of 1, 1.1 and 0.74 $mmol_{CO_2}\,g^{-1}$ (for MONO, DI, and TRI, respectively, under pure CO_2 at 25 °C).[3] This trend differed from that reported for silica modified materials.[5] More recent work by Zhu *et al.* investigated MgAl LDH exfoliated using the aqueous miscible organic solvent treatment (AMOST) and grafted with 3-[2-(2-aminoethylamino)ethylamino]propyl-trimethoxysilane (TRI) for DAC applications. The LDH synthesis used a low Mg:Al ratio of 0.5 : 1 leading to Al impurities, but showed an similar capacity of 1.05 $mmol\,g^{-1}$ even under low CO_2 concentrations in simulated air.[6]

Industrially produced LDHs typically have low specific surface areas (SSA) limiting the amount of amine which can be dispersed on the surface. In all of the Class 2 LDH materials reported, an exfoliation technique has been employed to increase the surface area, allowing a greater amount of amine to be loaded for an enhanced adsorption capacity. SLDHs derived from struvite offer an alternative route to high surface area LDH materials as shown in Chapter 3.3, avoiding the costly AMOST process and, as such, their use as support materials for solid supported amine DAC sorbents is investigated in this chapter. The effect of the grafting conditions is explored as well as the effect of different organo-amine functionalities.

4.2 Silane grafted SLDHs

Initially, N^1-(3-Trimethoxysilylpropyl)diethylenetriamine (TRI) was chosen as the amino silane for grafting, as it is commonly used in the literature. Typically, 0.2 g of SLDH was dried under vacuum at 100 °C and then suspended in 20 mL toluene before 0.6 mL TRI was added dropwise and left to stir for 15 min under a N_2

headspace before being heated to 85 °C and stirred for 16 h (see Chapter 4.3.2). The reaction involves the condensation of the silanol groups, typically methoxy or ethoxy, with the surface hydroxyl groups of the LDH:

$$\mathrm{M{-}OH} + \mathrm{Si}(R\mathrm{O})_3R' \longrightarrow \mathrm{M{-}O{-}Si}(\mathrm{O}R)_2R' + R\mathrm{OH}$$

(one condensation reaction)

$$\longrightarrow (\mathrm{M{-}O{-}})_2\mathrm{Si}(\mathrm{O}R)R' + 2\,R\mathrm{OH} \longrightarrow (\mathrm{M{-}O{-}})_3\mathrm{Si}R' + 3\,R\mathrm{OH}$$

(multiple condensation reactions)

Any H_2O present in the reaction mixture will hydrolyse the silanol which can lead to self-condensation/polymerisation and the formation of more complex oligomer grafted groups:

$$\mathrm{H_2O} + \mathrm{Si}(R\mathrm{O})_3R' \longrightarrow \mathrm{Si}(\mathrm{O}R)_2(\mathrm{OH})R' + R\mathrm{OH}$$

$$\mathrm{Si}(\mathrm{O}R)_2(\mathrm{OH})R' + \mathrm{Si}(R\mathrm{O})_3R' \longrightarrow R'(R\mathrm{O})_2\mathrm{Si{-}Si}(\mathrm{O}R)_2R'$$

Deliberate addition of H_2O has been utilised as a synthetic strategy to increase the amount of amine groups in a sorbent via formation of a multilayer of silica.[7,8]

FTIR spectra of the pristine and TRI grated SLDH are shown in Figure 4.2. The grafted SLDH shows the characteristic LDH absorptions (discussed in Chapter 3.2.1): 668 to 739 cm^{-1} (M−O stretching modes), 1365 cm^{-1} ($CO_3{}^{2-}$ antisymmetric stretch), 1644 cm^{-1} (interlayer H_2O bending), 3468 cm^{-1} (−OH); and also shows new sharp absorption bands from the grafted amino silane molecules: 1117 cm^{-1} (C−N stretching vibration), 1471 cm^{-1} ($-CH_2-$ bending modes), 1571 cm^{-1} (−NH bending mode) and 2933 cm^{-1} ($-CH_2-$ stretching vibration).[9] A broad −NH wagging vibration at 650 to 900 cm^{-1} overlaps with the M-O adsorption bands and the sharpening of the peak at 1024 cm^{-1} is attributed to the new Si−O−M adsorption band (M = Si, Mg, Al).[6]

^{29}Si SS-NMR of the grafted LDH is shown in Figure 4.3. There are three main environments corresponding to the T_1, T_2 and T_3 sites (−51.5, −60.8 and −69.4 ppm)

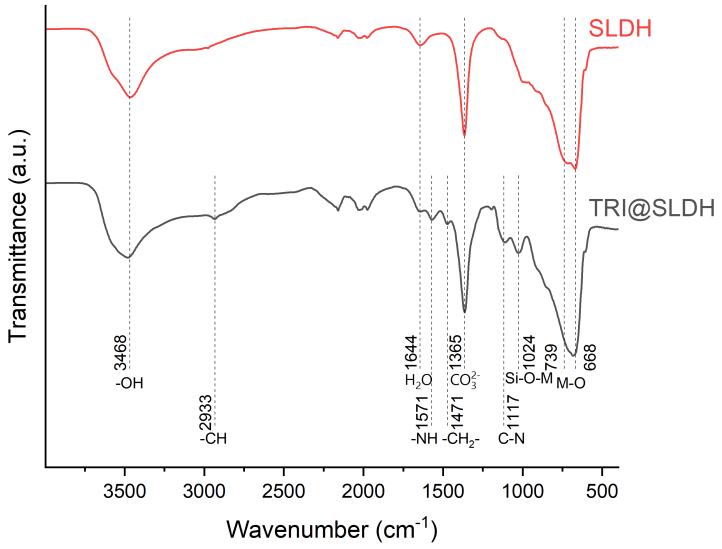

Figure 4.2: FTIR spectra of TRI-modified SLDH.

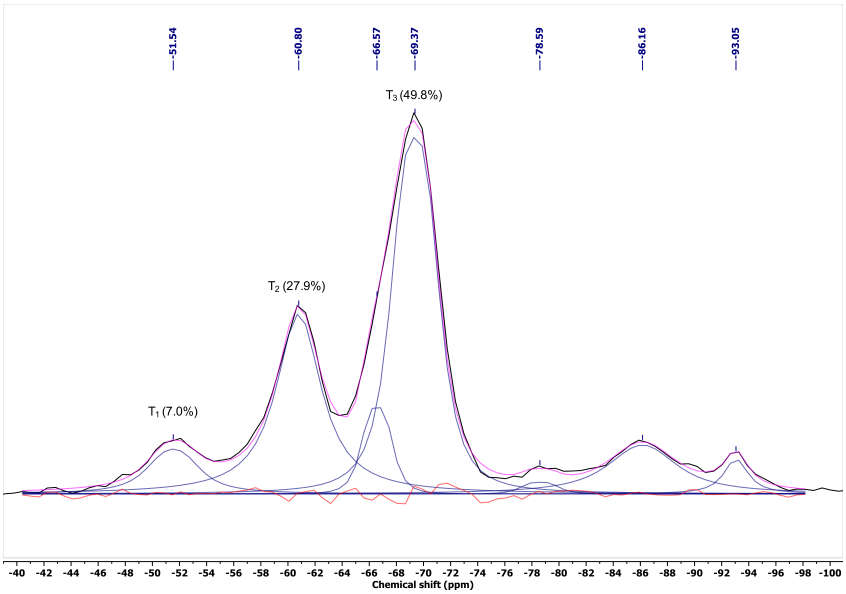

Figure 4.3: ^{29}Si CP-MAS NMR spectrum of TRI-modified SLDH measured at 10 kHz.

where T_x features x oxane bonds from the Si atom to the LDH surface or to other Si via hydrolysis and self-condensation and $3 - x$ silanol or silyl ether groups. The relative amounts of the different Si environments increases $T_3 > T_2 > T_1$ (7.1:4:1) indicating a preference for multiple condensation reactions on each Si. There are no T_0 signals (−45 ppm), indicating removal of any free unreacted silylamine. Peak fitting is improved by the inclusion of a peak (66.6 ppm) forming a shoulder to the T_3 peak (69.4 ppm), indicating a small amount of a distinct T_3 environment.[10] The T_1 and T_2 resonances are also broad, likely due to overlapping signals from environments with differing amounts of hydrolysis (differing silyl ether and silanol groups). There are also some small resonances at lower ppm (−76 to −96 ppm) which are not seen in literature spectra of similar materials. ^{29}Si resonances in this region are frequently observed for Q_{0-2} sites, specifically silicon with four Si−O bonds, Q_0 −71 to −81 ppm, Q_1 −83 to −89 ppm, and Q_2 −91 to −96 ppm. These should not be present, as the Si−C bond in the precursor is expected to be stable, and a Q_3 peak at −101 ppm is anticipated. Additionally, silsesquioxanes, which are cages formed by the hydrolysis of siloxanes, may also contribute. These silsesquioxanes are products of the self-condensation of aminosilane molecules. However, research by the group of Kaneko on related aminosilanes, namely 3-aminopropyl triethoxysilane (MONO, Figure 4.27(a)) and *N*-2-aminoethyl-3-aminopropyl trimethoxysilane (DI, Figure 4.27(b)), demonstrates ^{29}Si signals from −66.3 to −71.0 ppm, suggesting that this is not the origin of the unexpected signals but could explain the second T_3 environment.[11,12] Further discussion of these unusual resonances is in Chapter 4.2.2.

The TGA trace of the TRI-modified SLDH is shown in Figure 4.4. The overall decomposition of the modified SLDH is similar to that of the unmodified SLDH, but the derivative curve shows subtle changes to the thermal events. There is a change in the profile of weight loss below 150 °C, with a clear peak weight loss at 70 °C compared to the steady weight loss seen in the unmodified SLDH. In LDHs, this weight loss is due to the loss of physisorbed water;[13] in the amine-modified SLDH, this is accompanied by the loss of carbon dioxide and water bonded to the amine

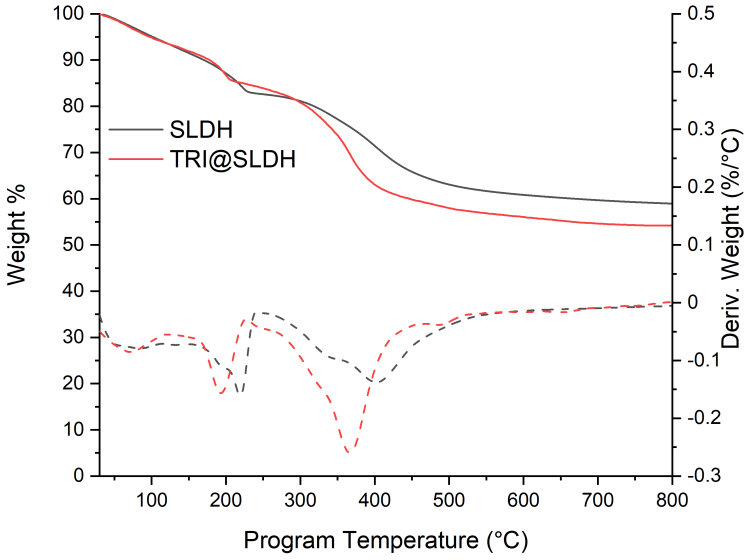

Figure 4.4: TGA thermal curve of SLDH and TRI-modified SLDH. The derivative trace is shown below (dotted line). TGA curves for TRI@SLDH shifted to lower temperature due to a reduced sample mass used for analysis.

Table 4.1: Weight changes for different thermal events measured by TGA (Figure 4.4).

Sample	Weight change (%) in temperature range (°C)					
	0 to 150	150 to 225	225 to 300	300 to 375	375 to 450	450 to 800
SLDH	8.49	7.86	2.53	6.51	8.79	6.87
TRI@SLDH	8.08	7.00	4.14	13.41	7.54	5.63

groups introduced (Figure B.2 shows the TGA-MS of TRI@SLDH up to 120 °C).[14] The next thermal event occurs between 150 to 230 °C; this is attributed to interlayer water loss in the unmodified SLDH. A shoulder seen in the unmodified SLDH at 195 °C, attributed to a distinct water environment, is no longer present in the amine-modified SLDH and the weight loss is decreased (7.0 and 7.9 % for TRI@SLDH and SLDH, respectively), indicating that this species of water is consumed during the grafting process.[15] There is an additional weight loss event at 250 °C in the TRI-modified SLDH (4.1 % vs 2.5 %), attributed to self-catalysed hydrolysis of surface bound silane, as seen for MONO-modified boehmite,[16] or desorption of physisorbed polycondensed silane.[17] In MONO substituted boehmite, there are

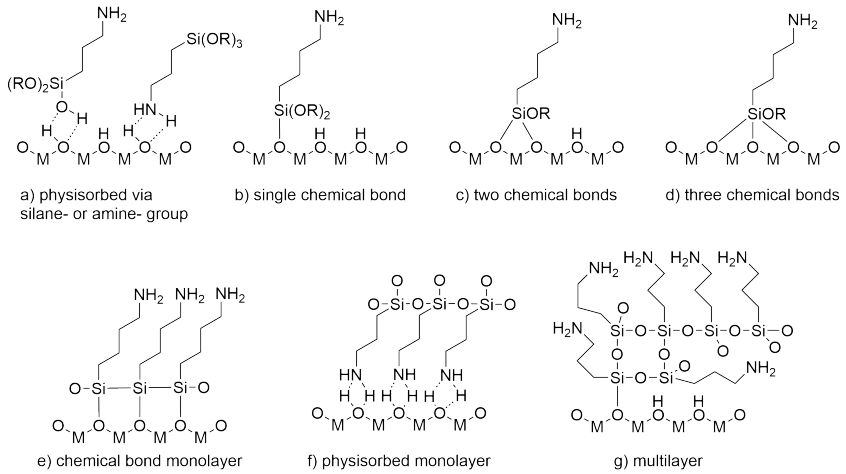

Figure 4.5: Possible binding modes of amino silanes on a hydroxylated surface as described by Zarinwall *et al.*[16] M = Mg, Al, R = H, Alkyl.

two events related to self-catalysed hydrolysis: monodentate bound amino silane at 85 °C (Figure 4.5 type b) and bidentate bound amino silane at 245 °C (Figure 4.5 type c) and, as such, some of the mass loss < 100 °C may be from loss of this monodentate amino silane. For the two thermal events between 250 to 500 °C attributed to dehydroxylation of Mg_2Al-OH (350 °C) and Mg_3-OH (400 °C) in the SLDH,[13,15,18,19] there is a new overlapping mass loss at 350 °C arising from the pyrolysis of the functional alkyl chains of the amino silane remaining, described as a chemical bond monolayer containing a mixture of surface bound (Mg, Al−O−Si) and self-condensed silanol (Si−O−Si) bonds between the silanes in MONO-modified boehmite (Figure 4.5 type e).[16,20,21] Further mass loss is due to decarboxylation as the structure changes to a solid solution of MgO and Al_2O_3[13,15] and dehydroxylation to form SiO_2 for the TRI-modified material.[16,20] After normalising by the mass loss due to physisorbed species below 150 °C, the total change in mass loss can be used to approximate the amount of silane grafted:

$$\Delta m_{TRI@SLDH} = (1 - x) * \Delta m_{SLDH} + x * \Delta m_{TRI}$$

Where $\Delta m_{TRI@SLDH}$ is the mass change in the grafted material, x is the mass fraction of the TRI in the grafted system, Δm_{SLDH} is the mass change in the ungrafted SLDH and Δm_{TRI} is the mass change of theoretical purely grafted TRI.

This equation can be rearranged for x:

$$x = \frac{\Delta m_{TRI@SLDH} - \Delta m_{SLDH}}{\Delta m_{TRI} - \Delta m_{SLDH}}$$

The change in residual weight ($\Delta m_{TRI@SLDH} - \Delta m_{SLDH}$) at 800 °C is 5.46 %, Δm_{SLDH} = 64.42 % and $\Delta m_{TRI} = \frac{MW_R}{MW_{Si-R}}$ = 83.70 %. Assuming the weight loss is due to Si−C bond cleavage, the silane forms three bonds with the surface and the loss of protons is negligible (MW_{Si-R} is the molecular weight of the organic moiety and silicon = 172.32 g mol^{-1}, MW_R is the molecular weight of the organic moiety= 144.24 g mol^{-1}). This gives $x = 0.28$ and the loading of TRI as $C_{TRI} = \frac{x}{MW_{Si-R}} = 1.64\,\mathrm{mmol_{TRI}\,g^{-1}}$. This silane loading is higher than that measured by CHN (Table 4.2, 0.328 $\mathrm{mmol_{Si}\,g^{-1}}$), suggesting an underestimate of Δm_{TRI} and implying additional components are lost such as unreacted alkoxy groups or loss of the entire TRI group, including the Si functional group.

N_2 adsorption and desorption isotherms are shown in Figure 4.6. There is a significant decrease in the surface area (256.8 to 158 $\mathrm{m^2\,g^{-1}}$) with the associated decrease in pore volume (0.74 to 0.44 $\mathrm{cm^3\,g^{-1}}$) seen in Figure 4.7. This shows the grafting process coats the pores of the SLDH with a similar profile of pore distribution to that seen in the parent material, but with smaller pore widths (the first maxima > 20 Å shifts from 34 to 27 Å. The pores of 15 Å observed in the parent material are not present in the TRI grafted material, indicating that these pores are filled by TRI molecules which have a similar size of ≈ 12.4 Å, preventing diffusion of N_2 into them.[22]

The CO_2 adsorption isotherm collected at 25 °C is presented in Figure 4.8. The DAC CO_2 capacity is defined as the amount of CO_2 taken up at 0.4 mbar (approximately the current partial pressure of CO_2 in the atmosphere). The DAC CO_2 capacity of the TRI-modified SLDH is 0.25 $\mathrm{mmol_{CO_2}\,g^{-1}}$. The adsorption isotherms of the pure SLDH and TRI-modified commercial SBA-15 are used as references. The DAC CO_2 capacities of these two materials are 0.29 and 0.32 $\mathrm{mmol_{CO_2}\,g^{-1}}$ respectively (Table 4.2). The higher CO_2 capacity of the modified SBA-15 is to be

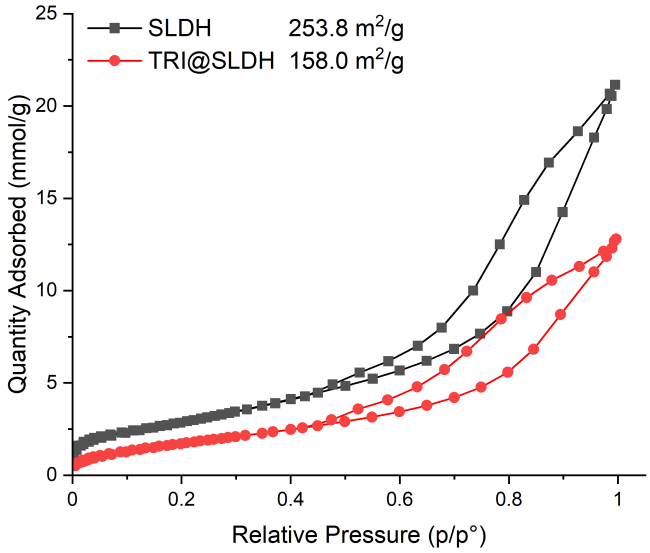

Figure 4.6: N_2 adsorption/desorption isotherm of TRI-modified SLDH. SSA of samples calculated via the BET method are given in the legend.

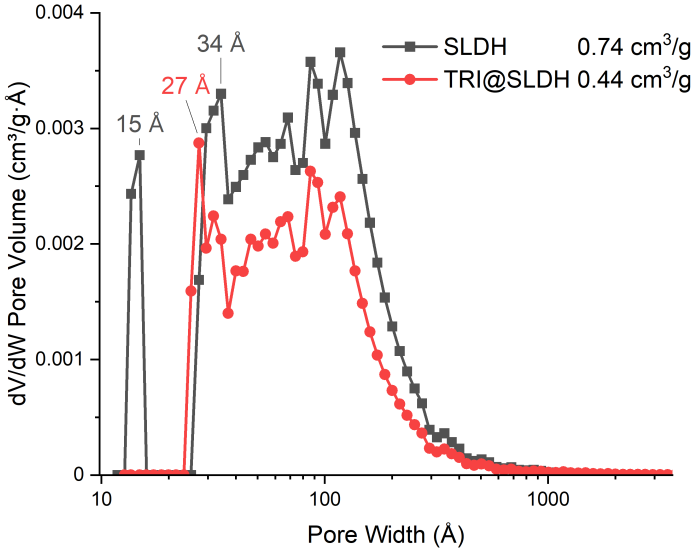

Figure 4.7: Pore size distribution calculated using a density functional theory model (slit) on N_2 adsorption isotherms of TRI-modified SLDH (Figure 4.6). The pore volumes at $p/p^0 = 1$ of the samples are given in the legend.

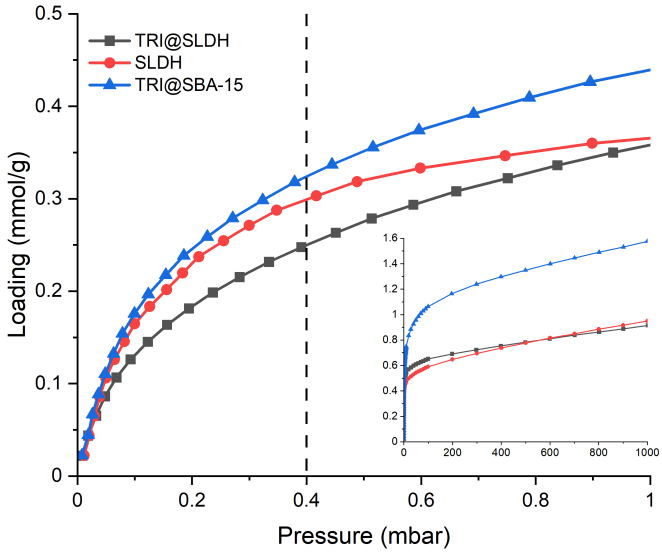

Figure 4.8: CO_2 adsorption isotherms for SLDH, amine-modified SLDH and amine-modified SBA-15. The low pressure region is shown in the main graph and the full isotherm is shown in the insert.

expected as it possess a higher surface area allowing for more amino silane to be grafted (1.099 $mmol_{TRI}\,g^{-1}$ vs 0.328 $mmol_{TRI}\,g^{-1}$ for TRI@SBA-15 and TRI@SLDH respectively). The DAC of the TRI grafted SBA-15 capacity is similar to those reported in the literature (0.33 $mmol_{CO_2}\,g^{-1}$ by Wadi *et al.* and 0.2 $mmol_{CO_2}\,g^{-1}$ by Wang *et al.*, providing validation for the experimental measurement setup.[4,23] Despite possessing a lower surface area (254 $m^2\,g^{-1}$) than the SBA-15 (571 $m^2\,g^{-1}$, Figure B.1) the SLDH performs comparably with 78% of the DAC CO_2 capacity. Surprisingly, the modified SLDH is also outperformed by the unmodified SLDH which has no clear chemisorption sites that are typically needed for uptake at low pressures and which is widely accepted as having no CO_2 capacity.[24] The SLDH displays a similar sharp uptake under low pressures of CO_2 to the amine-modified materials, suggesting it does also adsorb via a chemisorption mechanism.

Pristine LDHs have not been as extensively studied for CO_2 adsorption as their mixed metal oxide derivatives and no reports of their performance under DAC conditions were found in the literature. A brief summary of the investigations into LDH CO_2 interactions is given here. A comparative study by Radha and Navrotsky

on the energetics of CO_2 adsorption on both MgAl LDH and LDOs showed LDHs could adsorb up to $0.62\,\mathrm{mmol_{CO_2}\,g^{-1}}$ (at 25 °C, ≈ 0.6 bar) via chemisorption with high initial enthalpies ($-92\,\mathrm{kJ\,mol^{-1}}$), forming both monodentate and bidentate carbonate species with uptake onto Mg–O sites and within the basic interlayer region.[25] Ishihara *et al.* also showed low surface area MgAl LDH ($12.3\,\mathrm{m^2\,g^{-1}}$) can still adsorb up to ≈ $0.179\,\mathrm{mmol_{CO_2}\,g^{-1}}$ (25 °C, 0.5 bar), attributed to reaction with basic Mg–OH sites and with a significant proportion of the uptake occurring within the interlayer space.[26] Sharma, Tyagi and Jasra investigated the influence of the synthetic parameters of MgAl LDHs on the CO_2 adsorption capacity with a maximum of ≈ $0.89\,\mathrm{mmol_{CO_2}\,g^{-1}}$ at 1 bar (at 30 °C) for their optimised sample.[27] The CO_2 uptake was shown to correlate with the Al content, surface area and crystallinity, with both physisorption and chemisorption processes occurring. Shang *et al.* investigated high surface area MgAl LDHs ($455\,\mathrm{m^2\,g^{-1}}$ via the AMOST method) which adsorbed ≈ $0.75\,\mathrm{mmol_{CO_2}\,g^{-1}}$ under 1 bar CO_2 (at 50 °C) comparable with the capacity observed here.[28] In summary, LDHs can uptake CO_2 via chemisorption onto basic Mg–O sites as well as via physisorption, with a significant amount of the capacity attributed to the interlayer region. Comparison of the SLDH and TRI@SLDH isotherms shows two intersections of the curves at ≈ 1 mbar and 0.6 bar which indicates the SLDH possesses fewer chemisorption sites, but possesses a higher affinity for CO_2 and also a higher physisorption capacity (linked to the higher SSA, Figure 4.6).

Table 4.2 shows the measured N in the sample, the calculated amine and silane loadings and the amine efficiency at 0.4 mbar:

$$\text{amine efficiency} = \frac{\text{CO}_2\text{ capacity}}{\text{moles of amine}}$$

CHN analysis confirms the SLDH is free of nitrogen so all nitrogen present in the grafted samples was attributed to grafted silane. Although the amine density of the TRI@SBA-15 is higher than that of the TRI@SLDH, the capacity is not proportionally larger, giving it an amine efficiency of 0.098 which is comparable to values commonly seen in the literature (0.12).[4] Comparatively, the TRI@SLDH

Table 4.2: N weight percentage, amine and silane density, DAC CO_2 capacity and amine efficiency for SLDH grafted with TRI under standard and anhydrous conditions.

Sample	N (av. wt%)	N ($mmol\,g^{-1}$)	Silane loading ($mmol\,g^{-1}$)	CO_2 capacity ($mmol\,g^{-1}$)	Amine efficiency
SLDH	0	0	0	0.299	
TRI@SLDH	1.38	0.985	0.328	0.250	0.254
TRI@SBA-15	4.62	3.298	1.099	0.324	0.098

has a much higher amine efficiency of 0.254, suggesting a synergy with the SLDH; the intrinsic CO_2 capacity of the SLDH may still contribute to the overall capacity measured whilst not requiring any amines or the LDH surface may help to stabilise the carbamate species formed.

These isotherms are all Type I and were fitted using commonly used linear models. These models were developed to describe different adsorption phenomena and, as such, a good fit to the experimental data can help elucidate the mechanisms involved. The models and their equations are listed in Table 4.3 and their derivation is discussed in Chapter 2.1.2.

Table 4.3: Linear isotherm models and equations. C_e is the concentration of adsorbate at equilibrium (partial pressure), q_e and q_m are the equilibrium and maximum concentrations of the adsorbate on the surface. R^2 values for the fitting to the SLDH and TRI@SLDH isotherm data are also given.

Model	Equation	R^2 SLDH	R^2 TRI@SLDH
Langmuir	$\frac{C_e}{q_e} = \frac{1}{q_m K_e} + \frac{C_e}{q_m}$	0.979	0.994
Freundlich	$\log(q_e) = \log(K_F) + \frac{1}{n}\log(C_e)$	0.966	0.788
Temkin	$q_e = \frac{Rt}{b}\ln(K_T) + \frac{RT}{b}\ln(C_e)$	0.895	0.977
Elovich	$\ln(\frac{q_e}{C_e}) = \ln(K_e q_m) - \frac{q_e}{q_m}$	0.872	0.936

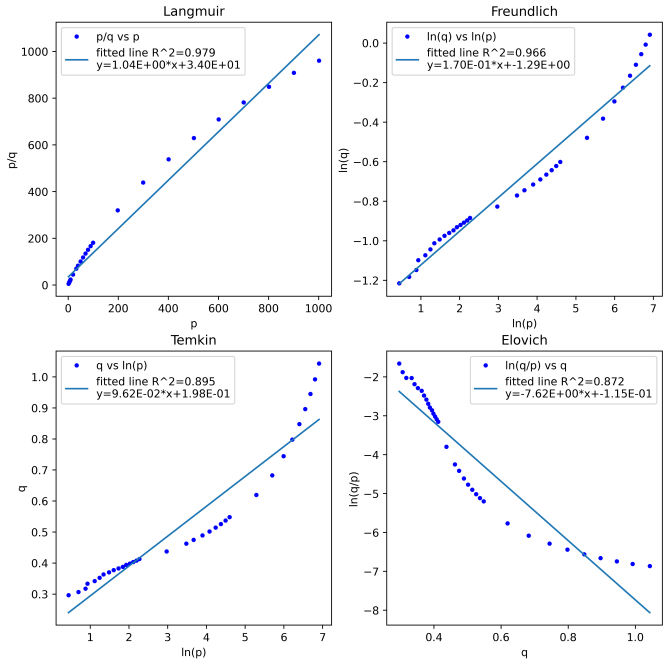

Figure 4.9: CO_2 adsorption isotherm data for unmodified SLDH transformed to fit common linear equations.

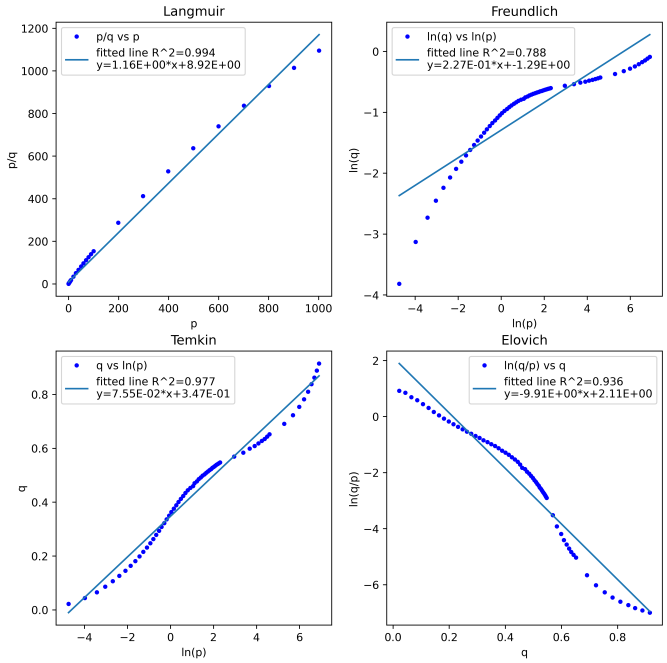

Figure 4.10: CO_2 adsorption isotherm data for amine-modified SLDH transformed to fit common linear equations.

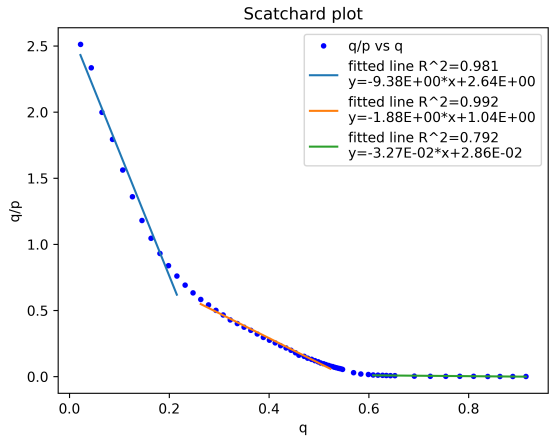

Figure 4.11: CO_2 adsorption isotherm data for amine-modified SLDH transformed to a Scatchard plot.

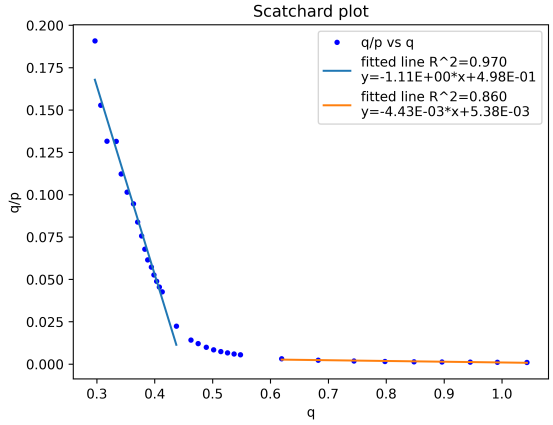

Figure 4.12: CO_2 adsorption isotherm data for unmodified SLDH transformed to a Scatchard plot.

Table 4.4: Extracted Langmuir parameters from the linear regions of the Scatchard plots in Figures 4.12 and 4.11. N is the density of the adsorption site and K is the Langmuir equilibrium constant of the site.

Sample	Parameters			
SLDH	N_1	4.48×10^{-1}	K_1	1.11
	N_2	1.21	K_2	4.43×10^{-3}
TRI@SLDH	N_1	2.81×10^{-1}	K_1	9.38
	N_2	5.54×10^{-1}	K_2	1.88
	N_3	8.75×10^{-1}	K_3	3.27×10^{-2}

The isotherm data, converted to align with the respective linear equations, is presented in Figures 4.9 and 4.10. For both the amine-modified and unmodified SLDH, the Langmuir model (homogeneous adsorption) has the highest R^2 value (0.994 and 0.979 respectively). The Temkin model (allowing for interactions between adsorbed species) also fits well for the amine-modified SLDH isotherm ($R^2 = 0.977$), but not for the unmodified SLDH ($R^2 = 0.895$), while the Freundlich model gives a good fit for the unmodified SLDH isotherm ($R^2 = 0.966$), but not the amine-modified SLDH ($R^2 = 0.788$). However, despite the high R^2 values, it is evident that none of the linear models sufficiently characterise the experimental data accurately. This discrepancy is highlighted by the observed reductions in the slope of both the transformed Langmuir plots as well as the presence of multiple inflection points within the Freundlich and Temkin isotherms. These deviations suggest a high degree of heterogeneity within the strength of the binding sites.

Using Scatchard analysis (Chapter 2.1.3) to probe the number of types of binding site in each isotherm yields the plots shown in Figures 4.11 and 4.12; both plots are non-linear, indicating at least two binding sites. A rudimentary categorisation of the types of binding sites can be inferred from the count of linear segments (each representing a simple Langmuir model within a multi-site Langmuir context). In this instance, two linear regions are observed for the SLDH, attributed to chemisorption and physisorption, whereas three regions are noted for the amine-modified SLDH, corresponding to strong and weak chemisorption and physisorption. The extracted Langmuir equilibrium constants and site density are shown in Table 4.4. The estimation of chemisorption sites on the amine-modified SLDH is $0.835\,\mathrm{mmol_N\,g^{-1}}$. Considering the total amine loading ($0.985\,\mathrm{mmol_N\,g^{-1}}$), there exists a theoretical maximum of 0.493 mmol potential ammonium carbamate sites, thus suggesting the presence of ≈ 0.34 mmol additional chemisorption sites of a different type. This figure is comparable to the number of sites predicted for the unmodified SLDH, implying that some of these sites remain in the modified material.

Non-linear modelling of the isotherms allows for more complex multi-parameter models to be used. The models and their equations are listed in Table 4.5 with their derivations discussed in Chapter 2.1.4.

Heterogeneous materials are more accurately represented through multi-parameter models capable of characterising the distribution of site energies, although they require fitting via non-linear optimisation. A description of the models used is given in Chapter 2.1.4 with the equations and $RMSE$ values of the fittings in Table 4.5. The isotherms and the fitted non-linear models are shown in Figures 4.13 and 4.14. In the linear representations, several models exhibit divergence from the experimental isotherm data at elevated pressures, although all models initially appear to provide an adequate fit in the low-pressure region. However, upon applying a logarithmic scale which expands this region (Figure B.3 and B.4), it becomes apparent that many of the models also fail to accurately represent this region.

The unmodified SLDH is well described by the DSLangmuir, TSLangmuir and JensenSeaton models with the TSLangmuir isotherm having the best fit ($RMSE = 0.00392$). Both the DSLangmuir and TSLangmuir show a strong (chemisorption) adsorption site with a capacity of $\approx 0.4\,\mathrm{mmol_{CO_2}\,g^{-1}}$ ($K \approx 1\,\mathrm{mbar^{-1}}$) with the additional site in the TSLangmuir model allowing it to better model the weak physisorption and the high pressure region. These values are comparable with those derived from Scatchard analysis and confirm a mixture of adsorption mechanisms. The Jensen-Seaton model accounts for the lack of saturation at high pressure as a result of gas compressibility. The adsorbed phase compressibility (b) calculated here is unreasonably high ($0.8735\,\mathrm{bar^{-1}}$), suggesting this factor is allowing this single site model to describe the dual types of adsorption.

The amine-modified SLDH is also well described by these models as well as the Quadratic model. The TSLangmuir model had the best fit ($RMSE = 0.00543$) with $0.18\,\mathrm{mmol\,g^{-1}}$ of a strong chemisorption site ($K = 12\,\mathrm{mbar^{-1}}$) and $0.41\,\mathrm{mmol\,g^{-1}}$ of a weaker site ($K = 0.8\,\mathrm{mbar^{-1}}$), again comparable to the values estimated by

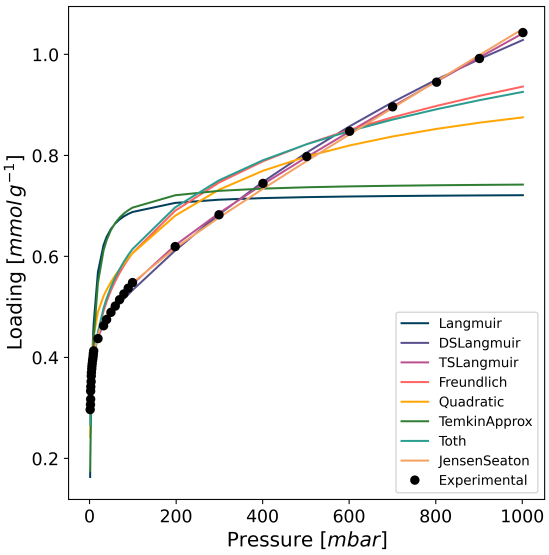

Figure 4.13: Unmodified SLDH CO_2 isotherm (○) and the optimised fittings of the models described in Table 4.5.

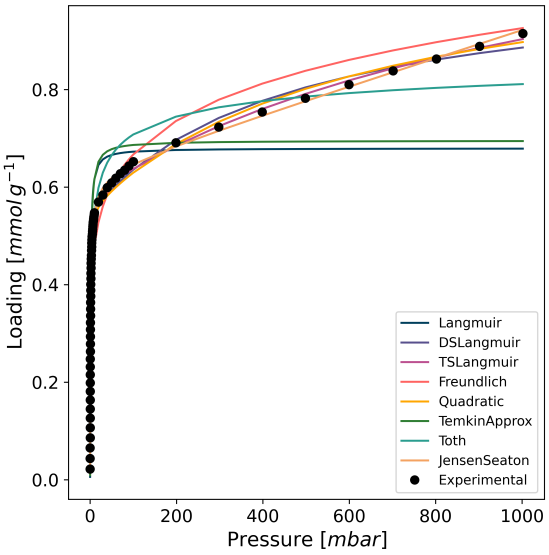

Figure 4.14: Amine-modified SLDH CO_2 isotherm (○) and the optimised fittings of the models described in Table 4.5.

Table 4.5: Non-linear isotherm models and their equations. $n(p)$ is the loading at pressure p, n_m is the maximum loading and K, θ, t, a, b, c are variables to be optimised. The root mean squared error (RMSE) for the fitting of the models to the isotherms in Figures 4.13 and 4.14 is also given.

Model	Equation	RMSE	
		SLDH	TRI@SLDH
Langmuir	$n(p) = n_m \frac{Kp}{1+Kp}$	1.75×10^{-1}	8.2×10^{-2}
DSLangmuir	$n(p) = n_{m_1} \frac{K_1 p}{1+K_1 p} + n_{m_2} \frac{K_2 p}{1+K_2 p}$	1.05×10^{-2}	1.81×10^{-2}
TSLangmuir	$n(p) = n_{m_1} \frac{K_1 p}{1+K_1 p} + n_{m_2} \frac{K_2 p}{1+K_2 p} + n_{m_3} \frac{K_3 p}{1+K_3 p}$	3.92×10^{-3}	5.43×10^{-3}
Freundlich	$n(p) = Kp^{1/m}$	5.67×10^{-2}	7.56×10^{-2}
Quadratic	$n(p) = n_m \frac{p(K_a + 2K_b p)}{1+K_a p + K_b p^2}$	7.41×10^{-2}	1.83×10^{-2}
TemkinApprox	$n(p) = n_m \frac{Kp}{1+Kp} + n_m \theta (\frac{Kp}{1+Kp})^2 (\frac{Kp}{1+Kp} - 1)$	1.67×10^{-1}	7.46×10^{-2}
Toth	$n(p) = n_m \frac{Kp}{\sqrt[t]{1+(Kp)^t}}$	6.4×10^{-2}	3.71×10^{-2}
JensenSeaton	$n(p) = Kp[1 + (\frac{Kp}{a(1+bp)})^c]^{-1/c}$	9.08×10^{-3}	6.09×10^{-3}

Scatchard analysis. The Jensen-Seaton model again has an unreasonable adsorbed phase compressibility (b =0.4418 bar^{-1}). The quadratic model is another one site model which shows a good fit to the data. For this model, the non-linearity at higher pressures is described by a weaker second interaction of each site with an additional molecule of adsorbate. The interaction between the molecules in the sites is strongly repulsive ($\phi = 0.003 < 1$), calculated by transforming the parameters to the form given in Chapter 2.1.4.

$$K_a = 2K \Rightarrow K = 1.004$$

$$K_b = K^2\phi \Rightarrow \phi = 0.003$$

Although the error is small ($RMSE = 0.0183$), the shape in the high pressure regions does not match well, with significant curvature instead of the linear trend observed, and it underestimates uptake at low pressure.

In summary, the non-linear modelling shows good agreement with the conclusions drawn from the Scatchard analysis. Both the amine-modified and unmodified SLDH show significant heterogeneity with both chemisorption and physisorption processes occurring. This is not well described by any of the single site models, but a good fit is achieved with both the dual- and triple-site Langmuir models.

The isosteric heat (enthalpy of adsorption) was then calculated from multiple isotherms at various temperatures (Figure **??** and **??**) via the Clausius-Clapeyron equation (Equation 2.2) and plotted in Figures 4.15(a) and 4.16(a).

As the the low loading data is missing for the unmodified SLDH, the enthalpy can only be calculated above 0.3 $\mathrm{mmol_{CO_2}\,g^{-1}}$ and shows a steady decline from 135.79 to 65.73 $\mathrm{kJ\,mol^{-1}}$. This trend is similar to that reported by Radha and Navrotsky: a steady decrease from 92.04 to 17 $\mathrm{kJ\,mol^{-1}}$.[25] A decreasing enthalpy is typical of a heterogeneous adsorbent with the strongest sites (high enthalpy of adsorption) bound first at lower pressures and weaker sites then filled once they are saturated. The large error range indicates that the regeneration process may

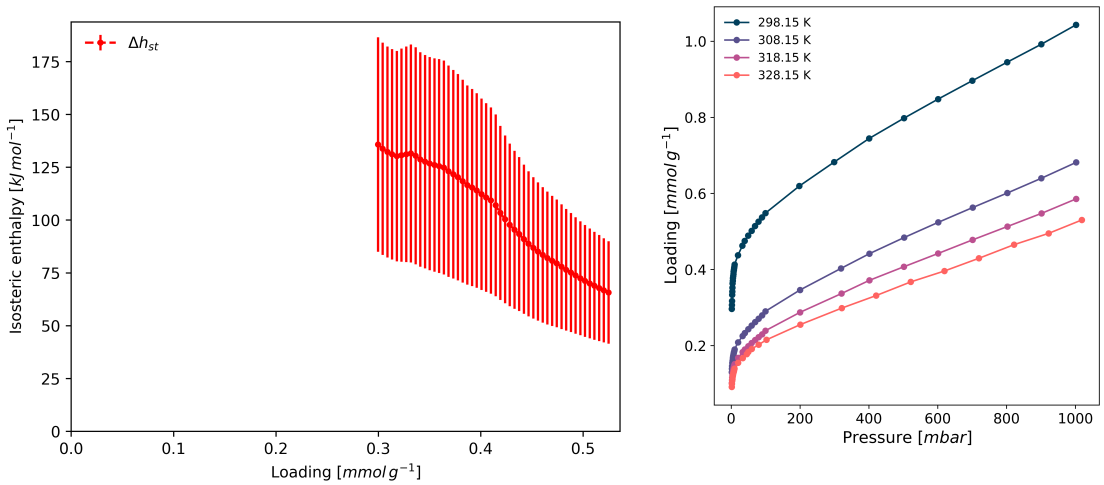

(a) **(b)**

Figure 4.15: (a) Isosteric heats of adsorption for unmodified SLDH calculated via the Clausius-Clapeyron equation from the CO_2 isotherms at varying temperatures in (b).

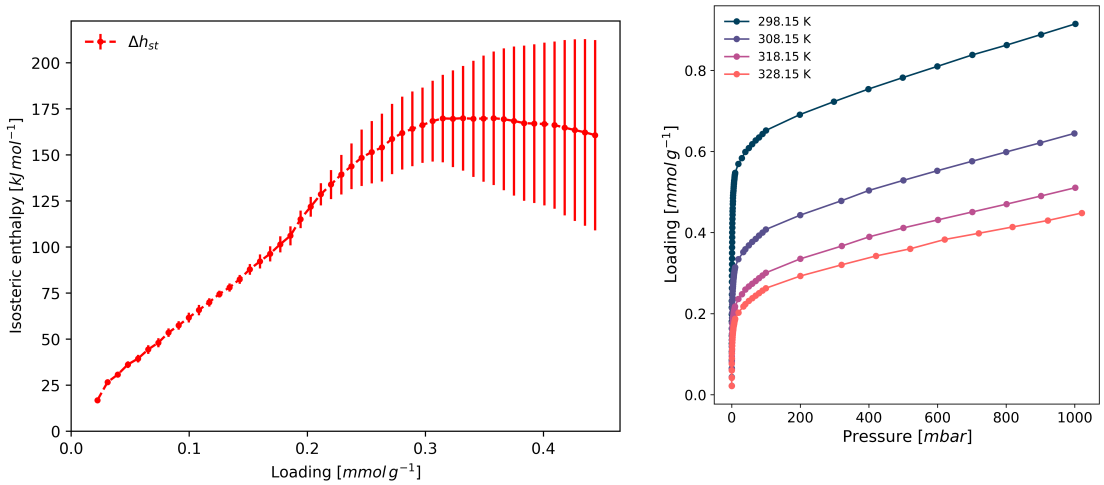

(a) **(b)**

Figure 4.16: Isosteric heats of adsorption for modified SLDH calculated via the Clausius-Clapeyron equation from the CO_2 isotherms at varying temperatures in (b).

not be fully complete or that the reactions are irreversible, such that uptake is by different sites on subsequent cycles.

The amine-modified SLDH shows a steadily increasing enthalpy from 16.78 to 169.89 kJ mol^{-1} before plateauing after a loading of 0.3 mmol$_{CO_2}$ g^{-1}. This suggests a cooperative adsorption mechanism. This differs from the isosteric heats reported for amine-modified silica materials; these typically show constant or decreasing enthalpies of adsorption as would be expected for non-interacting sites with a narrow distribution of adsorption enthalpies. Using only sequential temperature isotherms for the calculations yields a similar trend (Figures B.5, B.6 and B.7) at low coverage, suggesting it is not an artefact from site deactivation. Decreases in enthalpy are seen at decreasing onset loadings as the chemisorption capacity decreases with temperature.

While cooperative adsorption mechanisms for CO_2 are widely reported for metal organic frameworks, they are not commonly discussed for materials such as inorganic

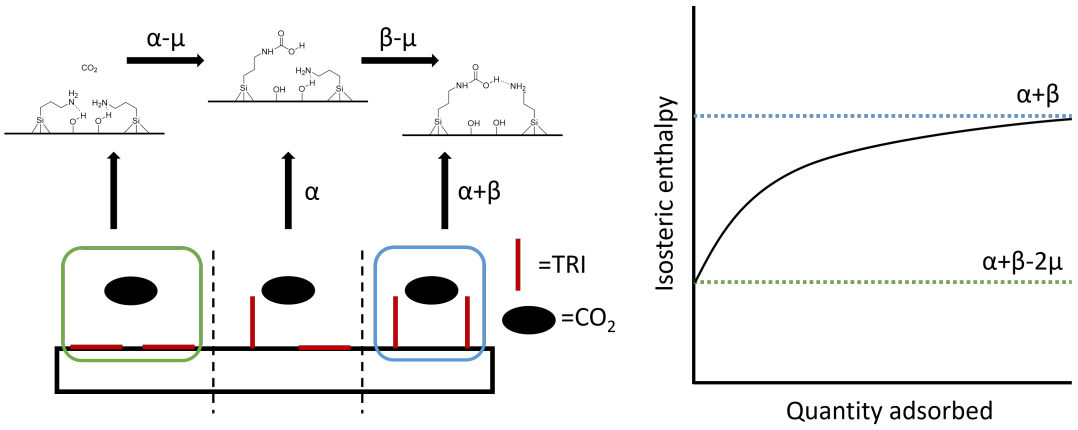

Figure 4.17: Schematic description of proposed adsorption mechanism. On initial uptake, most of the amines are parallel to the pore and are hydrogen-bonded to the LDH surface (green). Adsorption requires disruption of these hydrogen bonds, giving $\Delta H_{ads} = \alpha + \beta - 2\mu$ where α is the enthalpy of reaction to form a carbamate, β is the stabilisation of the carbamate with an adjacent base and μ is the interaction energy of the amine and the LDH surface. At higher coverages, some of the alkyl chains are perpendicular to the pore, due to interactions with CO_2 adsorbed on neighbouring sites. This gives a limit of $\Delta H_{ads} = \alpha + \beta$ if no hydrogen bonds must be broken. A material transitioning between these two states is a simplistic interpretation of Simon *et al.*'s model.[29]

amine-modified oxides.[30] In metal organic frameworks, the mechanism is described as the protonation of an amine in the grafted diamine group during the adsorption of an initial CO_2 molecule which destabilises the second amine group in the diamine, leading to an insertion adsorption mechanism where the next CO_2 molecule can insert into the weakened N–M bond (Figure 1.8). Such a mechanism is not possible here as there are no N–M bonds present; however, there are still multiple nitrogen atoms per grafted moiety and so a similar mechanism, where protonation of one of the amines disrupts a strong surface-amine interaction with another amine in the alkyl chain, could have a similar activating effect. Simon *et al.* have developed a statistical mechanical model for gas adsorption onto dynamic moieties which fits this description and leads to the phenomenon of increasing isosteric heat.[29] The amine-containing alkyl chains can have two orientations: parallel to the pore wall or a higher energy reactive conformation perpendicular to the pore wall. Initial isosteric heats are low, as the exothermic adsorption process is offset by the endothermic rotation of the site and its neighbours to their active conformation. As more of the sites rotate to their active form, subsequent adsorption has a higher percentage binding on already activated sites (Figure 4.17). An effect similar to this has been shown by Potter *et al.* for CO_2 adsorption on PEI-modified SBA-15 where the capacity and isosteric heat of adsorption increase with the PEI loading, attributed to a smaller proportion of the amines interacting with the support surface.[31]

Studies on the heat of adsorption have been conducted for silica-based sorbents, with the enthalpy depending on the grafting density[32], the type of silane used (number of amines in the alkyl chain)[33] and the availability of silanol groups[22] with values reported above $90\,\mathrm{kJ\,mol^{-1}}$.[34] The isosteric heat values calculated for TRI@SLDH are significantly higher ($> 150\,\mathrm{kJ\,mol^{-1}}$), indicating that the change in support from silica to LDH has a major influence on the species formed upon CO_2 adsorption. This value is closer to the $125\,\mathrm{kJ\,mol^{-1}}$ reported by Pinto *et al.* for amine-modified nanoporous clays.[35] The carbamates formed upon CO_2 capture have been shown to interact with the surface silanols via hydrogen bonding, leading

to a stabilisation of the chemisorbed CO_2 and so it is hypothesised that an increase in the strength of these support-carbamate interactions leads to the enhanced adsorption enthalpy.[36,37] A high adsorption enthalpy means the material requires a higher amount of energy for regeneration; however, as the DAC CO_2 capacity is $0.25\,\mathrm{mmol_{CO_2}\,g^{-1}}$, the average enthalpy of adsorption will be lower, making it comparable with other silica-based sorbents ($86.4\,\mathrm{kJ\,mol^{-1}}$).

In summary, amine functionalities were introduced into the sample with silane grafting, as evidenced by changes in the FTIR spectra and TGA traces. A decrease in the pore size compared to the unmodified SLDH indicates the amine is dispersed within the pores of the support and ^{29}Si SS-NMR shows the sample is free from adsorbed (unreacted) silanes, with all the amino silane bound (via a siloxane linkage) to another heteroatom. The DAC CO_2 capacity of the TRI@SLDH is comparable to the benchmark adsorbent TRI@SBA-15 (78% of the capacity). Modelling of the CO_2 isotherm shows that both chemisorption and physisorption processes occur and calculations of the isosteric heat of adsorption show an unusual increasing trend, with coverage suggesting a cooperative mechanism. Unexpectedly, the unmodified SLDH also shows a significant uptake under DAC conditions. Comparison of the isotherms of the modified and unmodified SLDH show clear changes to the CO_2 binding sites.

4.2.1 Effect of grafting solvent

While toluene is widely used as the grafting solvent, several papers have investigated the use of alternative grafting solvents. Feitosa *et al.* showed that various solvents could be used for silane grafting, but that non-polar solvents such as cyclohexane, toluene and hexane lead to the highest amine densities and this leads to enhanced CO_2 capacities, with cyclohexane performing the best.[38] This was attributed to a decreased solvation interaction between the solvent and both the silanol groups of the support and the alkoxy-silane groups of the amino silane, changing the reaction equilibrium. Sánchez-Vicente *et al.* also showed supercritical CO_2 is an effective and cheap solvent for industrial scale silane grafting.[39] Cyclohexane and xylene are

non-polar solvents that are less toxic than toluene (with immediately dangerous to life or health values of 1300 ppm and 900 ppm respectively vs 500 ppm) and were investigated as alternative solvents to see if they would affect the amount of silane grafted and to reduce the toxicity of the reaction in line with the principles of green chemistry.

The amine-modified SLDHs were prepared in a similar process to the TRI-modified SLDH discussed previously (Chapter 4.2). A full description of the experiments are given in Chapter 4.3.3. Typically, 1 g of SLDH was dried at 100 °C under vacuum and suspended in 75 mL of solvent (toluene, xylene or cyclohexane) before 3 mL TRI was added dropwise and left under stirring for 15 min under a N_2 headspace before being heated to 85 °C and stirred for 16 h.

The FTIR spectra of the amine-modifed SLDH in different solvents are shown in Figure B.8. The spectra all show the same adsorption bands with the additional $-$CH (2933 cm^{-1}), $-$NH (1571 cm^{-1}), $-CH_2-$ (1471 cm^{-1}) and C$-$N (1117 cm^{-1}) adsorptions present, irrespective of the grafting solvent, showing that they may all be used successfully as grafting solvents.

The TGA traces of the TRI-modified SLDHs are shown in Figure 4.18. The traces for all three show similar decomposition events, with the main differences in decomposition rate occurring during the events due to the amino silane functionality. The samples grafted in xylene and cyclohexane show increased rates of weight loss at < 150 °C and at 250 °C with higher corresponding mass losses (10.7 and 11.3 %, respectively vs 8.5 % for the sample grafted in toluene, Table 4.6). This is consistent with the samples having a higher amine density (Table 4.7), but the rate of decomposition at temperatures between 300 to 450 °C is approximately the same (18.7, 19.7 and 18.7 % for the samples grafted in xylene, cyclohexane and toluene, respectively), suggesting all three samples contain a similar quantity of this silane site. This is consistent with this type of silane belonging to a monolayer on the support, with all samples possessing a saturated surface.

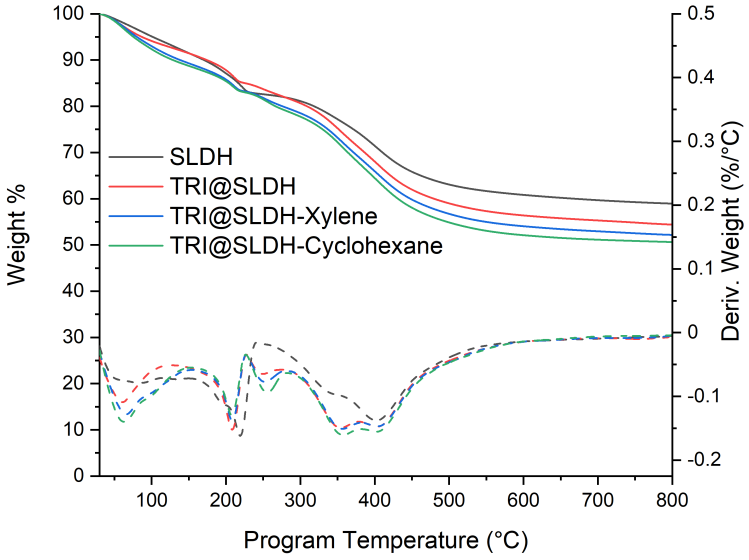

Figure 4.18: TGA thermal curve of SLDH and TRI-modified SLDH grafted in different solvents.The derivative trace is shown below (dotted line).

Table 4.6: Weight changes for different thermal events measured by TGA (Figure 4.18).

Sample	Weight change (%) in temperature range (°C)						
	0 to 150	150 to 225	225 to 300	300 to 375	375 to 450	450 to 800	300 to 450
SLDH	8.49	7.86	2.53	4.01	8.79	6.87	15.30
TRI@SLDH	8.53	6.44	4.36	5.73	9.63	7.57	18.68
TRI@SLDH-Xylene	10.70	6.08	4.71	5.77	9.70	7.63	18.70
TRI@SLDH-Cyclohexane	11.26	5.71	5.28	6.11	10.22	7.42	19.70

The CO_2 adsorption isotherms of the materials produced from grafting in the different solvents are shown in Figure 4.19. The form of all three isotherms is similar with a Type I shape with high uptake at low pressure and vary only in their adsorption capacities; the DAC CO_2 capacities of the three materials are 0.267, 0.244 and 0.196 $mmol_{CO_2}\,g^{-1}$ for the grafting using toluene, xylene and cyclohexane, respectively. This shows that the grafting solvent used does have an effect on the grafting process and, under these conditions, toluene produces the material with the highest DAC performance. This trend is different to that observed by Sánchez-Vicente *et al.*, where the use of cyclohexane as the grafting

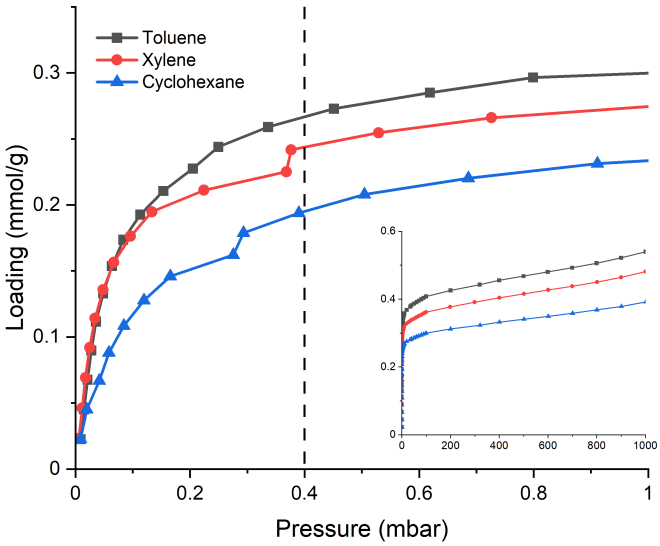

Figure 4.19: CO_2 adsorption isotherms for amine (TRI)-modified SLDH grafted in different solvents. The low pressure region is shown in the main graph and the full isotherm is shown in the insert. The irregular steps observed are attributed to measurement artefacts.

Table 4.7: N weight percentage, amine and silane density, DAC CO_2 capcity and amine efficiency for SLDH grafted with TRI in different solvents.

Sample	N (av. wt%)	N ($mmol\,g^{-1}$)	Silane loading ($mmol\,g^{-1}$)	CO_2 capacity ($mmol\,g^{-1}$)	Amine efficiency
SLDH	0	0	0	0.299	
TRI@SLDH-Toluene	3.42	2.442	0.814	0.267	0.109
TRI@SLDH-Xylene	3.88	2.770	0.923	0.244	0.088
TRI@SLDH-Cyclohexane	4.92	3.513	1.171	0.195	0.056

solvent increased the amine density compared to toluene, leading to an increase in capacity, although a similar increase in amine density is observed.[38]

Table 4.7 shows the measured N in the sample, the calculated amine and silane loadings and the amine efficiency at 0.4 mbar. The amine density shows an inverse trend to the DAC CO_2 capacity, with densities of 2.442, 2.770 and 3.153 $mmol_N\,g^{-1}$

for the grafting using toluene, xylene and cyclohexane, respectively. The reduction in capacity thus implies that although there are additional amine sites for CO_2 uptake, fewer of them are available for reaction, leading to a reduction in amine efficiency (0.109, 0.088 and 0.056). A hypothesis for the reduction in amine efficiency is that the increases in amine density lead to reduced diffusion of CO_2 to amines situated within the pores.[14] This behaviour has been demonstrated by Anyanwu *et al.*, who showed that for wet-grafted amine-modified silica (where water was deliberately added), amine density was enhanced by increasing the amount of water added, but at low temperatures (25 °C), this had an adverse effect on the adsorption capacity due to kinetic limitations, which did not effect the adsorbents at higher uptake temperatures.[40] An increase in the amine density may be due to changes in the solvent-surface interaction, as hypothesised by Feitosa *et al.*, or by an increase in self-condensation of the amino silyl ether.[38] The non-polar solvents used are immiscible with water, with water saturation concentrations of 0.003, 0.0217 and 0.027 mol L^{-1} for cyclohexane, xylene and toluene, respectively.[41] As the water saturation concentration for the solvents decreases with the increasing amine density observed, it is unlikely that the increase is due to enhanced self-condensation. The changes in the amounts of amino silane seen decomposing at $\approx$ 250 °C also correlate with the increased amine density (cyclohexane > xylene > toluene), indicating a change in the distribution of binding modes of the silyl products.

In summary, all three solvents allowed TRI to be successfully grafted on SLDH. Changing the grafting solvent increased the amine density in the order cyclohexane > xylene > toluene. Surprisingly, this led to a reduction in CO_2 capacity, implying that there is an optimal level of grafting beyond which kinetic limitations result in a decrease in performance. The increase in amine density is associated with an increase in the weight loss at 250 °C attributed to bidentate amino silane, suggesting that the grafting solvent influences the distribution of silyl products.

4.2.2 Effect of moisture on grafting

To investigate whether there was any effect caused by trace water present in the reaction on the grafting density, a further synthesis was conducted under anhydrous conditions. As discussed previously (Chapter 4.2.1), a lower amine density showed a higher amine efficiency, leading to a higher DAC CO_2 capacity. Further reductions in the amount of self-condensation may enhance this effect further.

SLDH was modified using similar conditions (Chapter 4.2.1) with the inclusion of Schlenk techniques; a full description is given in Chapter 4.3.4. In summary, 1 g of SLDH was dried at 100 °C under vacuum in a Schlenk flask overnight, cooled and 75 mL of dried (using a solvent purification system) toluene was added under a N_2 atmosphere. 3 mL TRI was added dropwise under vigorous stirring and left under stirring for 15 min before being heated to 85 °C and stirred for 16 h. The suspension was filtered and washed several times to remove excess TRI before being collected via vacuum filtration. This sample was labelled TRI@SLDH-Dry.

The FTIR spectra are shown in Figure B.9. The spectra all show the same adsorption bands arising from the grafted TRI (–NH at 1571 cm^{-1} and $-CH_2-$ at 1471 cm^{-1}), but a reduction in the band at 1117 cm^{-1}. Si–O–Si linkages display an adsorption band at $\approx$ 1100 cm^{-1} and, as such, may be a large contributor to this resonance; a large decrease in the adsorption indicates a reduction in hydrolysis to form these linkages, as intended.

The ^{29}Si SS-NMR spectrum is shown in Figure 4.20. The same signals are observed in the NMR spectrum as for the TRI@SLDH produced under standard conditions (Figure 4.3). T_{1-3} peaks at −49, −57 and −67 ppm and unknown peaks at −82, −85, −88 and −93 ppm. However, under the anhydrous conditions, the previously unattributed peaks in the range −75 to −100 ppm become the dominant environments, with the T_x sites suppressed to broad resonances of approximately equal area compared to the increasing trend seen in TRI@SLDH. The reduction in relative amount of silanes in the typical T_{1-3} environments suggests that these signals arise from species that require water (for hydrolysis) to form and are likely due to the

hydrolysis self-condensation polymerisation reaction. As the unknown signals are unaffected by the removal of water from the system, it is likely that they are due to the surface grafting reaction which does not require water. As these signals do not appear in previously reported silane grafted LDH systems, it is possible they arise due to P−O−Si coupling. This has been reported in the reaction of silica and phosphoric acid[42] which is used in the formation of silicophosphates.[43] The inclusion of a P linkage is shown to shift Q sites by -10 ppm.[44] The direct reaction of MONO with K_3PO_4, Na_3PO_4 and $PO(OMe)_3$ failed to show any new signals in the ^{29}Si spectrum and attempts to confirm the environment by heteronuclear P−O−Si HMQC MAS experiments were unsuccessful.[45]

The TGA traces are shown in Figure 4.21. There is no additional weight loss observed at 65 and 250 °C as seen for TRI@SLDH. This suggests these types of silanes result from the hydrolysis self-condensation reaction and require the presence of trace amounts of water to form. The weight loss at temperatures between 300 to 375 °C (5.13%) is comparable to that of TRI@SLDH, indicating this site does not require water to form and is therefore likely formed by reaction with the SLDH surface.

SEM images and EDX mapping of TRI@SLDH are shown in Figures 4.22 and 4.23. The morphology of the SLDH is retained (Figure 3.28) with large particles ≈ 20 µm in size made up of small platelets (Figure 4.22(d)). The elemental mapping shows there is a homogeneous distribution of nitrogen across the particle, indicating that surface modification is successful, with no obvious agglomerations that can be

Table 4.8: Weight changes for different thermal events measured by TGA (Figure 4.21).

Sample	Weight change (%) in temperature range (°C)						
	0 to 150	150 to 225	225 to 300	300 to 375	375 to 450	450 to 800	300 to 450
SLDH	8.49	7.86	2.53	4.01	8.79	6.87	15.30
TRI@SLDH	8.53	6.44	4.36	5.73	9.63	7.57	18.68
TRI@SLDH-Dry	7.82	6.20	2.75	5.13	9.81	7.70	17.65

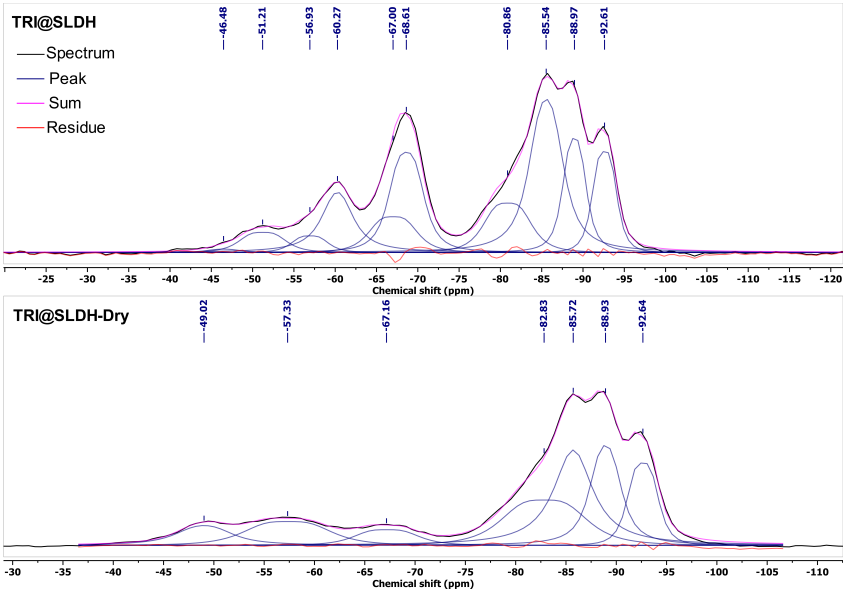

Figure 4.20: ^{29}Si CP-MAS NMR spectrum of TRI-modified SLDH measured at 10 kHz.

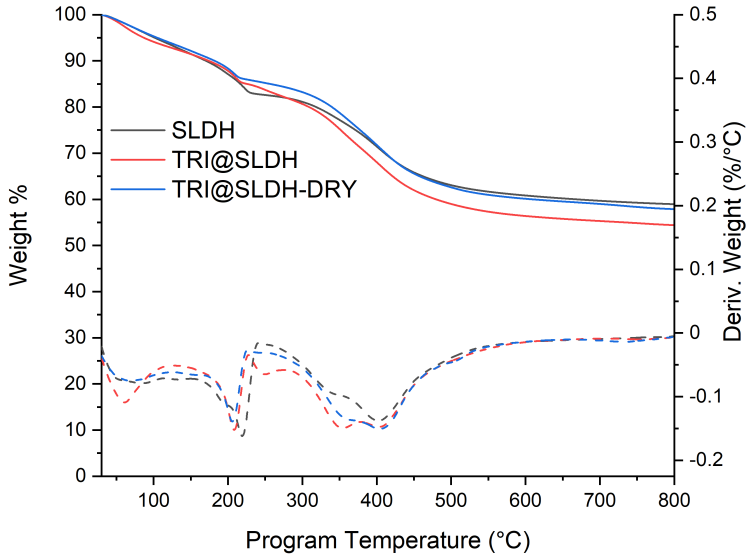

Figure 4.21: TGA thermal curve of SLDH and TRI-modified SLDH.The derivative trace is shown below (dotted line).

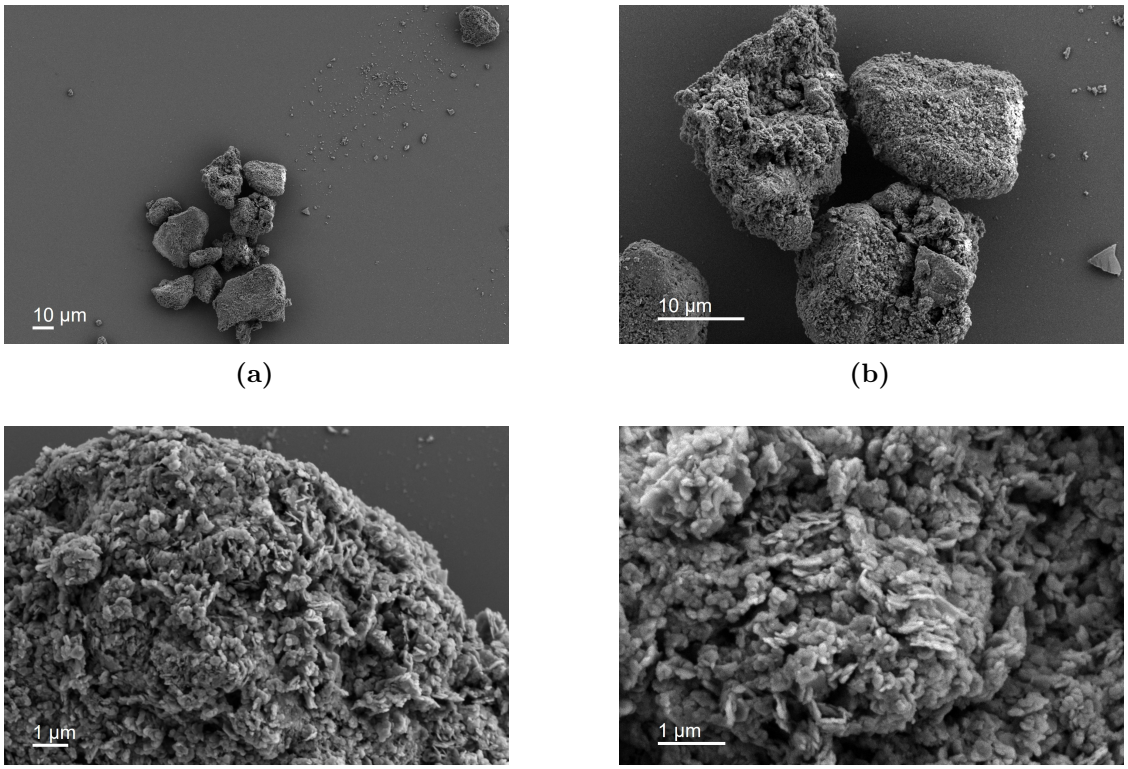

(a) (b)

(c) (d)

Figure 4.22: HR-SEM images of TRI@SLDH.

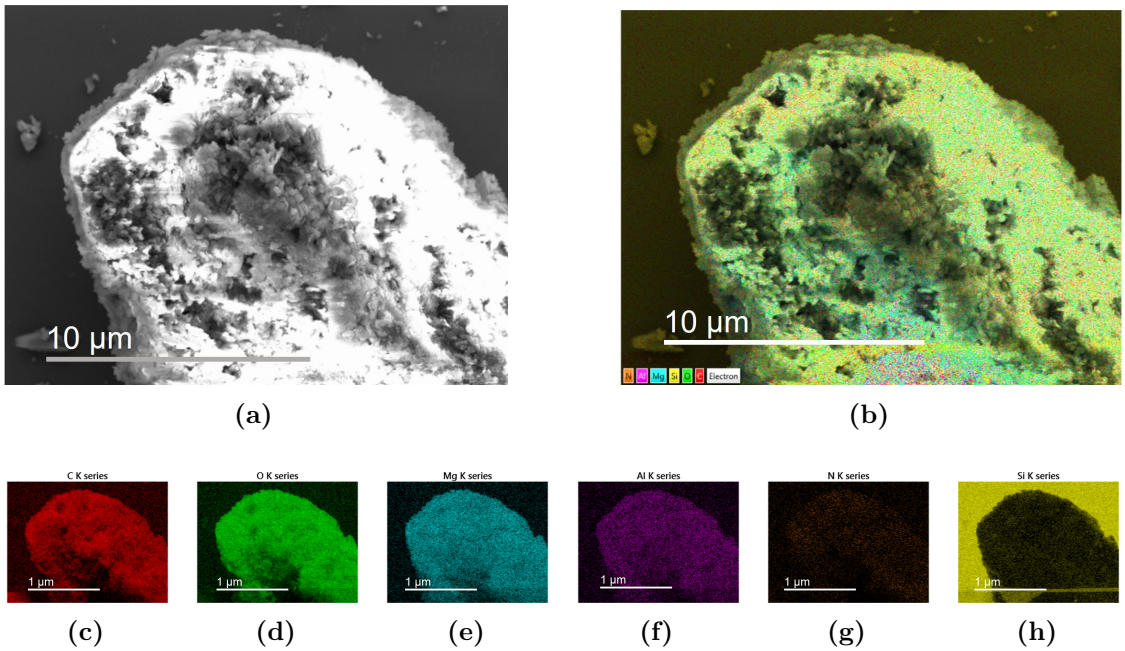

(a) (b)

(c) (d) (e) (f) (g) (h)

Figure 4.23: HR-SEM EDX mapping images of TRI@SLDH.

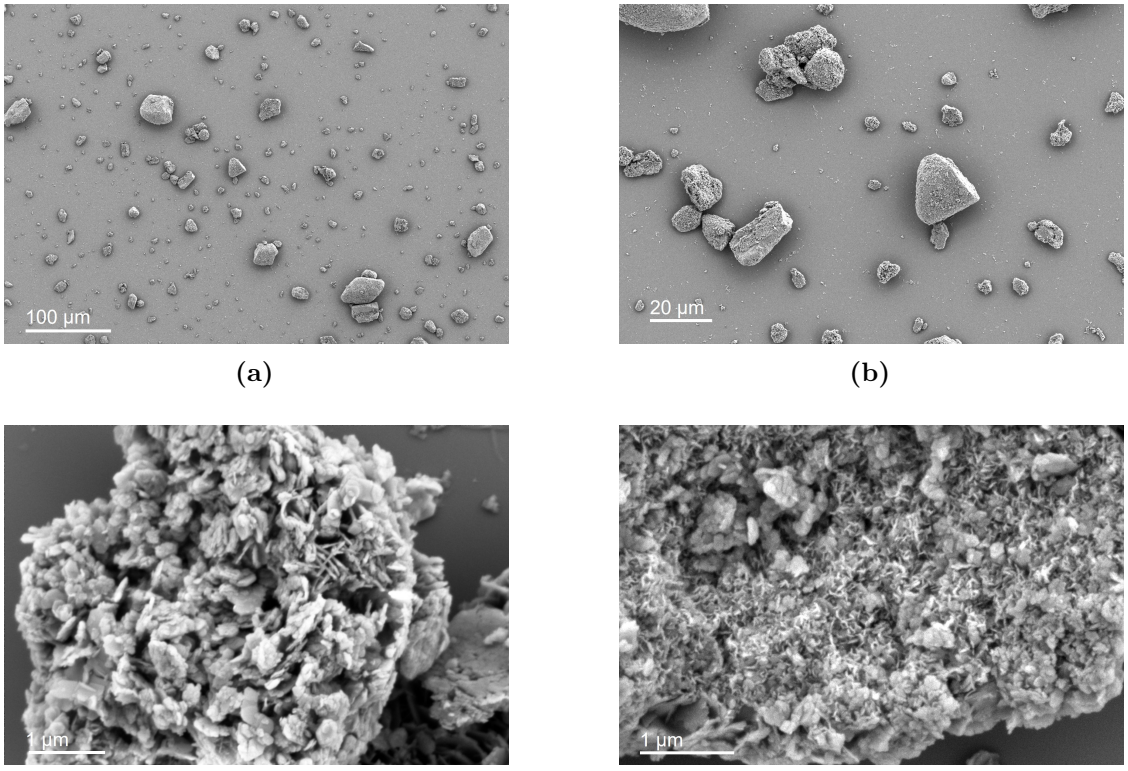

(a) (b)

(c) (d)

Figure 4.24: HR-SEM images of TRI@SLDH-Dry.

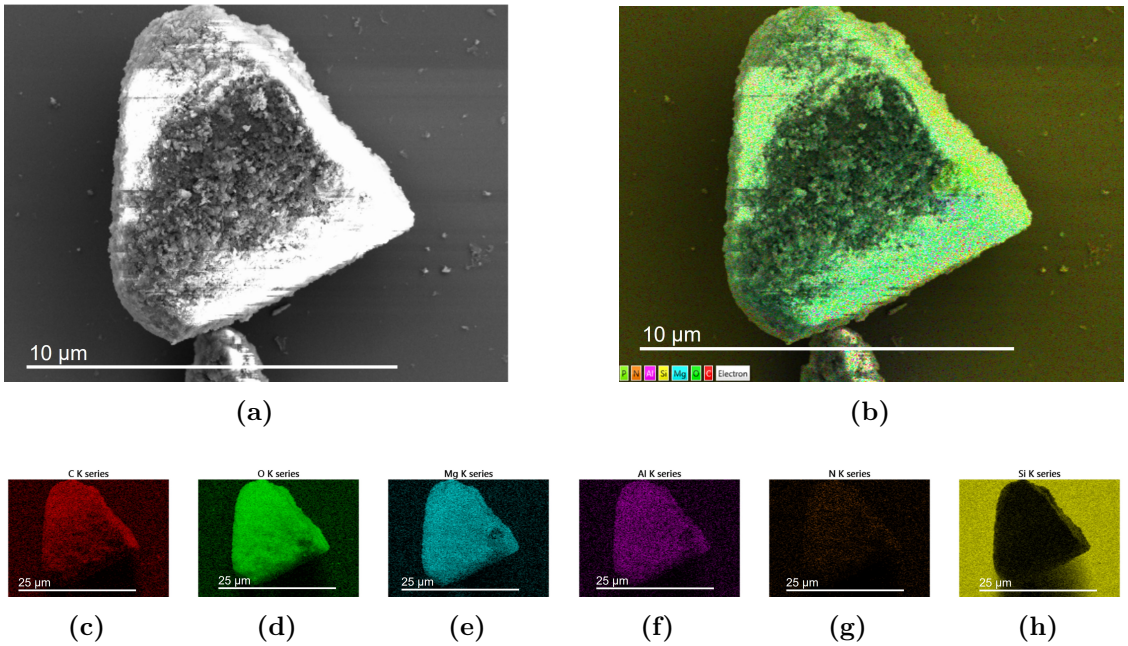

(a) (b)

(c) (d) (e) (f) (g) (h)

Figure 4.25: HR-SEM EDX mapping images of TRI@SLDH-Dry.

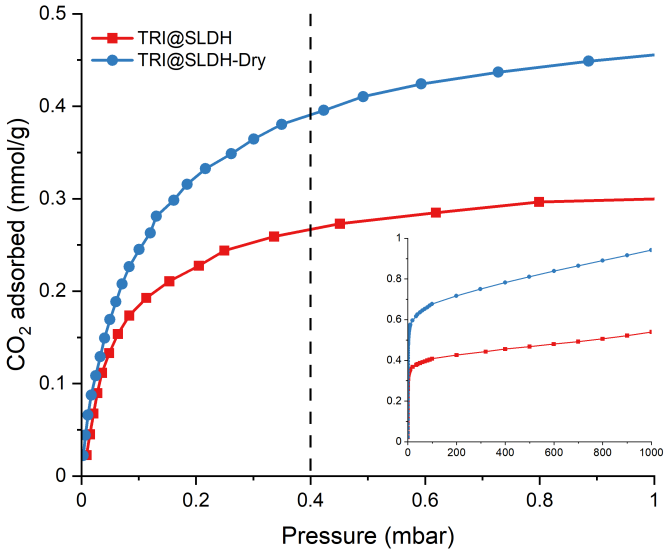

Figure 4.26: CO_2 adsorption isotherms for amine (TRI)-modified SLDH grafted under standard and anhydrous conditions. The low pressure region is shown in the main graph and the full isotherm is shown in the insert.

Table 4.9: N weight percentage, amine and silane density, DAC CO_2 capacity and amine efficiency for SLDH grafted with TRI under standard and anhydrous conditions.

Sample	N (av. wt%)	N ($mmol\,g^{-1}$)	Silane loading ($mmol\,g^{-1}$)	CO_2 capacity ($mmol\,g^{-1}$)	Amine efficiency
SLDH	0	0	0	0.299	
TRI@SLDH	3.42	2.442	0.814	0.267	0.109
TRI@SLDH-Dry	1.14	0.814	0.271	0.391	0.480

observed (Figure 4.23(g)). The SEM and EDX mapping of TRI@SLDH-Dry are shown in Figures 4.24 and 4.25. The morphology and elemental distribution match closely with the TRI@SLDH sample, indicating a similar grafting mechanism in both samples.

The CO_2 isotherms for the TRI@SLDH-Dry modified using the standard procedure and under the anhydrous conditions are shown in Figure 4.26. The change in grafting conditions has a clear improvement on the DAC CO_2 capture performance, with the capacity increasing from 0.267 to $0.390\,mmol_{CO_2}\,g^{-1}$. The

total number of available sites also has a large increase, with a capacity of 0.576 and 0.942 $\mathrm{mmol_{CO_2}\,g^{-1}}$ at 10 and 1000 mbar, respectively, compared to 0.358 and 0.540 $\mathrm{mmol_{CO_2}\,g^{-1}}$ for the SLDH modified using the standard procedure, due to an increase in both the amount of chemisorption and physisorption. Table 4.9 shows the amine density in the anhydrous grafted SLDH is significantly decreased (0.814 $\mathrm{mmol_N\,g^{-1}}$ compared to 2.442 $\mathrm{mmol_N\,g^{-1}}$), but the amine efficiency greatly increases to 0.48 (from 0.109) as was hypothesised. This is close to the maximum amine efficiency possible via the alkylammonium carbamate ion pair mechanism (≤ 0.5). At 10 mbar, the amine efficiency would be 0.708, indicating significant contribution from a different mechanism: either stabilisation via interaction with the SLDH support rather than an adjacent amine or CO_2 adsorption directly on the SLDH support.

In summary, under anhydrous conditions, the CO_2 adsorption capacity was shown to increase despite a significant decrease in the amine density, with the associated amine efficiency (0.48) approaching the theoretical maximum (0.5). A decrease in the weight loss observed at 65 and 250 °C implies that the silyl species decomposing at these temperatures require a hydrolysis reaction to form and that their formation is thus prevented under anhydrous conditions. A similar decrease in the resonances for the T_{1-3} environments in the ^{29}Si SS-NMR spectra suggest these too are from polymerised groups and the previously unreported environments in the -75 to -100 ppm region are the signals due to silane reactions with the SLDH.

4.2.3 Effect of amine

Number of amines in the alkyl chain

N^1-(3-Trimethoxysilylpropyl)diethylenetriamine (TRI) is commonly used during silica modification over the equivalent silanes with fewer amines: 3-aminopropyl-triethoxysilane (MONO, Figure 4.27(a)), *N*-2-aminoethyl-3-aminopropyl-trimethoxysilane (DI, Figure 4.27(b)). The work by Wang *et al.* showed the CO_2 uptake kinetics varied with different onset temperatures for fast uptake for the three LDHs

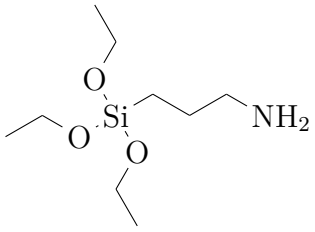

(a) 3-aminopropyl triethoxysilane (MONO).

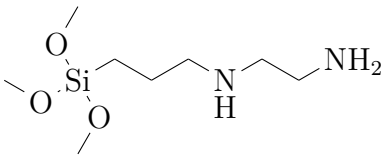

(b) N-2-aminoethyl-3-aminopropyl trimethoxysilane (DI).

Figure 4.27: Structures of MONO and DI.

modified with MONO, DI and TRI (28, 73 and 84 °C, respectively).[3] MONO-modified LDH had the fastest kinetics at all temperatures, with the DI- and TRI-modified LDHs reaching comparable rates at higher temperatures (approximately 0.41, 0.4 and 0.33 $mmol_{CO_2}\,g^{-1}\,min^{-1}$, respectively, at 80 °C). As fast reaction kinetics and capacity at ambient temperatures are necessary properties for DAC sorbent materials it was investigated whether a similar effect would be seen for modified SLDHs.

MONO- and DI-modified SLDHs were prepared in a similar process to the TRI-modified SLDH discussed previously (Chapter 4.2). A full description of the experiments are given in Chapter 4.3.5. Typically, 0.2 g of SLDH was dried at 100 °C under vacuum and suspended in 20 mL toluene before 0.6 mL MONO or DI was added dropwise and left under stirring for 15 min under a N_2 headspace before being heated to 85 °C and stirred for 16 h.

The FTIR spectra of the SLDH modified with the different amino silanes are shown in Figure 4.28. MONO- and DI-modified SLDH show the same adsorption bands as seen for TRI-modified SLDH (Figure 4.2), with no significant change in the intensity or positions of the adsorptions of the organic groups, despite a reduction in their concentration (Table 4.10).

^{13}C SS-NMR is shown in Figures 4.29 (CP-MAS) and 4.30 (CP-NQS). All three of the amine-modified SLDHs show similar C environments: Si–$\underline{C}H_2$–C (11 ppm), C–$\underline{C}H_2$–C (23 ppm), C–$\underline{C}H_2$–NH_2 (40 ppm), $\underline{C}H_3$–O and/or C–$\underline{C}H_2$–NH–C (50 ppm overlapping, DI and TRI), C–NH$\underline{C}O_2H$ (164 ppm) and CO_3 (170 ppm).

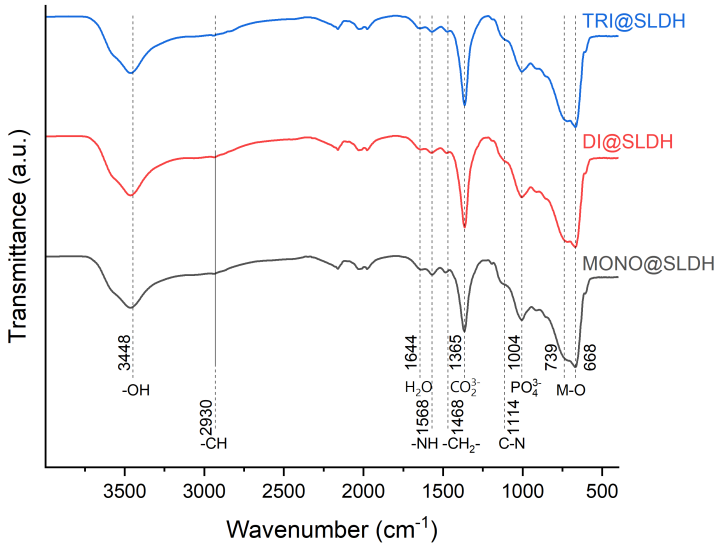

Figure 4.28: FTIR spectra of MONO-, DI- and TRI-modified SLDH.

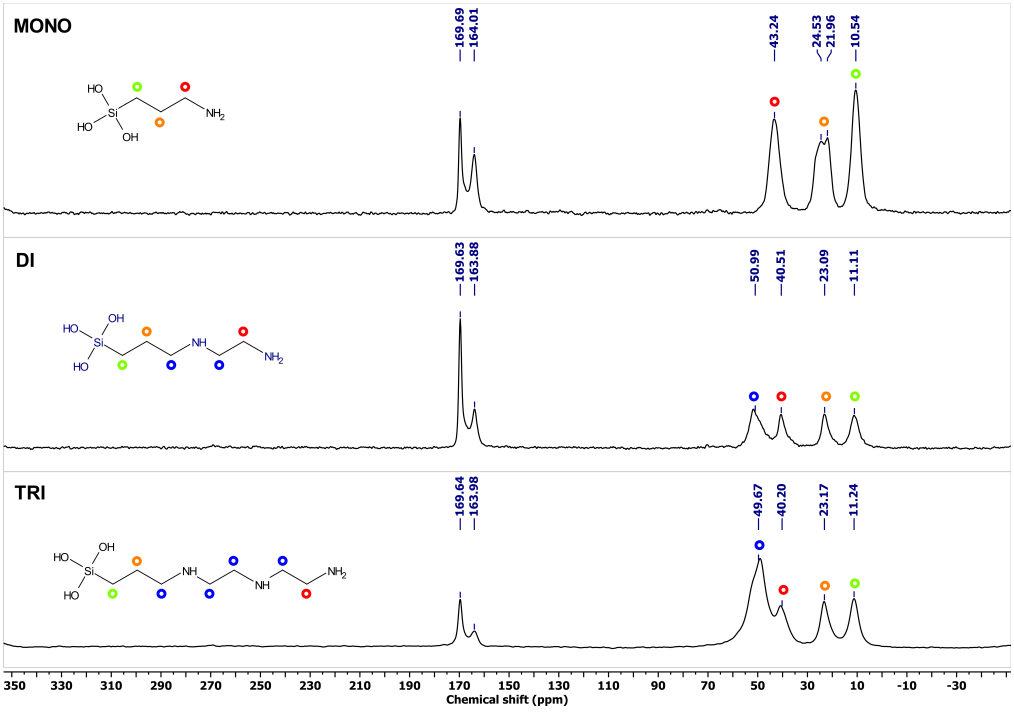

Figure 4.29: ^{13}C CP-MAS NMR spectrum of MONO-, DI- and TRI-modified SLDH measured at 10 kHz. Assignments indicated by coloured ○

In the MONO-modified SLDH, the only signals in the low shift region arise from the three carbon environments in the alkyl chain, with no signal from any ethoxy groups, indicating complete hydrolysis of the Si. In DI-modified SLDH, there are two new carbon environments overlapping at 51 ppm; the environments are not entirely equivalent, leading to a broad resonance. In the TRI-modified SLDH, there are four carbon environments at 51 ppm with an odd peak shape arising from small variations in chemical shift between the inequivalent sites. The peak at 170 ppm is from the CO_3 anion of the SLDH, as seen previously (Figure 3.32), and the peak at 164 ppm is from the carbamate formed upon exposure of the amine groups to atmospheric conditions.[46] The main FTIR stretching frequencies for ammonium carbamate are COO^- 1553 cm^{-1} and 1393 cm^{-1}, and CN 1117 cm^{-1}, overlapping with the NH, $CO_3{}^{2-}$ and CN adsorptions from the sorbent.[47]

The CP-NQS experiments (Figure 4.30) support these assignments with suppression of the CH_2 signals in the low shift region. The Si–$\underline{C}H_2$–C (11 ppm) and C–$\underline{C}H_2$–C (23 ppm) environments show the greatest suppression, indicating that they experience the least motional averaging. The reduced suppression of the C–$\underline{C}H_2$–NH–C (50 ppm) and C–$\underline{C}H_2$–NH_2 (40 ppm) resonances imply that they experience more motion with greater freedom of movement the further they are from the stationary surface bound Si tether.

^{29}Si SS-NMR of the SLDH grafted with the different amines (MONO, DI, TRI) is shown in Figure 4.31. They all show resonances at similar frequencies, as seen previously (Figure 4.3). The three expected environments corresponding to the T_1, T_2 and T_3 sites (seen at −51, −60 and −69 ppm) show similar shifts in all samples, indicating that the Si environment formed from the grafting reaction is similar, irrespective of the alkyl chain. All of these peaks are broad and fitting is improved by the addition of a second broad peak at higher shift. For the T_1 and T_2 environments, O–R hydrolysis to form O–H is expected to produce environments with a higher shift, due to an increase in the partial positive charge of $Si^{\delta+}$ which could account for these environments. However, previous reports of species in

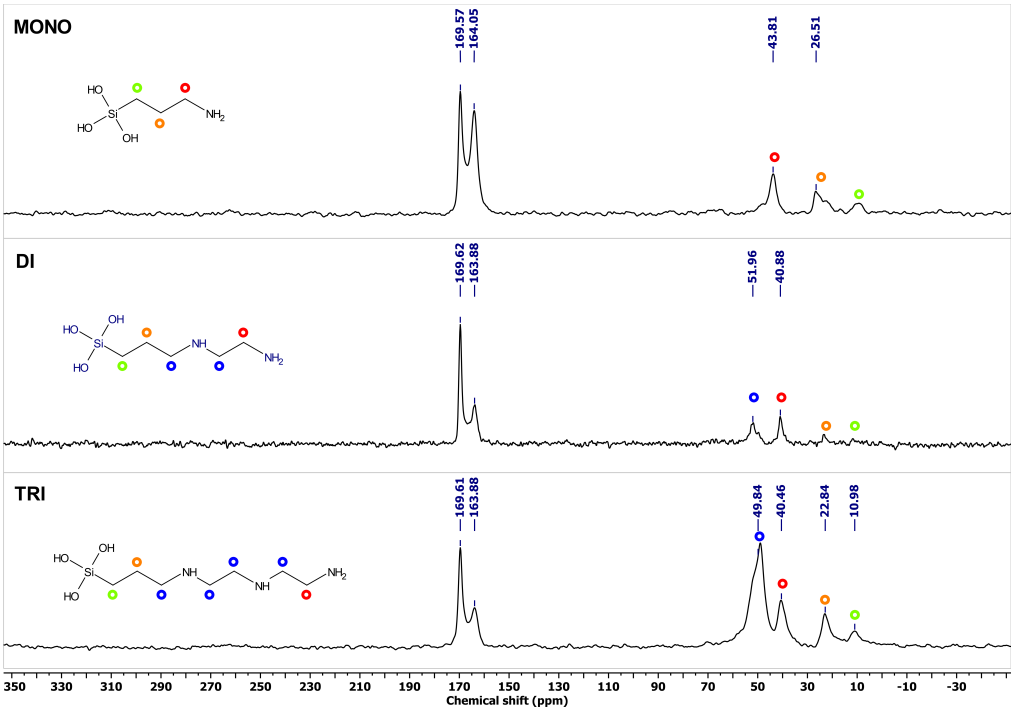

Figure 4.30: ^{13}C CPNQS NMR spectrum of MONO-, DI- and TRI-modified SLDH measured at 10 kHz.

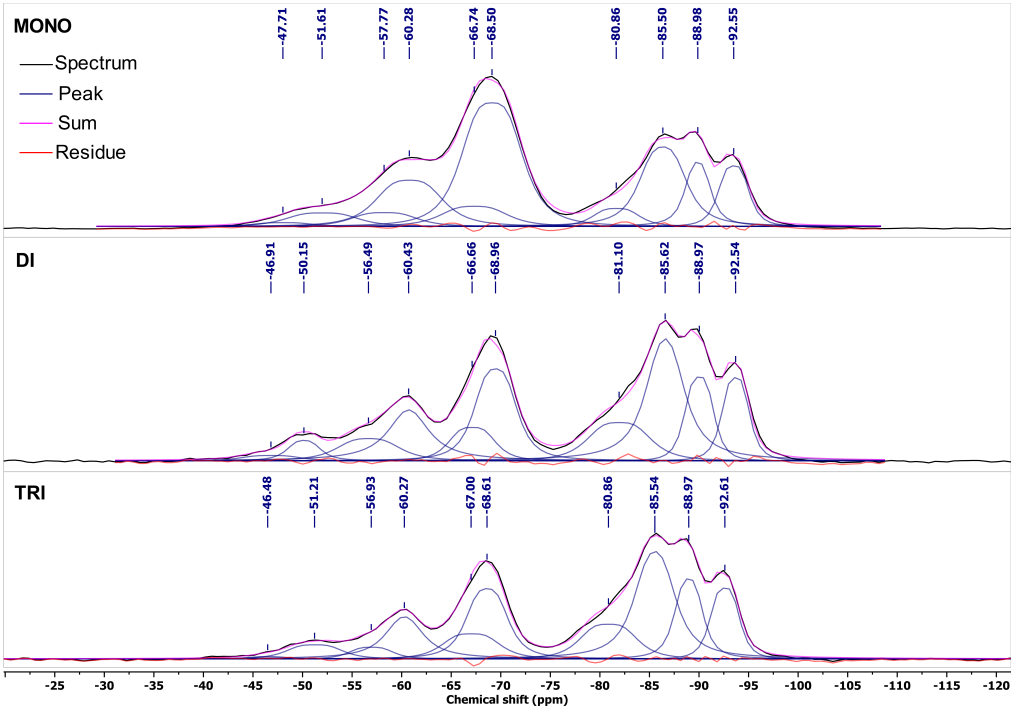

Figure 4.31: ^{29}Si CP-MAS NMR spectrum of MONO, DI and TRI-modified SLDH measured at 10 kHz.

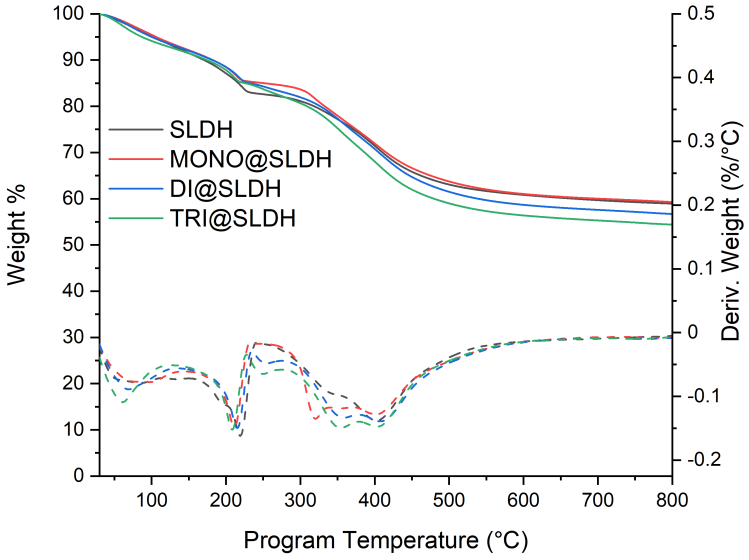

Figure 4.32: TGA thermal curve of SLDH and amine (MONO, DI, TRI)-modified SLDH.The derivative trace is shown below (dotted line).

solution show hydrolysed groups at lower shift due to the acid base reaction with the amino group of the alkyl chain ($Si-O^{-}\cdots H_3N^{+}-R$).[10,48] The resonances from -76 to -96 ppm discussed previously in more detail (Figure 4.20) are present in all samples and can be fitted by the same four distinct resonances at 81, 86, 89 and 93 ppm.

TGA traces of the different amino silane-modified SLDH are shown in Figure 4.32. The SLDH modified by the amino silanes with shorter alkyl chains show similar decomposition traces with two additional peaks in the derivative weight plot. The initial weight loss attributed to loss of H_2O and CO_2 shifts to a maximum weight loss at 70 and 80 °C (for DI@SLDH and MONO@SLDH, respectively), suggesting a stronger interaction energy with the sorbent. DI@SLDH has a decreased mass loss at 250 °C compared to TRI@SLDH although they have similar amine densities (Table 4.10); this is attributed to the lower molecular mass of the grafted silane. Unexpectedly, the MONO@SLDH does not show the thermal event at 250 °C, instead showing a new peak at 325 °C, suggesting that the shortening of the alkyl chain has stabilised this silane species. The thermal decomposition of the

monolayer at temperatures between 300 to 450 °C shows a similar trend with the mass loss decreasing due to the decreasing molecular weight of the alkyl chain being pyrolysed.

The CO_2 adsorption isotherms for the SLDH modified with the different amino silanes are shown in Figure 4.33. The SLDH modified with the MONO and DI amino silanes also show the Type I isotherm profile, but both show increased DAC CO_2 capacity: 0.44 and 0.311 $\mathrm{mmol_{CO_2}\,g^{-1}}$, respectively. This trend differs from those previously reported, with MONO-modified SLDH having a 1.4 and 1.7 times higher capacity than the DI and TRI-modified SLDH.[3] The amine density and amine efficiency are presented in Table 4.10. This shows that although the amine density increases with the number of amine groups in the functional chain of the silane, the amount of silane grafted decreases. This suggests that the shorter alkyl chains on the silane experience less steric interactions on the surface, allowing more efficient packing during the grafting process. Table 4.11 shows the calculated estimate for the surface density of the silanes, the average surface domain of each group and the average radius of the domain compared to the length of the alkyl chain. This estimate was made using the method described by Yoo *et al.*; total hydrolysis of the silane was assumed to calculate the amount grafted per gram of SLDH ($\text{Silane loading}_{g_{SLDH}} = \frac{\text{Silane loading}_{\%}}{1-(\text{Silane loading}_{\%} * MW)}$). The average surface density was then found by dividing this amount by the SLDH SSA ($347\,\mathrm{m^2\,g^{-1}}$, $D = \frac{\text{Silane loading}_{g_{SLDH}}}{\text{SSA}}$), with the average domain given by its inverse ($A = \frac{1}{D}$), from which the radius of the domain was calculated (assuming a circular domain, $R = \sqrt{\frac{1}{D\pi}}$).[22] The radius of the silane domain increases with the length of the alkyl chain of the amino-silane (3.982, 4.641 and 4.747 Å for MONO, DI and TRI, respectively), indicating that a higher grafting density is possible. For all the amino silanes, the radius remains shorter than the length of the alkyl chain, allowing interaction between the chains, both in the formation of a alkylammonium carbamate ion pair for CO_2 binding and sterically during the grafting process.

The amine efficiency increases with the decreasing amount of amine groups, indicating that more of the amine groups in MONO@SLDH and DI@SLDH are available to react with CO_2 and that the shorter chain enhances diffusion, as has been reported previously.[3] This is the opposite trend to that seen for MCM-48 where the amine efficiency increases with the alkyl chain length.[49] This is likely due to the decreased silane density (radius of domain = 5.66 Å for MONO@MCM-48) preventing interaction between the amines.

These samples were sent to our collaborators in the group of Dr. Xuancan Zhu at Shanghai Jiao Tong University for testing under dynamic conditions. Their measurements under static and dynamic conditions are shown in Figures B.11 and B.10. The trend observed under static conditions is the same as that discussed previously (MONO > DI > TRI) and with the unmodified SLDH outperforming the amine-modified samples. The DAC capacity values differ with the SLDH having a higher capacity of $0.353\,\mathrm{mmol_{CO_2}\,g^{-1}}$ and the amine-modified SLDH having lower capacities (TRI@SLDH $0.187\,\mathrm{mmol_{CO_2}\,g^{-1}}$ and DI, MONO $\approx 0.3\,\mathrm{mmol_{CO_2}\,g^{-1}}$). Under dynamic conditions, the trend of DAC adsorption capacities between the amine-modified SLDHs is inverted (TRI > DI > MONO). All the samples show similar adsorption rates for the first 15 min, reaching $0.15\,\mathrm{mmol_{CO_2}\,g^{-1}}$ the uptake rate then slows, with samples not saturated after 2 h at uptakes of $\approx 0.3\,\mathrm{mmol_{CO_2}\,g^{-1}}$. The enhancement of the TRI@SLDH DAC capacity implies either that the static capacity measurement is incorrect or that the uptake is enhanced in this setup, potentially by moisture in the gas stream. The samples reach a capacity of $> 0.225\,\mathrm{mmol_{CO_2}\,g^{-1}}$ after 40 min (75% of the uptake after 2 h), indicating potential for short cycle times.

Effect of amine substituent groups

As the MONO amino-silane produced modified SLDH with the highest DAC CO_2 capacity, the type of the amine was investigated to determine any influence on the reaction of the amine with CO_2 and the resulting DAC CO_2 capacity. Two commercially available silanes similar to MONO were selected, with the amine

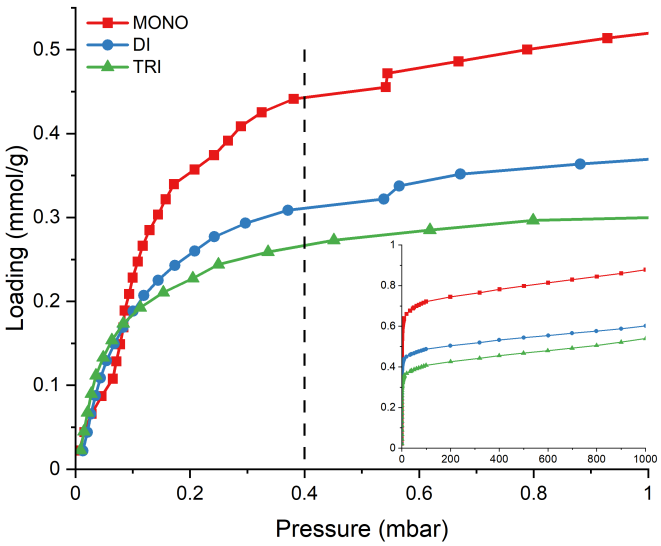

Figure 4.33: CO_2 adsorption isotherms for amine (MONO, DI and TRI)-modified SLDH. The low pressure region is shown in the main graph and the full isotherm is shown in the insert. The irregular steps observed are attributed to measurement artefacts.

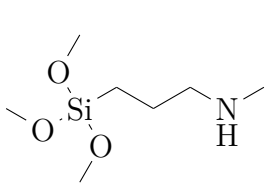

(a) Trimethoxy[3-(methylamino)propyl]-silane (MONO-Me).

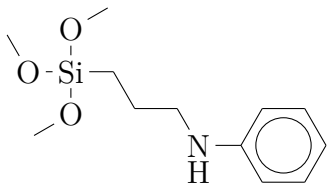

(b) N-[3-(trimethoxysilyl)propyl]aniline (MONO-Ph).

Figure 4.34: Structures of MONO-Me and MONO-Ph.

Table 4.10: N weight percentage, amine and silane density, DAC CO_2 capcity and amine efficiency for SLDH grafted with MONO, DI and TRI.

Sample	N (av. wt%)	N ($mmol_N\,g^{-1}$)	Silane loading ($mmol\,g^{-1}$)	CO_2 capacity ($mmol\,g^{-1}$)	Amine efficiency
SLDH	0	0	0	0.299	-
MONO@SLDH	1.62	1.157	1.157	0.443	0.383
DI@SLDH	2.385	1.703	0.851	0.311	0.183
TRI@SLDH	3.42	2.442	0.814	0.267	0.109

Table 4.11: The average silane density, domain and associated inter-silane distance for SLDH grafted with MONO, DI and TRI. SLDH SSA = $347\,m^2\,g^{-1}$

Sample	Silane loading ($mmol_N\,g^{-1}$)	M_r ($g\,mol^{-1}$)[a]	Silane loading ($mmol_N\,g^{-1}_{SLDH}$)[b]	Silane density (nm^{-2})[c]	Silane domain (nm^2)[d]	Radius of domain (Å)[e]	Alkyl chain length (Å)[f]
MONO@SLDH	1.157	86.19	1.285	2.007	0.498	3.982	5.2
DI@SLDH	0.851	129.26	0.957	1.478	0.677	4.641	8.9
TRI@SLDH	0.814	172.32	0.947	1.412	0.708	4.747	12.4

[a] Molecular weight (MW) of surface grafted organo-silane (Si + Alkyl chain)

[b] Silane loading per gram of SLDH calculated by $\frac{\text{Silane loading}}{1-(\text{Silane loading}*MW)}$

[c] Silane density (D) is calculated by dividing the silane density per g of SLDH by the surface area of the unmodified SLDH: $\frac{\text{Silane loading}}{\text{SSA}}$

[d] The average silane domain is given by $\frac{1}{D}$

[e] Assuming the domain of each grafted silane is circular the average radius (R) of the domain is given by $R = \sqrt{\frac{1}{D\pi}}$

[f] Estimates of the length of the alkyl chain as reported by Yoo, Lee and Jones[22]

group modified with a methyl (Trimethoxy[3-(methylamino)propyl]silane, MONO-Me) or phenyl (N-[3-(Trimethoxysilyl)propyl]aniline, MONO-Ph) group (Figure 4.34).

MONO-Me and MONO-Ph modified SLDHs were prepared in a similar process to the previously discussed amino-silane TRI-modified SLDH discussed previously (for example Chapter 4.2). A full description of the experiments are given in Chapter 4.3.6.

The FTIR spectra are shown in Figure 4.35. The adsorption bands are similar to those seen for MONO@SLDH (Figure 4.28), but are missing the strong N−H band at 1570 cm^{-1}, characteristic of primary amines, as both feature secondary amine groups. MONO-Ph@SLDH also has a C=C adsorption band at 1604 cm^{-1} from the aromatic phenyl group.

The TGA thermal traces are shown in Figure 4.36. Similar thermal events to those observed for MONO@SLDH (Figure 4.32) are seen: a slow mass loss up to 150 °C without the peak loss at ≈ 60 °C for MONO-Ph, attributed to its reduced CO_2

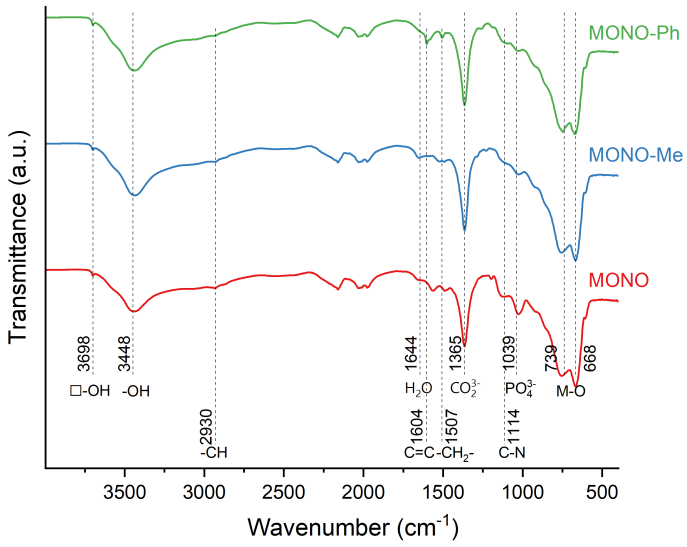

Figure 4.35: FTIR spectra of amine (MONO-Me and MONO-Ph)-modified SLDH. □ indicates a peak arising from brucite.

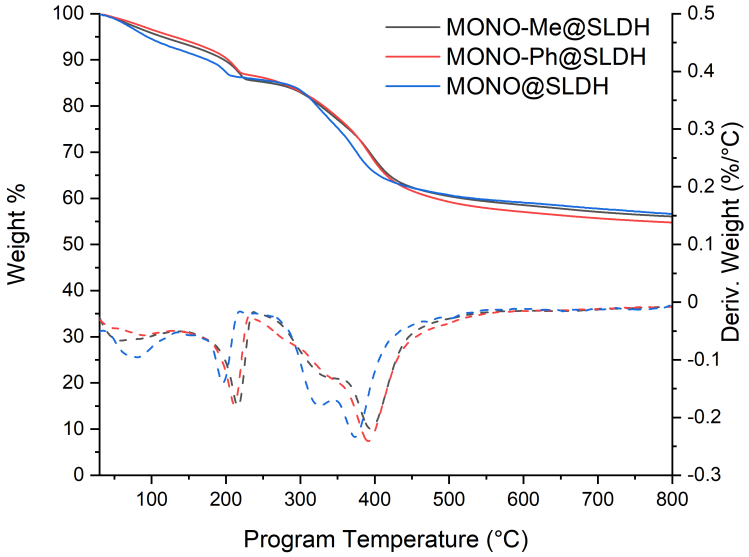

Figure 4.36: TGA thermal curve of SLDH and amine (MONO-Me, MONO-Ph)-modified SLDH. TGA curves for MONO@SLDH shifted to lower temperature due to a reduced sample mass used for analysis.

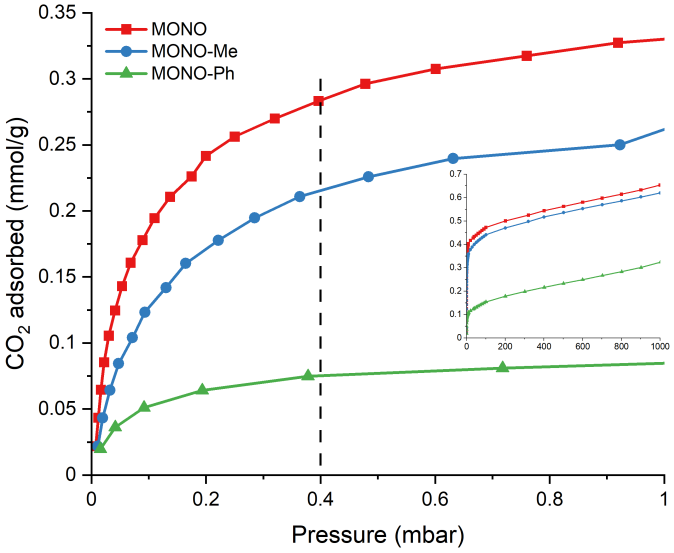

Figure 4.37: CO_2 adsorption isotherms for amine (MONO, MONO-Me and MONO-Ph) modified SLDH. The low pressure region is shown in the main graph and the full isotherm is shown in the insert.

Table 4.12: N weight percentage, amine and silane density, DAC CO_2 capacity and amine efficiency for amine (MONO, MONO-Me and MONO-Ph)-modified SLDH.

Sample	N (av. wt%)	N ($mmol_N\,g^{-1}$)	Silane loading ($mmol\,g^{-1}$)	CO_2 capacity ($mmol\,g^{-1}$)	Amine efficiency
SLDH	0	0	0	0.25	-
MONO@SLDH	1.9	1.356	1.356	0.284	0.209
MONO-Me@SLDH	0.98	0.700	0.700	0.215	0.308
MONO-Ph@SLDH	0.83	0.593	0.593	0.075	0.127

capacity (Figure 4.33), no clear thermal event at 250 °C as seen for DI@SLDH and TRI@SLDH or at 325 °C for MONO@SLDH, instead displaying a steady decrease before a higher mass loss ≈ 400 °C.

The CO_2 adsorption isotherms for the SLDH modified with MONO-Me and MONO-Ph are shown in Figure 4.37. All the isotherms show the Type I isotherm profile seen for the previously discussed amino-silane modified materials. The DAC CO_2 capacities for the secondary amine (MONO-Me and MONO-Ph)-modified SLDHs (0.22 and 0.07 $mmol_{CO_2}\,g^{-1}$, respectively) are lower than that of the primary amine-modified SLDH (0.284 $mmol_{CO_2}\,g^{-1}$). The amine density and amine efficiency are shown in Table 4.12, which shows that for all three amino-silane grafted SLDHs, the amount of silane grafted is lower for the substituted amines compared to the MONO@SLDH sample (1.356, 0.7 and 0.593 $mmol\,g^{-1}$ for MONO, MONO-Me and MONO-Ph).

The secondary amine modified with a methyl group (MONO-Me) exhibits a lower DAC capacity compared to the primary amine (MONO). However, it demonstrates a higher amine efficiency, suggesting that methylation positively influences the stability of the ammonium carbamate formed. Unfortunately, the overall capacity is limited by the reduced density of grafted silane.

The phenyl-modified secondary amine displays significantly different performance; although the amine density is similar to methyl-modified amine (with the slight decrease attributed to the increased bulk of the phenyl group) the DAC CO_2 capacity is approximately 33% of the MONO-Me@SLDH sample. The capacity at

higher pressures is also significantly reduced, reaching 0.109 and 0.301 $mmol_{CO_2}\ g^{-1}$ at 10 and 1000 mbar, respectively. If the decrease in amine efficiency were solely due to a decrease in affinity, it would be expected that the capacity would tend to a similar value at high pressures where all the sites are close to saturation in both samples. As they instead show similar increases due to physisorption (shown by similar gradients above 200 mbar), the number of sites available for chemisorption must decrease. Three potential explanations for this phenomenon are proposed: firstly, the phenylaniline moiety might not engage in a reaction with CO_2 in the solid sorbent, leading to any uptake being attributable to the SLDH support with a reduction in available sites due to the grafting process (this is likely given that aniline is a weak base ($pK_a = 4.63$) and that stronger bases are utilised in aqueous systems to form the ammonium component of the ion pair).[50,51] Alternatively, partial oxidation of aniline upon exposure to air may reduce the amount of amine sites.[52] Finally, the steric hindrance due to the phenyl group may prevent the proton transfer necessary for the formation of a stable alkylammonium carbamate ion pair. Further spectroscopic studies to identify the species formed upon CO_2 adsorption are needed to determine which of these causes is responsible for the decrease in amine efficiency. The low uptake of the MONO-Ph sample does provide a convenient control to demonstrate that the uptake under DAC conditions is primarily linked to the amine modification and is not simply residual uptake from the support.

4.2.4 Process energy calculations

The sorbent production cost and energy consumption are two of the crucial considerations when evaluating a DAC process. Amine-modified SLDHs provide a lower cost alternative to metal organic frameworks and templated mesoporous silicas, thus addressing the first point. A brief evaluation of the energy cost for their use in the DAC process is given below to address the second.

Several processes contribute to the energy consumption: fans to pass the air over the material in the contactor during the adsorption step and heaters and/or vacuum

pumps needed to induce CO_2 release during the desorption step. However, 84 to 96 % of the operational energy requirements are estimated to be used by the thermal regeneration process.[53] The minimum thermal energy required for the thermal regeneration (Q_{regen}) can be estimated thermodynamically depending on: the heat capacity ($C_{p,sorbent}$), temperature increase needed ($\Delta T = T_{desorb} - T_{adsorb}$), enthalpy of CO_2 adsorption (ΔH_{adsorb}) and the CO_2 adsorption capacity (q_{CO_2}). This is an underestimate as it does not account for H_2O adsorption which may be substantial.

$$Q_{regen} = \Big[\frac{C_{p,sorbent}}{q_{CO_2}} + C_{p,CO_{2\,(g)}}\Big]\Delta T + \Delta H_{adsorb}$$

Thus, it can be seen that to lower the energy of regeneration, a sorbent should posses a low specific heat capacity, a low regeneration temperature, high DAC CO_2 adsorption capacity and low enthalpy of adsorption. The specific heat capacity of the sorbents estimated from the heat flow during DSC experiments (Figure B.12 and Table B.3), a desorption temperature of 120 °C and the enthalpy of adsorption calculated for TRI@SLDH were used.

The average heat capacity of the SLDH from 30 to 120 °C is calculated from the DSC heat flow as $1.76\,J\,K^{-1}\,g^{-1}$. This is higher than that previously reported for Mg_3Al LDHs by Bernard *et al.* ($953\,J\,K^{-1}\,mol^{-1}$, $1.53\,J\,K^{-1}\,g^{-1}$)[54] and Prentice *et al.* ($958.67\,J\,K^{-1}\,mol^{-1}$, $1.61\,J\,K^{-1}\,g^{-1}$) at 298 K.[55] The amine-modified SLDHs possess similar heat capacities (1.63 to $1.89\,J\,K^{-1}\,g^{-1}$), with the increases attributed to the entropy changes from the mobile alkyl chains.

TGA-MS of TRI@SLDH desorption of CO_2 captured from dry air (Figure 4.38) shows a peak desorption temperature of 86.4 °C ($20\,K\,min^{-1}$) with total desorption complete 5 min after reaching the regeneration temperature (120 °C). Temperature programmed desorption of TRI@SLDH-Dry exposed to pure CO_2 (Figures 4.39 and B.13) shows the amine-modified SLDHs have a maximum release of CO_2 at 57.5 °C ($5\,K\,min^{-1}$) and 45 °C ($1\,K\,min^{-1}$) but continue to steadily release CO_2 up to the set desorption temperature (120 °C). Peak desorption occurring at temperatures lower than 120 °C suggests the potential for lowering the regeneration temperature,

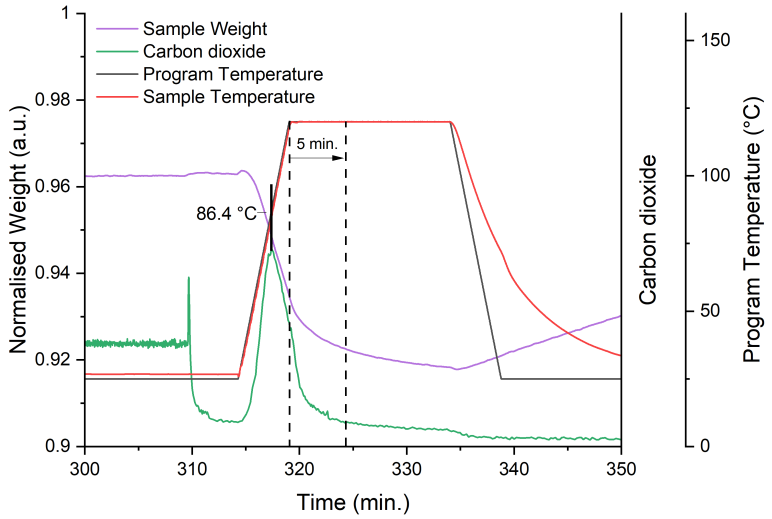

Figure 4.38: TGA-MS data of the desorption step of TRI@SLDH. The peak desorption temperature and the time where the CO_2 concentration has returned to background levels are marked.

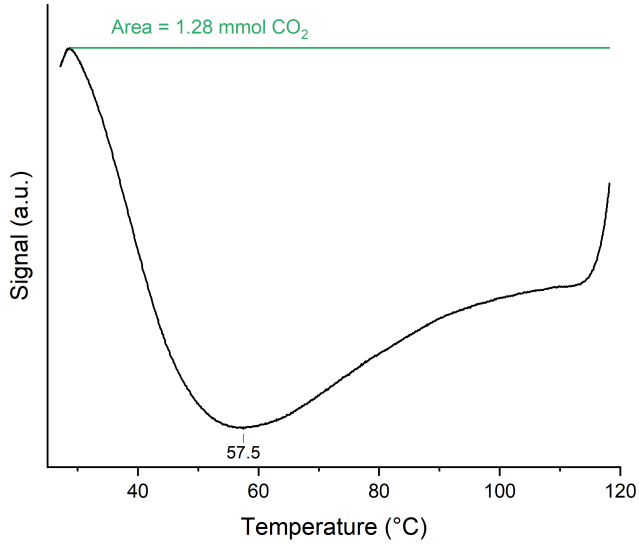

Figure 4.39: CO_2 TPD signal for TRI@SLDH-Dry at $5\,^{\circ}\mathrm{C\,min^{-1}}$. The CO_2 capacity calculated from the gas flow rate is given.

thereby reducing the associated energy cost (sensible energy). Specifically, heating from 25 to 120 °C contributes ≈ 80 % to the total calculated energy, with a regeneration temperature of 80 °C achieving a 42% reduction in sensible energy. However, this modification may lead to a decrease in capacity.

In a study by the US National Academies, modelling of a solid sorbent system was shown to have energy requirements from 1.93 to 23.09 $\mathrm{GJ\,t_{CO_2}^{-1}}$ (the minimum work thermodynamically possible being 0.45 $\mathrm{GJ\,t_{CO_2}^{-1}}$) between a best and worse case scenario with 1.85 to 19.3 $\mathrm{GJ\,t_{CO_2}^{-1}}$ required for the thermal desorption step.[53] In the worst-case scenario, achieving negative emissions is not feasible when fossil fuels remain in use, necessitating a fully green energy grid. However, moderate energy requirements, such as 4.8 $\mathrm{GJ_t\,t_{CO_2}^{-1}}$ of thermal energy, are still capable of producing negative emissions even when thermal energy is derived from coal combustion, with 0.44 $\mathrm{Mt_{CO_2}}$ produced per $\mathrm{Mt_{CO_2}}$ captured, at a cost of $ 288 $\mathrm{t_{CO_2}^{-1}}$.

The estimates of energy required for a process using amine-modified SLDHs are calculated using the thermodynamic parameters shown in Table 4.13 at 10.04 $\mathrm{GJ_t\,t_{CO_2}^{-1}}$ for MONO@SLDH and 11.73 $\mathrm{GJ_t\,t_{CO_2}^{-1}}$ TRI@SLDH-Dry.

Table 4.13: Thermodynamic parameters for process energy calculations. $C_{p,\mathrm{CO_{2(g)}}}$ is the molar heat capacity of CO_2. $C_{p,sorbent}$ is the heat capacity of the sorbent. $q_{\mathrm{CO_2}}$ is the quantity of CO_2 adsorbed per cycle. ΔT is the difference between the adsorption and desorption temperatures. ΔH_{adsorb} is the enthalpy of adsorption of CO_2 onto the sorbent. Q_{regen} is the energy requirement for CO_2 capture using the sorbent.

Parameter	Sample	Value
$C_{p,\mathrm{CO_{2(g)}}}$ [a]		37.2 $\mathrm{J\,mol^{-1}\,K^{-1}}$
ΔT		95 °C
$C_{p,sorbent}$	MONO@SLDH	1.629 $\mathrm{J\,K^{-1}\,g}$
$q_{\mathrm{CO_2}}$	MONO@SLDH	0.440 $\mathrm{mmol\,g^{-1}}$
ΔH_{adsorb}	TRI@SLDH	86.4 $\mathrm{kJ\,mol^{-1}}$
Q_{regen}	MONO@SLDH	441.650 $\mathrm{kJ_t\,mol^{-1}}$ 10.04 $\mathrm{GJ_t\,t_{CO_2}^{-1}}$
$C_{p,sorbent}$	TRI@SLDH-Dry	1.749 $\mathrm{J\,K^{-1}\,g}$
$q_{\mathrm{CO_2}}$	TRI@SLDH-Dry	0.390 $\mathrm{mmol\,g^{-1}}$
ΔH_{adsorb}	TRI@SLDH	86.4 $\mathrm{kJ\,mol^{-1}}$
Q_{regen}	TRI@SLDH-Dry	515.972 $\mathrm{kJ_t\,mol^{-1}}$ 11.73 $\mathrm{GJ_t\,t_{CO_2}^{-1}}$

[a] Heat capacity at 25 °C.[56]

These values are significantly higher than those previously reported for amine-modified LDH by Ge *et al.* ($4.2\,\mathrm{GJ_t\,t_{CO_2}^{-1}}$), due to increased values of C_p, ΔT and ΔH_{adsorb} and a reduced q_{CO_2}.[57] Their work showed that optimisation of the desorption temperature led to a reduction in the specific energy requirements, achieving a minimum of $2.27\,\mathrm{GJ_t\,t_{CO_2}^{-1}}$ at a desorption temperature of 40 °C. The calculated energy requirements for desorption align with those calculated by Surkatti *et al.* for PEI impregnated SBA-15 and the common commercial sorbent Lewatit, which are 150 and $225\,\mathrm{kJ_t\,mol_{CO_2}^{-1}}$, respectively, with adsorption at 21 °C and desorption at 90 °C.[14] Therefore further studies to optimise the process conditions are imperative to make these SLDH-based sorbents competitive compared to other materials currently reported.

4.2.5 CO_2 productivity

According to Balasubramaniam *et al.*, the key performance metrics for a DAC process are the dry CO_2 purity (molar fraction of CO_2 in the extract stream which depends on the regeneration method), the specific energy requirement (discussed previously) and the CO_2 productivity which is an indicator of how large the capture plant would be.[58] They define the productivity of a DAC process as the tonnes of CO_2 extracted per day per cubic metre ($\mathrm{t_{CO_2}\,d^{-1}\,m^{-3}}$).

$$Pr = \frac{\text{Mass of CO}_2\text{ captured}}{(\text{Volume of the sorbent})(\text{Cycle time})}$$

Balasubramaniam *et al.* estimated that the technology used by the Climeworks plant had a specific energy requirement of $\approx 10.8\,\mathrm{MJ_t\,kg^{-1}}$ and a productivity of $0.074\,\mathrm{t_{CO_2}\,d^{-1}\,m^{-3}}$, providing benchmark values for comparison. The specific energy requirement is comparable to that calculated for the SLDH sorbents and a brief evaluation of the productivity of SLDH-based sorbents is given for comparison.

The productivity is related to both the volumetric adsorption capacity and the length of the adsorption/desorption process. The high powder density of the parent SLDH material also results in the amine-modified sorbent possessing a high powder density (MONO@SLDH $0.727\,\mathrm{g\,mL^{-1}}$, TRI@SLDH-Dry $0.792\,\mathrm{g\,mL^{-1}}$).

This gives DAC volumetric adsorption capacities for the highest capacity materials of $0.320\,\mathrm{mmol_{CO_2}\,mL^{-1}}$ (MONO@SLDH) and $0.309\,\mathrm{mmol_{CO_2}\,mL^{-1}}$ (TRI@SLDH-Dry), significantly higher than the reference TRI@SBA-15 ($0.082\,\mathrm{mmol_{CO_2}\,mL^{-1}}$). From the TGA data in Figure B.10 and TGA-MS (Figure B.14), CO_2 adsorption to the saturation capacity takes $> 2\,\mathrm{h}$, but the uptake rate is minimal after this time. Figures 4.38 and B.2 show CO_2 desorption is complete after only 5 min using a $20\,^{\circ}\mathrm{C\,min^{-1}}$ temperature ramp rate. Using a 2 h adsorption period at 25 °C, a 10 min desorption period at 120 °C and a 20 °C/min ramp rate gives a cycle time of 139.5 min. This gives productivities of the MONO@SLDH and TRI@SLDH-Dry systems as $0.145\,\mathrm{t_{CO_2}\,d^{-1}\,m^{-3}}$ and $0.140\,\mathrm{t_{CO_2}\,d^{-1}\,m^{-3}}$ respectively.

$$Pr = \frac{q_{CO_2,V} * MR_{CO_2} * 10^{-3}}{\text{Cycle time}}$$

This surpasses both the Climeworks benchmarks and the materials evaluated by Balasubramaniam *et al.*, largely due to the high tap density and aided by a relatively short cycle time. Balasubramaniam *et al.* estimate the volume of the sorbent using an estimated bed voidage of 0.4 and the sorbent's particle density (average density within a particle including interstitial pores),[59] this corresponds to a loose packing and is slightly less dense than that for dense (tapped) bed voidage (0.375).[60]

4.3 Experimental details

4.3.1 Reagents and chemicals

The amino silanes: 3-aminopropyl-triethoxysilane (MONO), trimethoxy[3-(methylamino)propyl]-silane (MONO-Me), N-[3-(trimethoxysilyl)-propyl]-aniline (MONO-Ph), N-2-aminoethyl-3-aminopropyl-trimethoxysilane (DI) and N^1-(3-trimethoxysilylpropyl)diethylenetriamine (TRI) were purchased from Sigma Aldrich and used without further purification. The solvents: toluene, xylene, cyclohexane, hexane and methanol were purchased from Sigma Aldrich and used without further purification. Dry toluene was made by passing it through a solvent purification system (SPF) and was stored in an ampoule under a N_2 atmosphere prior to use.

4.3.2 Synthesis of TRI-modified SLDH

0.2 g of SLDH was dried under vacuum in a vacuum oven at 100 °C for 1 h and then suspended in 15 mL toluene before 0.6 mL TRI was added dropwise. It was then left to stir for 15 min (750 RPM) under a slow flow of N_2 through the headspace before being heated to 85 °C and stirred for 16 h. The solution was centrifuged at 1000 RPM for 10 min before washing by re-suspension and centrifuging sequentially in (two times 20 mL) toluene, (20 mL) hexane and (20 mL) methanol. The sample was then dried overnight at 60 °C under vacuum.

4.3.3 Effect of grafting solvent on TRI-modified SLDH

1 g of SLDH was dried under vacuum in a vacuum oven at 100 °C for 1 h and then suspended in 75 mL toluene before 3 mL of TRI was added dropwise. It was then left to stir (750 RPM) for 15 min under a slow flow of N_2 through the headspace before being heated to 85 °C and stirred for 16 h. The solution was filtered and washed with (two times 25 mL) toluene, (25 mL) hexane and (25 mL) methanol. The sample was then dried overnight at 60 °C under vacuum.

4.3.4 Effect of moisture on TRI-modified SLDH

TRI@SLDH dry was made under similar conditions (Chapter 4.3.3) with the inclusion of Schlenk techniques. In summary, 1 g of SLDH was dried at 100 °C under vacuum in a Schlenk flask overnight (16 h), cooled and then 75 mL of dried (using a solvent purification system) toluene was added via cannula. 3 mL TRI was added dropwise via syringe under vigorous stirring and left to stir for 15 min before being heated to 85 °C and stirred for 16 h. The suspension was filtered by filter cannula and washed by sequential resuspension and filtration with approximately (two times 25 mL) toluene, (25 mL) hexane and (25 mL) methanol to remove excess TRI before being collected via vacuum filtration. The sample was then dried overnight at 60 °C under vacuum.

4.3.5 Effect of amine number on amine-modified SLDH

4 g of SLDH was dried under vacuum in a vacuum oven at 100 °C for 1 h and then suspended in 300 mL toluene before 12 mL of amino silane (MONO, DI, TRI) was added dropwise. It was left to stir (750 RPM) for 15 min under a slow flow of N_2 through the headspace before being heated to 85 °C and stirred for 16 h. The solution was filtered and washed with (two times 100 mL) toluene, (100 mL) hexane and (100 mL) methanol. The sample was then dried overnight at 60 °C under vacuum.

4.3.6 Effect of amine type on amine-modified SLDH

0.2 g of SLDH was dried under vacuum in a vacuum oven at 100 °C for 1 h and then suspended in 15 mL toluene before 0.6 mL of amino silane (MONO, MONO-Me, MONO-Ph) was added dropwise. It was left to stir for 15 min (750 RPM) under a slow flow of N_2 through the headspace before being heated to 85 °C and stirred for 16 h. The solution was filtered and washed with (two times 20 mL) toluene, (20 mL) hexane and (20 mL) methanol. The sample was then dried overnight at 60 °C under vacuum.

4.4 Conclusions and future work

SLDHs were successfully grafted with amino silane moieties to produce materials which can be used as CO_2 sorbents. The grafted amine density can be varied by the solvent used and the removal of trace water, with lower amine densities giving higher DAC capacities. This was attributed to kinetic limitations caused by pore blocking of the material. Reducing the length of the amine-containing organic chains increased the DAC capacity, attributed to a similar kinetic phenomenon.

The best samples of MONO@SLDH and TRI@SLDH-Dry showed DAC capacities of $0.443\,\mathrm{mmol_{CO_2}\,g^{-1}}$ and $0.391\,\mathrm{mmol_{CO_2}\,g^{-1}}$. Estimates of the process energy and CO_2 productivity for the sorbents were comparable to that estimated for the

currently employed sorbents by Climeworks, but the process energy is larger than similar work reported in the literature.

The sorbents were characterised by FTIR, TGA and SS-NMR. The nature of the environments producing resonances from −75 to −100 ppm in the ^{29}Si SS-NMR still require conclusive identification, potentially by the synthesis of the novel organo-functionalised silicophosphates for comparison or further multi-nuclear quantum correlation experiments. TGA-MS may also help to confirm the origin of the different mass losses observed.

The unusual increasing enthalpy of adsorption observed for the sorbents should be corroborated by isothermal calorimetric measurements. If these results are in agreement, further modelling is needed to explain this phenomenon.

Lastly, the process energy and productivity for the two best sorbents (MONO@SLDH and TRI@SLDH-Dry) were calculated and are comparable to estimates of the materials used commercially. Many reports in the literature use lower regeneration temperatures and peak CO_2 release for these materials was observed at temperatures significantly below 120 °C, suggesting lower regeneration temperatures may be employed. Further work exploring the sorbent capacity at lower regeneration temperatures is needed which ideally will lower the process energy cost significantly.

Initial cyclic stability tests using a TGA-MS setup were conducted, but further work evaluating the sorbent under true process conditions is needed.

References

(1) X. Zhu, T. Ge, F. Yang, M. Lyu, C. Chen, D. O'Hare and R. Wang, *J. Mater. Chem. A*, 2020, **8**, 16421–16428.

(2) A.-Y. Park, H. Kwon, A. J. Woo and S.-J. Kim, *Adv. Mater.*, 2005, **17**, 106–109.

(3) J. Wang, L. A. Stevens, T. C. Drage and J. Wood, *Chem. Eng. Sci.*, 2012, **68**, 424–431.

(4) B. Wadi, A. Golmakani, V. Manovic and S. A. Nabavi, *Ind. & Eng. Chem. Res.*, 2021, **60**, 13309–13317.

(5) G. P. Knowles, S. W. Delaney and A. L. Chaffee, *Ind. & Eng. Chem. Res.*, 2006, **45**, 2626–2633.

(6) X. Zhu, M. Lyu, T. Ge, J. Wu, C. Chen, F. Yang, D. O'Hare and R. Wang, *Cell Rep. Phys. Sci.*, 2021, **2**, 100484.

(7) Q. Grossmann, V. Stampi-Bombelli, A. Yakimov, S. Docherty, C. Copéret and M. Mazzotti, *Ind. & Eng. Chem. Res.*, 2023, **62**, 13594–13611.

(8) P. J. E. Harlick and A. Sayari, *Ind. & Eng. Chem. Res.*, 2007, **46**, 446–458.

(9) K.-M. Li, J.-G. Jiang, S.-C. Tian, X.-J. Chen and F. Yan, *J. Phys. Chem. C*, 2014, **118**, 2454–2462.

(10) Y. Sato, R. Hayami and T. Gunji, *J. Sol-Gel Sci. Technol.*, 2022, **104**, 36–52.

(11) K. Imai and Y. Kaneko, *Inorg. Chem.*, 2017, **56**, 4133–4140.

(12) T. Matsumoto and Y. Kaneko, *Chem. Lett.*, 2018, **47**, 864–867.

(13) W. Yang, Y. Kim, P. K. T. Liu, M. Sahimi and T. T. Tsotsis, *Chem. Eng. Sci.*, 2002, **57**, 2945–2953.

(14) R. Surkatti, Y. M. Abdullatif, R. Muhammad, A. Sodiq, K. Mroue, T. Al-Ansari and A. I. Amhamed, *Sep. Purif. Technol.*, 2025, **354**, 128641.

(15) K. Matsuda, N. Iio, M. Kawashimo, A. Okuda, R. Fukuzaki, N. Tarutani, K. Katagiri and K. Inumaru, *Inorg. Chem.*, 2023, **62**, 17276–17287.

(16) A. Zarinwall, T. Waniek, R. Saadat, U. Braun, H. Sturm and G. Garnweitner, *Langmuir*, 2021, **37**, 171–179.

(17) R. Yamazaki, N. Karyu, M. Noda, S. Fujii and Y. Nakamura, *J. Appl. Polym. Sci.*, 2016, **133**, 43256.

(18) G. Yu, Y. Zhou, R. Yang, M. Wang, L. Shen, Y. Li, N. Xue, X. Guo, W. Ding and L. Peng, *J. Phys. Chem. C*, 2015, **119**, 12325–12334.

(19) P. Kenyon, S. Roberts, Z. R. Turner, N. H. Rees and D. O'Hare, *J. Phys. Chem. C*, 2024, **128**, 12249–12258.

(20) M. A. O. Lourenço, M. Fontana, P. Jagdale, C. F. Pirri and S. Bocchini, *Chem. Eng. J.*, 2021, **414**, 128763.

(21) M. Kristl, U. Ostroško, I. Ban, I. Petrinić and J. Stergar, *J. Therm. Anal. Calorim.*, 2024, **149**, 10449–10463.

(22) C.-J. Yoo, L.-C. Lee and C. W. Jones, *Langmuir*, 2015, **31**, 13350–13360.

(23) Y. Wang, J.-T. Anyanwu, Z. Hu and R. T. Yang, *Sep. Purif. Technol.*, 2023, **309**, 123030.

(24) Y. Gao, Z. Zhang, J. Wu, X. Yi, A. Zheng, A. Umar, D. O'Hare and Q. Wang, *J. Mater. Chem. A*, 2013, **1**, 12782–12790.

(25) S. Radha and A. Navrotsky, *J. Phys. Chem. C*, 2014, **118**, 29836–29844.

(26) S. Ishihara, P. Sahoo, K. Deguchi, S. Ohki, M. Tansho, T. Shimizu, J. Labuta, J. P. Hill, K. Ariga, K. Watanabe, Y. Yamauchi, S. Suehara and N. Iyi, *J. Am. Chem. Soc.*, 2013, **135**, 18040–18043.

(27) U. Sharma, B. Tyagi and R. V. Jasra, *Ind. & Eng. Chem. Res.*, 2008, **47**, 9588–9595.

(28) S. Shang, A. Hanif, M. Sun, Y. Tian, Y. S. Ok, I. K. M. Yu, D. C. W. Tsang, Q. Gu and J. Shang, *J. Hazard. Mater.*, 2019, **373**, 285–293.

(29) C. M. Simon, E. Braun, C. Carraro and B. Smit, *Proc. Natl. Acad. Sci.*, 2017, **114**, E287–E296.

(30) T. M. McDonald, J. A. Mason, X. Kong, E. D. Bloch, D. Gygi, A. Dani, V. Crocellà, F. Giordanino, S. O. Odoh, W. S. Drisdell, B. Vlaisavljevich, A. L. Dzubak, R. Poloni, S. K. Schnell, N. Planas, K. Lee, T. Pascal, L. F. Wan, D. Prendergast, J. B. Neaton, B. Smit, J. B. Kortright, L. Gagliardi, S. Bordiga, J. A. Reimer and J. R. Long, *Nature*, 2015, **519**, 303–308.

(31) M. E. Potter, S. H. Pang and C. W. Jones, *Langmuir*, 2017, **33**, 117–124.

(32) M. A. Alkhabbaz, P. Bollini, G. S. Foo, C. Sievers and C. W. Jones, *J. Am. Chem. Soc.*, 2014, **136**, 13170–13173.

(33) M. W. Hahn, J. Jelic, E. Berger, K. Reuter, A. Jentys and J. A. Lercher, *J. Phys. Chem. B*, 2016, **120**, 1988–1995.

(34) G. Gatti, D. Costenaro, C. Vittoni, G. Paul, V. Crocellà, E. Mangano, S. Brandani, S. Bordiga, M. Cossi, L. Marchese and C. Bisio, *Phys. Chem. Chem. Phys.*, 2017, **19**, 14114–14128.

(35) M. L. Pinto, L. Mafra, J. M. Guil, J. Pires and J. Rocha, *Chem. Mater.*, 2011, **23**, 1387–1395.

(36) L. Mafra, T. Čendak, S. Schneider, P. V. Wiper, J. Pires, J. R. B. Gomes and M. L. Pinto, *J. Am. Chem. Soc.*, 2017, **139**, 389–408.

(37) N. A. Brunelli, S. A. Didas, K. Venkatasubbaiah and C. W. Jones, *J. Am. Chem. Soc.*, 2012, **134**, 13950–13953.

(38) L. F. Feitosa, B. B. Pozes, A. S. Silva, L. F. Castro, L. S. C. Júnior, C. B. Quitete and M. A. Fraga, *J. Environ. Chem. Eng.*, 2021, **9**, 104951.

(39) Y. Sánchez-Vicente, L. A. Stevens, C. Pando, M. J. Torralvo, C. E. Snape, T. C. Drage and A. Cabañas, *Chem. Eng. J.*, 2015, **264**, 886–898.

(40) J.-T. Anyanwu, Y. Wang and R. T. Yang, *Chem. Eng. Sci.*, 2022, **254**, 117626.

(41) J. Kirchnerová and G. C. B. Cave, *Can. J. Chem.*, 1976, **54**, 3909–3916.

(42) I. Lukes, M. Borbaruah and L. D. Quin, *J. Am. Chem. Soc.*, 1994, **116**, 1737–1741.

(43) Neeraj, M. Eswaramoorthy and C. N. R. Rao, *Mater. Res. Bull.*, 1998, **33**, 1549–1554.

(44) T. R. Krawietz, P. Lin, K. E. Lotterhos, P. D. Torres, D. H. Barich, A. Clearfield and J. F. Haw, *J. Am. Chem. Soc.*, 1998, **120**, 8502–8511.

(45) C. Coelho, F. Babonneau, T. Azaïs, L. Bonhomme-Coury, J. Maquet, G. Laurent and C. Bonhomme, *J. Sol-Gel Sci. Technol.*, 2006, **40**, 181–189.

(46) N. Hedin and Z. Bacsik, *Curr. Opin. Green Sustain. Chem.*, 2019, **16**, 13–19.

(47) J. B. Bossa, P. Theulé, F. Duvernay, F. Borget and T. Chiavassa, *Astron. & Astrophys.*, 2008, **492**, 719–724.

(48) F. Rousseau, C. Poinsignon, J. Garcia and M. Popall, *Chem. Mater.*, 1995, **7**, 828–839.

(49) H. Nigar, B. Garcia-Baños, F. L. Peñaranda-Foix, J. M. Catalá-Civera, R. Mallada and J. Santamaría, *AIChE J.*, 2016, **62**, 547–555.

(50) D. D. Perrin, *Dissociation Constants of Organic Bases in Aqueous Solution: Supplement 1972*, Butterworths, London, 1972.

(51) B. Delibas, K. J. Kron, D. E. Cotton, N. Salazar, S. M. Sharada and J. M. Dawlaty, *J. Phys. Chem. A*, 2023, **127**, 5162–5170.

(52) T. V.-T. Mai, T. T.-D. Nguyen, H. T. Nguyen, T. T. Nguyen and L. K. Huynh, *Environ. Sci. & Technol.*, 2021, **55**, 7858–7868.

(53) National Academies of Sciences, Engineering and Medicine, *Negative Emissions Technologies and Reliable Sequestration: A Research Agenda*, The National Academies Press, Washington, DC, 2019.

(54) E. Bernard, W. J. Zucha, B. Lothenbach and U. Mäder, *Cem. Concr. Res.*, 2022, **152**, 106674.

(55) D. P. Prentice, L. Gomez-Zamorano, M. Balonis, B. Erdemli, K. Ellison, N. Neithalath, D. Simonetti and G. Sant, *J. Am. Ceram. Soc.*, 2020, **103**, 6025–6039.

(56) J. Chase, M.W., *NIST-JANAF Themochemical Tables, Fourth Edition, Monograph 9*, American Chemical Society, Fourth Edition, 1998, vol. 9, pp. 1–1951.

(57) B. Ge, C. Chen, Y. Xu, S. Roberts, M. Zhang, Q. Shao, D. O'Hare and X. Zhu, *Chem. Eng. J.*, 2024, **500**, 156782.

(58) B. M. Balasubramaniam, P.-T. Thierry, S. Lethier, V. Pugnet, P. Llewellyn and A. Rajendran, *Chem. Eng. J.*, 2024, **485**, 149568.

(59) L. Coucoulas, in *Encyclopedia of Food Sciences and Nutrition (Second Edition)*, ed. B. Caballero, Academic Press, Oxford, 2003, pp. 73–80.

(60) A. de Klerk, *AIChE J.*, 2003, **49**, 2022–2029.

5

Catalytic polypropylene pyrolysis using transition metal-doped SLDHs

Contents

5.1 Introduction

As discussed in Chapter 1.3.1 the plastic crisis has been of growing concern, with the amount produced annually continuing to increase, and with demand outpacing the increase in recycled plastic. Polyolefins such as polyethylene (PE) and polypropylene (PP) account for 67% of post-consumer plastic[1] and cannot be easily recycled, either reaching their end of life in landfill or incineration for energy recovery. Mechanical recycling of the polymers is difficult as contaminants prevent their use in food packaging, one of their common applications. Additionally, hot spots during thermal treatment cause the chains to break, reducing their mechanical strength, and restricting their useful life to a single reprocessing cycle. Chemical recycling is difficult because the polymers lack functional groups and have high bond stability. Pyrolysis, which is thermal degradation without oxygen, is often employed, yielding a distribution of products due to a statistical cleavage of bonds. The process has been well studied and occurs via homolytic bond fission to produce radicals that can stabilise themselves via intramolecular hydrogen transfer before producing lower molecular weight fragments by β-scission. Pyrolysis can be performed at various temperatures with low-temperature pyrolysis ($< 300\,^{\circ}\mathrm{C}$) yielding a higher amount of liquid products than high-temperature pyrolysis ($> 700\,^{\circ}\mathrm{C}$) which produces mostly gaseous products. PP is also noted to be more susceptible to bond scission as a result of the higher stability of the secondary radical formed. Catalytic pyrolysis introduces a catalyst into the pyrolysis reactor that can lower the temperature at which bond fission occurs as well as narrow the product distribution and increase the selectivity. Numerous materials such as Fe_2O_3, $Al_2Si_2O_5(OH)_4$ and Zeolites have been used for catalytic pyrolysis of polypropylene to produce fuel range oils (at $\approx 500\,^{\circ}\mathrm{C}$), with an emphasis on the low cost of the catalyst.[2,3] These catalysts are not selective, producing a range of products up C_{25} and there is a need for more selective catalysts if the products are to be used for applications other than fuel.

In addition to use as a sorbent, the high surface area of the SLDHs produced in Chapter 3.3.1 makes them appealing as catalysts or catalyst precursors, as a higher

surface area typically correlates with a higher number of exposed catalytic sites. This chapter explores the development of these SLDH materials to include catalytically active (transition) metals (TM) and their use in the catalytic pyrolysis of polypropylene at moderate temperatures ($\leq 300\,^{\circ}\mathrm{C}$) to produce gaseous products.

5.2 Development of TM-doped SLDH catalysts

Previously reported catalysts for catalytic polyolefin pyrolysis include supported Co, Ni, Zn, Fe, and Cu.[4,5] Zn, Fe and Ni were chosen as targets for potential SLDH-based catalysts, due to their high natural abundance, low cost and the relative ease of their reported LDH synthesis.

5.2.1 Zn-doped SLDH

Mg_2ZnAl SLDH synthesis was attempted by partially substituting Mg with Zn during the synthesis. The methodology was the same as that developed in Chapter 3.3.6 and given in detail in Chapter 5.4.2.

The powder XRD pattern for the material produced is shown in Figure 5.1. Alongside sharp Bragg reflections corresponding to a hydrotalcite-like phase, there are also sharp peaks which correspond to a zincite phase (ZnO), indicating that the some of the Zn is not contained within the LDH structure and precipitates independently. ZnO is a common impurity during ZnAl LDH synthesis,[6] forming when the Al^{3+} concentration is low.[7] Aqueous Zn^{2+} is stable vs ZnO at pH ≤ 8,[8] with its minium solubility at pH ≈ 10;[9] therefore synthesis under less alkaline conditions was carried out in an attempt to prevent ZnO formation. The initial pH was varied by reducing the amount of 1 M NaOH solution (described in Chapter 5.4.2); the powder XRD patterns of the produced materials are shown in Figure C.1. The pH of the solution of metal salts was initially ≈ 3.8 and was increased to 9, 9.5 and 10 by addition of approximately 4, 4.5 and 5 mL of 1 M NaOH solution. The powder XRD patterns show similar features with a broad amorphous halo from 15° to 50°, potentially from unreacted starting material (A-$MgHPO_4$), two broad

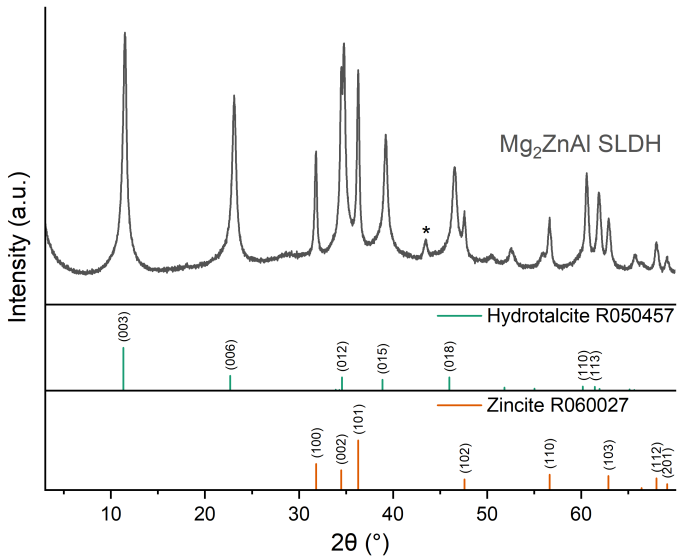

Figure 5.1: Powder XRD pattern of material produced from partial substitution of Mg for Zn during SLDH synthesis. Peaks can be indexed to the patterns below (RRUFF Project R050457 - Hydrotalcite and R060027 - Zincite).[10] * indicates a reflection due to the sample holder.

Bragg reflections at 35° and 61°, tentitatively assigned to amorphous LDH, and low intensity Bragg reflections at 8, 16.6, 27.5, 29.3 and 30.8° which correspond to the (001), (111), (212), (122) and (221)/(203) reflections of $Mg_2P_2O_7 \cdot 3.5\,H_2O$, as reported by Chen *et al.*[11] and Kongshaug *et al.*,[12] which is formed from the hydrothermal reaction of Mg^{2+} and H_3PO_4 in the presence of a base.

Failure to form an LDH phase using this method was attributed to the low amount of base added (although the initial pH was in the range known for LDH precipitation),[13] as the LDH consumes OH^- ions as it precipitates, making the solution more acidic. 3.2 mmol of metals were used in the reaction, so at least 6.4 mmol of NaOH (> 6.4 mL 1 M NaOH) is required to maintain an alkaline environment during the coprecipitation. To prevent further increases in pH during addition, the NaOH solution was added dropwise (0.1 mL min^{-1}, as detailed in Chapter 5.4.2).

The powder XRD patterns for the materials formed upon addition of 6.5, 8, 10 and 12 mL 1 M NaOH are shown in Figure 5.2. The patterns for the materials made using 6.5 and 8 mmol NaOH (Figure C.2) appear similar to those discussed

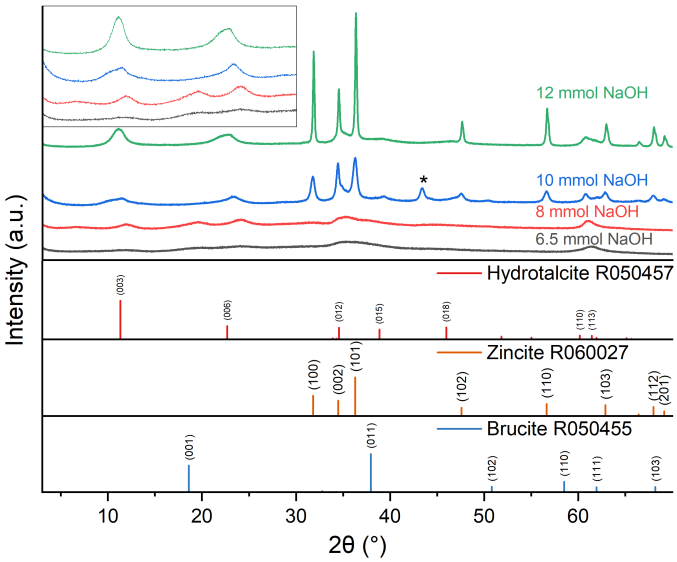

Figure 5.2: Powder XRD pattern of material produced from partial substitution of Mg for Zn during SLDH synthesis using slow addition of various amounts of 1 M NaOH. Peaks can be indexed to the patterns below (RRUFF Project R050457 - Hydrotalcite, R060027 - Zincite and R050455 - Brucite).[10] * indicates a reflection due to the sample holder.

previously (Figure C.1 4 to 5 mmol). The reflections assigned to $Mg_2P_2O_4 \cdot 3.6\,H_2O$ are not observed, the broad reflections at 35° and 61° have an increased intensity and new reflections are seen at 12, 19 and 24°. These are attributed to a mixture of a hydrotalcite-like phase ((003), (006), (012), (018) and (110)/(113) at 12, 24, 35, 45 and 61°) and brucite phase ((001) and (011) at 19 and 38°). As the amount of base added increases (10 and 12 mmol), the intensity of the hydrotalcite-like phase increases and the brucite phase is not observed. However, the ZnO phase is present instead. Based on these observations, it is concluded that Zn is not compatible with the developed SLDH synthesis, with low crystallinity SLDH and brucite formed using low amounts of base and ZnO forming when higher amounts are used.

5.2.2 Fe-doped SLDH

Similarly to Zn, inclusion of Fe was attempted via partial substitution of Al during the SLDH synthesis. Figure 5.3 (a) shows the powder XRD pattern of the

synthesised material. The pattern contains sharp peaks which can be indexed to hydrotalcite, as well as a shoulder at 20° assigned to a minor brucite impurity.

Following the success of the synthesis of the partially substituted $Mg_3Fe_{0.5}Al_{0.5}$ SLDH, the fully substituted Mg_3Fe SLDH was synthesised (Figure 5.3 (b)). The intensity of the SLDH peaks is significantly reduced, similar to that reported for MgFe LDH produced via variable pH coprecipitation by Silva *et al.*[14] Extraction of the lattice parameters (Table 5.1) shows a linear change in the a unit cell parameter with increased Al substitution (Figure C.3) in accordance with Vergard's law: the observed lattice parameter is the weighted average of the constituent components in a solid solution. The a parameter (0.313 nm) is comparable to the literature value of 0.311 nm.[15] There is also a significant amount of brucite impurity ((001), (011), (102) and (110) at 19, 38, 51 and 59°). Attempting to remove this impurity, the ratio of Mg used was lowered to Mg_2Fe which reduced the intensity of the (011) and (110) brucite reflections (Figure C.4). A further decline in the intensity of these Bragg reflections was observed upon reducing the quantity of NaOH employed in the synthesis. (Mg_xFe SLDH Figure C.5, $Mg_xFe_{0.5}Al_{0.5}$ LDH Figure C.6). The samples are all brown powders (Figure 5.4), with the shade of the samples getting darker with increased Fe content.

The elemental composition of $Mg_2Al_{0.5}Fe_{0.5}$ and Mg_2Fe SLDHs are shown in Table 5.2, with the calculated formulas as:

$[Mg_{0.698}Al_{0.164}Fe_{0.138}(OH)_2][(CO_3)_{0.15}] \cdot 0.034\,H_3PO_4 \cdot 0\,H_2O$ and

$[Mg_{0.65}Fe_{0.34}(OH)_2][(CO_3)_{0.17}] \cdot 0.06\,H_2CO_3 \cdot 0.016\,H_3PO_4 \cdot 0.8\,H_2O$.

The metal ratios are similar to the amounts of metal precursors added, indicating that all the metals precipitate to a similar degree. The main anion is carbonate with the amount observed approximately equal to half the M^{III} cations. There is a minor amount of phosphate present, but it is not the main anion as it is present at a concentration that is an order of magnitude lower. The phosphate concentration also decreases without the addition of Al, which provides further

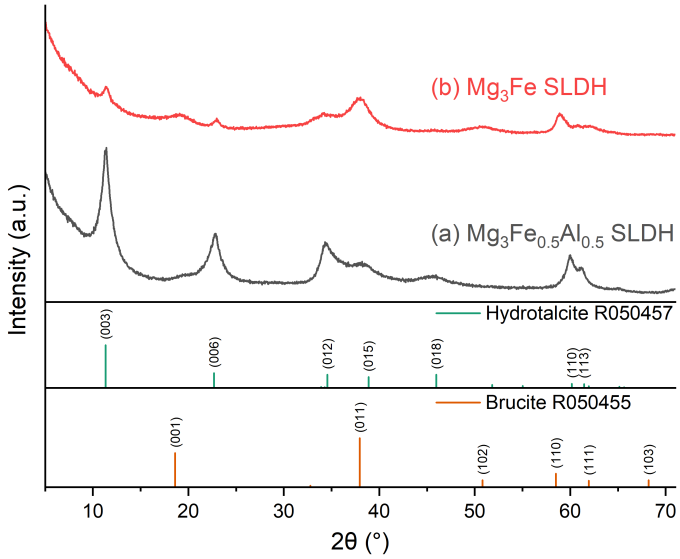

Figure 5.3: Powder XRD pattern of material produced from partial and total substitution of Al for Fe during SLDH synthesis. Peaks can be indexed to the patterns below (RRUFF Project R050457 - Hydrotalcite and R050455 - Brucite).[10]

Table 5.1: Lattice parameters (a, c) of the $Mg_xFe_yAl_{1-y}$ SLDHs and their respective crystallite domain lengths (CDL).

Sample	d_{110} (nm)	a (nm)	CDL_a (nm)	d_{003} (nm)	c (nm)	CDL_c (nm)
Mg_3Al	0.1528	0.3056	19.7995	0.7716	2.3149	8.0168
$Mg_3Fe_{0.5}Al_{0.5}$	0.1533	0.3067	6.2369	0.7767	2.3300	4.6729
Mg_3Fe	0.1565	0.3131	12.8598	0.7712	2.3137	7.8530

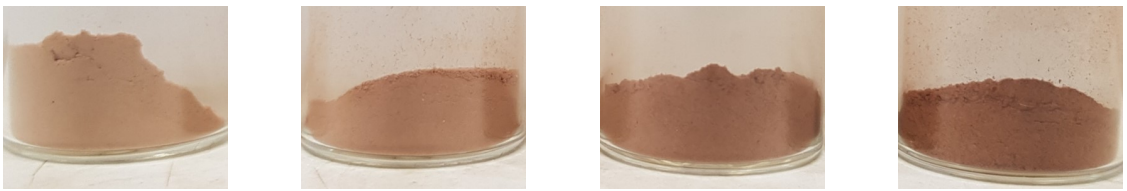

(a) $Mg_3Fe_{0.5}Al_{0.5}$ SLDH **(b)** $Mg_2Fe_{0.5}Al_{0.5}$ SLDH **(c)** Mg_3Fe SLDH **(d)** Mg_2Fe SLDH

Figure 5.4: Photographs of $Mg_xFe_yAl_{1-y}$ SLDHs $(x = 2, 3, y = 0.5, 1)$.

evidence of enhanced phosphate binding by Al. The overestimate of all the elements in Mg_3Fe SLDH suggests there is some metal oxide present.

To assess the morphology of the Fe-doped SLDHs, HR-SEM was used with EDX mapping to assess the distribution of elements within the sample. Figures 5.5 and 5.6 and Figures 5.7 and 5.8 show the microscopy images and EDX mapping for Mg_2Fe and $Mg_2Fe_{0.5}Al_{0.5}$ SLDH, respectively. $Mg_2Fe_{0.5}Al_{0.5}$ SLDH exhibits particles of a similar form to that of the undoped Mg_3Al SLDH materials, characterised by large particles ($\leq 30\,\mu m$) composed of intergrown platelets. However, the morphology has changed, with the characteristic coffin shape of the struvite precursor not observed, suggesting a change from the solid-solid transformation previously observed. Figure 5.7(c) illustrates that these platelets possess a hexagonal shape, with a diameter of 500 nm and a thickness of 30 nm. The EDX mapping reveals a uniform distribution of C, O, Mg, and Al within the particle, although areas of increased Fe concentration suggest some degree of phase segregation. Mg_2Fe SLDH shows a different morphology with smaller particles ($\leq 4\,\mu m$) and a lumpy surface which appears as an agglomeration of smaller ≈ 150 nm spherical particles. This morphology appears similar to that reported for MgFe LDHs by Kim *et al.*[16] This variation in morphology suggests a change in the growth mechanism of the SLDH. The EDX mapping shows C, O, Mg and Fe are present throughout the particle, but small regions of high Mg concentration suggest a small amount of the A-$MgHPO_4$ precursor may remain.

A further two ratios of Fe:Al were synthesised ($Mg_2Fe_{0.7}Al_{0.3}$ and $Mg_2Fe_{0.8}Al_{0.2}$); the powder XRD patterns are shown in Figure 5.9. As well as a decrease in intensity

Table 5.2: Elemental composition (wt%) of $Mg_2Al_{0.5}Fe_{0.5}$ and Mg_2Fe SLDHs and the elemental composition calculated for their estimated formula.

Sample	C	H	N	Al	Fe	Mg	P	Na
$Mg_2Al_{0.5}Fe_{0.5}$	2.75	3.07	0.00	5.9	10.34	22.68	1.43	0.02
Calculated	2.39	2.81	0.00	5.87	10.22	22.49	1.40	0.00
Mg_2Fe	2.81	2.57	0.00	0.00	19.68	16.03	0.51	0.06
Calculated	2.82	3.82	0.00	0.00	19.81	16.15	0.51	0.00

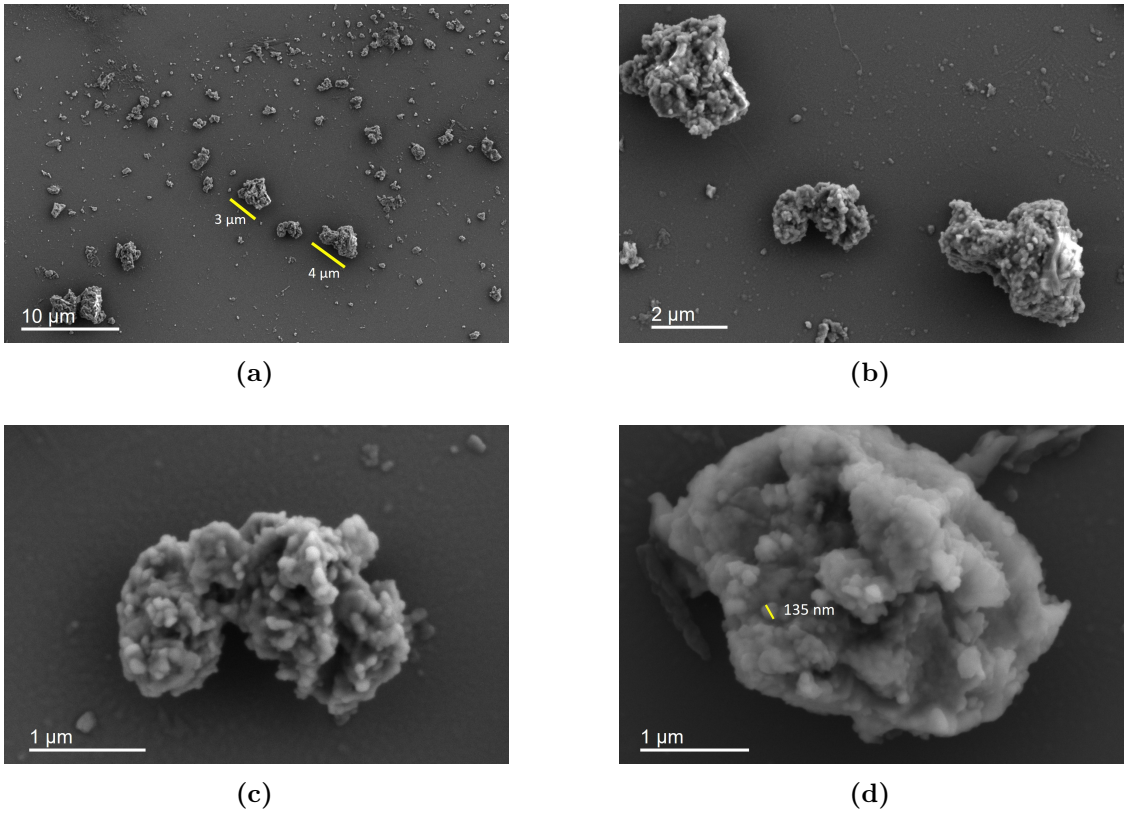

(a) (b)

(c) (d)

Figure 5.5: HR-SEM images of Mg_2Fe SLDH.

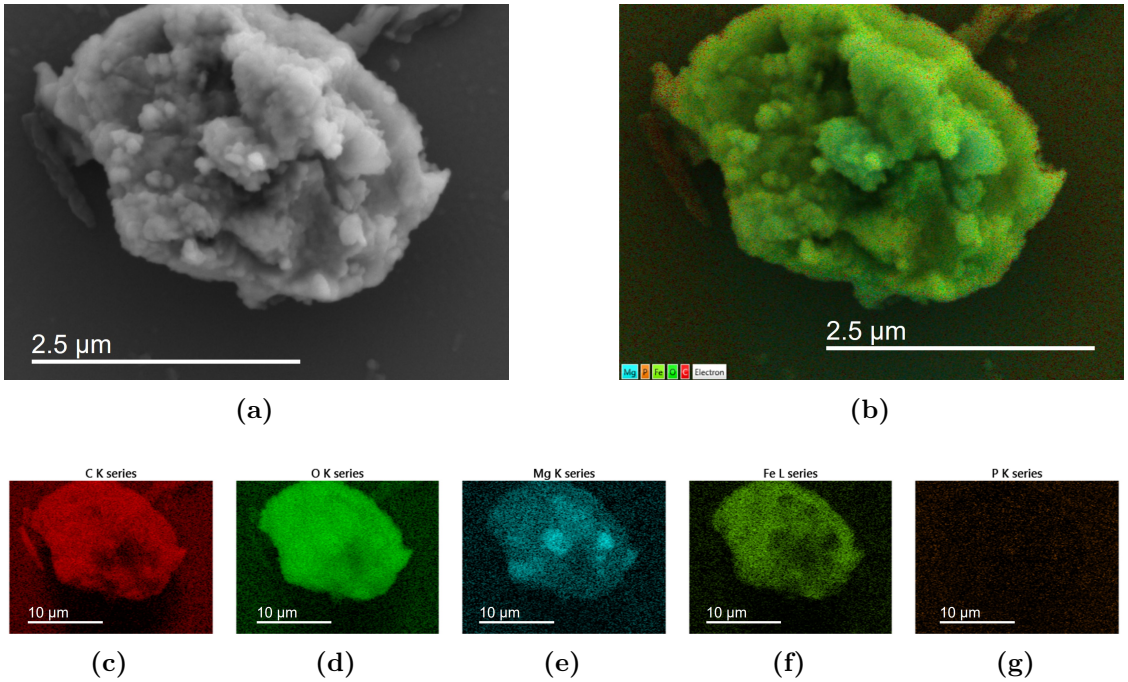

(a) (b)

(c) (d) (e) (f) (g)

Figure 5.6: HR-SEM EDX mapping of Mg_2Fe SLDH.

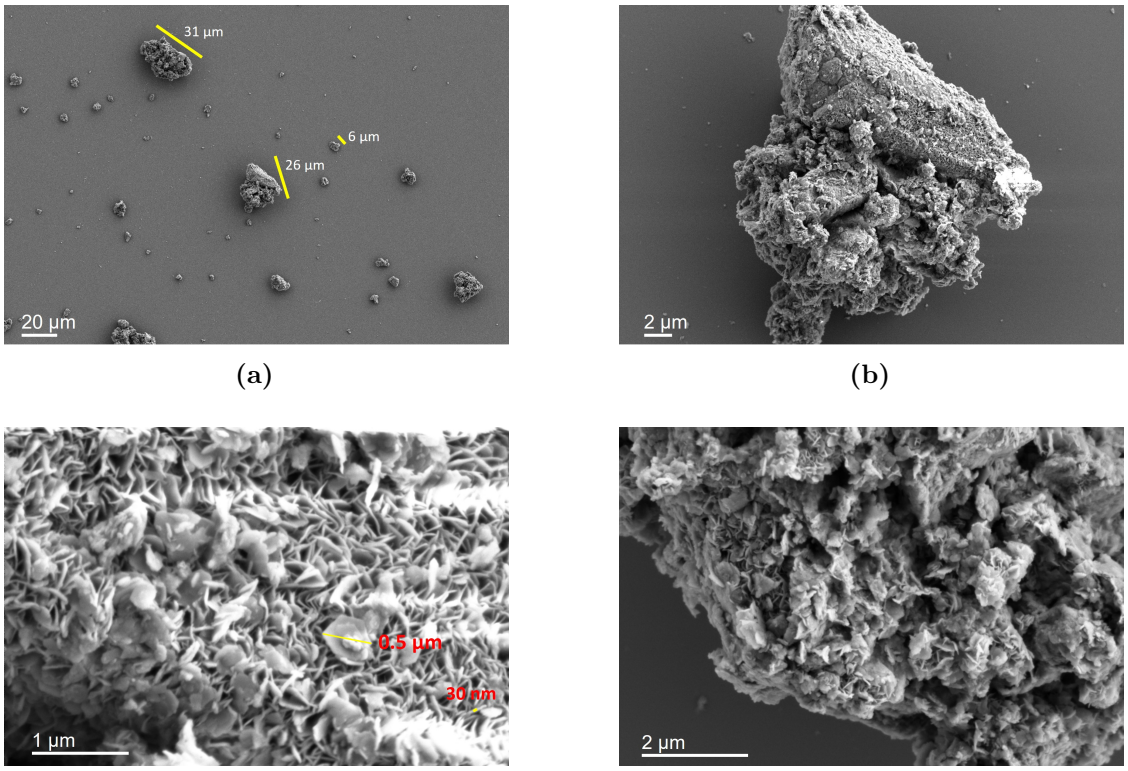

(a) (b)

(c) (d)

Figure 5.7: HR-SEM images of $Mg_2Al_{0.5}Fe_{0.5}$ SLDH.

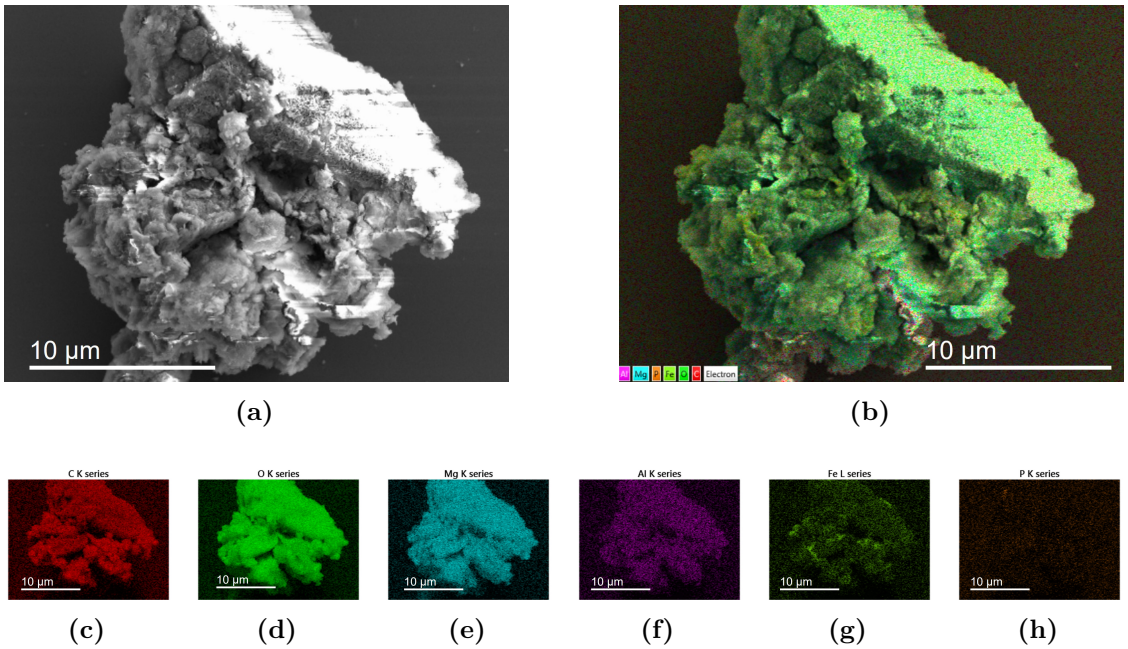

(a) (b)

(c) (d) (e) (f) (g) (h)

Figure 5.8: HR-SEM EDX mapping of $Mg_2Al_{0.5}Fe_{0.5}$ SLDH.

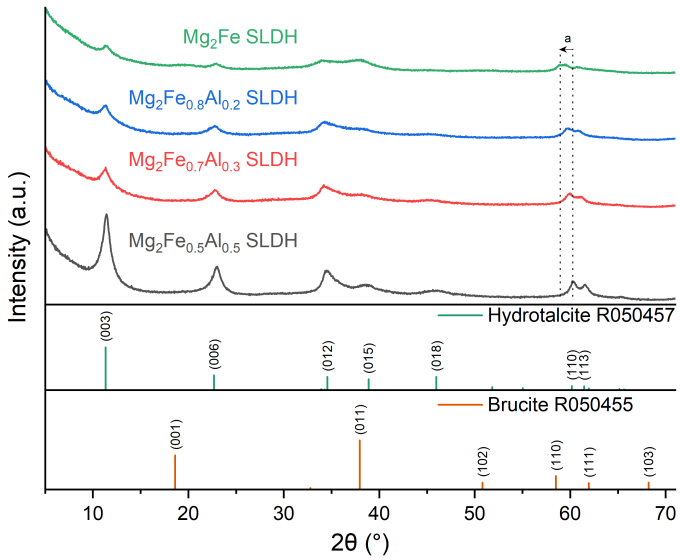

Figure 5.9: Powder XRD pattern of material produced from different levels of substitution of Al for Fe during SLDH synthesis. Peaks can be indexed to the patterns below (RRUFF Project R050457 - Hydrotalcite and R050455 - Brucite).[10]

Table 5.3: Lattice parameters (a, c) of the $Mg_xFe_yAl_{1-y}$ SLDHs and their respective crystallite domain lengths (CDL).

Sample	d_{110} (nm)	a (nm)	CDL_a (nm)	d_{003} (nm)	c (nm)	CDL_c (nm)
$Mg_2Fe_{0.5}Al_{0.5}$	0.1534	0.3069	12.9230	0.7754	2.3261	5.8238
$Mg_2Fe_{0.7}Al_{0.3}$	0.1544	0.3088	10.8740	0.7819	2.3456	6.1267
$Mg_2Fe_{0.8}Al_{0.2}$	0.1548	0.3097	11.7170	0.7819	2.3456	6.3037
Mg_2Fe	0.1561	0.3122	10.2109	0.7716	2.3148	7.6660

with increased substitution, there is also a change in lattice parameters (Table 5.3, Figure C.7). The c lattice parameter remains similar ($\approx 2.33\,\text{nm}$), but there is a linear change in the a lattice parameter (0.307 to 0.312 nm), as seen for the Mg_3M^{III} SLDH samples. The limits of the linear fit shown in Figure C.7 ($y = 0 \Rightarrow a = 0.3015\,\text{nm}$, $y = 1 \Rightarrow a = 0.312\,\text{nm}$) provide different bounds from the literature values of $a = 0.3046\,\text{nm}$ Mg_2Al LDH[18] and $a = 0.310\,\text{nm}$ Mg_2Fe LDH,[19] suggesting the Fe incorporation is not complete and the Mg content in the SLDH is higher than attributed. As the CDLs of the SLDHs remain similar, the reduced intensity observed must be due to the sample composition. This could be due to the

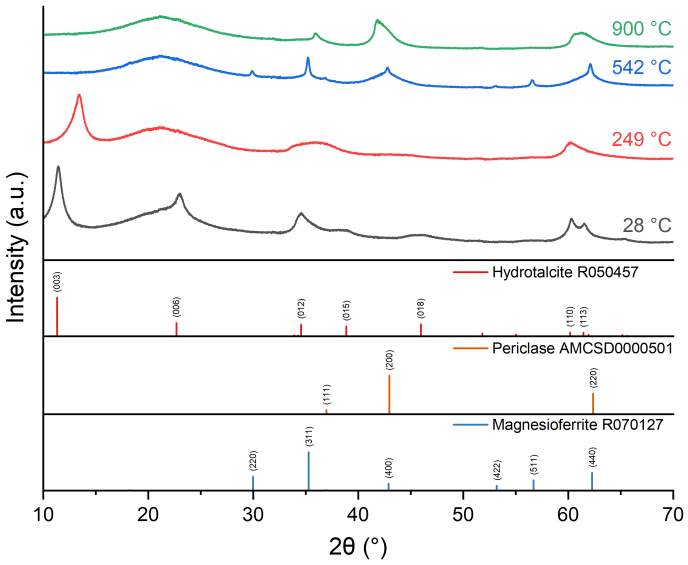

Figure 5.10: Variable temperature powder XRD patterns of $Mg_2Fe_{0.5}Al_{0.5}$ SLDH. Pattern measured at λ =0.825 276 Å and converted to the equivalent pattern at λ_{α_1} = 1.540 57 Å for ease of comparison. Peaks can be indexed to the patterns below (RRUFF Project R050457 - Hydrotalcite, R070127 - Magnesioferrite and AMCSD 0000501 - Periclase).[10,17]

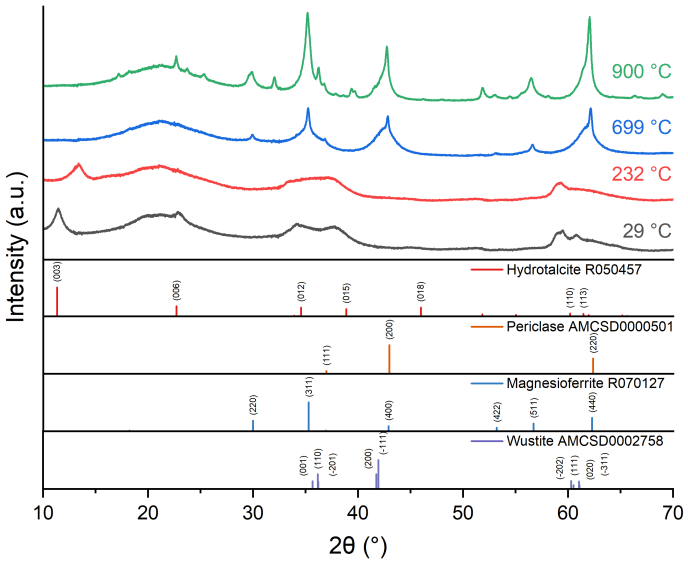

Figure 5.11: Variable temperature powder XRD patterns of Mg_2Fe SLDH. Pattern measured at λ =0.825 276 Å and converted to the equivalent pattern at λ_{α_1} = 1.540 57 Å for ease of comparison. Peaks can be indexed to the patterns below (RRUFF Project R050457 - Hydrotalcite, R070127 - Magnesioferrite, AMCSD 0000501 and AMCSD 0002758 - Periclase).[10,17]

increased formation of an amorphous phase (suggested as α-FeO(OH) by Manohara *et al.* after a limiting composition of Mg_4Fe LDH), although no amorphous halo is observed, or alternatively it could be due to a reduction in beam intensity due to K-edge adsorption by the Fe atoms as discussed by Mos, Vermeulen, Buisman and Weijma (the Fe fraction of the metal ions doubles from $\frac{1}{6}$ to $\frac{1}{3}$).[20]

Variable temperature powder XRD measurements were conducted to evaluate the thermal evolution of the materials (Figures C.8 and C.8), with Figures 5.10 and 5.11 showing representative patterns from different stages of the thermal evolutions.

Both materials show similar phase transformations: breakdown of the LDH structure followed by the formation of metal oxides. The loss of interlayer water is clearly observable with a decrease in the basal spacing (the change in d-spacing of the (003) Bragg reflection with temperature is shown in Figure C.10) and the loss of the (006) Bragg reflection. The partially doped material has a higher thermal stability than the fully doped material, with (003) Bragg reflection visible until $> 400\,^{\circ}C$ compared to $> 300\,^{\circ}C$. Above $400\,^{\circ}C$, there are broad Bragg reflections from periclase (MgO) and a sharp reflection from a spinel-like phase assigned to magnesioferrite ($MgFe_2O_4$) for Mg_2Fe SLDH and a solid solution $Mg_2(Al, Fe)O_4$[21] of magnesioferrite and spinel ($MgAlO_4$) for $Mg_2Fe_{0.5}Al_{0.5}$ SLDH. For the Mg_2Fe SLDH, these grow and get sharper with increasing temperature, with an additional set of sharp reflections from an unknown phase appearing above $800\,^{\circ}C$ (17.2, 22.7, 23.8, 25.3, 32, 36.2, 51.8 and 69°). For the $Mg_2Fe_{0.5}Al_{0.5}$ SLDH, the spinel-like phase is lost above $700\,^{\circ}C$ with only broad peaks attributed to a MgO-type phase ((Mg, Fe)O) remaining. This differs from that observed for both pure MgAl[22] and MgFe systems and from that previously reported for their mixture, which remain as a mixture of MgO and a spinel-type phase.[23]

5.2.3 Ni-doped SLDH

Ni was also introduced in a similar method with partial Mg substitution. The powder XRD pattern of the Mg_2NiAl LDH synthesised is shown in Figure 5.12 and

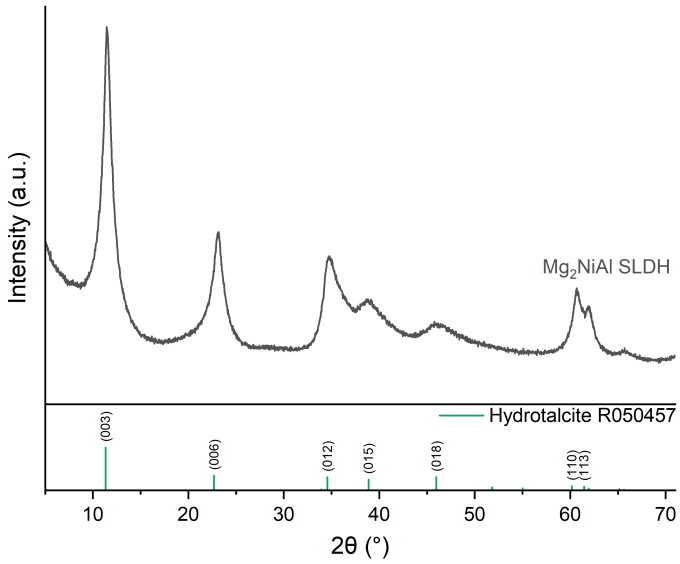

Figure 5.12: Powder XRD pattern of material produced from partial substitution of Mg for Ni during SLDH synthesis. Peaks can be indexed to the patterns below (RRUFF Project R050457 - Hydrotalcite).[10]

Table 5.4: Lattice parameters (a, c) of the Mg_2NiAl SLDH and their respective crystallite domain lengths (CDL).

Sample	d_{110} (nm)	a (nm)	CDL_a (nm)	d_{003} (nm)	c (nm)	CDL_c (nm)
Mg_3Al	0.1528	0.3056	19.7995	0.7716	2.3149	8.0168
Mg_2NiAl	0.1526	0.3053	10.4985	0.7675	2.3024	4.9207

Figure 5.13: Photograph of Mg_2NiAl SLDH.

a photograph of the light-blue sample in Figure 5.13. The powder XRD pattern shows only reflections for a hydrotalcite-like material showing the Ni does not precipitate as a separate crystalline material. Extraction of the unit cell parameters (Table 5.4) shows similar values to the Mg_3Al SLDHs, but with a lower crystallinity. The a lattice parameter (0.3053 nm) is higher than that reported in the literature (0.3043 nm), but the decrease from the Mg_3Al SLDH is similar to that predicted by the differences in Shannon radii (O_h : $Ni^{2+}/Mg^{2+}/Al^{3+} = 0.69/0.72/0.535$Å).[24] The elemental composition of the Mg_2NiAl is given in Table 5.5 with an estimated formula of $[Mg_{0.526}Ni_{0.224}Al_{0.25}(OH)_2][(CO_3)_{0.1}(HPO_4)_{0.02}] \cdot 0.011\,H_3PO_4 \cdot 0.77\,H_2O$.

Table 5.5: Elemental composition (wt%) of Mg_2NiAl SLDHs and the elemental composition calculated for its estimated formula.

Sample	C	H	N	Al	Ni	Mg	P	Na
Mg_2NiAl	1.4	3.15	0.16	7.59	14.82	14.41	1.11	0.04
Calculated	1.36	3.94	0.00	7.64	14.89	14.48	1.09	0.00

HR-SEM and EDX mapping of the particles are shown in Figures 5.14 and 5.15. Similar to the Fe-doped SLDHs, there are a variety of particle sizes with the largest observed possessing a diameter of 9.2 µm. Comparably to the other Al-containing SLDHs, platelets can be observed on the particles' surfaces (Figure 5.14(d)), but regions with a smoother texture can also be observed (Figure 5.14(c)). The lack of coffin-shaped particles indicates a change from the solid-solid transformation as seen for the Fe-doped SLDH. EDX mapping reveals a uniform distribution of C, O, and Al across the particle, which also include both Mg and Ni. However, areas which show elevated concentrations of Ni contain minimal Mg, and similarly, regions with high Mg concentrations show a negligible Ni. This suggests a degree of phase segregation, perhaps into a mixture of MgAl and NiAl LDHs.

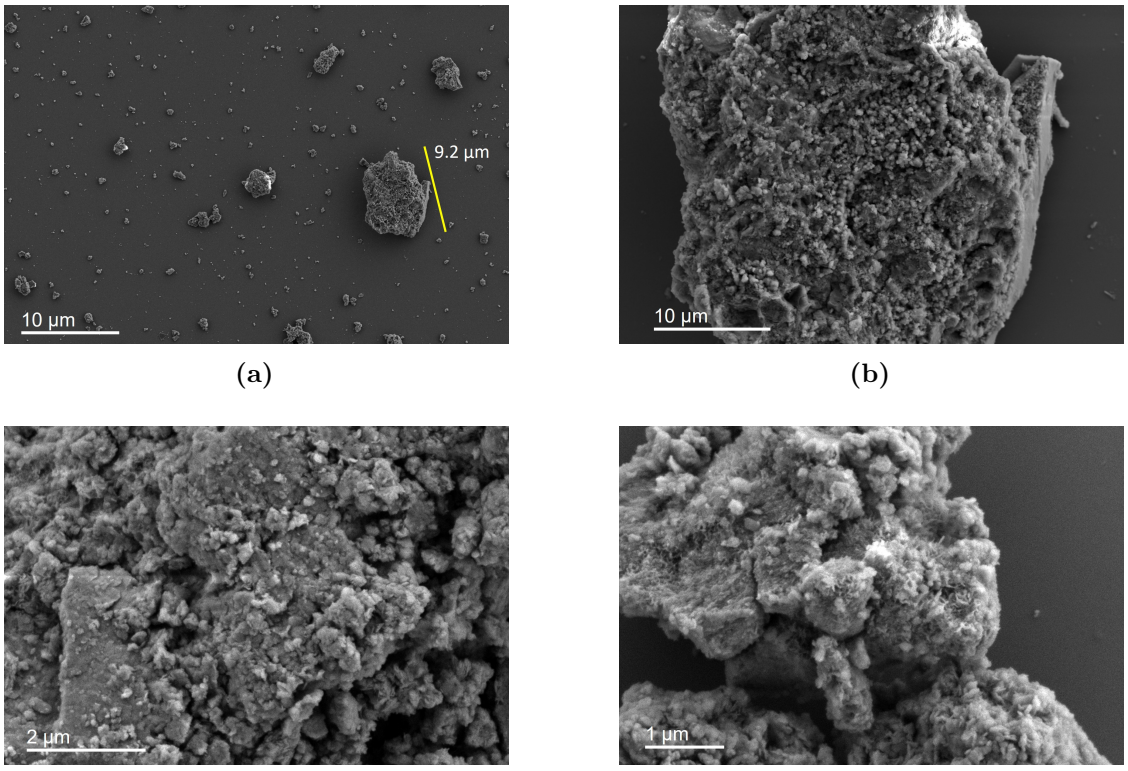

(a) (b)

(c) (d)

Figure 5.14: HR-SEM images of Mg_2NiAl SLDH.

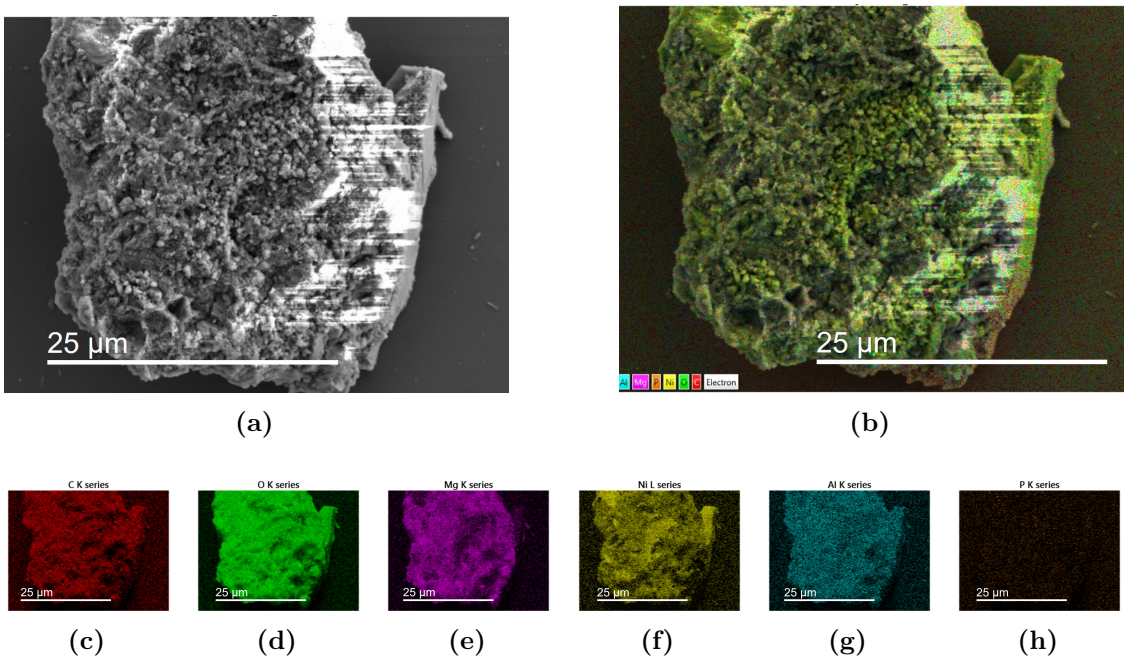

(a) (b)

(c) (d) (e) (f) (g) (h)

Figure 5.15: HR-SEM EDX mapping of Mg_2NiAl SLDH.

5.3 Catalytic polypropylene pyrolysis

5.3.1 TGA experiments

Initial screening of the catalysts was conducted using a TGA-MS setup. PP and the SLDH catalysts were blended together by mixing the SLDH (10 wt%) into a hot solution of polypropylene in Xylene followed by precipitation in cold acetone (Chapter 5.4.5). This yielded well-mixed samples of fine powder (Figure 5.16) which ensured good contact during the pyrolysis.

The TGA traces are shown in Figure 5.17 with an onset temperature for the pyrolysis of around 300 °C. Although the onset temperature is the same for the SLDH-blended PP, the peak weight loss moves to a higher temperature (448 to 457 °C), indicating that the SLDH stabilises the PP. This has been previously reported for PP-LDH systems, where LDHs are added as a flame retardment via catalytic enhancement of char formation and endothermic decomposition. The thermal stability of such materials is often given by the temperature at which 10 and 50 % of the mass is lost (T_{10}, T_{50}) which increases by 18.2 to 30.3 °C for T_{10} and 41.9 to 45.4 °C for T_{50} (stability enhancement: PP-$Mg_2Fe_{0.5}Al_{0.5}$ SLDH > PP-Mg_2Fe SLDH > PP-Mg_2NiAl SLDH) and is accompanied by a residual ≈ 5 % char from the SLDH (Table 5.6). These thermal stability enhancements are comparable with those reported in the literature.[25,26]

Further investigation into the relative thermal stability of the PP-SLDH blends is shown in Figure C.11; the samples were held at each of 250, 300, 350 and 400 °C

Figure 5.16: Photograph of re-precipitated blends of polypropylene and TM-SLDHs. Left to right: pure PP, PP-Mg_2Fe SLDH, PP-$Mg_2Fe_{0.5}Al_{0.5}$ SLDH and PP-Mg_2NiAl SLDH.

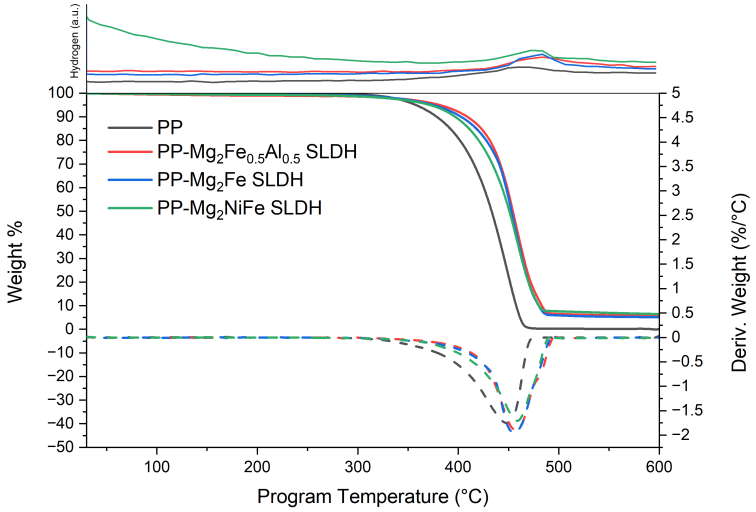

Figure 5.17: TGA analysis of PP and PP-SLDH blends. The derivative is shown as the dotted line. The H_2 MS signal is shown above.

Table 5.6: Flame retardment parameters from the TGA of PP-SLDH composites (Figure 5.17).

Sample	T_{10} (°C)	T_{50} (°C)	Char (%)
PP	378.6	408.9	0.02
PP-$Mg_2Fe_{0.5}Al_{0.5}$ SLDH	408.9	454.3	5.69
PP-Mg_2Fe SLDH	402.7	452.9	5.14
PP-Mg_2NiAl SLDH	396.8	450.8	6.46

for 1 h while they decomposed. There is minimal degradation observed at 250 °C for any of the samples, but increasing rates of decomposition are observed as the temperature is increased. As seen in the continuous temperature ramp experiments (Figure 5.17), the pure PP degrades at a faster rate than the SLDH-blended samples (Table 5.7), with the Fe-containing samples degrading at similar rates and the Mg_2NiAl SLDH degrading the slowest. The pure PP shows a maximum weight loss during the heating step from 300 to 350 °C and the SLDH blends show a maximum weight loss upon heating from 350 to 400 °C.

During the PP degradation numerous products were evolved; the H_2 signal and that for ions with m/z ratio from 30 to 150 are shown in Figures 5.17 (top)

Table 5.7: Maximum PP-SLDH degradation rate observed at each isothermal hold temperature (Figure C.11).

Sample	250 °C (% min^{-1})	300 °C (% min^{-1})	350 °C (% min^{-1})	400 °C (% min^{-1})
No catalyst	−0.504	−0.877	−3.091	−2.214
$Mg_2Fe_{0.5}Al_{0.5}$ SLDH	−0.667	−0.517	−1.401	−4.152
Mg_2Fe SLDH	−0.516	−0.501	−1.311	−4.332
Mg_2NiAl SLDH	−0.507	−0.377	−0.962	−4.432

and 5.18 (for pure PP). An increase in ion counts is seen above 330 °C with a maximum concentration at ≈ 450 °C corresponding to the maximum weight loss rate seen in the TGA analysis. The most intense ion signals are observed in clusters at m/z 39 to 43, 55 to 57 and 69 to70, corresponding to C_3, C_4 and C_5 products, respectively, with weaker signals observed at higher masses in intervals of 14 (additional CH_2 units), up to 124 (C_9). Although this distribution of ions is indicative of hydrocarbon species, it does not identify the particular molecules or isomers present; due to the many overlapping signals, deconvolution to determine the relative concentrations of the specific ions was not successful.

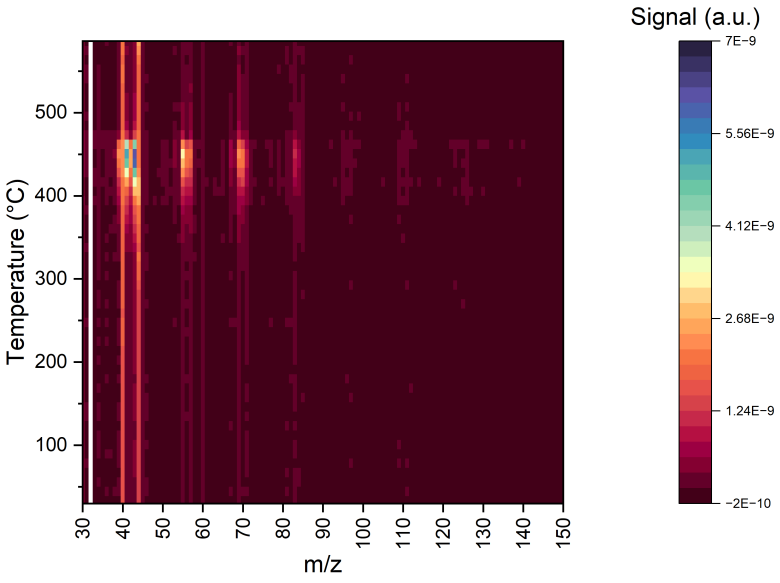

Figure 5.18: Heat-map of ions detected by TGA-MS during the pyrolysis of PP.

5.3.2 Batch reactor experiments

To enable identification of the products formed during the pyrolysis, samples were heated in a sealed pressure vessel for 24 h before the gaseous products were identified using GC-MS and quantified via GC using an FID. Details of the experimental setup are given in Chapter 5.4.6. Figure C.12(b) shows a typical GC-MS chromatogram; the major compound peaks are marked by their retention time and their respective mass spectrums are shown in Figures C.12(c) to C.12(m), with the major ion peaks labelled with their constituent molecular fragment ion. The corresponding quantitative GC chromatogram is shown in Figure C.12(a) with the major compound peaks labelled.

The product yield was then estimated from the gas volume fraction ($V_{f,product}$) and gas yield (M_{gas}).

$$\text{Yield}_{product} = \text{Mass}_{gas} * M_{f,product}$$

$$M_{f,product} = V_{f,product} * MW_{product} / \sum^{products} V_{f,i} * MW_i$$

The TM-doped SLDHs were introduced into the reaction vessel to evaluate if they provided any catalytic activity.

Figure 5.19 shows the distribution of solid, liquid and gas products; the gas product distribution by volume; hydrogen conversion (assuming all H_2 produced is from the PP) and gas product yields. The addition of Mg_2NiAl SLDH to the pyrolysis reaction increases the proportion of gaseous products produced. The distribution of the hydrocarbon gases remains similar; however, the volume fraction of H_2 is greatly increased (from 11 to 53 %), suggesting the addition of Mg_2NiAl SLDH promotes H_2 formation. From the CHN results discussed previously, there is hydrogen present in the Mg_2NiAl SLDH (3.15 wt%); however, if all of this were converted to H_2 via steam reforming with the pyrolysis gases, it would only lead to a increase in yield of $0.003\,15\,g_{H_2}\,g_{PP}^{-1}$, significantly lower than the observed increase of $0.008\,25\,g_{H_2}\,g_{PP}^{-1}$.

Figure 5.20 shows gel permeation chromatography (GPC) data of the pure PP, the pyrolysed PP and the PP after pyrolysis with or without the Mg_2NiAl SLDH

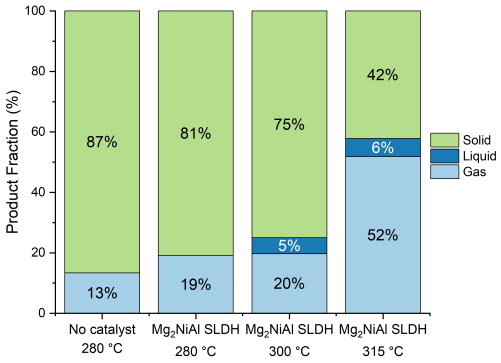

(a) Distribution of solid, liquid and gas products

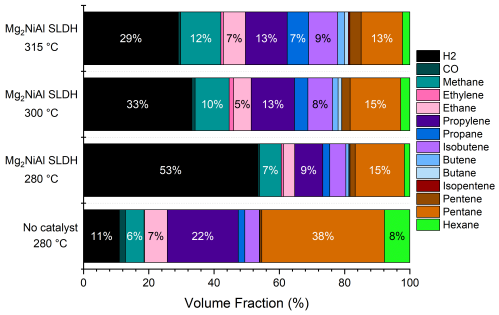

(b) Gas product distribution by volume.

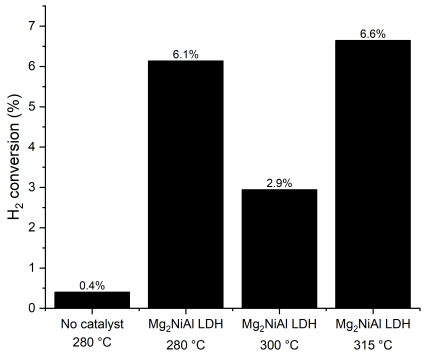

(c) Hydrogen conversion as fraction of the amount present in the PP.

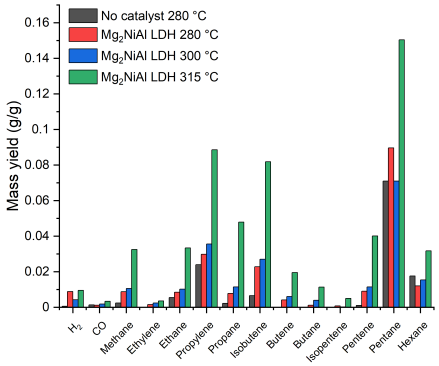

(d) Gas product yields.

Figure 5.19: PP pyrolysis data using 10 wt% Mg_2NiAl SLDH at different temperatures.

catalyst. The pure PP has a molecular weight $M_w = 255.6\,\text{kDa}$ (6075 monomer units) and a polydispersity index (PDI) of 9.6. The PDI is a measure of the distribution of molecular weights of a polymer sample. It is defined as $\text{PDI} = \frac{M_w}{M_n} \geq 1$ where M_w and M_n are the weight average and number average molecular weight respectively. Higher values indicate a wider distribution of molecular masses. After pyrolysis, the polymer chains show clear signs of chain scission with a molecular weight $M_w = 9.6\,\text{kDa}$ (228 monomer units, 3.76% of the original value) and PDI = 2.4. This is in the range for PP waxes,[27] and is the typical product for PP pyrolysis at moderate temperature.[28] These waxes are suitable for further catalytic cracking to produce petrochemical products.[28] The addition of the SLDH catalyst leads to a

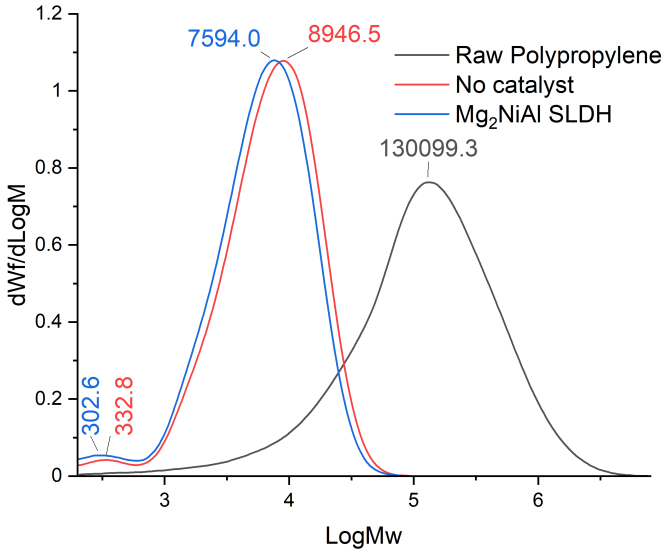

Figure 5.20: Molecular mass distribution (M_w) of PP before and after pyrolysis. the M_w of the maxima are labelled.

Table 5.8: Molecular mass and polydispersity index (PDI) data for PP and the solid product after pyrolysis. $M_n = \sum n_i M_i$, $M_w = \sum w_i M_i$ (where $w_i = \frac{n_i M_i}{M_n}$)

Result-ID and Sample name	M_w ($\mathrm{g\,mol^{-1}}$)	M_n ($\mathrm{g\,mol^{-1}}$)	PDI (M_w/M_n)
Raw Polypropylene	255650	26650	9.6
No catalyst	9600	4000	2.4
Mg_2NiAl SLDH	8350	3400	2.4

small decrease in polymer length $M_w = 8.35\,\mathrm{kDa}$ (198 monomer units), PDI = 2.4 suggesting it does not significantly promote the rate of chain scission. There is also a secondary peak in the M_w distribution of the pyrolysed samples with a maxima $\approx 300\,\mathrm{Da}$ (7 monomer units). Smaller chains may be present, but are outside the range of the GPC measurement (200 Da, 4.75 monomer units).

Control experiments using dried (at 110 °C) SLDH, calcined (at 600 °C) SLDH, ZSM-5 (a zeolite used commercially to form light olefins) and NiO (nanopowder) are shown in Figure C.18. NiO and calcined Mg_2NiAl SLDH (SLDO formed after dehydroxylation) still show high H_2 selectivity (60% and 46% respectively), indicating that the Ni species are catalytically active, enhancing H_2 formation from PP. The dried SLDH still shows enhanced H_2 selectivity compared to no catalyst, with

the decrease from the non-dried SLDH attributed to the loss of H_2 produced by the steam reforming reaction of water from the SLDH and the olefin products.[29] $Mg_3Fe_{0.5}Al_{0.5}$ SLDH was also tested, with only a small boost to H_2 selectivity and was not investigated further. Decreases in the amount of gas produced and subsequent product yields are attributed to the lower temperatures recorded within the reactor, limiting further comparison. The zeolite ZSM-5 catalyst displays markedly different catalytic performance, with a solid yield of 42%. ZSM-5 has been widely reported for use in cracking reactions due to its high number of acidic sites.[30] Among the gaseous products observed, a significant increase in the selectivity for C_{3-4} and pentene is observed. This selectivity has been previously reported and is ascribed to the shape selectivity of the catalyst's pores.[31]

Upon increasing the pyrolysis temperature, the fraction of gas products increases and a small amount of liquid products are observed. The H_2 volume fractions are lower at the higher pyrolysis temperatures, indicating the rate of C−C bond scission increases faster than the rate of dehydrogenation, with no enhancement of the H_2 yield observed. Higher pyrolysis temperatures could not be explored due to limitations of the experimental setup.

The hydrocarbons formed after thermal pyrolysis are in agreement with those reported by Kruse *et al.*[32] They developed a series of differential equations detailing the various reactions and intermediates they expected, which gave a prediction in good agreement with the product distribution to that measured experimentally at 350 °C. The radical mechanism is initiated by C−C bond fission to form a primary and secondary radical. The resulting chemistry results from the more stable secondary radical which can undergo inter- and intra-molecular hydrogen transfers to form various intermediate radicals which form the different products after β-scission. There is an increased energy barrier for 1,3- and 1,4-hydrogen atom transfer due to the ring strain of the transition state and an entropic barrier for higher order 1,n-hydrogen atom transfer reactions, explaining the preference for 1,5-hydrogen transfer and subsequent pentane formation.[33]

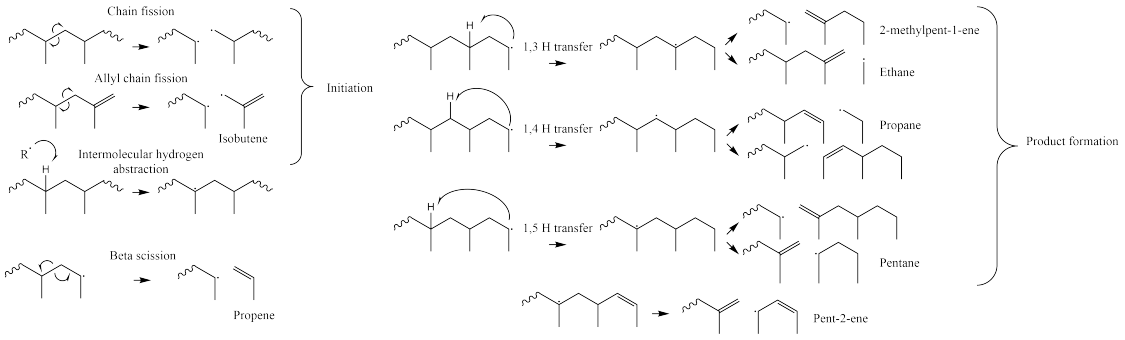

Figure 5.21: Mechanism for the formation of the major gaseous products observed during thermal pyrolysis of PP suggested by Kruse *et al.*[32]

Previous studies have demonstrated that variations in reaction times during the synthesis of SDLH impact the surface area and crystallinity of the resultant product. Given that these characteristics may influence the number of active sites within the material, extended ageing periods were investigated for Mg_2NiAl SLDH. Figures C.14, C.15, C.16 and C.17 depict the XRD patterns, FTIR spectra, N_2 adsorption/desorption isotherms and calculated pore distributions of the Mg_2NiAl SLDHs synthesised using reaction times of 1, 2 and 3 d. Analogously to the pure Mg_3Al SLDHs, crystallinity is observed to decrease with prolonged ageing (Table C.1), while FTIR absorption of CO_3 diminishes and the PO_4 absorption augments. Notably, the surface area continues to increase with extended ageing, rising from $74\,m^2\,g^{-1}$ after one day to $216\,m^2\,g^{-1}$ post three days.

Figure C.18 illustrates the product distribution from PP pyrolysis utilising these catalysts (at 300 °C). The product distribution for all three catalysts is similar, with the predominant gas fractions comprising H_2, propylene, and pentane. Nonetheless, the gas yield increases with the ageing time of the catalyst, signifying an enhancement in activity (13%, 24%, and 31%, respectively).

5.3.3 Comparison with traditionally synthesised Ni LDHs

To isolate the origin of the enhancement in catalytic activity seen previously, which is likely due to the increase in ${PO_4}^{3-}$ or the higher surface area, four LDH samples were produced following the conventional coprecipitation method. Mg_2NiAl LDH was synthesised with ${CO_3}^{2-}$ or ${PO_4}^{3-}$ as the interlayer anion and half of the product

Figure 5.22: Photograph of Mg_2NiAl LDHs. Left to right: Mg_2NiAl-CO_3, Mg_2NiAl-PO_4, Mg_2NiAl-CO_3-AMOST and Mg_2NiAl-PO_4-AMOST.

was given the AMOST treatment with isopropyl alcohol to increase the surface area. Full experimental details are given in Chapter 5.4.7. The materials are a similar blue-green colour to the Ni-doped SLDHs (Figure 5.22).

The XRD patterns of the four LDHs are given in Figure 5.23. The CO_3^{2-} containing LDHs show the typical LDH Bragg reflections with the extracted unit cell parameter given in Table 5.9. The AMOST treated sample does not show a decrease in CDL_c compared to the untreated sample (13.6 nm vs 12.5 nm), as is typically reported, arising from reduced layer stacking indicating that the treatment has not affected the LDH stacking.[34] The PO_4^{3-} containing LDHs do not show the typical LDH reflections, with the only features being broad halos centred at 35.5° and 61.8°. This is similar to previously reported PO_4^{3-} LDH phases, with a loss of crystallinity in the c-axis causing the disappearance of the basal reflections (00l) and with only the reflections with a component parallel to the plane remaining ((012), (110) and (113)).[35,36]

The elemental composition of the synthesised LDHs is given in Table 5.10. The estimated formulas for Mg_2NiAl-CO_3, Mg_2NiAl-PO_4, Mg_2NiAl-CO_3-AMOST and Mg_2NiAl-PO_4-AMOST are:

$[Mg_{0.506}Ni_{0.245}Al_{0.249}(OH)_2][(CO_3)_{0.125}] \cdot 0.06\,H_2CO_3 \cdot 0.6\,H_2O$,

$[Mg_{0.507}Ni_{0.235}Al_{0.258}(OH)_2][(H_2PO_4)_{0.258}] \cdot 0.05\,H_3PO_4 \cdot 1.3\,H_2O$,

$[Mg_{0.489}Ni_{0.253}Al_{0.258}(OH)_2][(CO_3)_{0.129}] \cdot 0.1\,H_2CO_3 \cdot 0\,C_3H_7OH \cdot 0.45\,H_2O$ and

$[Mg_{0.518}Ni_{0.228}Al_{0.254}(OH)_2][(H_2PO_4)_{0.418}] \cdot 0.05\,PO_4 \cdot 0.072\,C_3H_8O \cdot 0.3\,H_2O$.

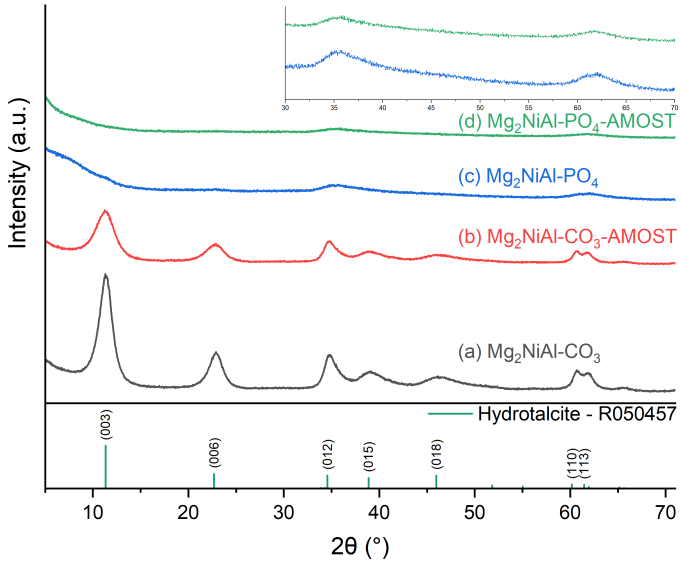

Figure 5.23: XRD patterns of the conventionally synthesised Mg_2NiAl LDHs. Enlarged pattern of the $PO_4{}^{2-}$ LDHs between 30° to 70° shown in the insert.

Table 5.9: Lattice parameters (a, c) of the $Mg_2NiAl\,CO_3{}^{2-}$ LDHs and their respective crystallite domain lengths (CDL).

Sample	d_{110} (nm)	a (nm)	CDL_a (nm)	d_{003} (nm)	c (nm)	CDL_c (nm)
Mg_2NiAl-CO_3	0.153	0.305	12.501	0.780	2.340	3.815
Mg_2NiAl-CO_3-AMOST	0.153	0.305	13.606	0.784	2.353	2.772

Table 5.10: Elemental composition (wt%) of Mg_2NiAl SLDHs and the elemental composition calculated for its estimated formula.

Sample	C	H	N	Al	Ni	Mg	P	Na
Mg_2NiAl-CO_3	2.37	3.53	0.00	7.45	15.97	13.64	0.00	0.04
Calculated	2.43	3.75	0.00	7.54	16.13	13.80	0.00	0.00
Mg_2NiAl-PO_4	0.22	3.3	0.00	5.70	11.32	10.11	7.95	0.09
Calculated	0	4.41	0.00	5.78	11.45	10.23	7.92	0.00
Mg_2NiAl-CO_3-AMOST	3.05	3.27	0.00	7.69	16.37	13.11	0.00	0.03
Calculated	3.06	3.48	0.00	7.76	16.54	13.24	0.00	0.00
Mg_2NiAl-PO_4-AMOST	2.46	2.72	0.00	6.48	12.63	11.89	9.03	0.11
Calculated	2.45	3.64	0.00	6.46	12.61	11.87	8.87	0.00

The metal stoichiometry measured is almost the same as the reactants (Mg:Ni:Al is 2.1:1.0:1.0, 2.2:1.0:1.1, 1.9:1.0:1.0 and 2.3:1.0:1.1, respectively), indicating that all the metals have precipitated. The phosphate anion is clearly included within the PO_3^{3-} based materials, with minimal carbon in the Mg_2NiAl-PO_4 sample. The amount of water was adjusted to achieve correct mass percentages for the other elements; however, the overestimation of the hydrogen mass indicates that an additional element is present which has not been accounted for. The high P:Al ratio of the PO_3^{3-} based materials (1:1.22 and 1:1.21 for Mg_2NiAl-PO_4 and Mg_2NiAl-PO_4-AMOST, respectively) may indicate the formation of a non-LDH metal phosphate phase.

To assess the functional groups present in the materials, FTIR spectra were measured and are shown in Figure 5.24. All samples feature M−O (550 to 1100 cm^{-1}), H_2O (1644 cm^{-1}) and O−H (2600 to 3750 cm^{-1}) adsorptions, as are characteristic for LDHs. Additional adsorptions are observed at 1365 cm^{-1} for the CO_3^{2-} containing LDHs, at 1039 cm^{-1} for the PO_4^{3-} containing LDHs (with minimal CO_3^{2-} contamination observed) and at 3698 cm^{-1} (residual IPA) for the AMOST treated LDHs. The broad O−H adsorption is also shifted to lower wavenumbers for the PO_4^{3-} vs CO_3^{2-} (maximum at 3291 cm^{-1} vs 3448 cm^{-1}, respectively) which is associated with a stronger interaction with the interlayer anion.[37]

To confirm the success of the AMOST process, the N_2 adsorption isotherms were measured (shown in Figure 5.25 with the calculated pore distributions shown in Figure C.19) and the BET SSA calculated. Both the CO_3^{2-} and the PO_4^{3-} conventionally produced LDHs show similar properties with surface areas of 44 $m^2\,g^{-1}$ and 55 $m^2\,g^{-1}$, respectively. The pore size distribution is also similar, with the main difference being a small decrease in the size of the micropores in PO_4^{3-} (11.8 Å from 12.7 Å). The isotherms of the AMOST treated samples change significantly: the surface area increases by 5.4 and 8 times for the CO_3^{2-} and PO_4^{3-} LDHs, respectively, with the CO_3^{2-} LDH featuring a large H2(a) type hysteresis loop, indicating ink-bottle type pores leading to window-induced cavitation.[38] The increase

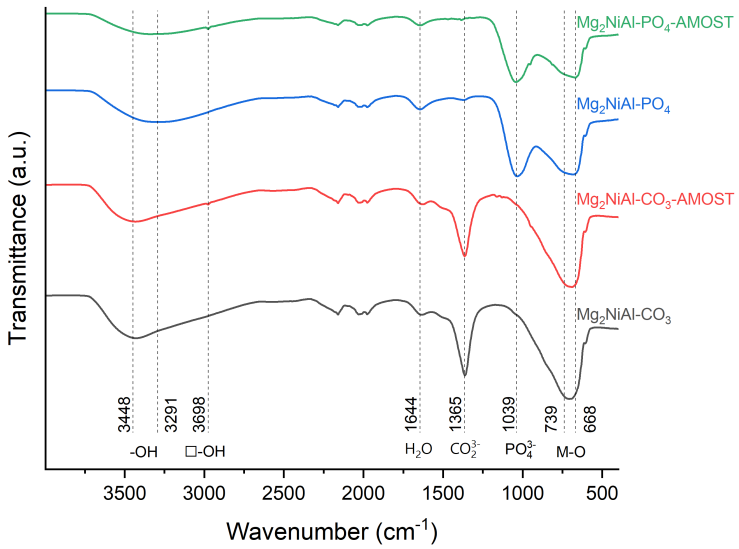

Figure 5.24: FTIR spectra of the conventionally synthesised Mg_2NiAl LDHs.

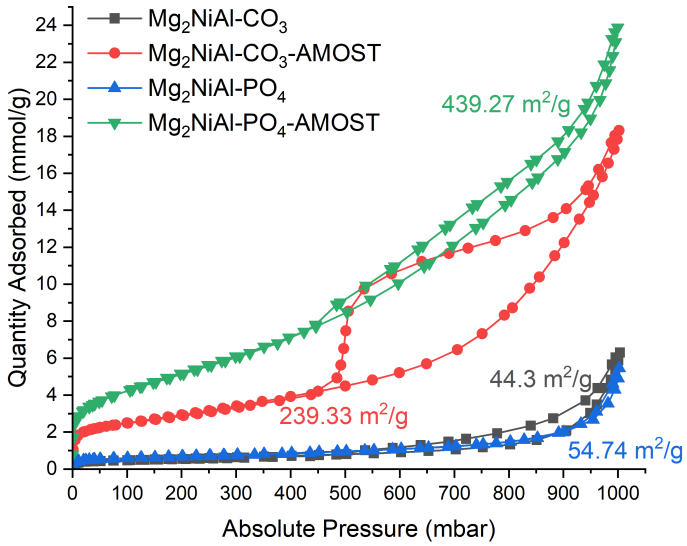

Figure 5.25: N_2 adsorption/desorption isotherms of the conventionally synthesised Mg_2NiAl LDHs. BET SSAs are shown next to the isotherms

in surface area is associated with an increase in the number of micropores (11 to 16 Å) and mesopores (20 to 300 Å). The surface area increases indicated the process was successful with the increases for the CO_3^{2-} system typical of AMOST treated LDHs.[34] The increase in surface area seen for the PO_4^{3-} system is almost twice that of the AMOST CO_3^{2-} material, indicating that the material is particularly susceptible to delamination, perhaps due to the poor stacking crystallinity of the layers, although the surface area is within the range that has been previously reported.[39]

TGA measurements of the materials were conducted to investigate their thermal evolutions (Figure 5.26). The Mg_2NiAl-CO_3 LDHs show the thermal events typical of a carbonate LDH: steady mass loss from 30 to 200 °C, due to loss of physisorbed and interlayer water,[40] before dehydroxylation and decarbonation between 250 to 450 °C. The AMOST sample shows a destabilisation, with the max decomposition rate occurring at 330 °C compared to 382 °C for the untreated sample, with the relative sizes of the $M^{II}_2M^{III}OH$ and M^{II}_3OH and decomposition peaks reversing.[40–43] The Mg_2NiAl-PO_4 LDHs show clearly different thermal events: there is enhanced mass loss < 200 °C and no obvious thermal event from 250 to 450 °C. The enhanced mass loss in the dehydration region is attributed to the larger hydration sphere of the PO_4^{3-} compared to the CO_3^{2-} anion,[44,45] while the lack of thermal events at higher temperatures is due to the different thermal decomposition pathway of PO_4^{3-} which polymerises to form metaphosphates or reacts with the surface rather than being liberated as a gas.[46,47]

To investigate the influence of the anion on the Ni in the system, temperature programmed reduction (TPR) experiments were conducted with the profiles shown in Figure 5.27. Ni reduction does not occur until above 350 °C in either system as is typical for Ni oxides. Ni reduction can be classified into three regions based on the strength of the interaction with the support: weak (400 to 500 °C), medium (500 to 600 °C) and strong (600 to 800 °C).[48] The reduction profiles are significantly different between the samples, with the CO_3^{2-} system showing a small amount of a

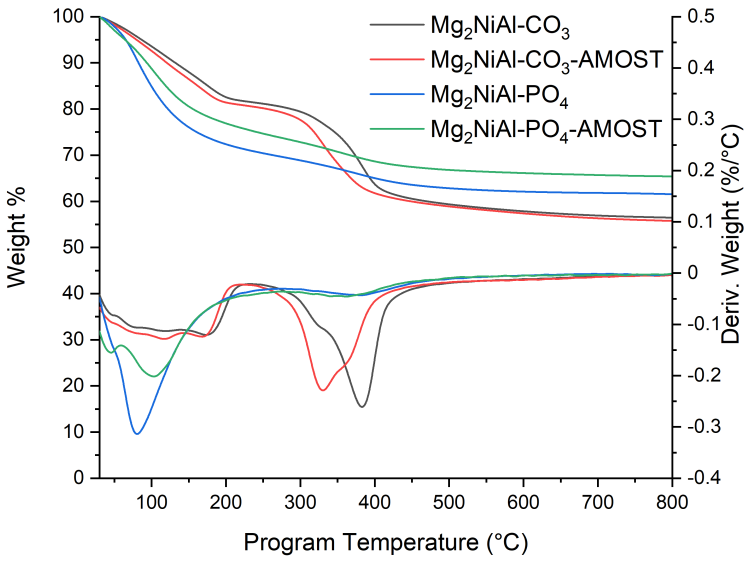

Figure 5.26: TGA thermal curves of the conventionally synthesised Mg_2NiAl LDHs.

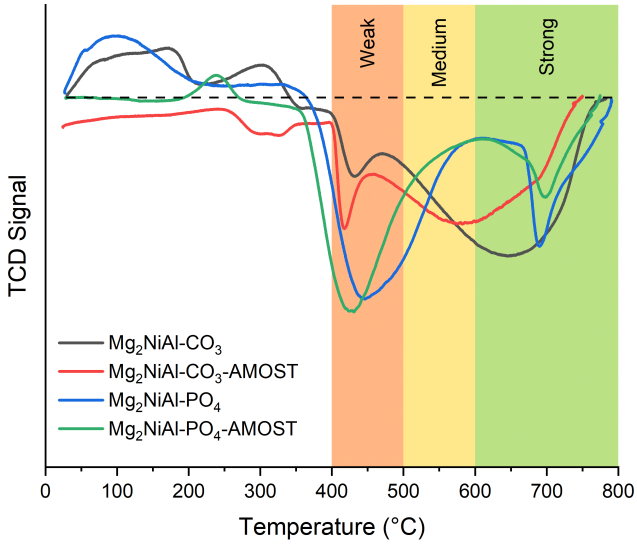

Figure 5.27: TPR signals of the conventionally synthesised Mg_2NiAl LDHs.

well-defined weak site (peak at 430 °C for the non-treated sample and 420 °C for the AMOST sample) and a less well-defined medium to strong site (broad peak from 475 to 750 °C) compared to the PO_4^{3-} system, which shows most Ni in a poorly defined weak to medium site (broad peak from 355 to 600 °C) and a small amount of Ni in a well-defined strong site (peak at 690 °C for the non-treated sample and 700 °C for the AMOST sample). This indicates that the anion does interact with the Ni species, with at least two types present in the materials in varying amounts. The peaks for the CO_3^{2-} LDH can be assigned to bulk NiO (400 °C)[49] and Ni in the Mg(Ni, Al)O solid solution (LDO phase formed on calcination).[50] Multiple phases may be present in the LDO material, leading to a convolution of curves forming the broad feature observed such as $NiAlO_4$ (592 °C) and Ni_2AlO_4 (681 °C.[51] The well-defined peak for the PO_4^{3-} LDHs at ≈ 700 °C matches that seen for $Ni_3(PO_4)_2$ and for mixed Ni^{2+} and PO_4^{3-} impregnated SiO_2 by Chen *et al.* indicating this is a PO_4^{3-} complexed Ni species.[52] The broad peak at 450 °C in the PO_4^{3-} LDHs is also attributed to bulk NiO, with the increase in relative amount indicating that the LDH is less stable to segregation. The similarity of the AMOST treated LDHs and the non-treated LDHs indicate the AMOST process does not effect the distribution or stability of the Ni species.

SEM images and EDX mapping of the LDHs are shown in Figures: C.20 and C.21; C.22 and C.23; C.24 and C.25; C.26 and C.27 for $Mg_2NiAl\,CO_3$, $Mg_2NiAl\,PO_4$, $Mg_2NiAl\,CO_3$ AMOST and $Mg_2NiAl\,PO_4$ AMOST SLDHs respectively. The particles are all large agglomerations of smaller spherical particles. In the images of the CO_3^{2-} based LDHs, the largest particles are 58 µm and the smaller spherical particles are 100 to 700 nm. High magnification images show these spherical particles are made of intergrown platelets in the typical sand-rose morphology of LDHs with a platelet thickness ≈ 20 nm (Figures C.20(d) and C.24(d)). EDX mapping shows a homogeneous distribution of Mg, Al and Ni throughout the particles with no phase segregation, as seen for the SLDH. In the PO_4^{3-} based LDHs, the largest particles observed are 42 µm and the smaller spherical particles (≈ 350 nm) possess a smooth surface. A lack of plate-like particles is in agreement with the XRD

pattern (Figure 5.23) which shows no strong LDH reflections from sufficiently large LDH crystallites. There is no observed difference in morphology between the normal and AMOST treated samples, in contrast to previous work by Chen *et al.* which showed a decrease in agglomeration from smooth densely stacked particles to loose flower-shaped agglomerates.[53]

In summary, a CO_3^{2-} and an unconfirmed PO_4^{3-} Mg_2NiAl LDH phase were synthesised with the presence of the desired anion confirmed by FTIR and elemental analysis. The SSA of the samples were successfully increased using the AMOST method with the PO_4^{3-} based material showing a high BET SSA of $439\,m^2\,g^{-1}$. The changing of the anion used in the synthesis influences the distribution of Ni sites in the material, as seen by the temperature programmed reduction profile, suggesting a degree of Ni anion interaction.

These catalysts were tested for PP pyrolysis using a similar experimental setup to that used for the SLDHs, with an increase of the catalyst loading to 20% and a degrease in the reaction time to 5 hours. All the LDH materials were catalytically active, changing the product distribution of the reaction (Figure 5.28). All the catalysts showed a similar gas yield, which is significantly lower than the conversion observed previously, attributed to the decreased reaction time. For the non-AMOST samples, both catalysts enhanced the H_2 production, with the PO_4^{3-} LDH showing a slightly higher selectivity than the CO_3^{2-} LDH (18% vs 13% respectively), likely due to the higher amount of water within the catalyst, as evidenced by the higher TGA loss $< 200\,°C$.

The AMOST samples had a much higher H_2 yield, but also a significant amount of acetone present. This was attributed to the dehydrogenation of residual isopropyl alcohol within the catalysts. Similar materials have been used to this effect, such as Ni-SiO_2, prepared by Lokras *et al.* by impregnation and reduction at 300 °C, which showed 20.4% conversion to acetone after 24 h at 300 °C.[54] Assuming the carbon content of Mg_2NiAl-PO_4 LDH is all from isopropanol (2.46%, $0.683\,mmol_{IPA}\,g_{LDH}^{-1}$), this gives a theoretical yield of $39.6\,mg_{Acetone}\,g_{LDH}^{-1}$ compared to the experimental

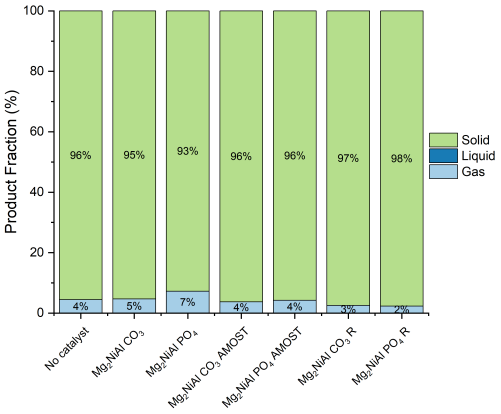

(a) Distribution of solid, liquid and gas products

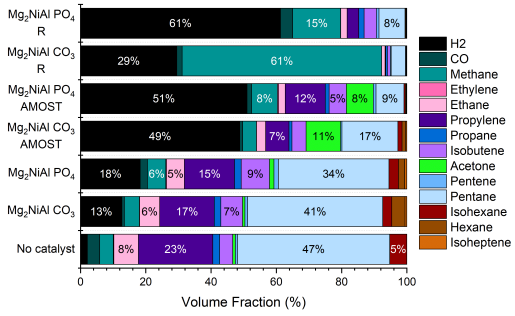

(b) Gas product distribution by volume.

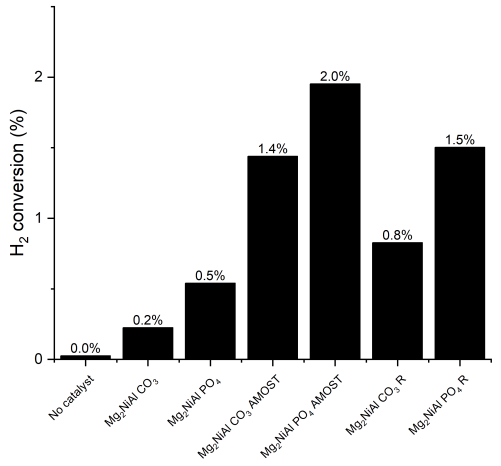

(c) Hydrogen conversion as fraction of the amount present in the PP.

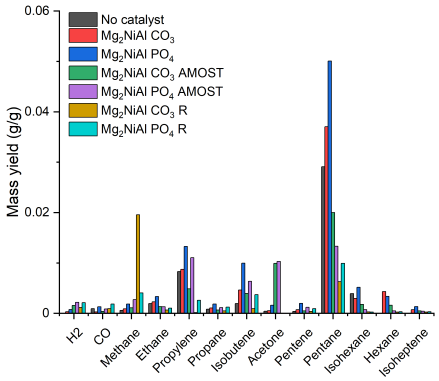

(d) Gas product yields.

Figure 5.28: PP pyrolysis data using 20 wt% of different Mg_2NiAl LDH catalysts at 290 °C.

yield of 51.2 $mg_{Acetone}\ g^{-1}_{LDH}$ (some acetone is observed for the non-AMOST treated samples to which the excess yield is attributed). The high yield indicates that full conversion of the IPA to acetone may be occurring. High selectivity for acetone is rarely reported for Ni-based catalysts, with the competitive dehydration reaction to form propene also occurring, with the selectivity depending on the other metals present.[55] For example, CuO-NiO nanocomposites developed by Said *et al.* show 98% conversion and 100% selectivity to acetone at 200 °C in a fixed bed setup. Given the high conversion rate observed for the Mg_2NiAl LDH, further work should

be conducted to evaluate it as an effective catalyst for this application.

To evaluate if there was an increase in H_2 production from the PP with the increase in surface area, the catalysts were dried at 200 °C under vacuum to remove any residual solvent before the reaction. A colour change was observed, indicating a change in the Ni coordination sphere (Figure C.28). The product yield from the use of the dried catalysts is shown in Figure C.29. There is no significant variation in the gas fraction produced, but there are noticeable changes to the gas product selectivity. Of note, the CO_3^{2-} based catalysts show a higher conversion and hydrogen selectivity. The H_2 selectivity for all the dried samples is similar ($\approx$ 25%); with an increase observed for the non-AMOST treated samples, suggesting an increase in activity and a decrease for the AMOST treated samples as expected, without the formation of significant amounts of acetone. All the samples also show significant amounts of methane produced (selectivity 44% to 53%) whilst the yields of other hydrocarbons remain similar. This change in selectivity is unexpected and suggests that a new active site which promotes the formation of methane is formed during the drying process. In Ni-based catalysts reported in the literature, a major problem is reduction of the Ni^{II} species under the reaction conditions to form Ni nanoparticles which are highly active for C−C bond cleavage, forming methane, hydrogen and coke. This trend aligns with the observed selectivity, and low-temperature heat treatments of Ni-based materials have been demonstrated to affect their structure.[56] However, further investigations are required to elucidate why this transformation is detected at 200 °C, rather than at the elevated temperatures applied during pyrolysis.

Although the TPR profiles (Figure 5.27) suggest there is no reduction reaction below 400 °C, the catalysts were calcined and reduced at 600 °C (denoted as Mg_2NiAl-X-R) to evaluate any changes to catalytic performance from reduced Ni species. Figure C.30 shows the XRD pattern of the reduced samples with weak broad reflections at at 44.7° and 52° indexed to the (111) and (110), indicating the formation of Ni nanoparticles. The reflections are stronger for the PO_4^{3-} based material

and weak periclase reflections are also observed for the CO_3^{2-} based material. Figures C.31 to C.34 show SEM and EDX mapping of the two reduced samples. The materials morphologies are similar to the pre-calcined samples with isolated particles ($\leq 10\,\mu m$) observed for the CO_3^{2-} based sample and large agglomerations ($\leq 32\,\mu m$) for the PO_4^{3-} based sample. The surface of the CO_3^{2-} based sample still shows the intergrown sand-rose texture and the surface of the PO_4^{3-} based samples is no longer dominated by the smooth lumpy spheres previously observed, but with a similar sand-rose morphology to the CO_3^{2-} samples (Figure C.33(d)). EDX mapping shows the elements are still homogeneously distributed within the samples, with no obvious agglomeration of Ni.

The product distribution when the reduced catalysts are used for catalytic PP pyrolysis is significantly altered with H_2 and methane selectivity enhanced compared to the unreduced catalysts. However, there is significant differences in the product distribution between the PO_4^{3-} and CO_3^{2-} based catalysts. The Mg_2NiAl-PO_4-R catalyst is highly selective for H_2 (61%) with 15% selectivity for methane compared to the Mg_2NiAl-CO_3-R catalyst which is only 29% selective for H_2 and 61% selective for methane. The Mg_2NiAl-CO_3-R catalyst shows a similar product distribution to dried catalyst, indicating further calcination and reduction has little effect on the catalyst. The significant enhancement of H_2 production using the Mg_2NiAl-PO_4-R catalyst suggests that after calcination and reduction, the PO_4^{3-} within the material exerts a significant influence in the catalyst, forming a different active site than in the precursor material. Ni phosphate materials have been reported for dehydrogenation reactions such as $Ca_8Ni(PO_4)_6$, which was used for the dehydrogenation of n-butane to 1,3-butadiene by Britton *et al.*,[57] or Ni^{II} phosphosilicate used for the dehydrogenation of propane by Zhang *et al.*[58] Zhang *et al.* discuss how the Ni−O−P bond stabilises the Ni^{II} species, preventing its reduction and the formation of Ni clusters during the reaction. Ni^0 nanoparticles show high methane selectivity and poor stability. This behaviour correlates with the activity observed for the reduced catalysts with the CO_3^{2-} catalyst showing high methane selectivity compared to the PO_4^{3-} catalyst which shows high H_2

selectivity. This suggests the selectivity of the catalysts may be improved by calcination without reduction to decrease the amount of Ni^0 present, while enabling the stabilising Ni−O−P interactions.

In summary, the anion used to prepare the catalyst has a minimal effect on the catalyst performance during polypropylene pyrolysis, with the PO_4^{3-} catalysts showing a slight increase in activity. The AMOST treated samples show the catalysts are active for isopropanol dehydrogenation to acetone. After drying, the selectivity of the catalysts changes, with a significant amount of methane formed and the CO_3^{2-} catalysts showing a higher conversion to gas than the PO_4^{3-} materials. After calcination and reduction, the selectivity of the catalysts is further changed: the CO_3^{2-} based material is highly selective for H_2 (29%) and CH_4 (61%) whilst the PO_4^{3-} based material has a higher preference for H_2 (61% vs 15% CH_4). The gas yields are lower ($\approx$ 3%) but the H_2 yield is enhanced (0.8% and 1.5%) compared to the non-reduced catalysts.

5.4 Experimental details for Chapter 5

5.4.1 Reagents and chemicals

Aluminium nitrate ($Al(NO_3)_3 \cdot 9\,H_2O$), iron nitrate ($Fe(NO_3)_3 \cdot 9\,H_2O$), magnesium nitrate ($Mg(NO_3)_2 \cdot 6\,H_2O$), nickel nitrate ($Ni(NO_3)_2 \cdot 6\,H_2O$), sodium hydroxide (NaOH), trisodium phosphate (Na_3PO_4) and sodium carbonate (Na_2CO_3) were purchased from Sigma Aldrich. Xylene and acetone were purchased from Sigma Aldrich and used without further purification. 1 M NaOH was made by dissolving 40 g of NaOH in 1 L of D.I. water. 0.75 M NaOH was made by mixing 3 : 1 1 M NaOH to D.I. water. Polypropylene beads (M_W =255.6 kDa, PDI = 9.6) were supplied by SCGC, Thailand.

5.4.2 Synthesis of Zn SLDH

0.192 g (1.6 mmol) A-$MgHPO_4$ (calcined struvite, Chapter 3.4.8), 0.238 g (0.8 mmol) $Zn(NO_3)_2 \cdot 6\,H_2O$ and 0.300 g (0.8 mmol) $Al(NO_3)_3 \cdot 9\,H_2O$ were added to 20 mL 1 M

NaOH and stirred at 80 °C for 20 h at 750 RPM. The mixture was then filtered and washed with D.I. water until the filtrate was at pH 7. The solid residue was then dried overnight at 30 °C under vacuum.

Reduced NaOH

0.192 g (1.6 mmol) A-$MgHPO_4$ (calcined struvite, Chapter 3.4.8), 0.238 g (0.8 mmol) $Zn(NO_3)_2 \cdot 6\,H_2O$ and 0.300 g (0.8 mmol) $Al(NO_3)_3 \cdot 9\,H_2O$ were added to 20 mL D.I. water, the pH adjusted to the desired level by addition of 1 M NaOH (4, 4.5 and 5 mL for pH 9.15, 9.56 and 10.14) and stirred at 80 °C for 20 h at 750 RPM. The mixture was then filtered and washed with D.I. water until the filtrate was at pH 7. The solid residue was then dried overnight at 30 °C under vacuum.

Slow addition of NaOH

0.192 g (1.6 mmol) A-$MgHPO_4$ (calcined struvite, Chapter 3.4.8), 0.238 g (0.8 mmol) $Zn(NO_3)_2 \cdot 6\,H_2O$ and 0.300 g (0.8 mmol) $Al(NO_3)_3 \cdot 9\,H_2O$ were added to 20 mL D.I. water, the chosen amount of 1 M NaOH (6.5, 8, 10 and 12 mL) was added slowly (0.1 mL min^{-1}) and stirred at 80 °C for 20 h at 750 RPM. The mixture was then filtered and washed with D.I. water until the filtrate was at pH 7. The solid residue was then dried overnight at 30 °C under vacuum.

5.4.3 Synthesis of Fe SLDH

$Mg_xFe_yAl_{1-y}$ SLDH were synthesised using the following methodology with the quantities of reagents given in Table 5.11. *A* g A-$MgHPO_4$ (calcined struvite, Chapter 3.4.8), *B* g $Fe(NO_3)_3 \cdot 9\,H_2O$ and *C* g $Al(NO_3)_3 \cdot 9\,H_2O$ were added to either 20 mL 1 M or 0.75 M NaOH and stirred at 80 °C for 20 h at 750 RPM. The mixture was then filtered and washed with D.I. water until the filtrate was at pH 7. The solid residue was then dried overnight at 30 °C under vacuum.

5.4.4 Synthesis of Ni SLDH

0.192 g (1.6 mmol) A-$MgHPO_4$ (calcined struvite, Chapter 3.4.8), 0.233 g (0.8 mmol) $Ni(NO_3)_2 \cdot 6\,H_2O$ and 0.300 g (0.8 mmol) $Al(NO_3)_3 \cdot 9\,H_2O$ were added to 20 mL 1 M

Table 5.11: The amount of metal precursors used to produce MgFeAl SLDHs of different ratios

Sample	A	B	C
$Mg_3Fe_{0.5}Al_{0.5}$	0.2901 g (2.41 mmol)	0.1616 g (0.4 mmol)	0.1501 g (0.4 mmol)
Mg_3Fe	0.2901 g (2.41 mmol)	0.3232 g (0.8 mmol)	
$Mg_2Fe_{0.5}Al_{0.5}$	0.2901 g (2.41 mmol)	0.2424 g (0.6 mmol)	0.2251 g (0.6 mmol)
$Mg_2Fe_{0.7}Al_{0.3}$	0.2886 g (2.4 mmol)	0.3394 g (0.84 mmol)	0.1350 g (0.36 mmol)
$Mg_2Fe_{0.8}Al_{0.2}$	0.2886 g (2.4 mmol)	0.3878 g (0.96 mmol)	0.0900 g (0.24 mmol)
Mg_2Fe	0.2901 g (2.41 mmol)	0.4848 g (1.2 mmol)	

NaOH and stirred at 80 °C for 20 h at 750 RPM. The mixture was then filtered and washed with D.I. water until the filtrate was at pH 7. The solid residue was then dried overnight at 30 °C under vacuum.

The synthesis was scaled up five times using 0.96 g (8 mmol) A-$MgHPO_4$, 1.163 g (4 mmol) $Ni(NO_3)_2 \cdot 6\,H_2O$ and 1.5 g (4 mmol) $Al(NO_3)_3 \cdot 9\,H_2O$ and 100 mL 1 M NaOH

5.4.5 Preparation of polypropylene SLDH blends

10 wt% SLDH in polypropylene blends were prepared via mixing a SLDH suspension and a solution of dissolved polypropylene and re-precipitating the mixture. 0.02 g of SLDH was added to 10 mL of xylene and suspended via sonication for 30 min and 0.2 g polypropylene was separately dissolved in 40 mL xylene at 130 °C. The SLDH suspension was added to the dissolved polypropylene and left to stir for 1 h. The resulting mixture (still at 130 °C) was then added dropwise to a vigorously stirred beaker of 100 mL of acetone (at RT) which caused precipitation of the polypropylene/SLDH blend. The suspension was separated via vacuum filtration and washed three times with acetone. The collected powders were then dried overnight under vacuum at 30 °C

5.4.6 Batch polypropylene pyrolysis

Batch pyrolysis reactions were conducted in a 50 mL high pressure vessel from Parr. Approximately 0.5 g of polypropylene beads and the desired catalyst (typically 0.05 g or 0.1 g) were added to a pre-weighed glass liner with a glass stir bar and sealed within the pressure vessel. The inlet was attached via hose to a Schlenck line, degassed and filled with 2 bar N_2. The vessel was placed within a home-built heating mantle and heated to the desired temperature, monitored by a thermocouple within the vessel. After the experiment was complete, the vessel was allowed to return to room temperature and the gas products were analysed by GC and GC-MS (Chapter 2.1.11 and 2.1.11). The mass of the products and liner were measured to calculate the gas yield.

5.4.7 Synthesis of conventional Ni LDH

6.41 g $Mg(NO_3)_2 \cdot 6\,H_2O$ (25 mmol), 3.63 g $Ni(NO_3)_2 \cdot 6\,H_2O$ (12.5 mmol) and 4.69 g $Al(NO_3)_3 \cdot 9\,H_2O$ (12.5 mmol) were dissolved in 58 mL degassed (boiled) D.I. water. This was added to a solution of 4.1 g Na_3PO_4 (25 mmol) or 2.65 g (25 mmol) in 50 mL degassed D.I. water at a rate of 0.833 mL/min under a flow of N_2 with the pH kept at 9.5 via addition of 1 M NaOH. The mixture was aged for 20 h (overnight) under stirring. The mixture was then filtered and washed with D.I. water until the filtrate was at pH 7. The precipitate was divided in two, and half was subjected to the AMOST treatment: the solid was resuspended in 1 L of isopropyl alcohol and stirred over night before being collected by vacuum filtration. Both the AMOST-treated and the non-AMOST-treated solid residues after filtration were then dried overnight at 30 °C under vacuum. Depending on the anion used, and whether the AMOST treatment was used, the samples were labelled as Mg_2NiAl-CO_3, Mg_2NiAl-PO_4, Mg_2NiAl-CO_3-AMOST and Mg_2NiAl-PO_4-AMOST.

Dried samples were prepared by taking 0.15 g of the respective catalysts and heating them to 200 °C under vacuum for 2 h. A colour change from blue/green to light brown was observed. Samples were cooled and then stored in a desiccator.

Calcined and reduced samples were prepared by loading 0.4 g of the catalyst into an alumina boat, heating the sample to 650 °C (5 °C min^{-1}) under a flow of H_2 (50 mL min^{-1}) for 2 h. After cooling, the samples were transferred to a glove box for storage until use.

5.5 Conclusions

Both Fe and Ni were included into SLDH materials via the addition of their salts during the synthesis procedure. EDX mapping of the particles indicates that there is some segregation of the metals and the crystallinity of the materials is reduced. Further work may explore the inclusions of other metals into the material such as Cu and Co. Mg_2NiAl SLDH was shown to be a catalyst for the production of H_2 during PP pyrolysis, although it does not appear to promote chain scission.

Variation of the reaction time in the preparation of the Ni SLDH increases the surface area and PO_4^{3-} content and led to increased catalytic activity. Catalysts were prepared by conventional LDH precipitation processes to investigate the effect of the PO_4^{3-} anion and the surface area on the catalyst performance. The PO_4^{3-} based material appeared largely amorphous from their XRD patterns, but the EDX mapping shows that the particles contain a homogeneous mixture of P, Mg, Al and Ni. These materials catalyse the formation of H_2 during PP pyrolysis, with similar product selectivities and activities irrespective of the anion used or the specific surface area of the catalyst. Upon drying or calcination, the materials catalyse the formation of methane, suggesting the formation of Ni^0 nanoparticles, while the reduced PO_4^{3-} catalyst shows the highest selectivity for H_2 (61%) of the catalysts tested, indicating that a Ni-O-P interaction occurs. Although the catalysts show catalytic activity for H_2 production, the conversion to gas is low. Further work should explore increasing the gas conversion either through increasing the reaction temperature via modification of the experimental setup or via the inclusion of a co-catalyst such as ZSM-5 to promote low temperature cracking.

Actual post-consumer waste comprises a variety of contaminants, including plasticisers incorporated during the production phase, as well as contaminants accumulated throughout their usage. Further work should investigate any effect these may have on the pyrolysis system.

References

(1) A. Gala, M. Guerrero and J. M. Serra, *Waste Manag.*, 2020, **111**, 22–33.

(2) A. I. Eldahshory, K. Emara, M. S. Abd-Elhady and M. A. Ismail, *Sci. Rep.*, 2023, **13**, 11766.

(3) C. Kassargy, S. Awad, G. Burnens, K. Kahine and M. Tazerout, *J. Anal. Appl. Pyrolysis*, 2017, **127**, 31–37.

(4) S. Papuga, M. Djurdjevic, A. Ciccioli and S. Vecchio Ciprioti, *Symmetry*, 2022, **15**, 38.

(5) S. Wang, Y. Zhang, R. Shan, J. Gu, T. Huhe, X. Ling, H. Yuan and Y. Chen, *J. Clean. Prod.*, 2022, **352**, 131566.

(6) M. Szabados, C. Bús, M. Ádok-Sipiczki, Z. Kónya, Á. Kukovecz, P. Sipos and I. Pálinkó, *Particuology*, 2016, **27**, 29–33.

(7) J. Liu, X. Huang, Y. Li, K. M. Sulieman, X. He and F. Sun, *J. Phys. Chem. B*, 2006, **110**, 21865–21872.

(8) X. Guo and G. He, *J. Mater. Chem. A*, 2023, **11**, 11987–12001.

(9) H.-X. Li, Y. Wang and D.-Q. Cang, *J. Cent. South Univ. Technol.*, 2010, **17**, 967–971.

(10) *Highlights in Mineralogical Crystallography*, ed. T. Armbruster and R. M. Danisi, DE GRUYTER, 2015.

(11) J. Chen, S. Natarajan, P. A. Wright, R. H. Jones, J. M. Thomas, C. R. A. Catlow and R. P. Townsend, *J. Solid State Chem.*, 1993, **103**, 519–522.

(12) K. O. Kongshaug, H. Fjellvåg and K. P. Lillerud, *Solid State Sci.*, 2000, **2**, 205–214.

(13) J. T. Kloprogge, L. Hickey and R. L. Frost, *J. Solid State Chem.*, 2004, **177**, 4047–4057.

(14) A. F. d. Silva, J. L. d. S. Duarte and L. Meili, *Sep. Purif. Technol.*, 2021, **264**, 118353.

(15) R. Elmoubarki, F. Z. Mahjoubi, A. Elhalil, H. Tounsadi, M. Abdennouri, M. Sadiq, S. Qourzal, A. Zouhri and N. Barka, *J. Mater. Res. Technol.*, 2017, **6**, 271–283.

(16) T.-H. Kim, L. Lundehøj and U. G. Nielsen, *Appl. Clay Sci.*, 2020, **189**, 105521.

(17) R. Downs and M. Hall-Wallace, *Am. Mineral.*, 2003, **88**, 247–250.

(18) C. Xiong, X. Chen, L. Jin, P. Zhang, L. Gao, B. Liu and Y. Lin, *ChemistrySelect*, 2024, **9**, e202403697.

(19) G. V. Manohara, S. V. Prasanna and P. V. Kamath, *Eur. J. Inorg. Chem.*, 2011, **2011**, 2624–2630.

(20) Y. M. Mos, A. C. Vermeulen, C. J. N. Buisman and J. Weijma, *Geomicrobiol. J.*, 2018, **35**, 511–517.

(21) A. Nakatsuka, H. Ueno, N. Nakayama, T. Mizota and H. Maekawa, *Phys. Chem. Miner.*, 2004, **31**, 278–287.

(22) W. Xu, M. Mertens, T. Kenis, E. Derveaux, P. Adriaensens and V. Meynen, *Mater. Chem. Phys.*, 2023, **295**, 127113.

(23) J. Maria Fernández, M. Angeles Ulibarri, F. M. Labajos and V. Rives, *J. Mater. Chem.*, 1998, **8**, 2507–2514.

(24) R. Birjega, A. Vlad, A. Matei, V. Ion, C. Luculescu, M. Dinescu and R. Zavoianu, *Thin Solid Films*, 2016, **614**, 36–41.

(25) Y. Shi, F. Chen, J. Yang and M. Zhong, *Appl. Clay Sci.*, 2010, **50**, 87–91.

(26) L. Wang, M. Zhang and B. Zhou, *Appl. Sci.*, 2017, **7**, 55.

(27) E. Krendlinger, in *Kirk-Othmer Encyclopedia of Chemical Technology*, 2023, pp. 1–28.

(28) M. Arabiourrutia, G. Elordi, G. Lopez, E. Borsella, J. Bilbao and M. Olazar, *J. Anal. Appl. Pyrolysis*, 2012, **94**, 230–237.

(29) W. Tongamp, Q. Zhang and F. Saito, *Fuel Process. Technol.*, 2009, **90**, 909–913.

(30) R. Song, Z. Jiang, W. Bi, W. Cheng, J. Lu, B. Huang and T. Tang, *Chem. – Eur. J.*, 2007, **13**, 3234–3240.

(31) A. López, I. de Marco, B. M. Caballero, M. F. Laresgoiti, A. Adrados and A. Aranzabal, *Appl. Catal. B: Environ.*, 2011, **104**, 211–219.

(32) T. M. Kruse, H.-W. Wong and L. J. Broadbelt, *Macromolecules*, 2003, **36**, 9594–9607.

(33) S. Sarkar, K. P. S. Cheung and V. Gevorgyan, *Chem. Sci.*, 2020, **11**, 12974–12993.

(34) C. Chen, A. Wangriya, J.-C. Buffet and D. O'Hare, *Dalton Trans.*, 2015, **44**, 16392–16398.

(35) S. Ding, B. Zheng, X. Wang, Y. Zhou, Z. Pan, Y. Chen, G. Liu and L. Lang, *Langmuir*, 2024, **40**, 10384–10392.

(36) R. L. Frost, A. W. Musumeci, M. O. Adebajo and W. Martens, *J. Therm. Anal. Calorim.*, 2007, **89**, 95–99.

(37) J. D. Dillenburger, L. Schulte, P. Mahale, M. Suleiman and T. E. Mallouk, *Chem. Mater.*, 2023, **35**, 6437–6446.

(38) Q. K. Loi, S. J. Tan, D. D. Do and D. Nicholson, *Ind. & Eng. Chem. Res.*, 2021, **60**, 15343–15351.

(39) S. Shang, A. Hanif, M. Sun, Y. Tian, Y. S. Ok, I. K. M. Yu, D. C. W. Tsang, Q. Gu and J. Shang, *J. Hazard. Mater.*, 2019, **373**, 285–293.

(40) W. Yang, Y. Kim, P. K. T. Liu, M. Sahimi and T. T. Tsotsis, *Chem. Eng. Sci.*, 2002, **57**, 2945–2953.

(41) K. Matsuda, N. Iio, M. Kawashimo, A. Okuda, R. Fukuzaki, N. Tarutani, K. Katagiri and K. Inumaru, *Inorg. Chem.*, 2023, **62**, 17276–17287.

(42) G. Yu, Y. Zhou, R. Yang, M. Wang, L. Shen, Y. Li, N. Xue, X. Guo, W. Ding and L. Peng, *J. Phys. Chem. C*, 2015, **119**, 12325–12334.

(43) P. Kenyon, S. Roberts, Z. R. Turner, N. H. Rees and D. O'Hare, *J. Phys. Chem. C*, 2024, **128**, 12249–12258.

(44) S. Marappa and P. Vishnu Kamath, *Z. Anorg. Allg. Chem.*, 2015, **641**, 927–934.

(45) I. Persson, *Dalton Trans.*, 2024, **53**, 15517–15538.

(46) A. S. Roy, M. de Beer, S. K. Pillai and S. S. Ray, *ACS Omega*, 2023, **8**, 15017–15030.

(47) A. Shimamura, E. Kanezaki, M. I. Jones and J. B. Metson, *J. Solid State Chem.*, 2012, **186**, 116–123.

(48) I. Pedroarena, L. Grande, J. J. Torrez-Herera, S. A. Korili and A. Gil, *Fuel*, 2023, **334**, 126789.

(49) A. V. Fedorov, R. G. Kukushkin, P. M. Yeletsky, O. A. Bulavchenko, Y. A. Ches l v and V. A. Yakovlev, *J. Alloy. Compd.*, 2020, **844**, 156135.

(50) D. Díez, A. Urueña and G. Antolín, *Processes*, 2020, **9**, 76.

(51) D. d. S. Lima, Y. R. Dias and O. W. Perez-Lopez, *Sustain. Energy & Fuels*, 2020, **4**, 5747–5756.

(52) J. Chen, Y. Chen, Q. Yang, K. Li and C. Yao, *Catal. Commun.*, 2010, **11**, 571–575.

(53) C. Chen, M. Yang, Q. Wang, J.-C. Buffet and D. O'Hare, *J. Mater. Chem. A*, 2014, **2**, 15102–15110.

(54) S. S. Lokras, P. K. Deshpande and N. R. Kuloor, *Ind. & Eng. Chem. Process. Des. Dev.*, 1970, **9**, 293–297.

(55) A. E.-A. A. Said, M. M. M. Abd El-Wahab and M. N. Goda, *Egypt. J. Basic Appl. Sci.*, 2016, **3**, 357–365.

(56) F. Basharat, U. A. Rana, M. Shahid and M. Serwar, *RSC Adv.*, 2015, **5**, 86713–86722.

(57) E. C. Britton, A. J. Dietzler and C. R. Noddings, *Ind. & Eng. Chem.*, 1951, **43**, 2871–2874.

(58) G. Zhang, C. Yang and J. T. Miller, *ChemCatChem*, 2018, **10**, 961–964.

6

Conclusions and outlook

Contents

6.1 Conclusions

The work in this thesis has focused on developing the synthesis of LDHs derived from struvite and their applications in sustainable technologies. The effects of different reaction parameters on the direct conversion of struvite to LDHs were explored, such as the reaction temperature, the amount of base, and the size of the precursor particles. Non-obvious parameters such as how quickly the reaction mixture was heated were shown to have a significant effect, with faster ramp rates hindering conversion. An unusual intermediate phase was identified as the ammonium analogue of hazenite, which has not been previously synthesised directly, as far as could be ascertained.

An alternative synthesis pathway was developed using a separate calcination step. This produced SLDHs with elevated surface areas ($> 180\,\mathrm{m^2\,g^{-1}}$). Different meth-

ods for the calcination of struvite were explored, with struvite produced under a flow of N_2 found to produce SLDHs with the highest surface area ($218\,m^2\,g^{-1}$). The calcination method strongly affected the properties of the product formed, with significant changes in the pore distributions between those calcined under vacuum and those under N_2. The humidity was also crucial, with the presence of water causing formation of the mineral dittmarite. This process is simple and easy to scale up with 25 g produced and can be carried out at high solid loadings (up to $40\,g\,L^{-1}$). The synthesis was improved according to the principles of green chemistry by using $NaAlO_2$ as the aluminium source, which has an improved atom economy compared to $Al(NO_3)_3 \cdot 9\,H_2O$ and can be easily derived from other waste products, such as blast furnace slag.

In line with the goal of developing sustainable technologies, the use of SLDHs as CO_2 sorbents was explored. SLDHs were functionalised with a variety of different amino silylethers and showed the ability to capture CO_2 under atmospheric conditions (up to $0.443\,mmol_{CO_2}\,g^{-1}$ at the ultra-low pressure of 0.4 mbar (equivalent to 400 ppm)). The isotherms were fitted to various theoretical models, and the best fit was found using a triple-site Langmuir model (with a RMSE value of 5.43×10^{-3}). At least two sites are needed to fit the experimental isotherm well, indicating that a mixture of chemisorption and physisorption processes occur. The amount of grafted amine was found to vary with the grafting solvent and whether anhydrous conditions were employed, with a maximum loading of $1.171\,mmol\,g^{-1}$ when cyclohexane was used as the grafting solvent. Surprisingly, the CO_2 capture performance was increased with lower amine loadings ($0.391\,mmol_{CO_2}\,g^{-1}$ for TRI@SLDH-Dry, with an amine efficiency of 0.48), suggesting the presence of diffusion-based limitations on CO_2 performance.

Various thermodynamic properties of the sorbents were measured and the process energy and productivity were calculated ($10.04\,GJ\,t_{CO_2}^{-1}$, $0.145\,t_{CO_2}\,d^{-1}\,m^{-3}$). These values are comparable to estimates of the commercial process used by Climeworks (a specific energy requirement of $\approx$ $10.8\,MJ_t\,kg^{-1}$ and a productivity

of $0.074\,t_{CO_2}\,d^{-1}\,m^{-3}$). The high tap density of these sorbents is unusual ($\approx 0.7\,g\,mL^{-1}$) and is a key factor in the high productivity. TPD measurements suggest that a lower regeneration temperature could be used ($\leq 80\,°C$), which would decrease the process energy costs to levels more competitive with materials previously reported in the literature ($4.2\,GJ\,t_{CO_2}^{-1}$).[1]

Finally, the introduction of other elements into the SLDH materials was investigated. Iron and nickel were successfully incorporated into the structure via the addition of their salts during the synthesis. Elemental mapping confirmed the introduction of these metals into the material, although a small amount of segregation was observed. Preliminary experiments using these materials as catalysts for catalytic polypropylene pyrolysis are reported. The materials are catalytically active, enhancing the production of H_2 (from 11 to 53%); however, the gas yields are low ($\approx 20\%$), limiting the overall conversion with a large amount of wax formed.

The effect of ageing time upon the performance of the MgNiAl SLDH catalysts was evaluated with longer ageing times increasing catalytic activity (the gas yield increased from 13 to 31% upon increasing the ageing time from 1 to 3 days). Conventional LDHs were prepared for comparison, varying the anion (CO_3^{2-} or PO_4^{3-}) and employing a solvent treatment (AMOST) to increase the surface area. The reaction using PO_4^{3-} yields an amorphous material which displays a high surface area after solvent treatment ($439\,m^2\,g^{-1}$, compared to $239\,m^2\,g^{-1}$ for the solvent treated CO_3^{2-} material). TPR measurements show that changing the anion influences the nickel-support interaction, with the PO_4^{3-}-based material showing more well-defined sites and a greater amount of weakly interacting nickel species. Surprisingly, the product distribution and catalytic activity of all of the catalysts were very similar. After drying or calcination and reduction, the materials show enhanced selectivity for methane (up to 61% by volume), suggesting the formation of nickel nanoparticles.[2] A more noticeable difference in catalyst selectivity is observed in the calcined and reduced catalysts, where the PO_4^{3-}-based material shows a high H_2 selectivity (61%), albeit with a low gas conversion (2%).

6.2 Future Work

These waste derived SLDH materials with high density and surface area have a wide scope for application. Additional technologies utilising these SLDHs should be developed, with potential applications in other sustainable technologies such as wastewater remediation to absorb harmful substances in water streams such as pharmaceuticals or per- and polyfluoroalkyl substances or to catalyse PET plastic hydrolysis.[3–6] There are several unexplained results that would also warrant further investigation, such as the increasing enthalpy of adsorption on the amine-modified SLDH and the unexplained ^{29}Si NMR signals (-75 to -100 ppm). Further materials may also be developed by the inclusion of other metals, such as Cu, into the structure.[7]

Further work should investigate phosphate recovery from the supernatant and reuse of the water for subsequent batches in a process similar to that described by Zhang *et al.* In the field of DAC sorbents, there has been recent work designing MOFs (and similar classes of porous sorbents) which include hydrophobic components to increase the CO_2 adsorption selectivity and enable capture from humid air without the significant additional energy costs associated with desorbing water during the thermal regeneration step.[9,10] Perhaps a similar modification can be achieved for LDH-based absorbents by capping the residual hydroxyl groups with silanes containing hydrophobic groups such as octadecyltrimethoxysilane or hexamethyldisilazane.[11,12] Considering the materials developed for polypropylene catalytic pyrolysis, there is scope for further work to improve the gas conversion, perhaps with the use of an acidic zeolite co-catalyst (such as HZSM-5) to promote low-temperature cracking, whilst the Ni-based catalysts further decompose the pyrolysis gases produced.[13]

In a broader outlook, waste derived LDHs have the potential to solve many issues currently facing society as they exhibit a broad range of chemistries and work in this area should be continued. As listed in the introduction to this thesis, there have been numerous reports of waste derived LDH from a variety of different

waste sources. Many of these reports simply extract the desired metal cations into solution for use in a conventional LDH synthesis, but as demonstrated in this thesis, direct transformation of these waste materials can produce unique structural features which may enhance their performance. It should be investigated if other waste materials can produce further unique materials.

References

(1) B. Ge, C. Chen, Y. Xu, S. Roberts, M. Zhang, Q. Shao, D. O'Hare and X. Zhu, *Chem. Eng. J.*, 2024, **500**, 156782.

(2) G. Zhang, C. Yang and J. T. Miller, *ChemCatChem*, 2018, **10**, 961–964.

(3) K. Nava-Andrade, G. G. Carbajal-Arízaga, S. Obregón and V. Rodríguez-González, *J. Environ. Manag.*, 2021, **288**, 112399.

(4) H.-H. Kim, P. G. Koster van Groos, Y. Zhao and A. L.-T. Pham, *Water Res.*, 2024, **260**, 121925.

(5) A. P. Arcanjo, D. O. Liborio, S. Arias, F. R. Carvalho, J. P. Silva, B. D. Ribeiro, M. L. Dias, A. M. Castro, R. Fréty, C. M. B. M. Barbosa and J. G. A. Pacheco, *Polymers*, 2023, **15**, 3274.

(6) D. Thomas, R. Ranjan and B. K. George, *RSC Sustain.*, 2023, **1**, 2277–2286.

(7) Y. Liu, R. Zhou, J. Qu, F. Han, S. Zhang and X. Xu, *Appl. Catal. A: Gen.*, 2022, **630**, 118444.

(8) Y. Zhang, J. Wang, X. Liu, P. Gao, C. Gong and L. Lei, *Environ. Prog. & Sustain. Energy*, 2015, **34**, 234–239.

(9) R. Das, H. Li, H. A. Evans, Z. Deng, D. Zhao and A. K. Cheetham, *J. Am. Chem. Soc.*, 2025, **147**, 8377–8385.

(10) Z. Zhou, T. Ma, H. Zhang, S. Chheda, H. Li, K. Wang, S. Ehrling, R. Giovine, C. Li, A. H. Alawadhi, M. M. Abduljawad, M. O. Alawad, L. Gagliardi, J. Sauer and O. M. Yaghi, *Nature*, 2024, **635**, 96–101.

(11) C.-J. Yoo, L.-C. Lee and C. W. Jones, *Langmuir*, 2015, **31**, 13350–13360.

(12) Y. Wang, X. Zhou, M. Yin, J. Pu, N. Yuan and J. Ding, *Langmuir*, 2021, **37**, 8129–8138.

(13) J. Liu, Z. Jiang, H. Yu and T. Tang, *Polym. Degrad. Stab.*, 2011, **96**, 1711–1719.

Appendices

A

Appendix for Chapter 3

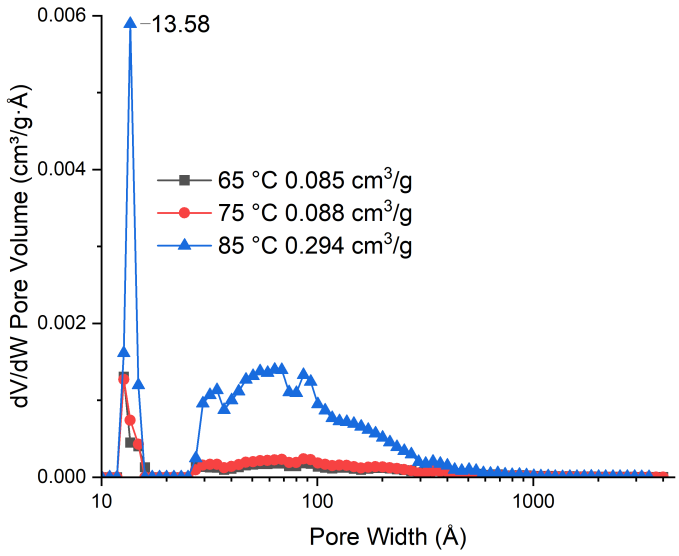

Figure A.1: Pore size distribution calculated using a density functional theory model (slit) on N_2 adsorption isotherms of SLDHs (Figure 3.7) produced via the previously reported method at different temperatures. The pore volumes at $p/p^0 = 1$ of the samples are given in the legend.

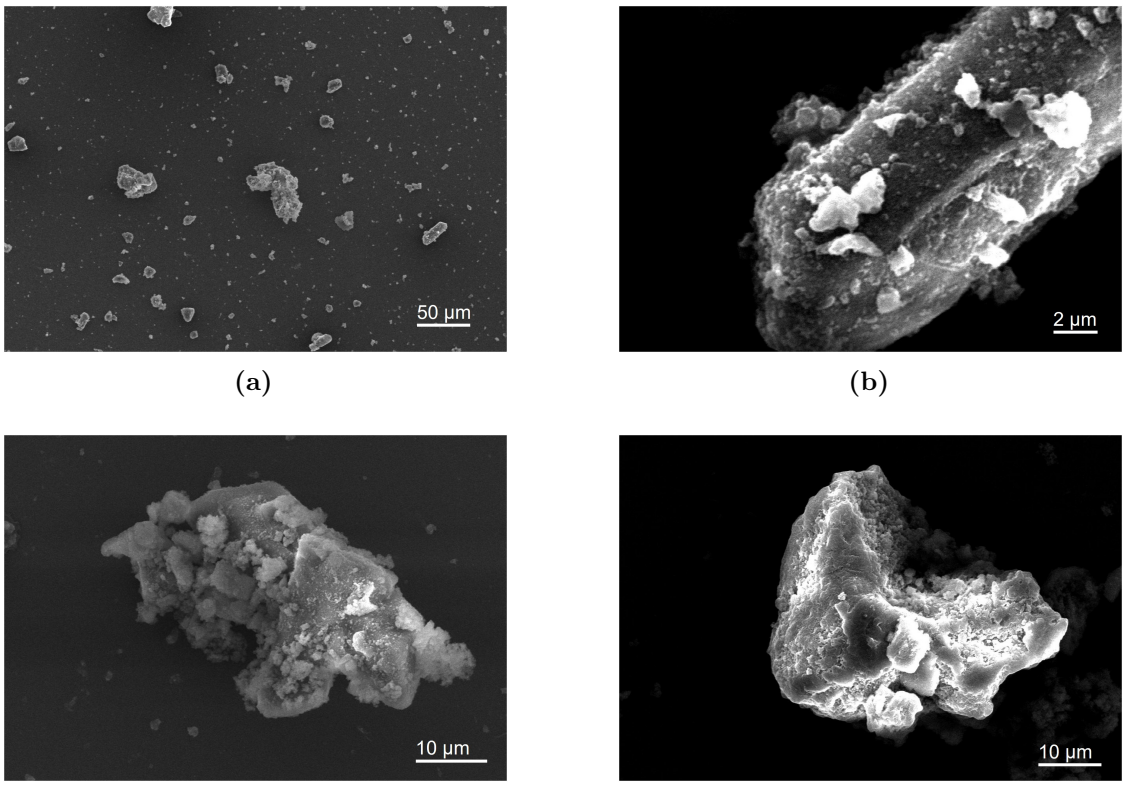

(a) **(b)**

(c) **(d)**

Figure A.2: SEM images of SLDHs produced via the previously reported method at 75 °C.

Table A.1: Variation of lattice parameters (a, c) of the SLDHs made using different reaction times, extracted from Figure A.27.

Solid content ($g\,L^{-1}$)	d_{110} (nm)	a (nm)	CDL_a (nm)	d_{003} (nm)	c (nm)	CDL_c (nm)
0.66	0.153	0.305	8.073	0.788	2.365	2.867
1	0.153	0.305	11.024	0.781	2.344	3.673
1.5	0.153	0.305	8.133	0.784	2.352	3.314
2	0.153	0.305	8.997	0.781	2.344	3.569
2.5	0.153	0.305	9.521	0.781	2.344	3.676
3	0.153	0.305	10.909	0.781	2.343	4.322
3	0.153	0.305	13.681	0.780	2.339	4.656
4	0.153	0.305	12.045	0.779	2.337	4.000
4	0.153	0.306	14.280	0.780	2.341	4.631
5	0.153	0.305	12.939	0.780	2.340	4.526
6.5	0.153	0.306	14.108	0.777	2.331	5.873
16	0.153	0.306	14.199	0.774	2.322	6.718
24.33	0.153	0.306	11.750	0.771	2.313	6.018
48.5	0.153	0.306	10.113	0.763	2.290	4.415
72	0.153	0.306	9.484	0.755	2.266	3.962

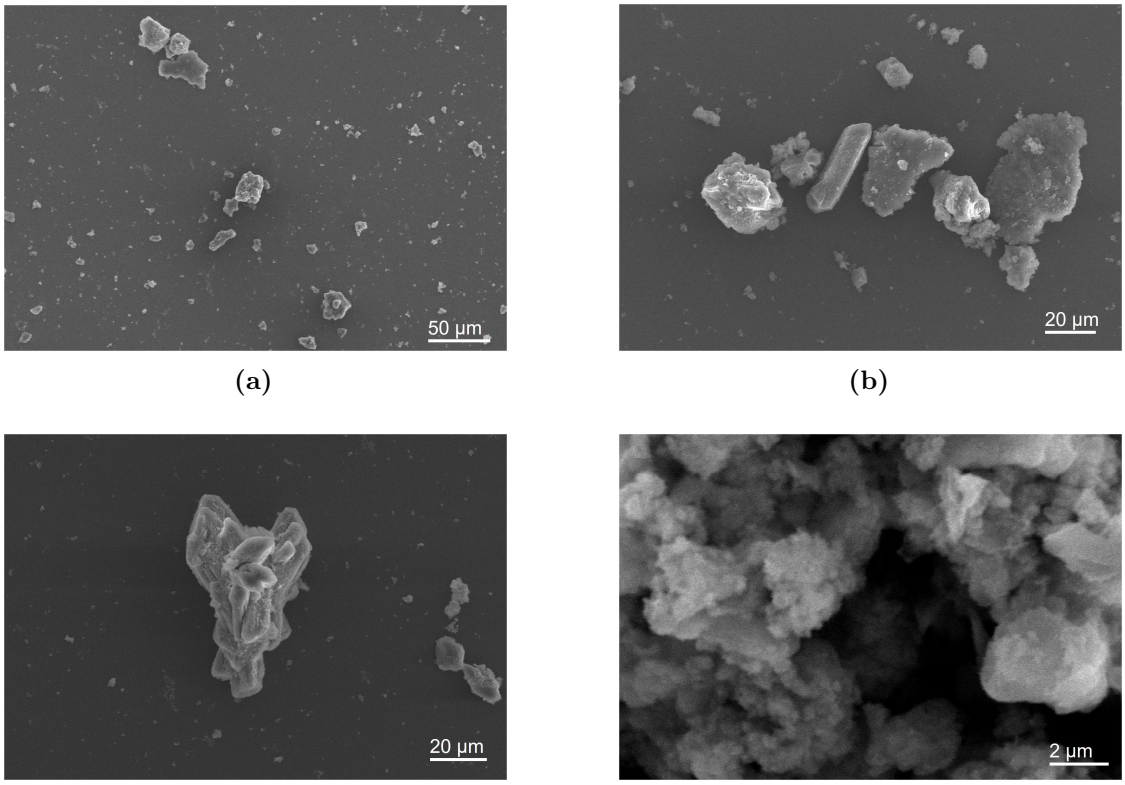

(a) **(b)**

(c) **(d)**

Figure A.3: SEM images of SLDHs produced via the previously reported method at 85 °C.

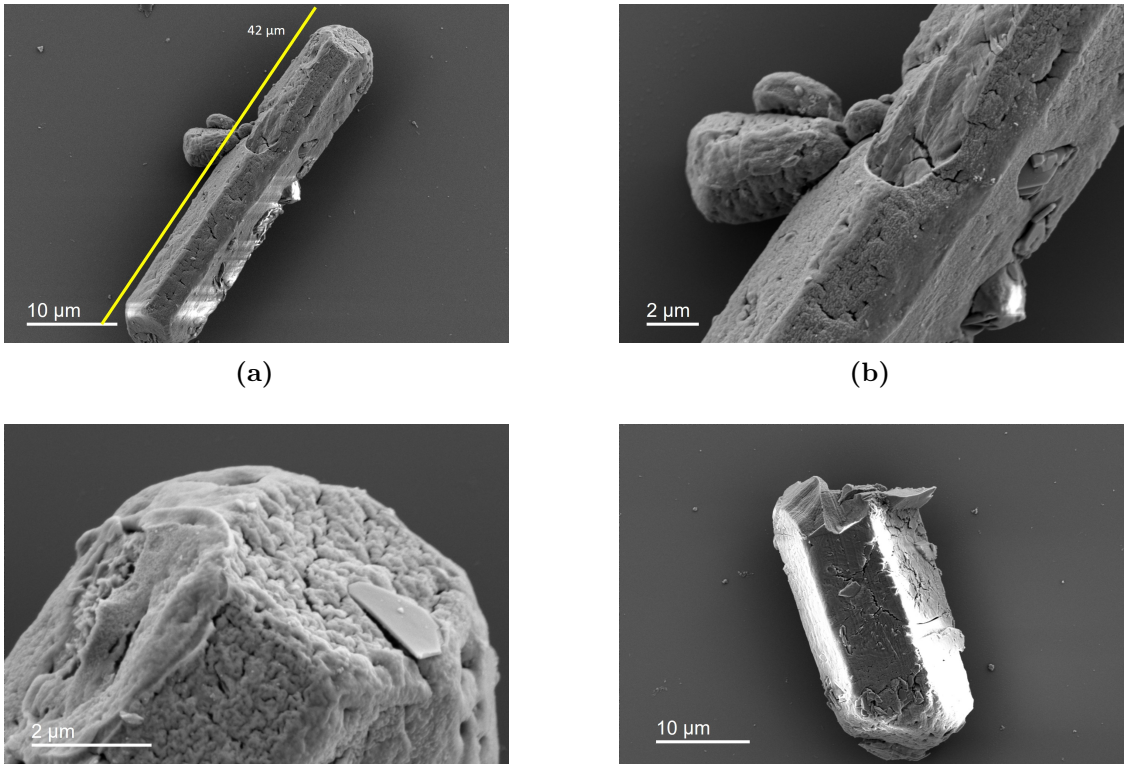

(a) **(b)**

(c) **(d)**

Figure A.4: SEM images of struvite purchased from Alfa Aesar.

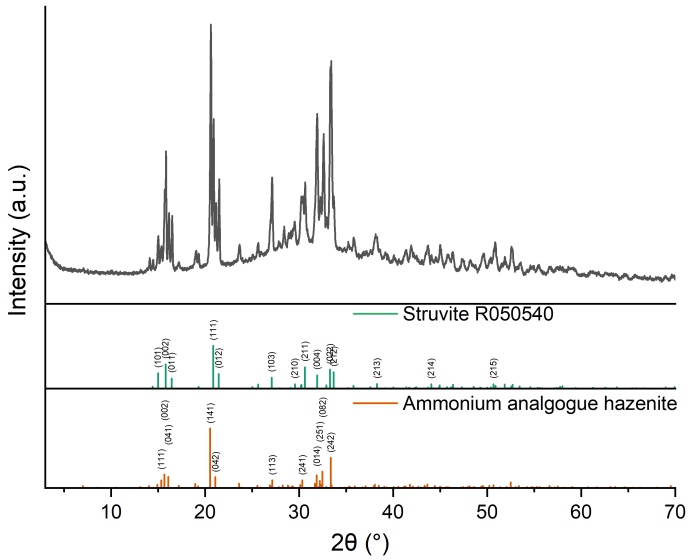

Figure A.5: XRD patterns of SLDH produced using a reduced amount of 1 M NaOH. Peaks can be indexed to the patterns bellow (RRUFF Project[1] R050540 - Struvite and the ammonium analogue of hazenite).[2]

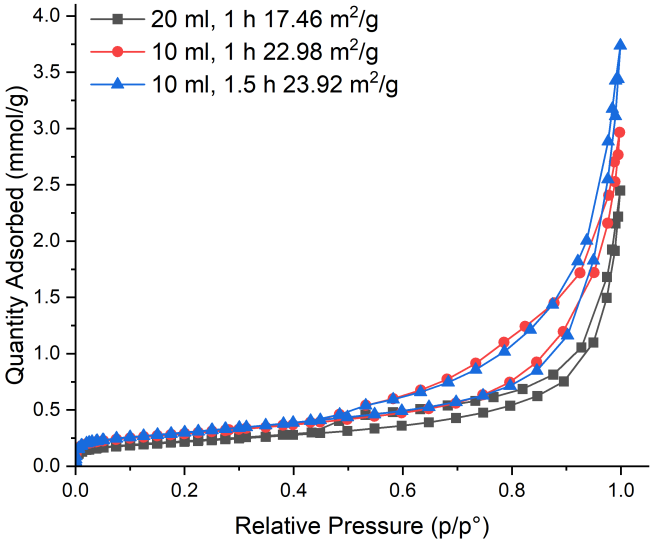

Figure A.6: N_2 adsorption/desorption isotherms of SLDHs produced using varying activation steps, labelled by the amount of 1 M NaOH used and the activation time. SSA of samples calculated via the BET method are given in the legend.

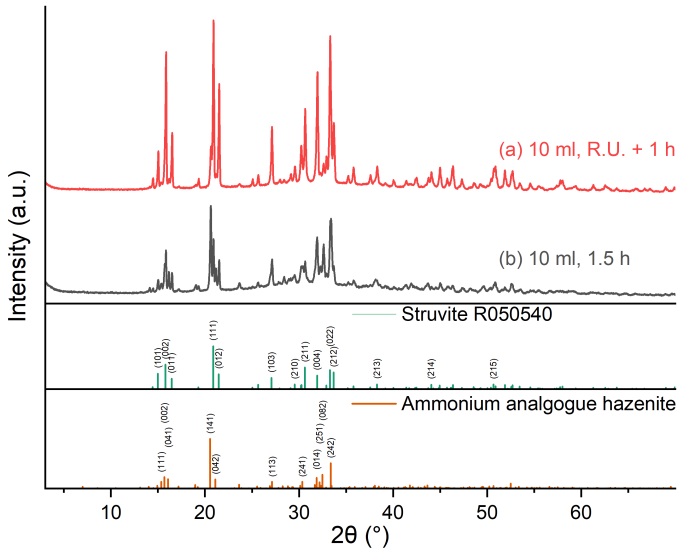

Figure A.7: XRD patterns of intermediate produced using varying activation steps, labelled by the amount of 1 M NaOH used and the activation time. R.U. = Ramp Up (approximately 20 min). Peaks can be indexed to the patterns bellow (RRUFF Project[1] R050540 - Struvite and the ammonium analogue of hazenite).[2]

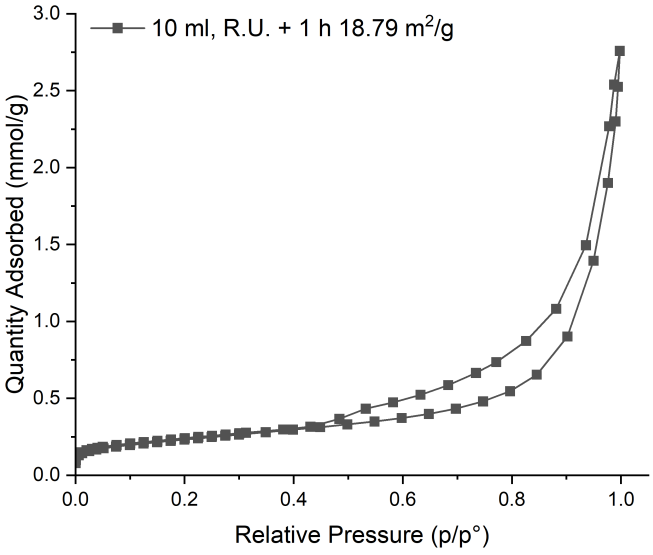

Figure A.8: N_2 adsorption/desorption isotherms of SLDHs produced using varying activation steps, labelled by the amount of 1 M NaOH used and the activation time. R.U. = Ramp up (approximately 20 min). SSA of samples calculated via the BET method are given in the legend.

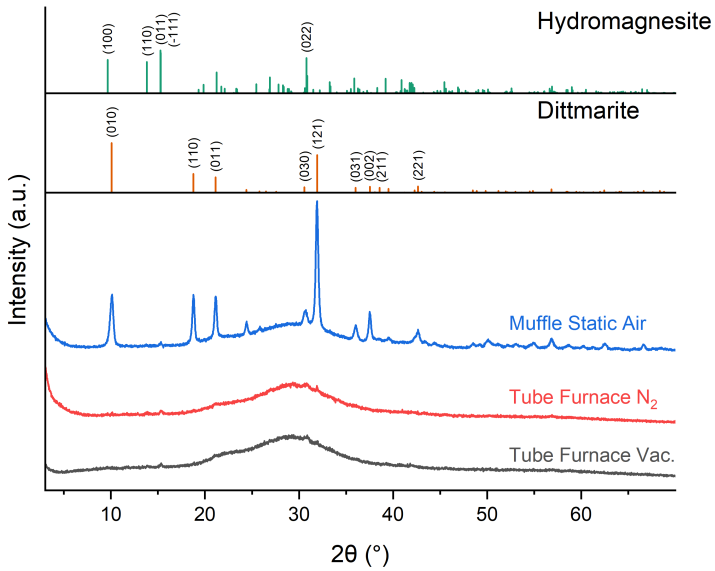

Figure A.9: XRD patterns of calcined struvite. Peaks can be indexed to the patterns above (RRUFF Project R060011 - Hydromagnesite and SpringerMaterials sd_1400160 - Dittmarite)[1,3].

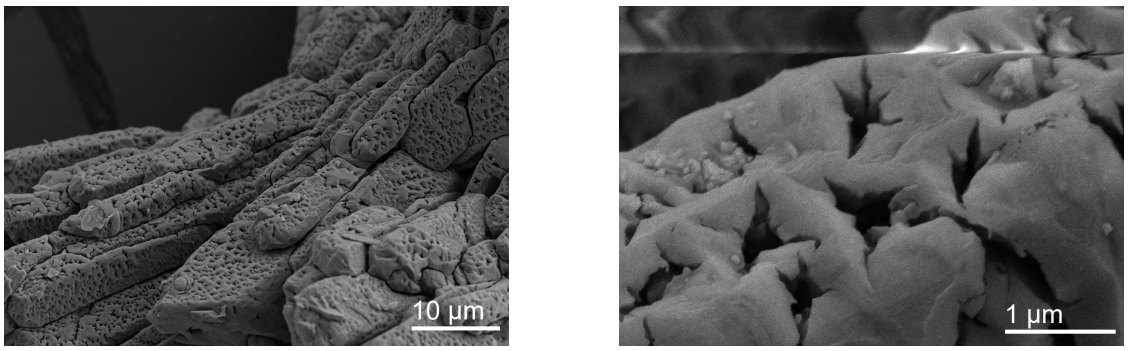

(a) **(b)**

Figure A.10: HR-SEM images of A-$MgHPO_4$ made under vacuum.

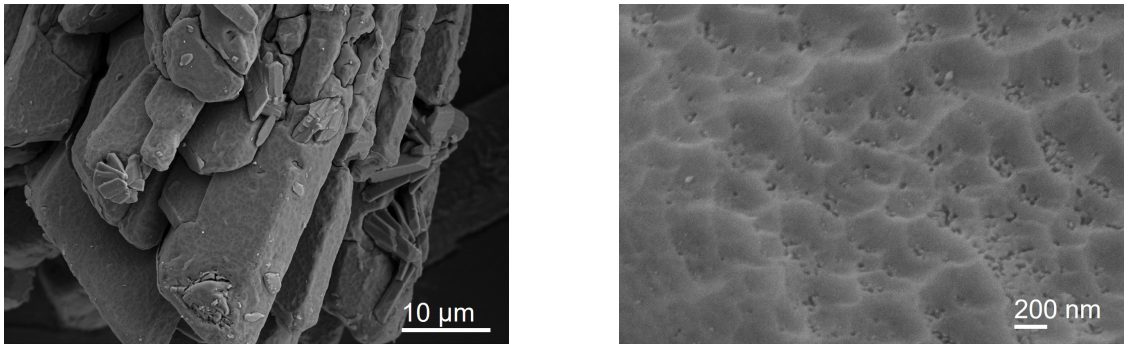

(a) **(b)**

Figure A.11: HR-SEM images of A-$MgHPO_4$ made under N_2.

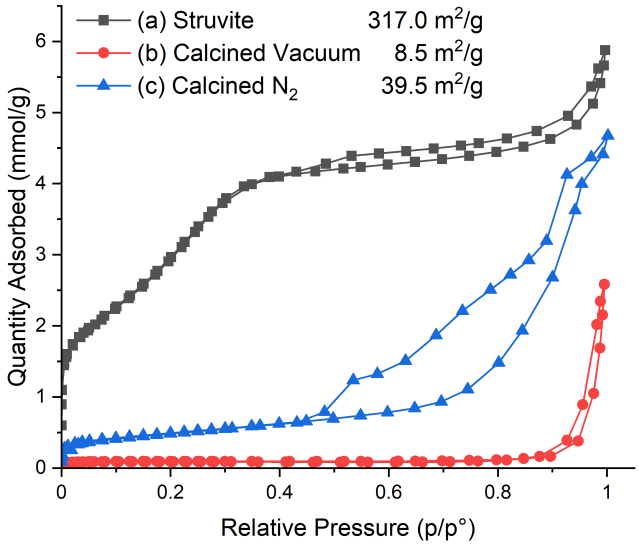

Figure A.12: N_2 adsorption/desorption isotherms of struvite and calcined struvite after degassing at 110 °C. (a) Struvite, (b) Struvite calcined under vacuum at 110 °C and (c) Struvite calcined under N_2 at 110 °C. SSA of samples calculated via the BET method are given in the legend.

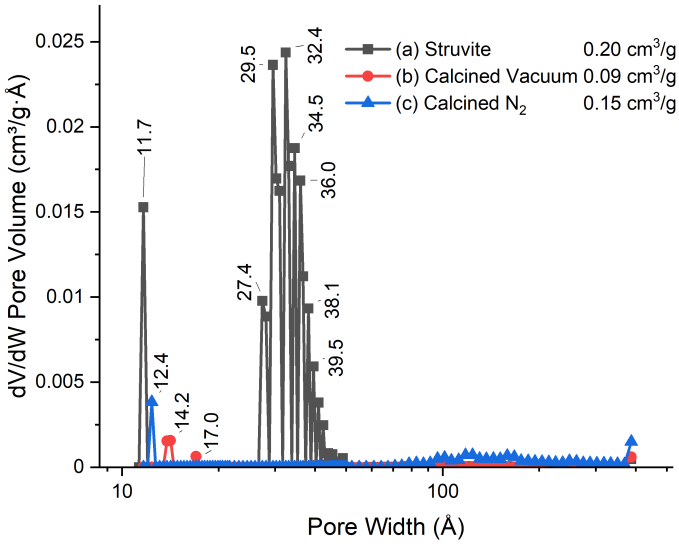

Figure A.13: Pore size distribution calculated using a density functional theory model (cylindrical) on N_2 adsorption isotherms of struvite and calcined struvite after degassing at 110 °C (Figure A.12). (a) Struvite, (b) Struvite calcined under vacuum at 110 °C and (c) Struvite calcined under N_2 at 110 °C. The pore volumes at $p/p^0 = 1$ of the samples are given in the legend.

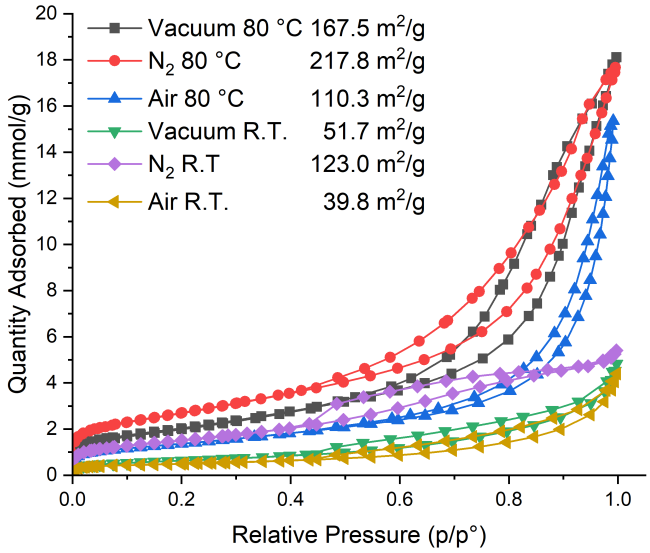

Figure A.14: N_2 isotherms of SLDH made from struvite calcined under different conditions. SSAs of samples calculated via the BET method are given in the legend.

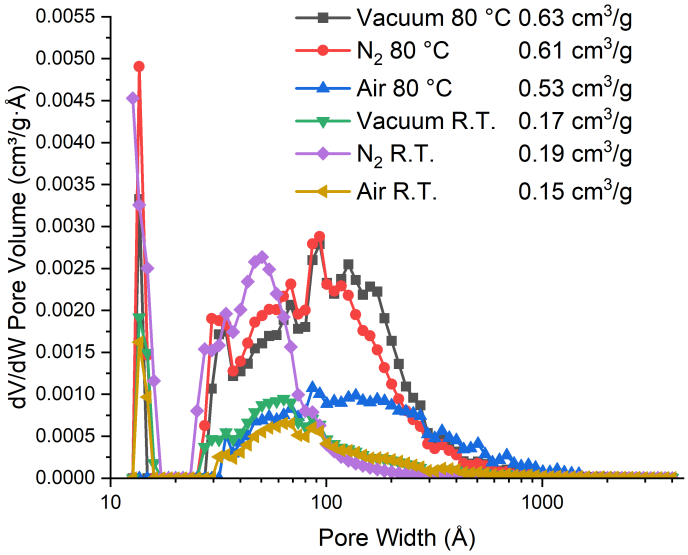

Figure A.15: Pore size distribution calculated using a density functional theory model (slit) on N_2 adsorption isotherms of SLDH made from calcined struvite calcined under different conditions (Figure A.14). The pore volumes at $p/p^0 = 1$ of the samples are given in the legend.

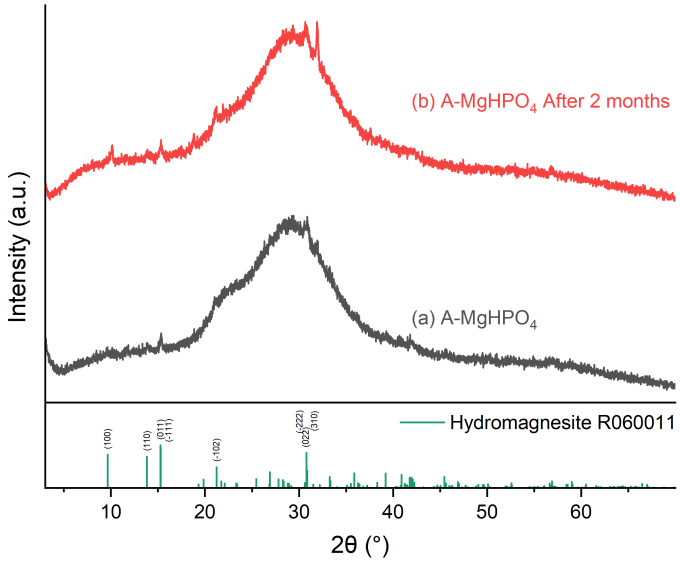

Figure A.16: XRD patterns of calcined struvite freshly made and after 2 months. Peaks can be indexed to the pattern bellow (RRUFF Project R060011 - Hydromagnesite).[1]

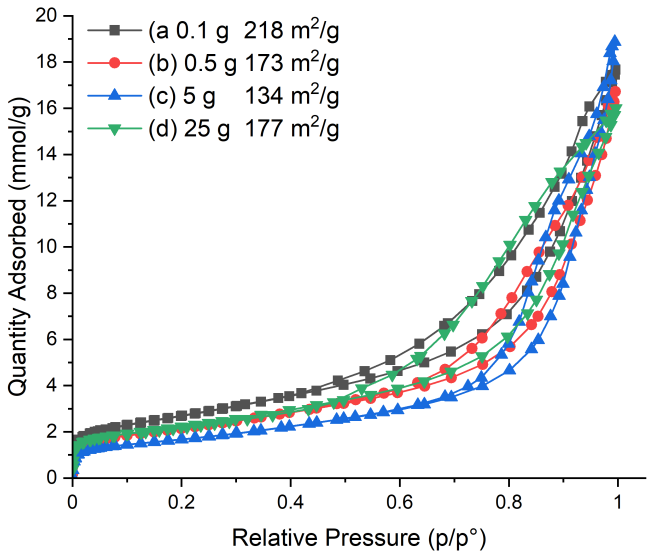

Figure A.17: N_2 isotherm of SLDH produced from A-$MgHPO_4$ on different scales. SSA of samples calculated via the BET method are given in the legend.

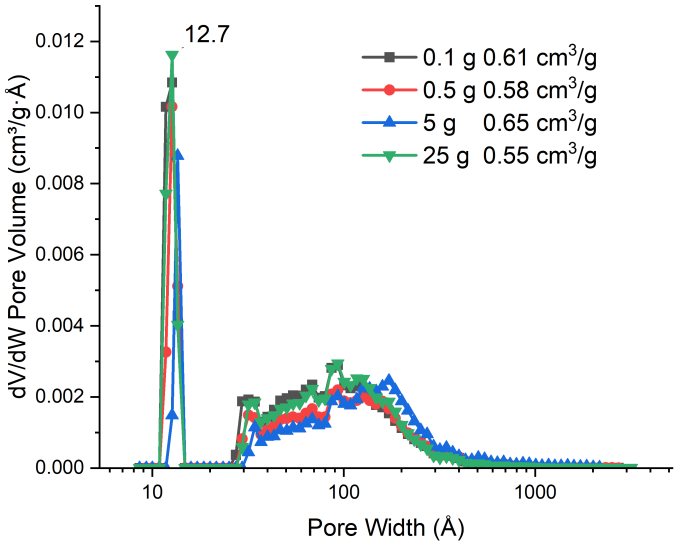

Figure A.18: Pore size distribution calculated using a density functional theory model (slit) on N_2 adsorption isotherms of SLDH made from A-$MgHPO_4$ on different scales. (Figure A.17). The pore volumes at $p/p^0 = 1$ of the samples are given in the legend.

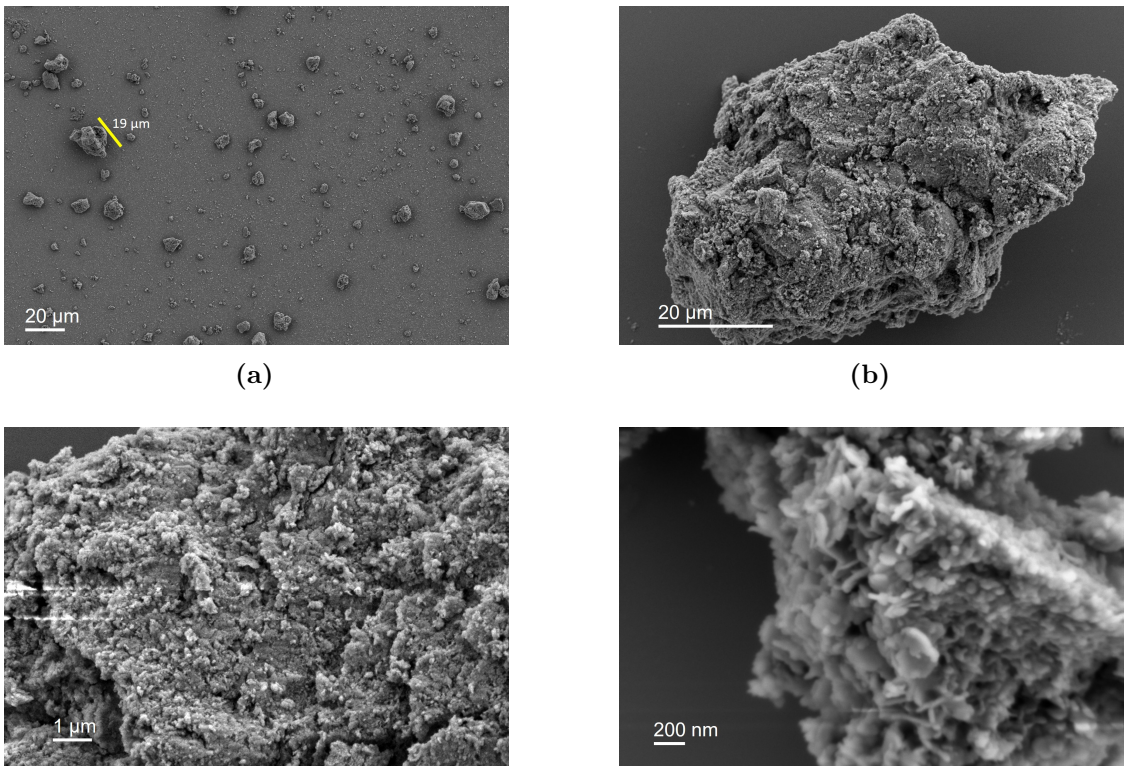

Figure A.19: HR-SEM images of SLDH made from A-$MgHPO_4$ at a 0.1 g scale reaction.

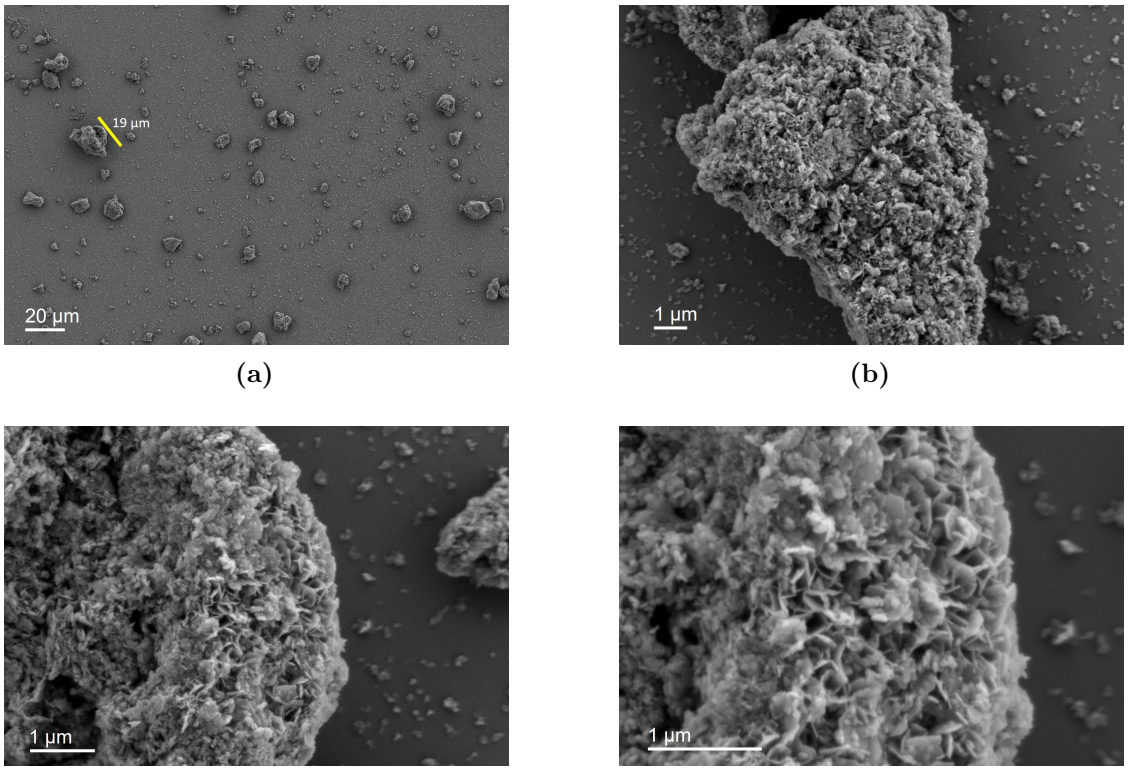

(a) **(b)**

(c) **(d)**

Figure A.20: HR-SEM images of SLDH made from A-$MgHPO_4$ at a 0.5 g scale reaction.

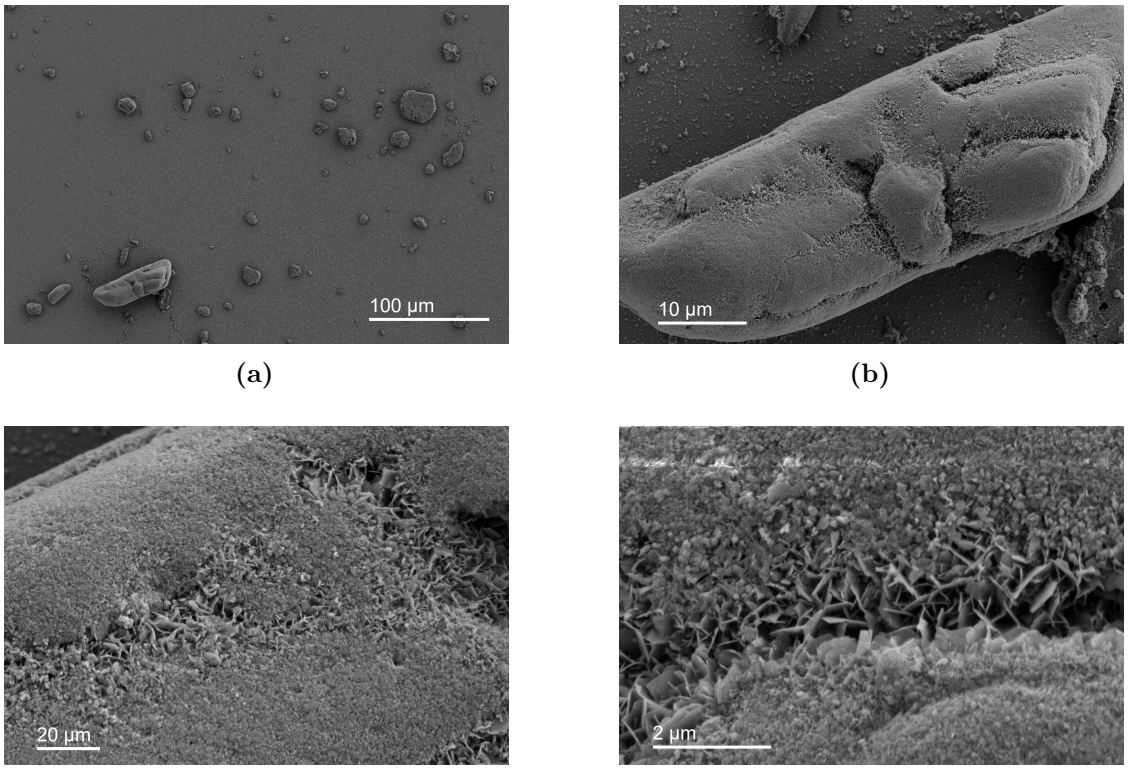

(a) **(b)**

(c) **(d)**

Figure A.21: HR-SEM images of SLDH made from A-$MgHPO_4$ at a 5 g scale reaction.

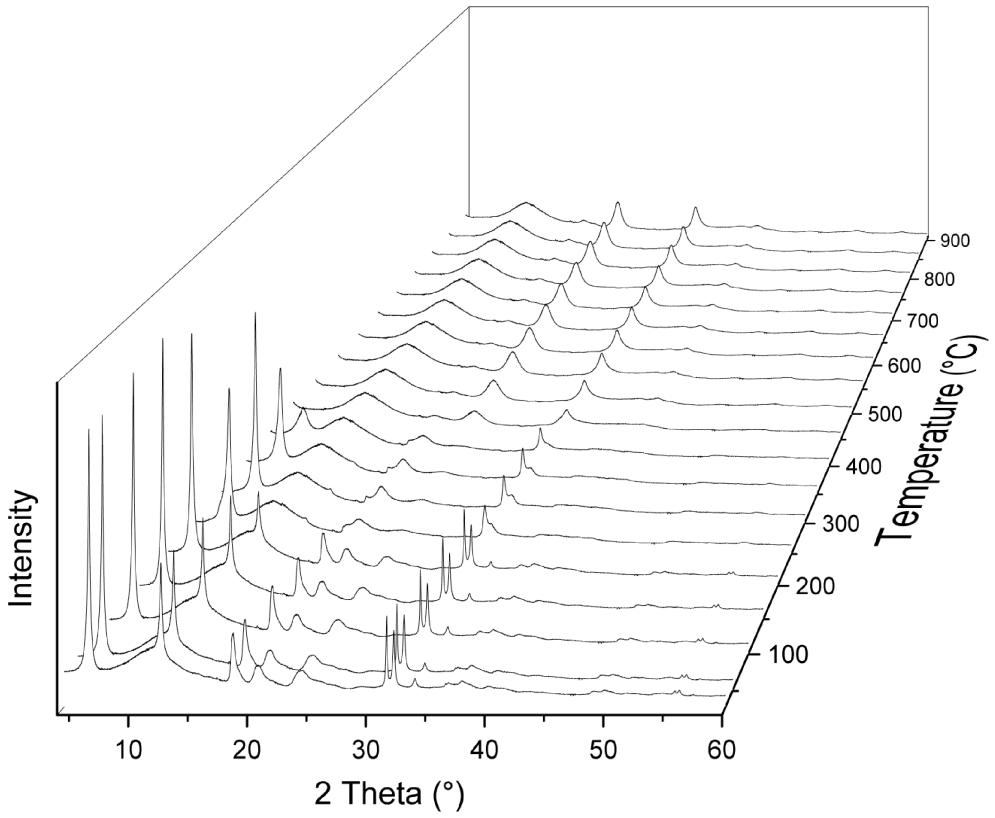

Figure A.22: Variation in the basal spacing $d_{(003)}$ with temperature for Mg_3Al SLDHs extracted from Figure A.22

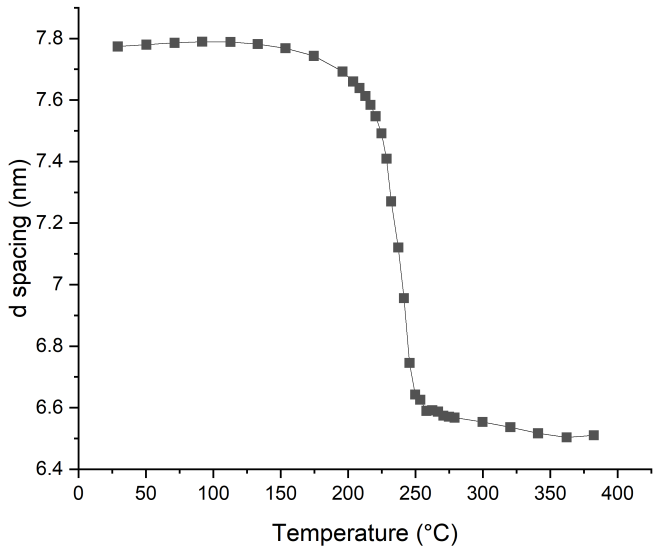

.

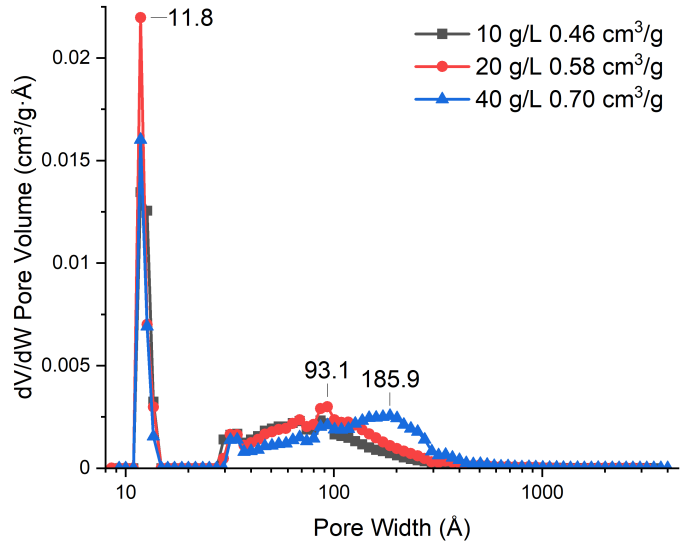

Figure A.24: Pore size distribution calculated using a density functional theory model (slit) on N_2 adsorption isotherms of SLDH made from A-$MgHPO_4$ with different solid contents (Figure 3.36). The pore volumes at $p/p^0 = 1$ of the samples are given in the legend.

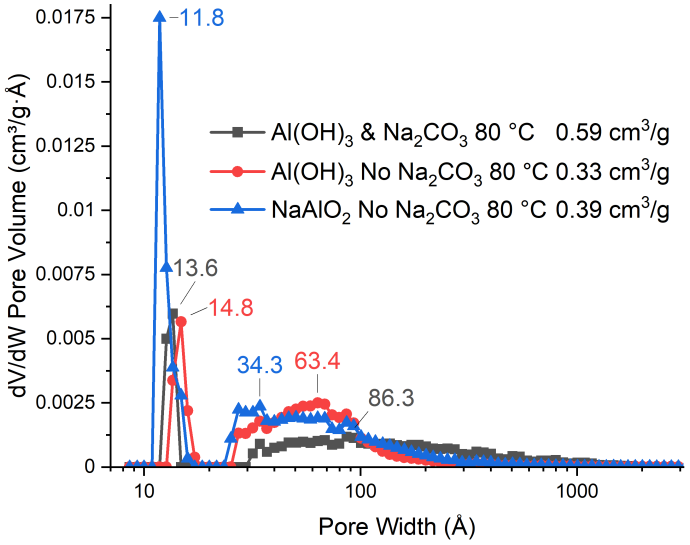

Figure A.25: Pore size distribution calculated using a density functional theory model (slit) on N_2 adsorption isotherms of SLDH made from $Al(OH)_3$ or $NaAlO_2$ (Figure 3.38). The pore volumes at $p/p^0 = 1$ of the samples are given in the legend.

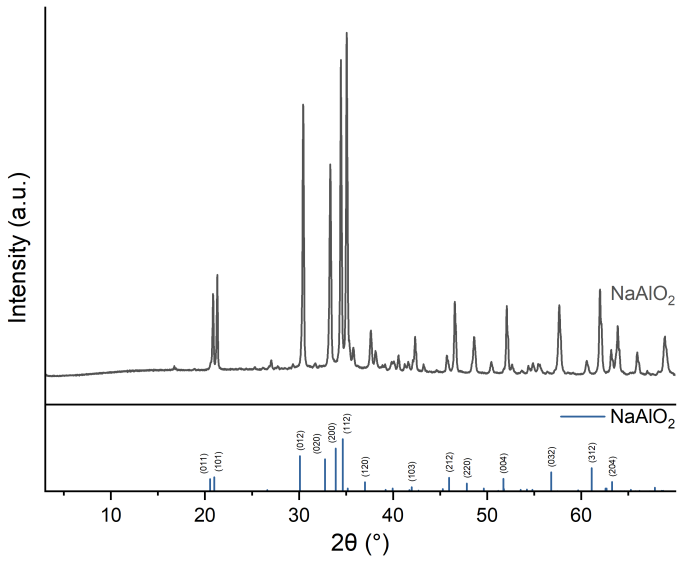

Figure A.26: XRD of sodium aluminate ($NaAlO_2$). Peaks can be assigned to the pattern below (simulated from Materials Project mp-9212).[4]

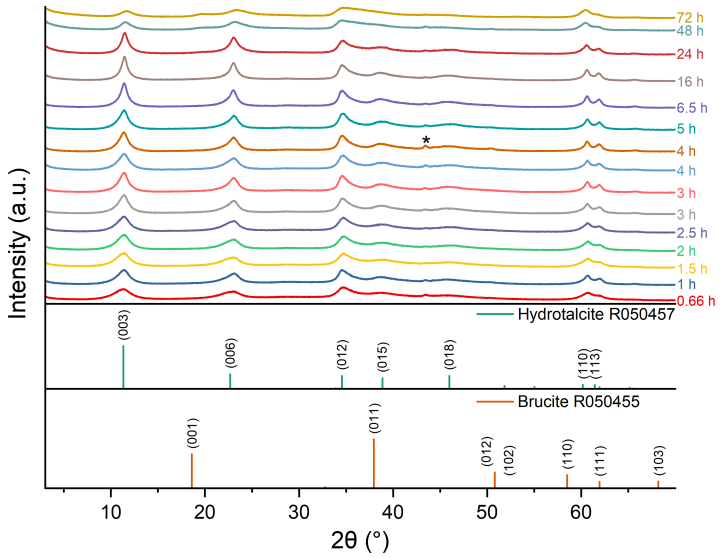

Figure A.27: XRD patterns of SLDH made after different reaction times. * indicates a reflection due to the sample holder. Peaks can be indexed to the patterns bellow (RRUFF Project R050457 - Hydrotalcite and R050455 Brucite).[1]

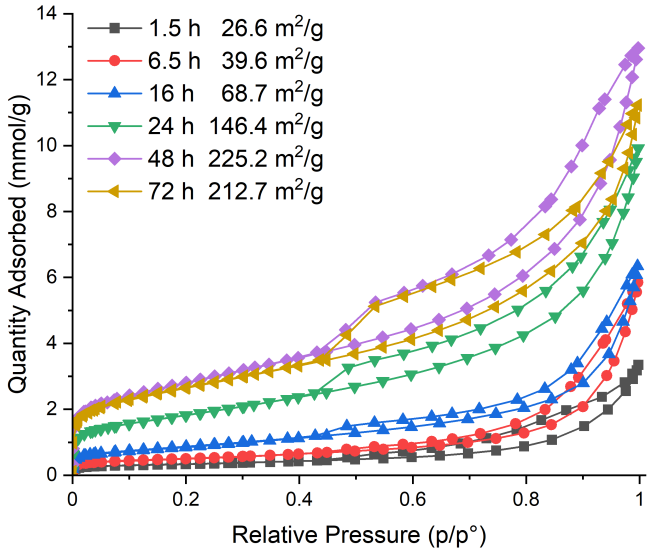

Figure A.28: N_2 isotherm of SLDH produced from A-$MgHPO_4$ using different reaction times. SSA of samples calculated via the BET method are given in the legend.

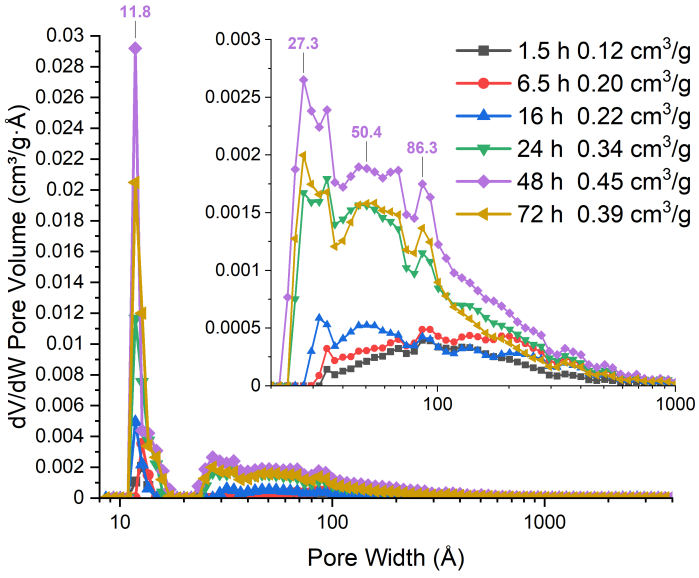

Figure A.29: Pore size distribution calculated using a density functional theory model (slit) on N_2 adsorption isotherms of SLDH made with various reaction times (Figure A.28). The pore volumes at $p/p^0 = 1$ of the samples are given in the legend.

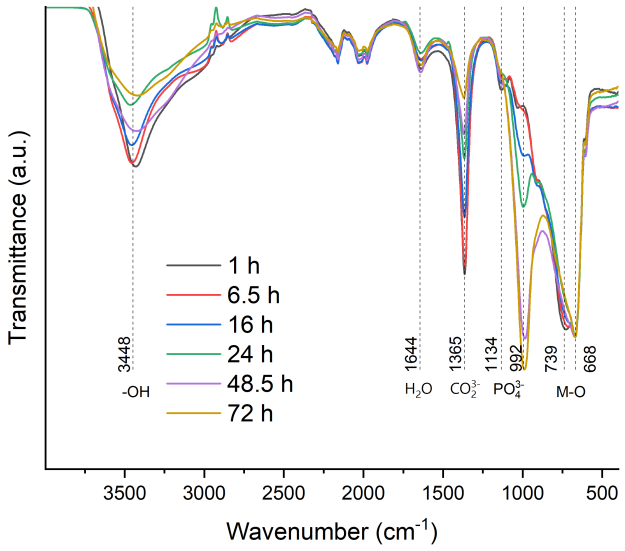

Figure A.30: Variation of the FTIR spectra of SLDH with the reaction time.

B

Appendix for Chapter 4

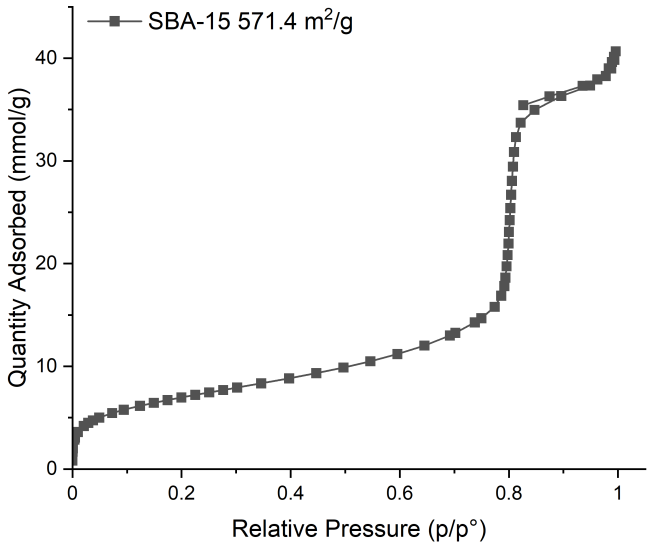

Figure B.1: CO_2 adsorption isotherms of SBA-15. The BET SSA is given in the legend.

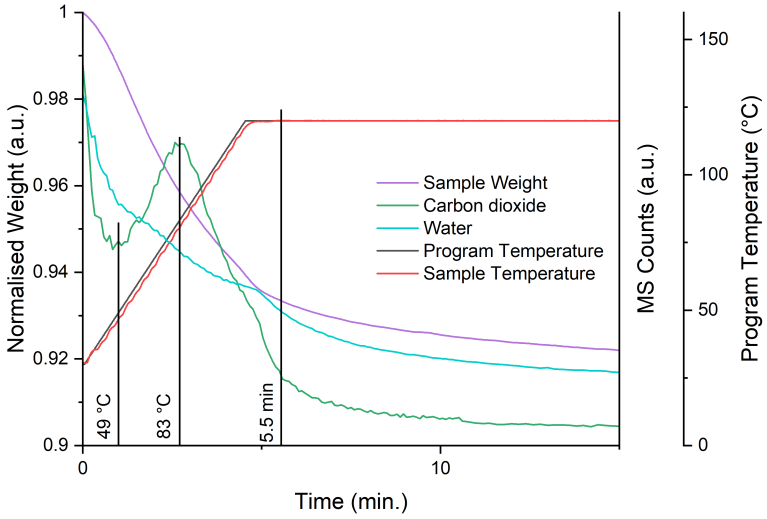

Figure B.2: TGA-MS data of the desorption step of TRI@SLDH. The temperature of peak CO_2 desorption and its onset and where the CO_2 concentration have returned to background levels are marked.

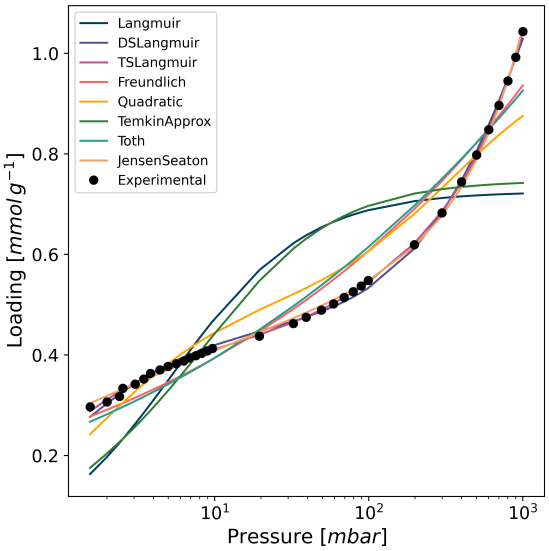

Figure B.3: Unmodified SLDH CO_2 isotherm (○) and the optimised fittings of the models described in Table 4.5.

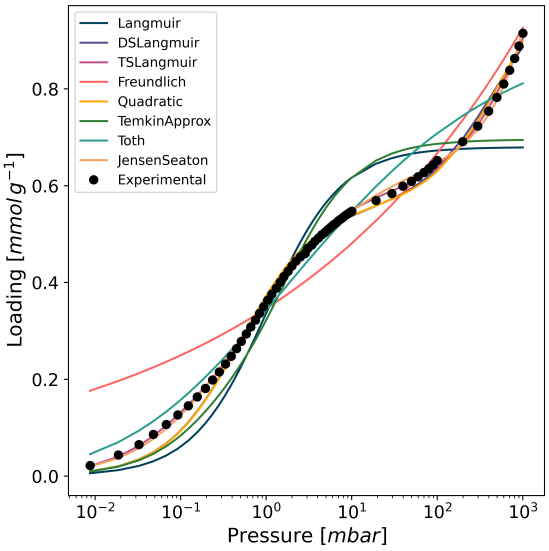

Figure B.4: Amine modified SLDH CO_2 isotherm (○) and the optimised fittings of the models described in Table 4.5.

Table B.1: Optimised parameter values for the best fitting models seen in Figure 4.13

Model	Equation	RMSE	Parameters				
DSLangmuir	$n(p) = n_{m_1}\frac{K_1 p}{1+K_1 p} + n_{m_2}\frac{K_2 p}{1+K_2 p}$	1.05×10^{-2}	n_{m_1}	1.56	K_1	5.871	$\times 10^{-4}$
			n_{m_2}	0.4513	K_2	1.007	
TSLangmuir	$n(p) = n_{m_1}\frac{K_1 p}{1+K_1 p} + n_{m_2}\frac{K_2 p}{1+K_2 p} + n_{m_3}\frac{K_3 p}{1+K_3 p}$	3.92×10^{-3}	n_{m_1}	26.03	K_1	1.82	$\times 10^{-5}$
			n_{m_2}	0.1718	K_2	8.532	$\times 10^{-3}$
			n_{m_3}	0.4219	K_3	1.339	
JensenSeaton	$n(p) = Kp[1 + (\frac{Kp}{a(1+bp)})^c]^{-1/c}$	9.08×10^{-3}	K	117	a	0.6775	
			b	8.735×10^{-4}	c	0.2607	

Table B.2: Optimised parameter values for the best fitting models seen in Figure 4.14

Model	Equation	RMSE	Parameters			
DSLangmuir	$n(p) = n_{m_1}\frac{K_1 p}{1+K_1 p} + n_{m_2}\frac{K_2 p}{1+K_2 p}$	1.81×10^{-2}	n_{m_1}	0.4909	K_1	0.002 121
			n_{m_2}	0.5525	K_2	2.044
TSLangmuir	$n(p) = n_{m_1}\frac{K_1 p}{1+K_1 p} + n_{m_2}\frac{K_2 p}{1+K_2 p} + n_{m_3}\frac{K_3 p}{1+K_3 p}$	5.43×10^{-3}	n_{m_1}	0.6938	K_1	8.296×10^{-4}
			n_{m_2}	0.1827	K_2	12.17
			n_{m_3}	0.4062	K_3	0.8264
Quadratic	$n(p) = n_m\frac{p(K_a+2K_b p)}{1+K_a p+K_b p^2}$	1.83×10^{-2}	n_m	0.5559	K_a	2.008
					K_b	0.003 195
JensenSeaton	$n(p) = Kp[1 + (\frac{Kp}{a(1+bp)})^c]^{-1/c}$	6.09×10^{-3}	K	2.796	a	0.6489
			b	4.418	c	0.5911

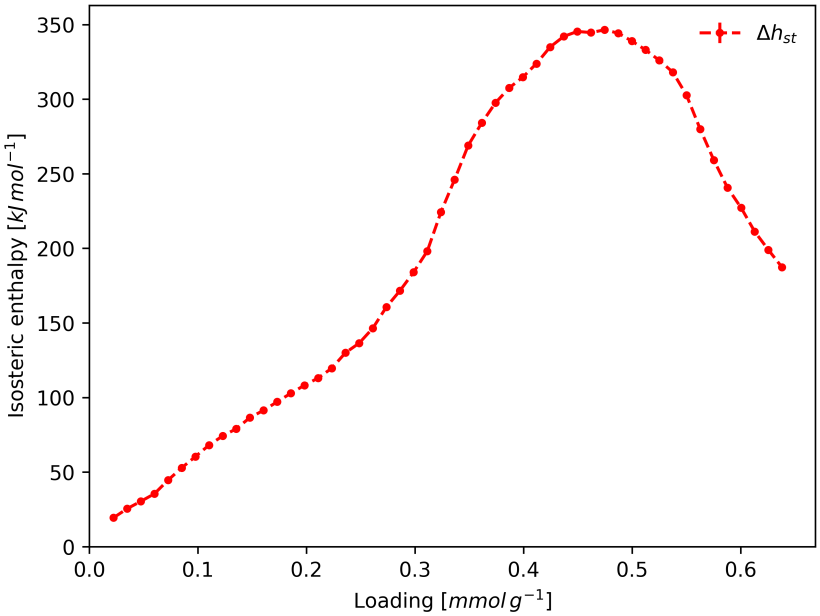

Figure B.5: Isosteric heats of adsorption for TRI@SLDH calculated via the Clausius-Clapeyron equation from the isotherms at 25 and 35 °C in Figure **??**.

Table B.3: Heat capacities derived from the calorimetry measurements in Figures B.12(b) and B.12(c).

Sample	Heat capacity ($10.00\,°C\,min^{-1}$)	Heat capacity ($5.00\,°C\,min^{-1}$)	Average heat capacity (C_p)
SLDH	1.75	1.77	1.76
MONO@SLDH	1.64	1.62	1.63
DI@SLDH	1.88	1.89	1.89
TRI@SLDH	1.78	1.82	1.80
TRI@SLDH-Dry	1.74	1.76	1.75

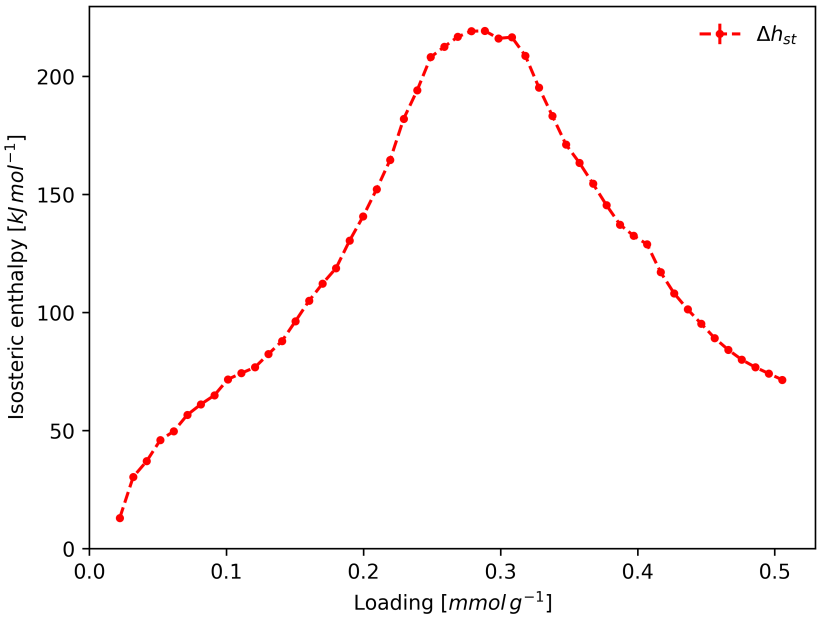

Figure B.6: Isosteric heats of adsorption for TRI@SLDH calculated via the Clausius-Clapeyron equation from the isotherms at 35 and 45 °C in Figure **??**.

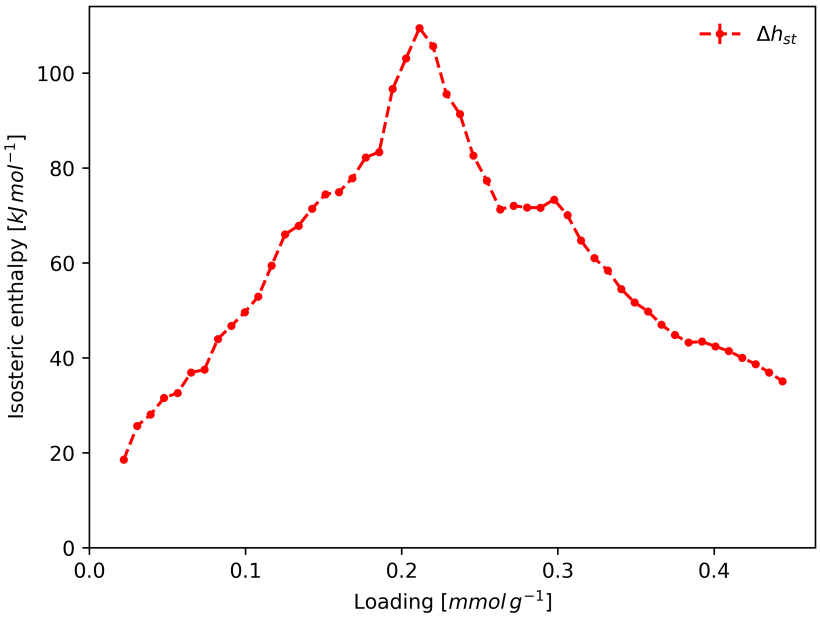

Figure B.7: Isosteric heats of adsorption for TRI@SLDH calculated via the Clausius-Clapeyron equation from the isotherms at 45 and 55 °C in Figure **??**.

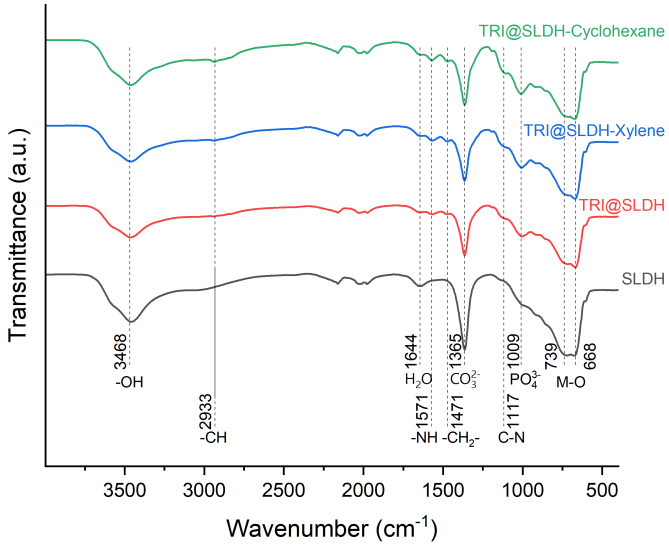

Figure B.8: FTIR spectra of TRI modified SLDH grafted in different solvents.

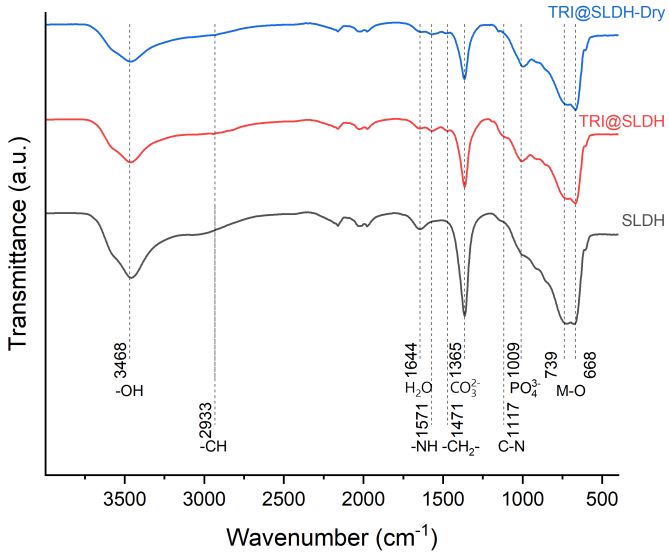

Figure B.9: FTIR spectra of TRI modified SLDH grafted under standard and anhydrous conditions.

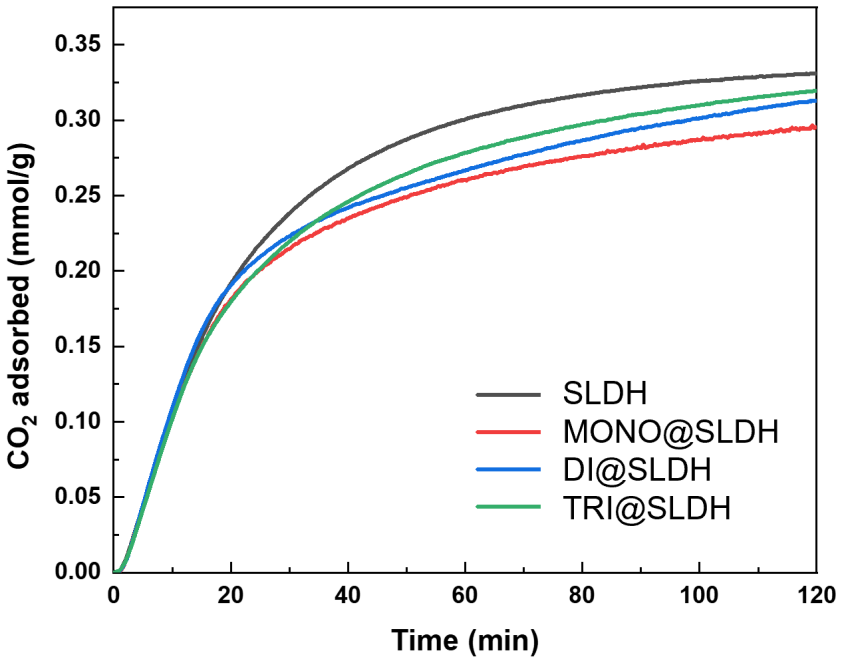

Figure B.10: Dynamic CO_2 uptake experiment of amine functionalised SLDH using 400 ppm CO_2 at 25 °C using a PerkinElmer TGA 8000. The samples were pre-treated by degassing at 120 °C for 2 h and pre-balanced at 25 °C for 3 h under N_2 flow. Approximately 10 mg of each sample was used during the tests.

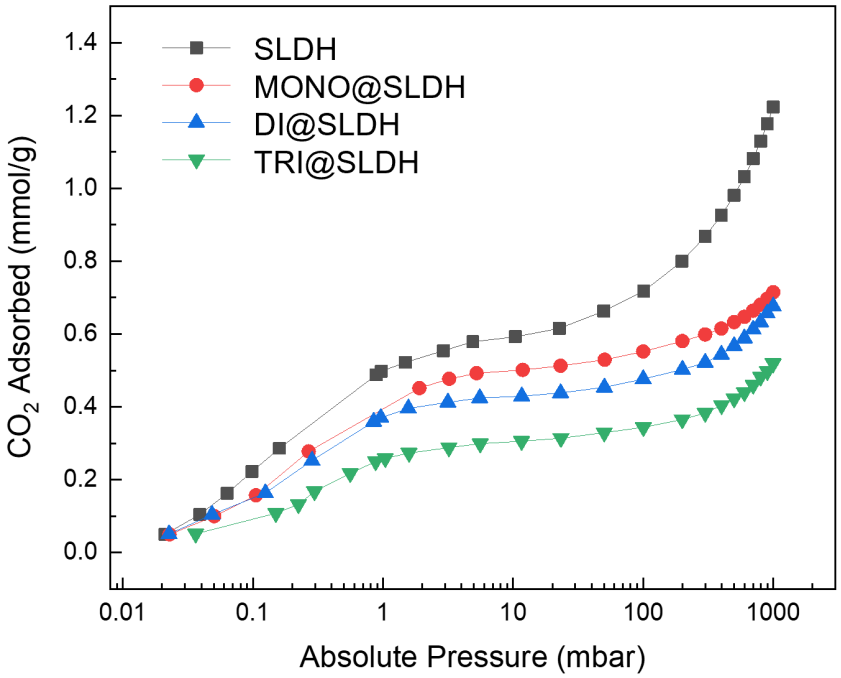

Figure B.11: Static CO_2 uptake isotherms of amine functionalised SLDH. The samples were pre-treated by degassing at 120 °C under vacuum for 6 h.

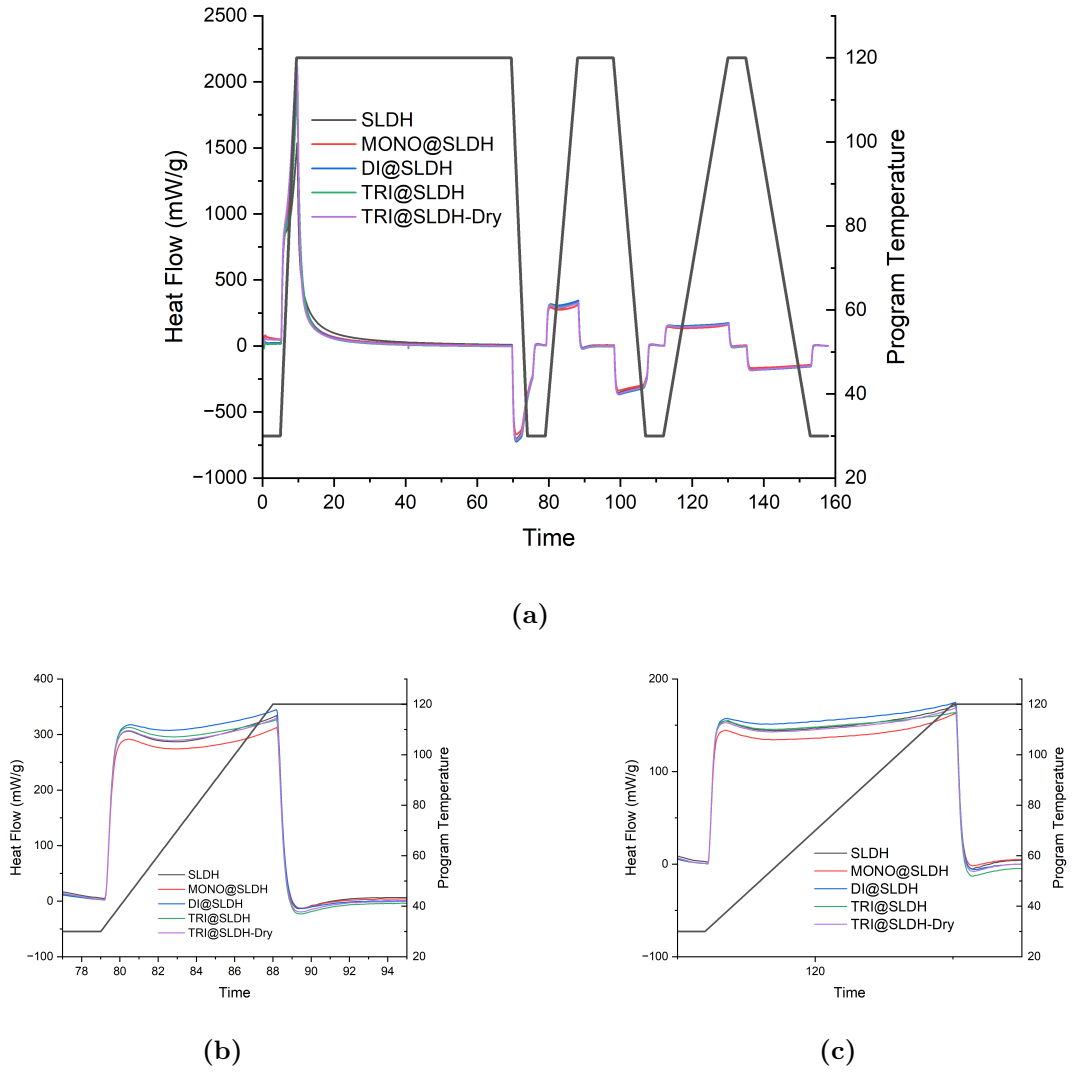

Figure B.12: DSC measurements of SLDH and amine modified SLDHs. The baseline heat flow for an empty sample pan has been subtracted and the values normalised by the sample mass.

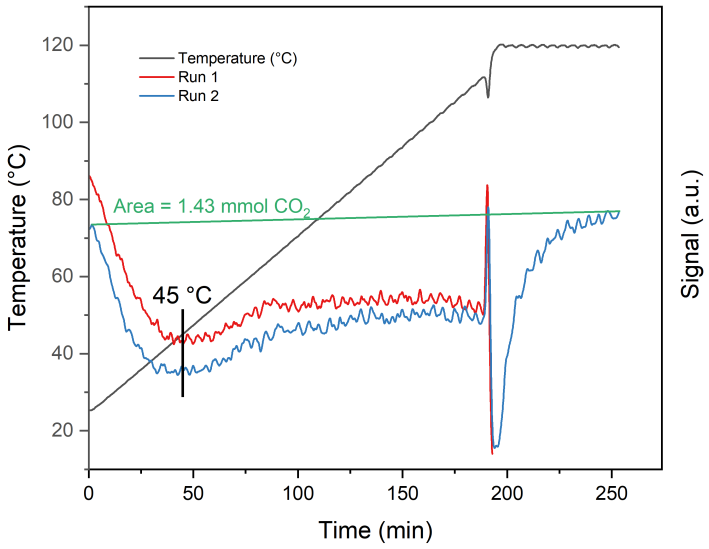

Figure B.13: CO_2 TPD signal for TRI@SLDH-Dry at $1\,^{\circ}C\,min^{-1}$. The CO_2 capacity calculated from the gas flow rate is given.

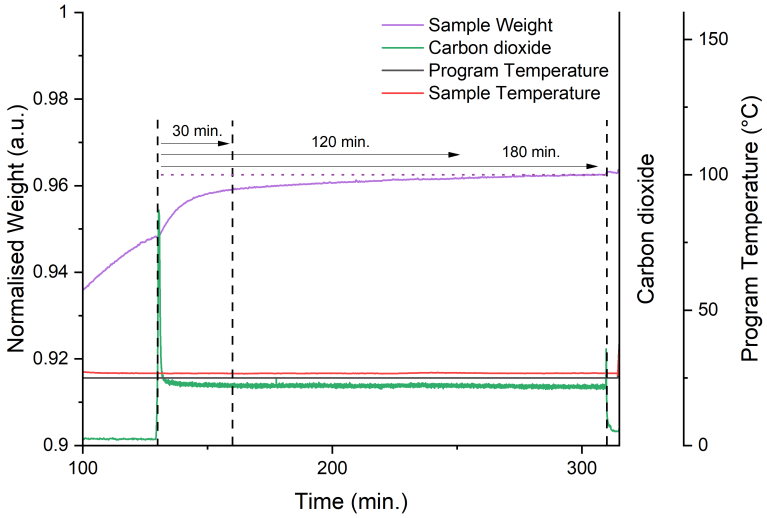

Figure B.14: TGA-MS data for TRI@SLDH. Different CO_2 adsorption times are marked

C

Appendix for Chapter 5

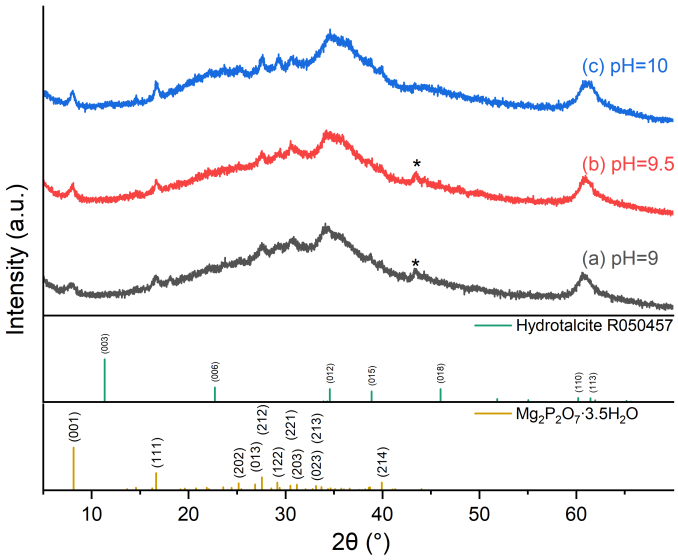

Figure C.1: Powder XRD pattern of material produced from partial substitution of Mg for Zn during SLDH synthesis at different starting pH. Peaks can be indexed to the patterns bellow (RRUFF Project R050457 - Hydrotalcite and $Mg_2P_2O_7 \cdot 3.5\,H_2O$)[1,5]. * indicates a reflection due to the sample holder.

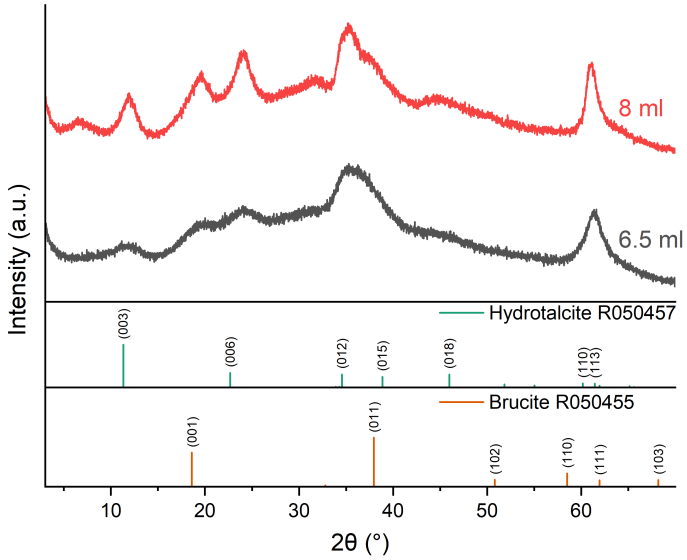

Figure C.2: PXRD pattern of material produced from partial substitution of Mg for Zn during SLDH synthesis at different starting pH. Peaks can be indexed to the patterns bellow (RRUFF Project R050457 - Hydrotalcite and R050455 - Brucite)[1].

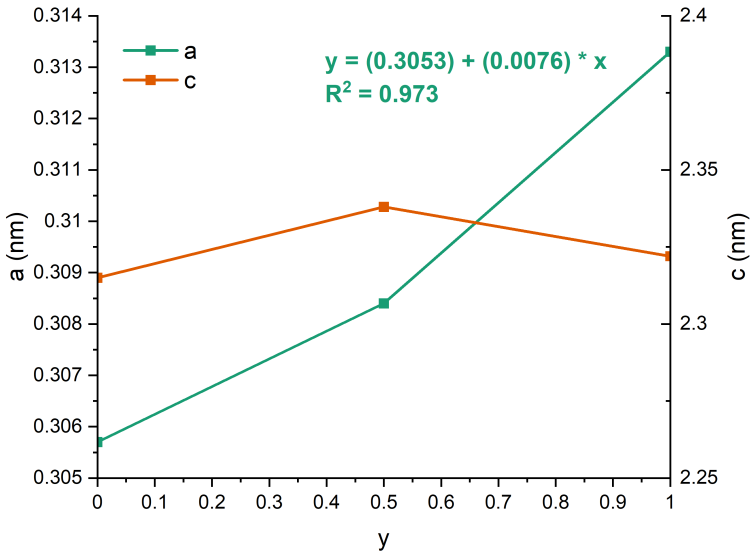

Figure C.3: Variation of the unit cell parameters for $Mg_3Fe_yAl_{1-y}$ SLDH.

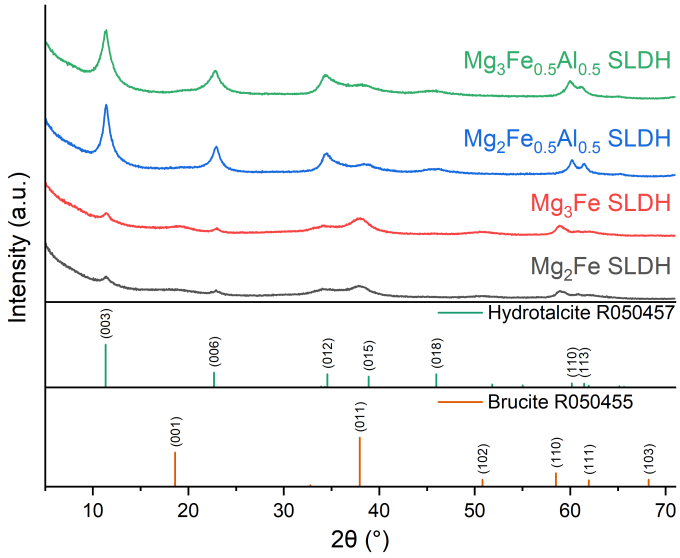

Figure C.4: XRD patterns of Fe substituted SLDHs. Peaks can be indexed to the patterns bellow (RRUFF Project R050457 - Hydrotalcite and R050455 - Brucite)[1].

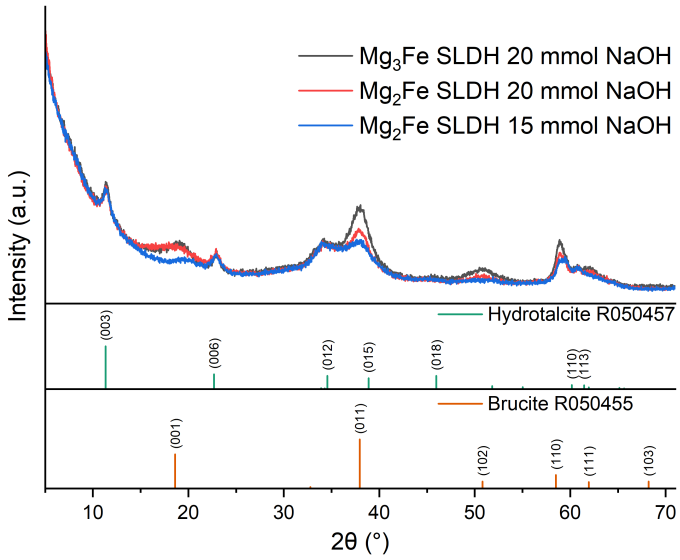

Figure C.5: XRD patterns of Fe substituted SLDHs. Peaks can be indexed to the patterns bellow (RRUFF Project R050457 - Hydrotalcite and R050455 - Brucite)[1].

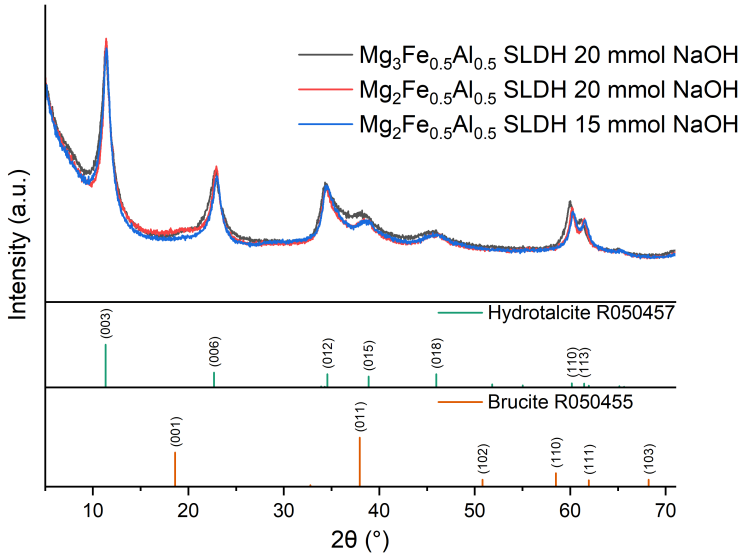

Figure C.6: XRD patterns of partially Fe substituted SLDHs. Peaks can be indexed to the patterns bellow (RRUFF Project R050457 - Hydrotalcite and R050455 - Brucite)[1].

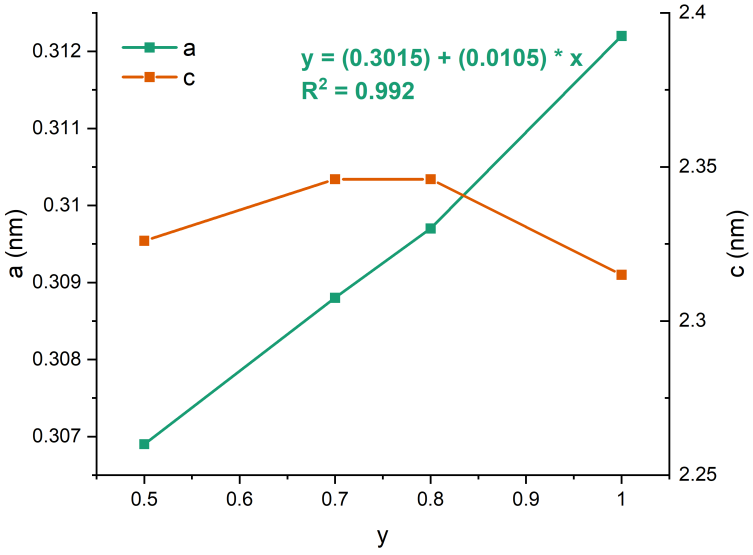

Figure C.7: Variation of the unit cell parameters for $Mg_2Fe_yAl_{1-y}$ SLDH.

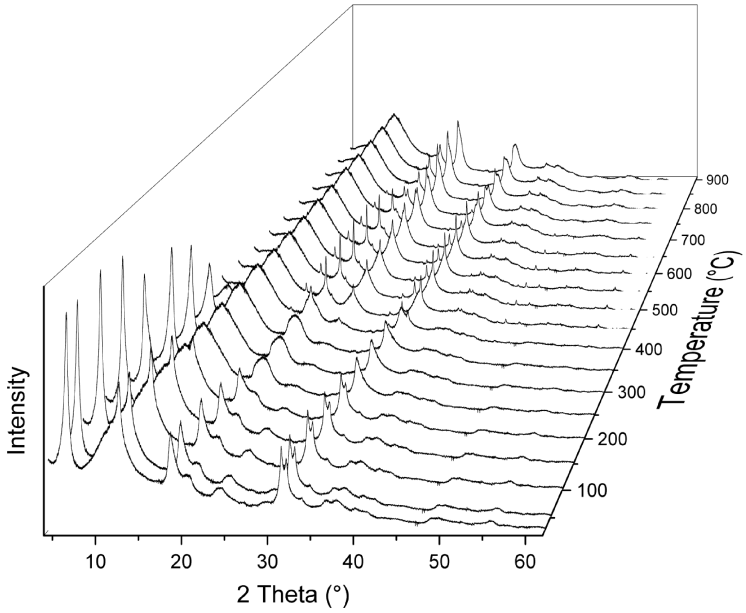

Figure C.8: Variable temperature powder XRD spectra of $Mg_2Fe_{0.5}Al_{0.5}$ SLDH.

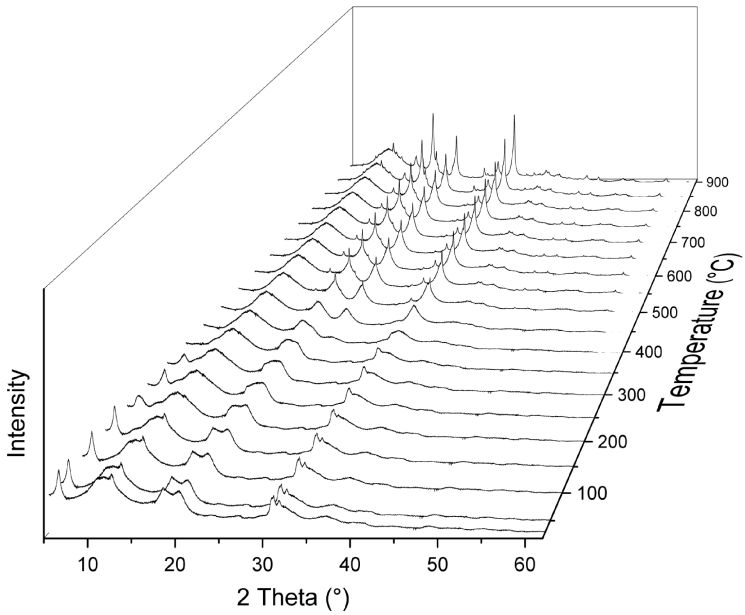

Figure C.9: Variable temperature powder XRD spectra of Mg_2Fe SLDH.

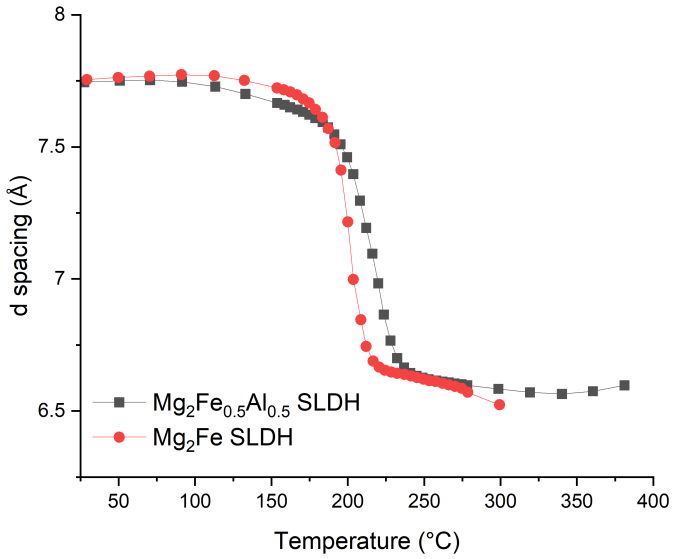

Figure C.10: Variation in the basal spacing $d_{(003)}$ with temperature for MgFe SLDHs extracted from Figures C.8 and C.9.

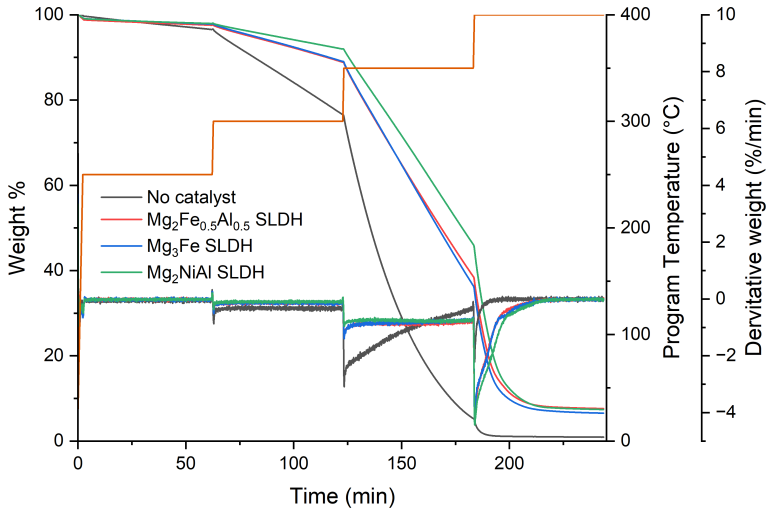

Figure C.11: TGA trace of PP-SLDH blends with isothermal steps at 250, 300, 350 and 400 °C.

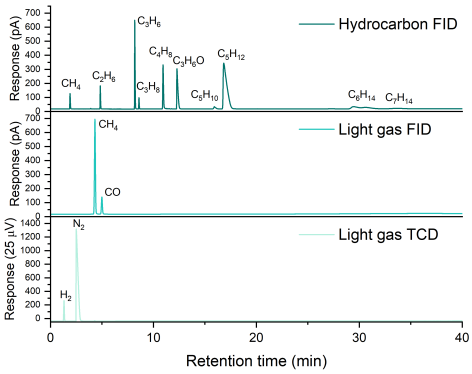

(a)

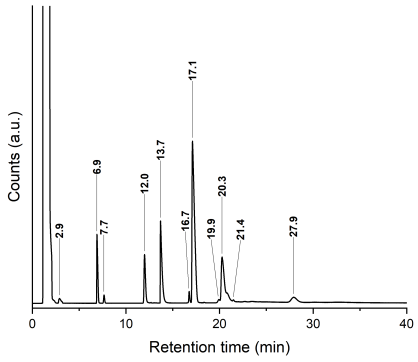

(b)

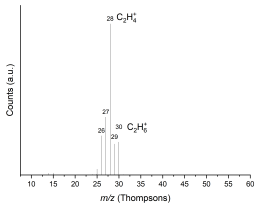

(c) 2.9 min Ethane

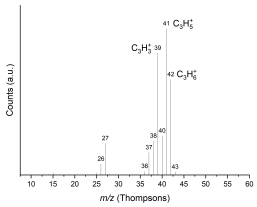

(d) 6.9 min Propene

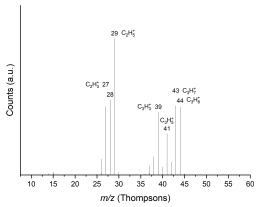

(e) 7.7 min Propane

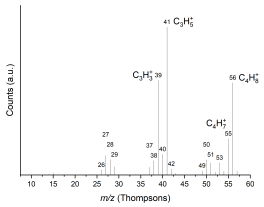

(f) 12 min Butane

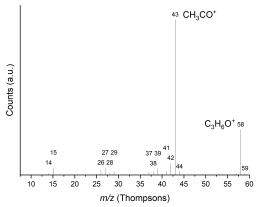

(g) 13.7 min Acetone

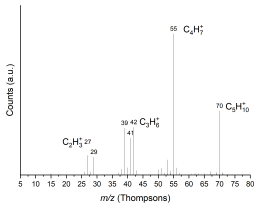

(h) 16.7 min Pent-2-ene

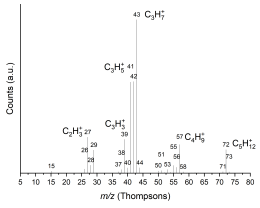

(i) 17.1 min Pentane

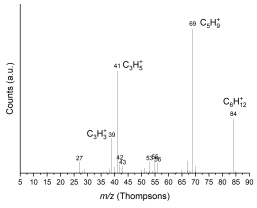

(j) 19.9 min 4-methyl-pent-2-ene

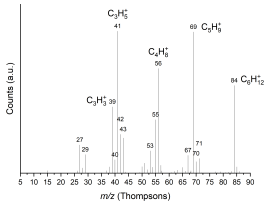

(k) 20.3 min 3-methyl-pent-2-ene

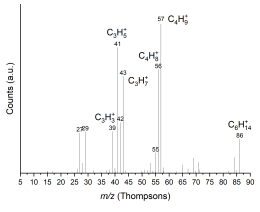

(l) 21.4 min Hexane

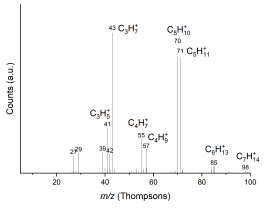

(m) 27.9 min 2,4-dimethyl-1-heptene

Figure C.12: Representative GC (a) and GC-MS (b) chromatograms of pyrolysis gases. Mass spectrums of major peaks are shown denoted by retention time (c to m).

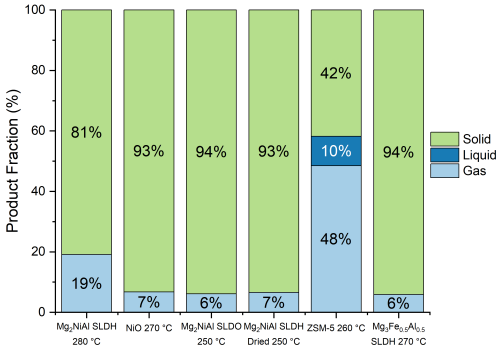

(a) Distribution of solid, liquid and gas products

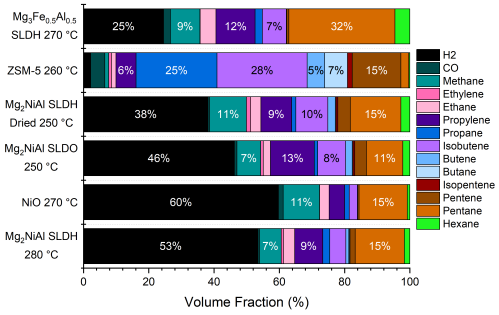

(b) Gas product distribution by volume.

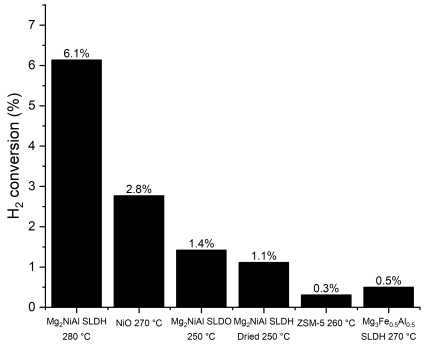

(c) Hydrogen conversion as fraction of the amount present in the polypropylene.

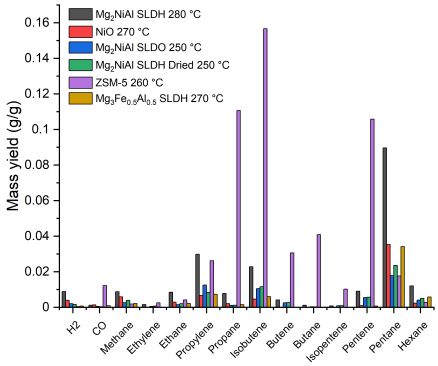

(d) Gas product yields.

Figure C.13: Polypropylene pyrolysis data using 10 wt% dried Mg_2NiAl SLDH, calcined Mg_2NiAl SLDH, NiO, ZSM-5 and $Mg_2Fe_{0.5}Al_{0.5}$ SLDH.

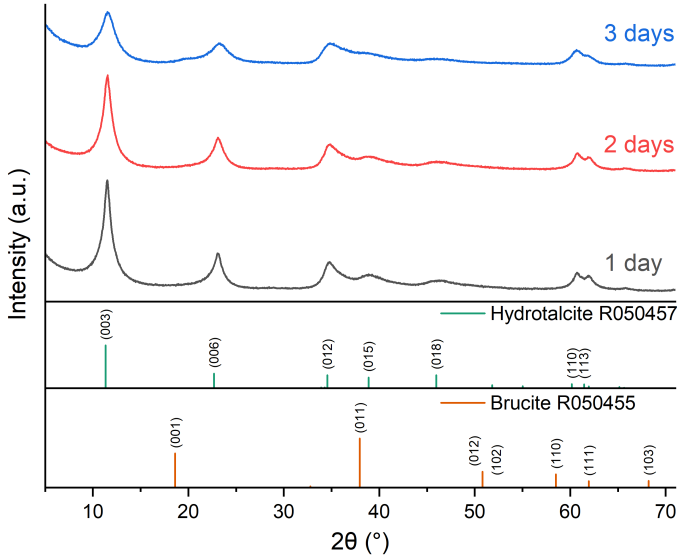

Figure C.14: Variation of the powder XRD patterns of Mg_2NiAl SLDH with the reaction time. Patterns can be indexed to the patterns bellow (RRUFF Project Hydotalcite - R050457 and Brucite - R050455).[1]

Table C.1: Lattice parameters (a, c) of the $Mg_2NiAl\,CO_3{}^{2-}$ SLDHs prepared using different reaction times and their respective crystallite domain lengths (CDL).

Sample	d_{110} (nm)	a (nm)	CDL_a (nm)	d_{003} (nm)	c (nm)	CDL_c (nm)
1 day	0.153	0.305	11.006	0.770	2.309	5.121
2 days	0.152	0.305	10.405	0.768	2.305	4.784
3 days	0.153	0.305	8.799	0.763	2.290	3.633

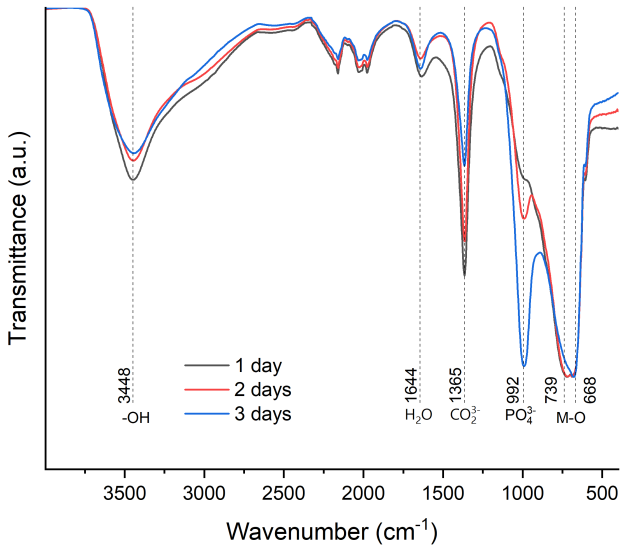

Figure C.15: Variation of the FTIR of Mg_2NiAl SLDH with the reaction time.

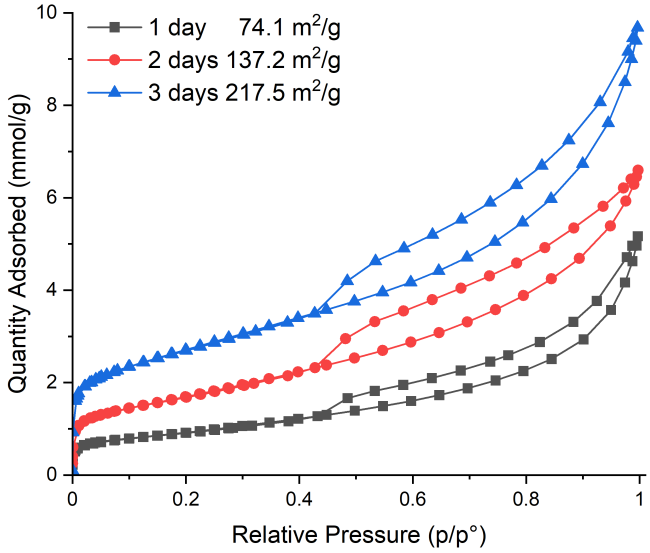

Figure C.16: N_2 adsorption/desorption isotherms of Mg_2NiAl SLDHs prepared with different reaction times

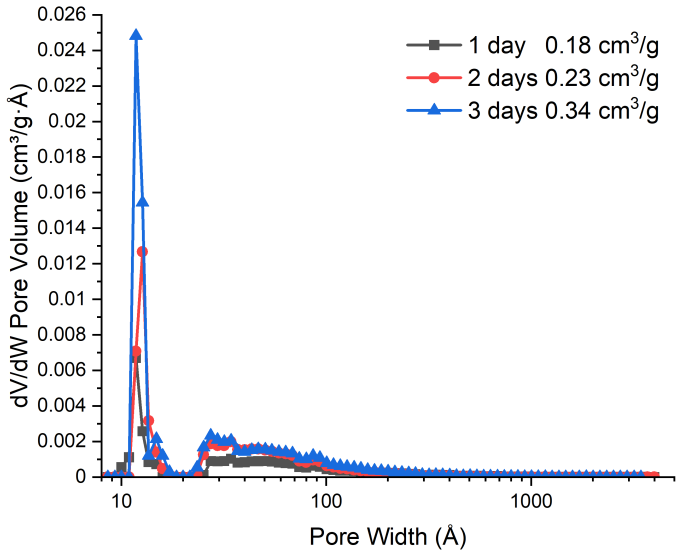

Figure C.17: Pore size distribution calculated using a density functional theory model (slit) on N_2 adsorption isotherms of Mg_2NiAl SLDHs prepared with different reaction times (Figure C.16). The pore volumes at $p/p^0 = 1$ of the samples are given in the legend.

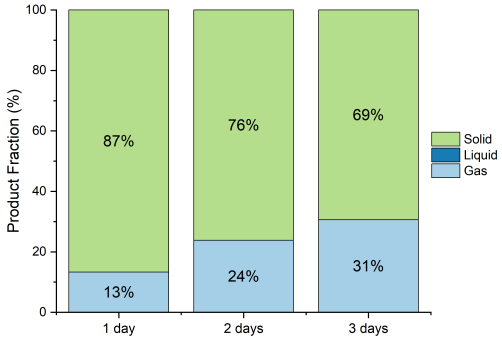

(a) Distribution of solid, liquid and gas products

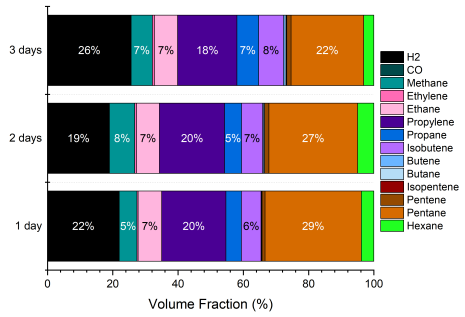

(b) Gas product distribution by volume.

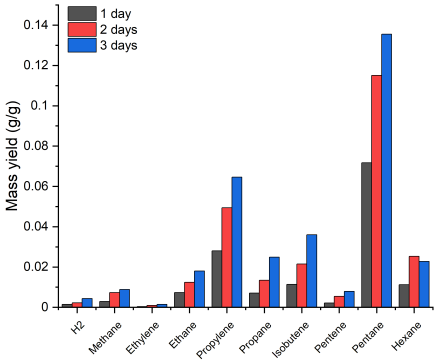

(c) Gas product yields.

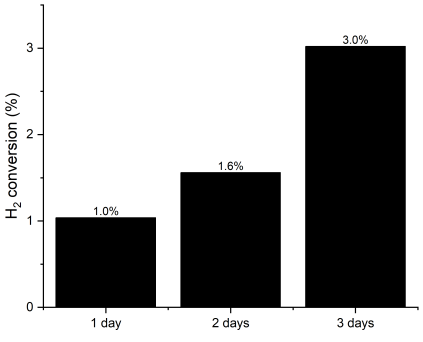

(d) Hydrogen conversion as fraction of the amount present in the polypropylene.

Figure C.18: Polypropylene pyrolysis data using 10 wt% Mg_2NiAl SLDH catalysts prepared using different ageing times at 300 °C.

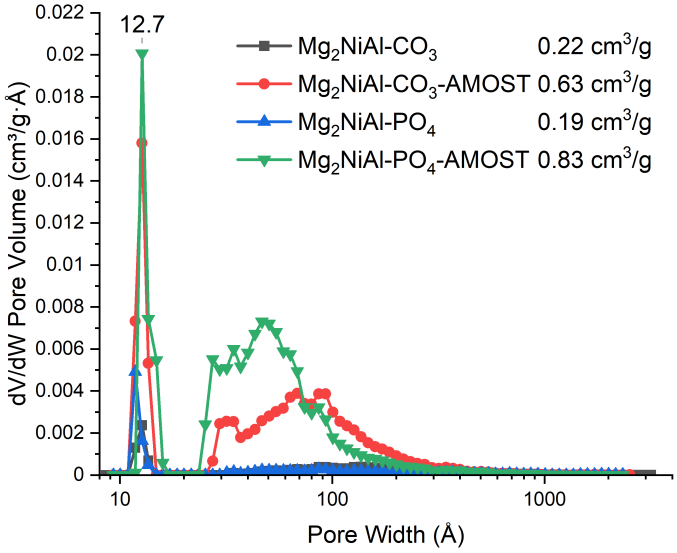

Figure C.19: Pore size distribution calculated using a density functional theory model (slit) on N_2 adsorption isotherms of Mg_2NiAl LDHs (Figure 5.25). The pore volumes at $p/p^0 = 1$ of the samples are given in the legend.

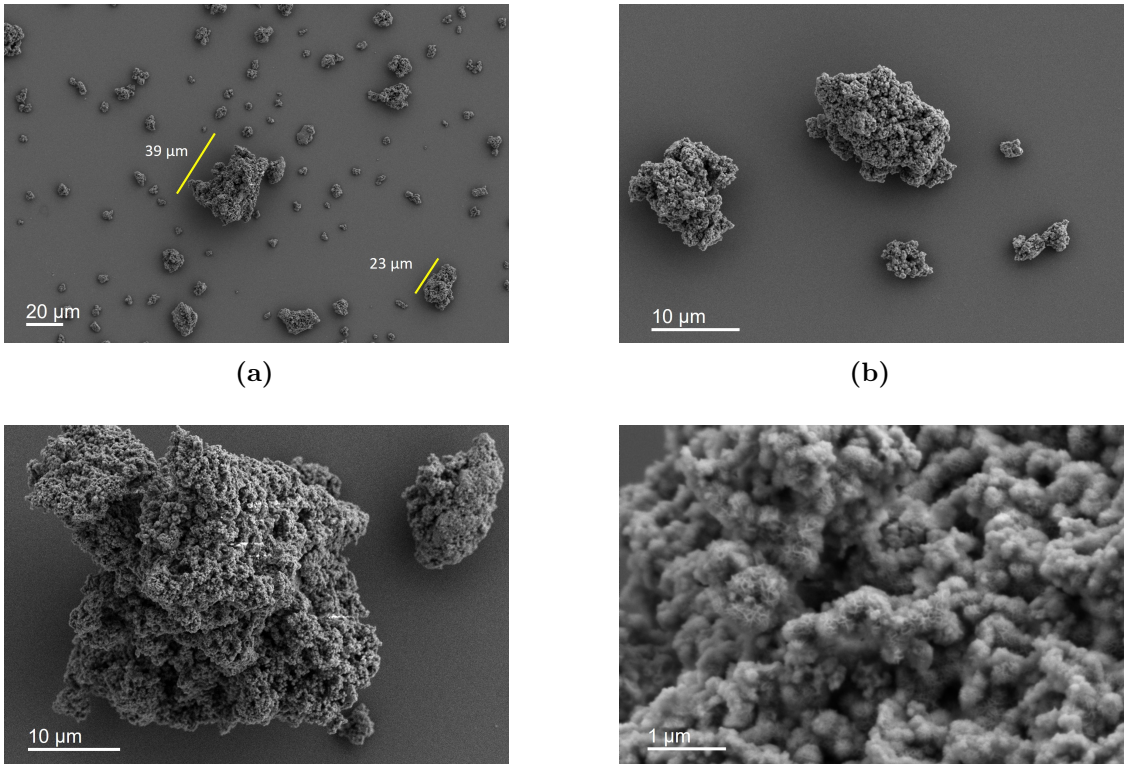

(a) (b)

(c) (d)

Figure C.20: HR-SEM images of $Mg_2NiAl\,CO_3$ LDH.

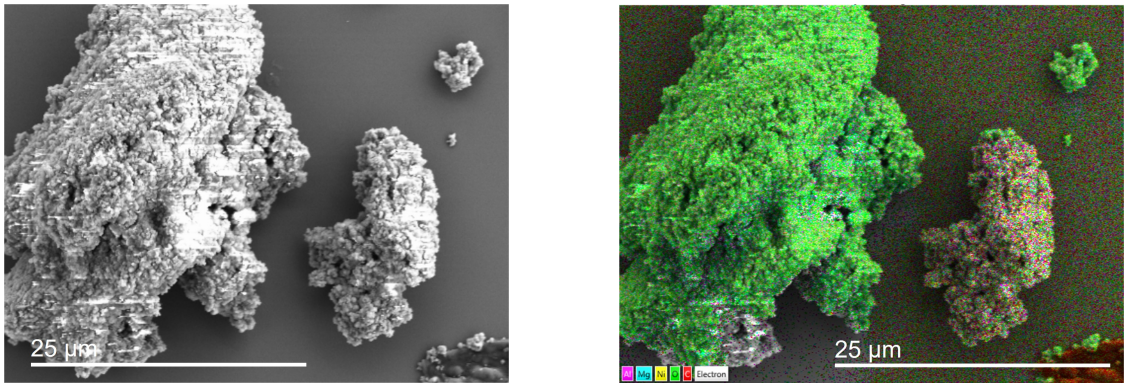

(a) (b)

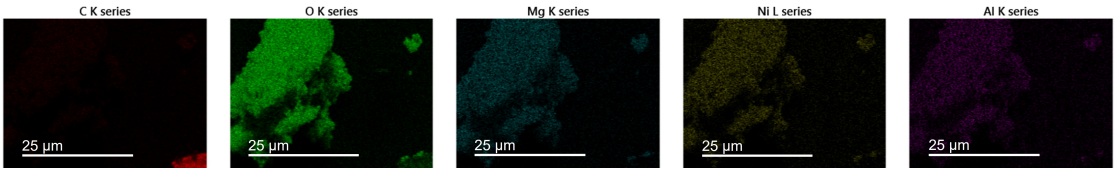

(c) (d) (e) (f) (g)

Figure C.21: HR-SEM EDX mapping of $Mg_2NiAl\,CO_3$ LDH.

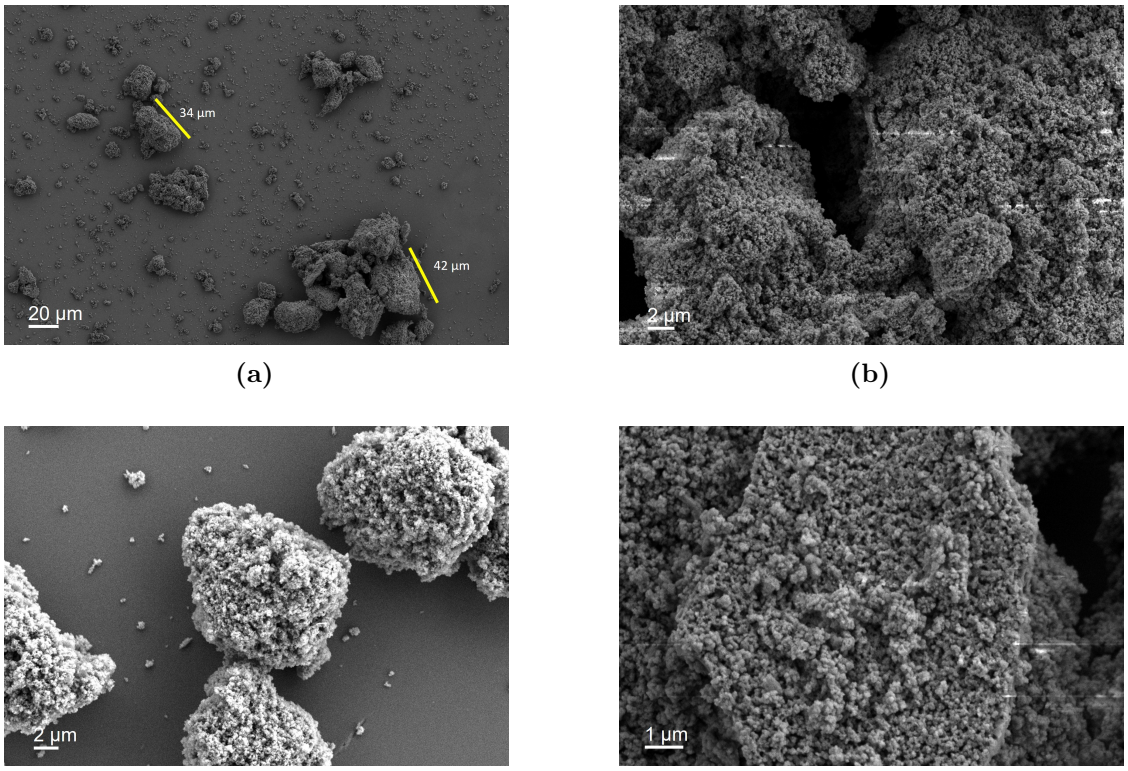

(a) (b)

(c) (d)

Figure C.22: HR-SEM images of $Mg_2NiAl\,PO_4$ LDH.

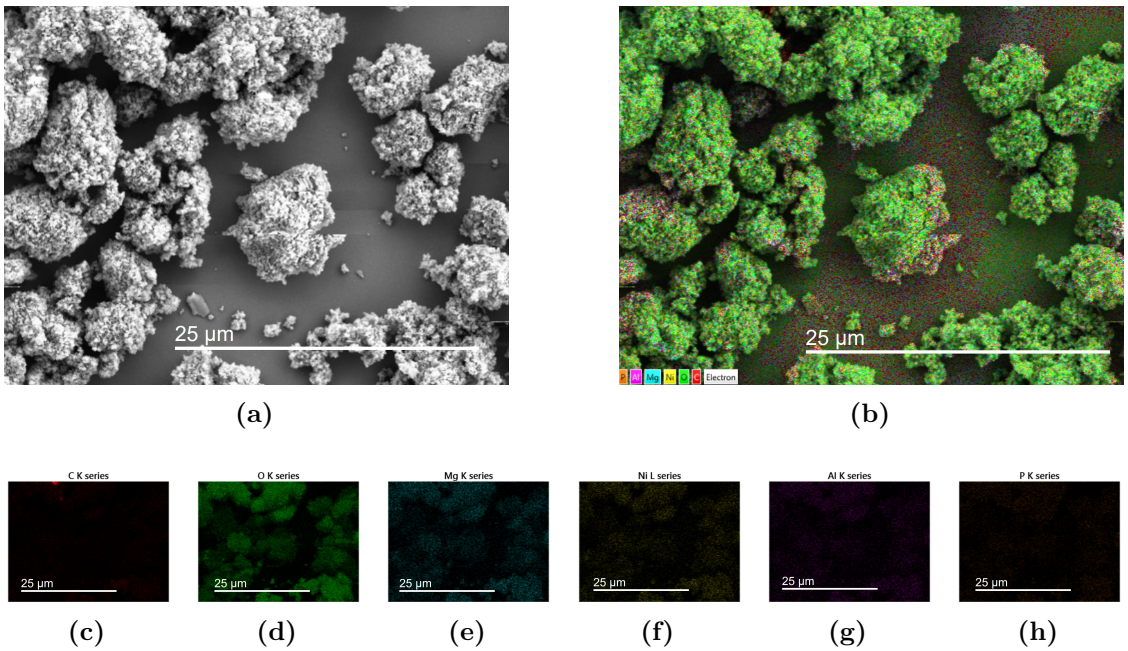

(a) (b)

(c) (d) (e) (f) (g) (h)

Figure C.23: HR-SEM EDX mapping of $Mg_2NiAl\,PO_4$ LDH.

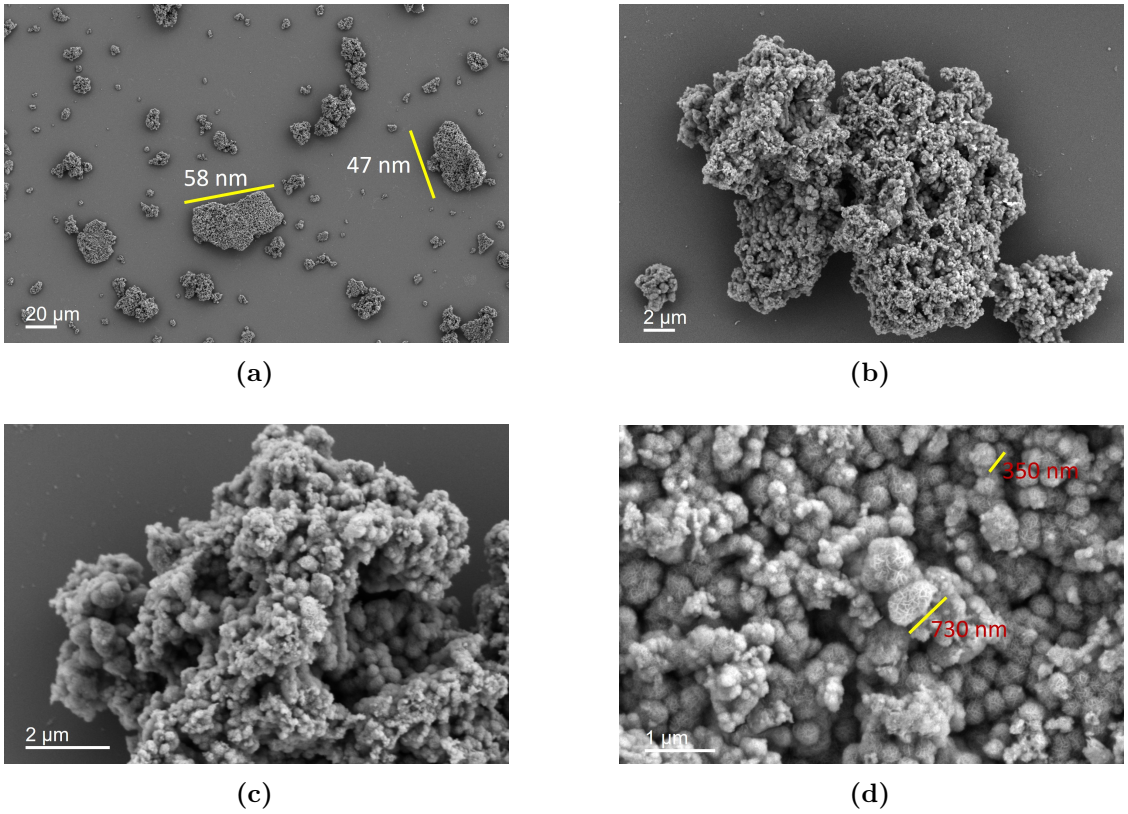

(a) (b)

(c) (d)

Figure C.24: HR-SEM images of $Mg_2NiAl\,CO_3$ LDH with AMOST treatment.

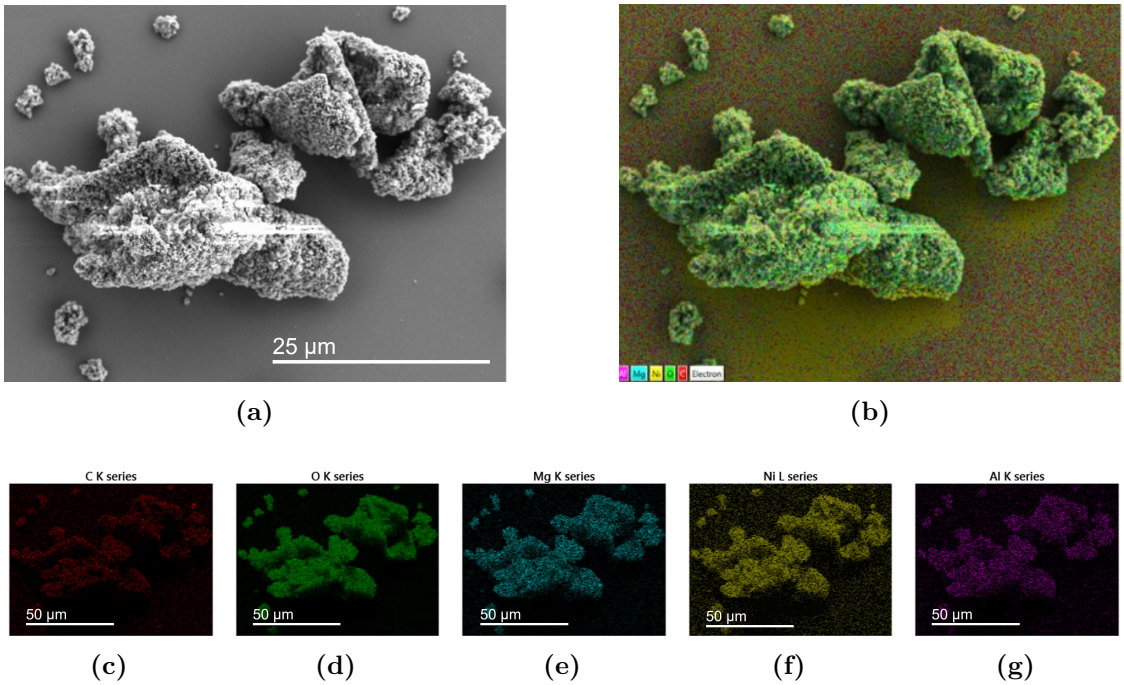

(a) (b)

(c) (d) (e) (f) (g)

Figure C.25: HR-SEM EDX mapping of HR-SEM images of $Mg_2NiAl\,CO_3$ LDH with AMOST treatment.

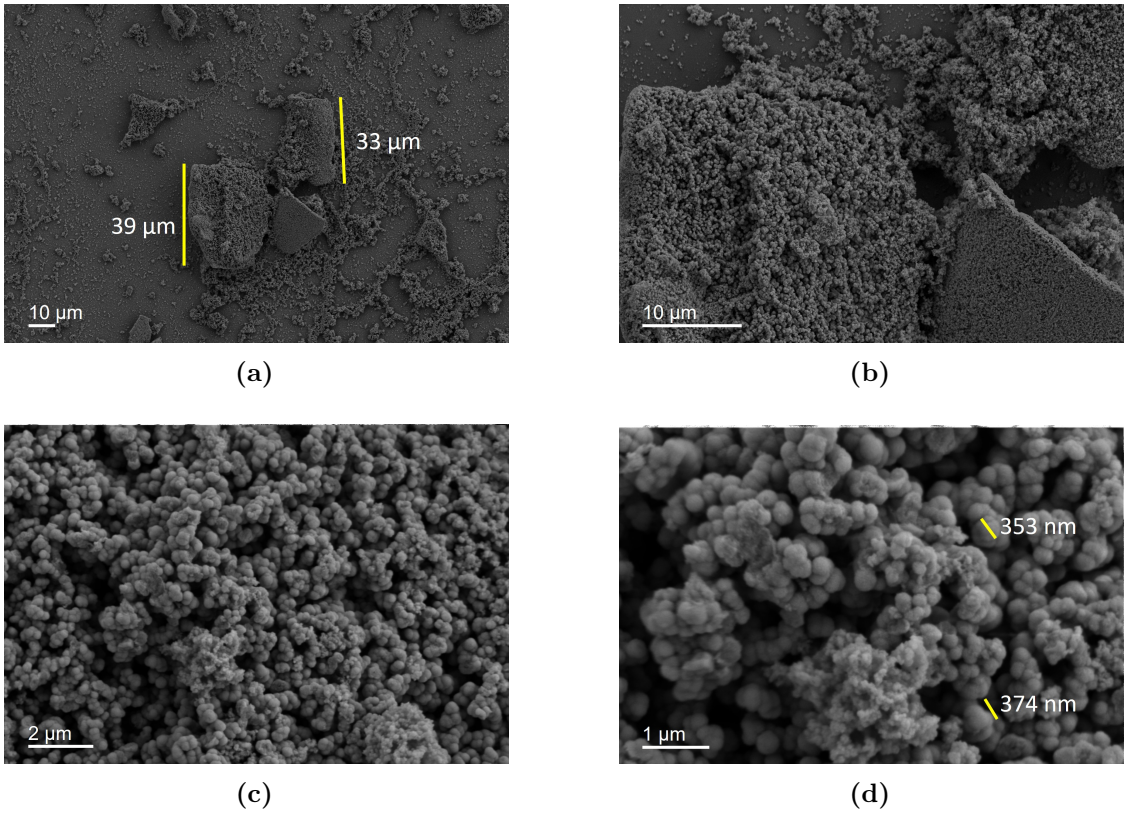

(a) (b)

(c) (d)

Figure C.26: HR-SEM images of $Mg_2NiAl\,PO_4$ LDH with AMOST treatment.

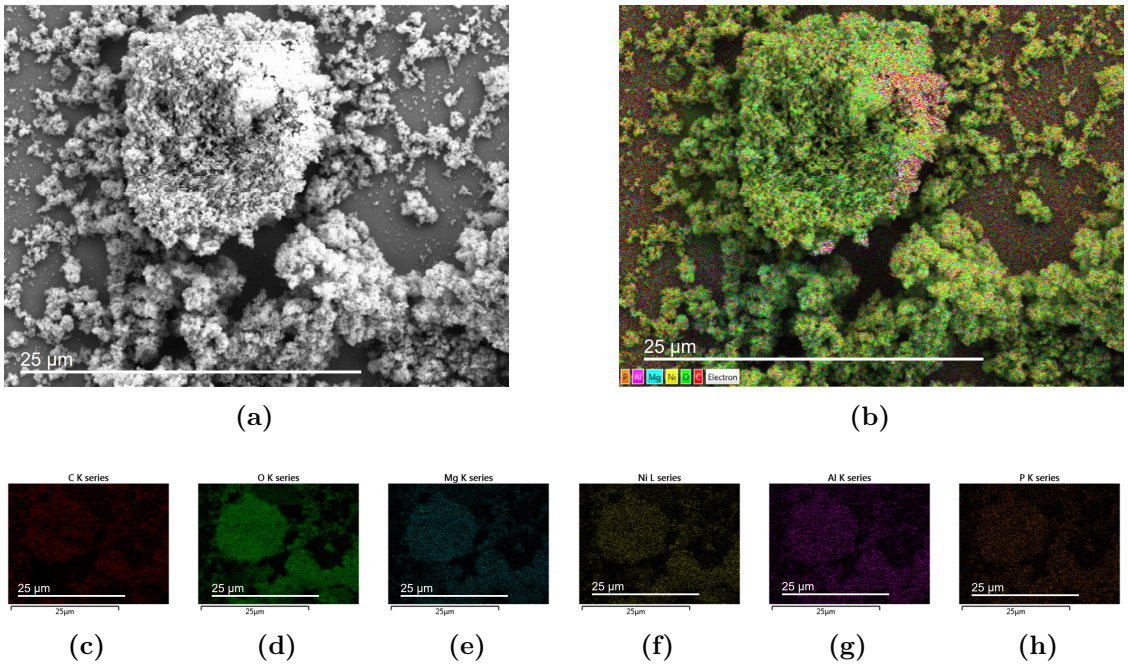

(a) (b)

(c) (d) (e) (f) (g) (h)

Figure C.27: HR-SEM EDX mapping of $Mg_2NiAl\,PO_4$ LDH with AMOST treatment.

Figure C.28: Photograph of dried $Mg_2NiAl\,CO_3$ LDH catalysts. Left to right: $Mg_2NiAl\,CO_3$, $Mg_2NiAl\,CO_3$ AMOST, $Mg_2NiAl\,PO_4$ and $Mg_2NiAl\,PO_4$ AMOST.

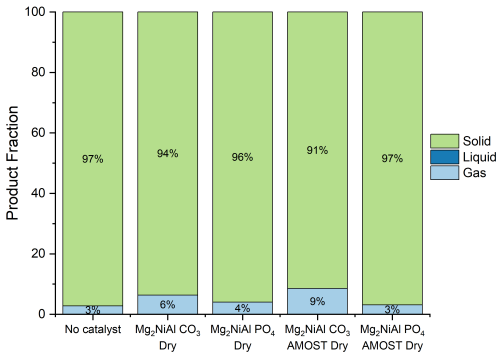

(a) Distribution of solid, liquid and gas products

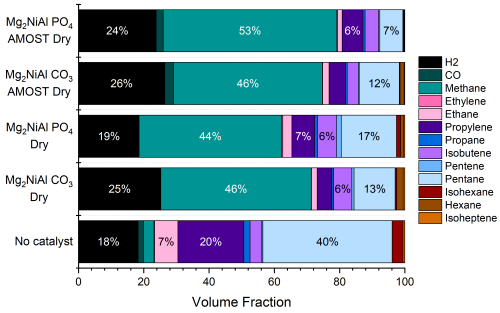

(b) Gas product distribution by volume.

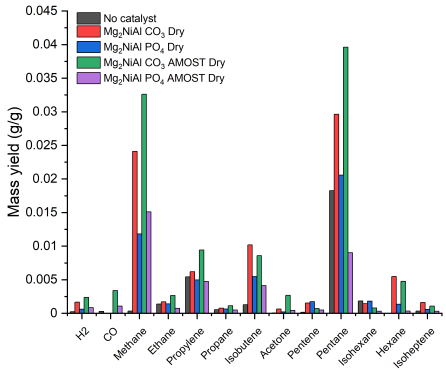

(c) Hydrogen conversion as fraction of the amount present in the polypropylene.

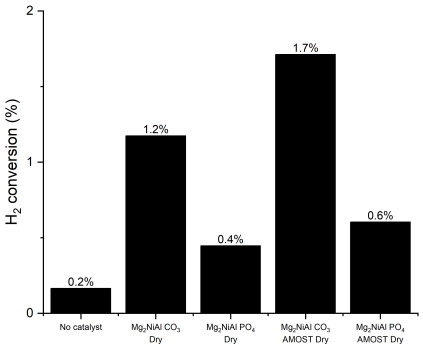

(d) Gas product yields.

Figure C.29: Polypropylene pyrolysis data using 20 wt% dried Mg_2NiAl SLDHs at 290 °C.

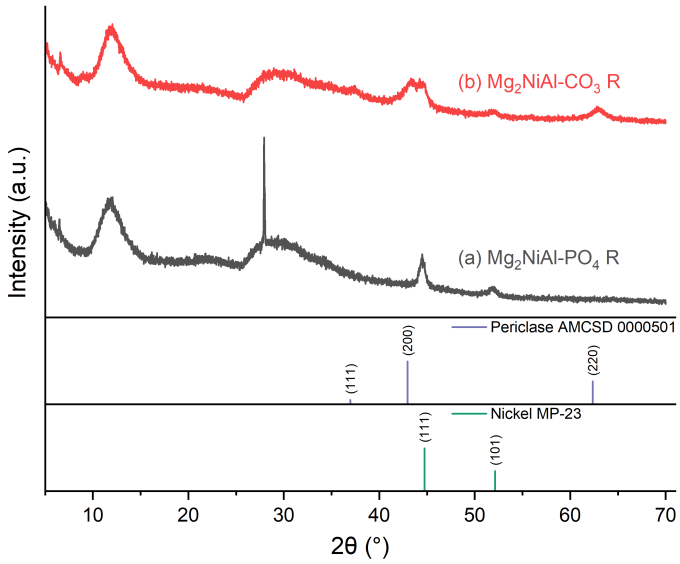

Figure C.30: XRD patterns of Mg_2NiAl LDHs reduced at 650 °C Peaks can be indexed to the pattern below (Periclase - AMCSD 0000501 and Nickel - MP-23).[6,7]

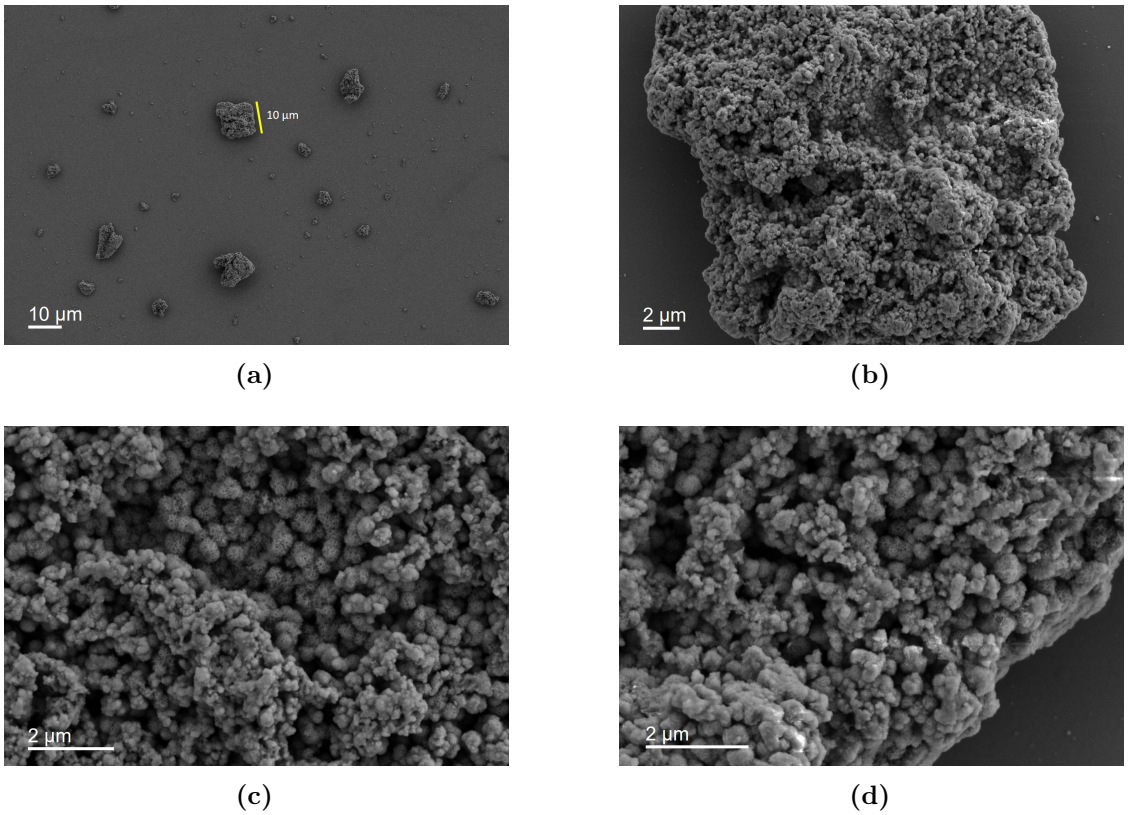

(a) (b)

(c) (d)

Figure C.31: HR-SEM images of calcined and reduced (at 650 °C) $Mg_2NiAl\,CO_3$ LDH.

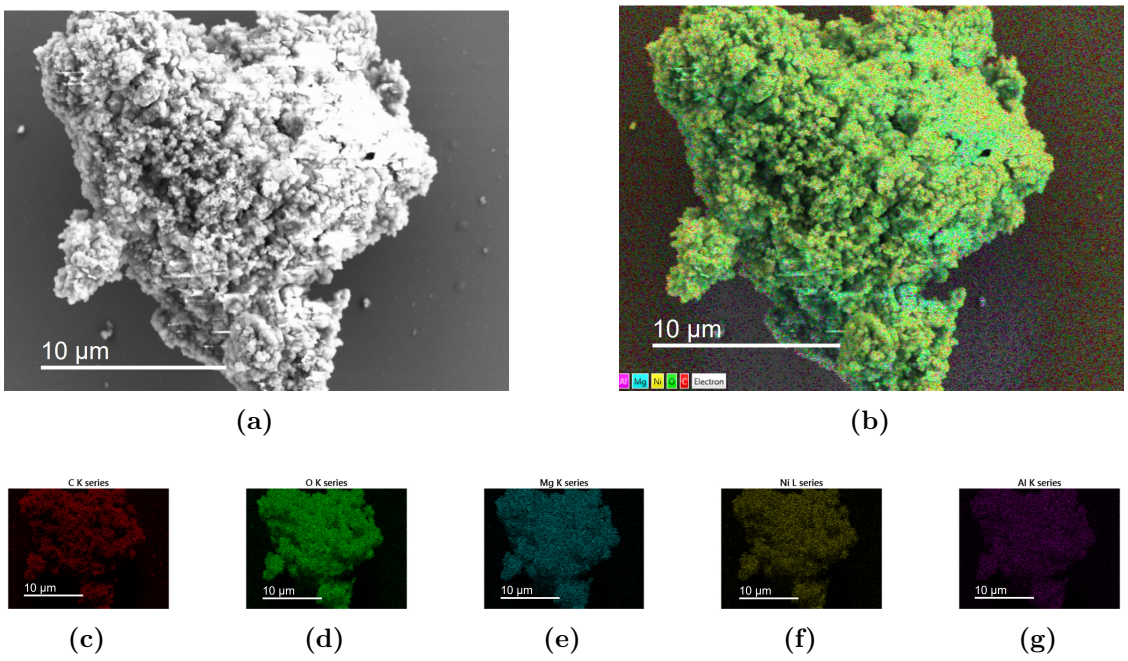

(a) (b)

(c) (d) (e) (f) (g)

Figure C.32: HR-SEM EDX mapping of calcined and reduced (at 650 °C) $Mg_2NiAl\,CO_3$ LDH.

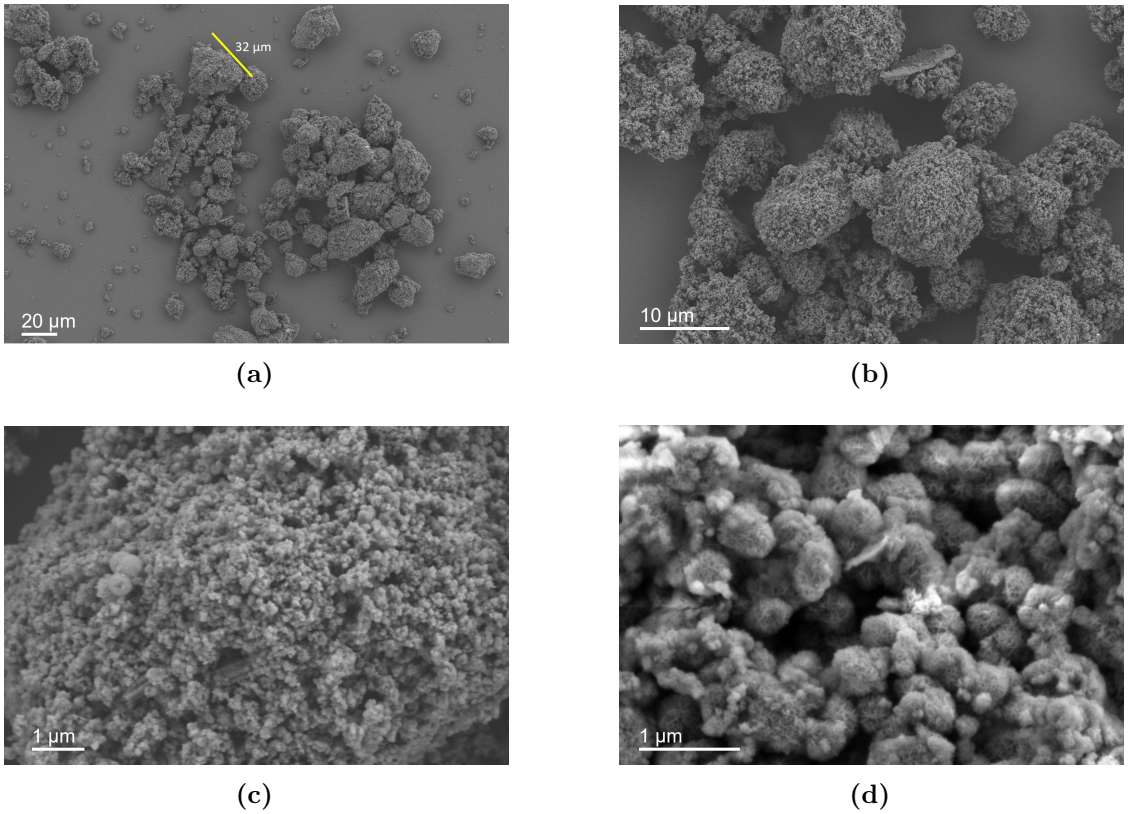

(a) (b)

(c) (d)

Figure C.33: HR-SEM images of calcined and reduced (at 650 °C) $Mg_2NiAl\,PO_4$ LDH.

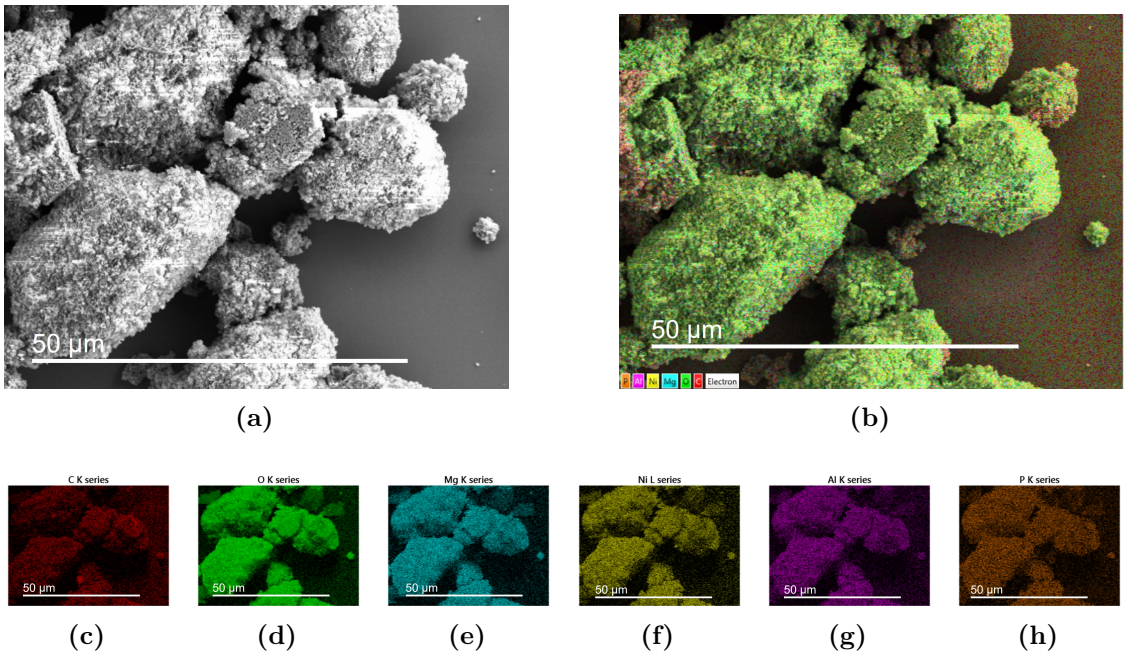

(a) (b)

(c) (d) (e) (f) (g) (h)

Figure C.34: HR-SEM EDX mapping of calcined and reduced (at 650 °C) $Mg_2NiAl\,PO_4$ LDH.

References

(1) *Highlights in Mineralogical Crystallography*, ed. T. Armbruster and R. M. Danisi, DE GRUYTER, 2015.

(2) H. Yang, L. Martinelli, F. Tasso, A. R. Sprocati, F. Pinzari, Z. Liu, R. T. Downs and H. J. Sun, 2014, **99**, 1761–1766.

(3) P. Villars and K. Cenzual, eds., *NH4MgPO4 · H2O ([NH4]Mg[PO4][H2O]) Crystal Structure: Datasheet from "PAULING FILE Multinaries Edition – 2022" in SpringerMaterials (https://materials.springer.com/isp/crystallographic/docs/sd_1400160).*

(4) K. Persson, *Materials Data on NaAlO2 (SG:33) by Materials Project*, 2014.

(5) K. O. Kongshaug, H. Fjellvåg and K. P. Lillerud, *Solid State Sci.*, 2000, **2**, 205–214.

(6) R. Downs and M. Hall-Wallace, *Am. Mineral.*, 2003, **88**, 247–250.

(7) K. Persson, *Materials Data on Ni (SG:225) by Materials Project*, 2016.